Technische Universität München
TUM School of Life Sciences

Synthesis and studies on interactions and amyloid inhibitor function of peptides containing cyclic constraints

Beatrice Dalla Volta

Vollständiger Abdruck der von der TUM School of Life Sciences der Technischen Universität München zur Erlangung einer

Doktorin der Naturwissenschaften (Dr. rer. nat.)

genehmigten Dissertation.

Vorsitz: Prof. Dr. Dmitrij Frischmann

Prüfer*innen der Dissertation:

1. Prof. Dr. Aphrodite Kapurniotu
2. Prof. Dr. Johannes Buchner

Die Dissertation wurde am 30.05.2023 bei der Technischen Universität München eingereicht und durch die TUM School of Life Sciences am 19.07.2023 angenommen.

Part of this thesis was previously published in:

> Karin Taş, Beatrice Dalla Volta, Christina Lindner, Omar El Bounkari, Kathleen Hille, Yuan Tian, Xènia Puig-Bosch, Markus Ballmann, Simon Hornung, Martin Ortner, Sophia Prem, Laura Meier, Gerhard Rammes, Martin Haslbeck, Christian Weber, Remco T. A. Megens, Jürgen Bernhagen and Aphrodite Kapurniotu. Designed peptides as nanomolar cross-amyloid inhibitors acting via supramolecular nanofiber co-assembly. Nat. Commun 2022;13(1):5004.

Abstract

Protein misfolding and self-assembly in amyloid fibrils have been documented for numerous proteins and polypeptides. Circa 40 of them are associated with devastating cell-degenerative diseases, such as Aβ peptides (Aβ40(42)) and islet amyloid polypeptide (IAPP), which are involved in the development of Alzheimer's disease and type 2 diabetes (T2D), respectively.

Increasing evidence suggests similarities and links between AD and T2D. Moreover, several studies suggest the colocalization of IAPP and Aβ42 peptides in the brain and the pancreas of AD and T2D patients. IAPP and Aβ40(42) sequences share 25% identity and 50% similarity. Furthermore, earlier *in vitro* studies of our group revealed that Aβ40(42) and IAPP interact with each other with high affinity. We also showed that their interaction is mediated by specific short "hot segments" of Aβ and IAPP and that the same segments are also crucial for the self-assembly of the two peptides. In addition to the above findings, various *in vitro* and *in vivo* studies have suggested that cross-seeding interactions between IAPP and Aβ40(42) might accelerate amyloid formation in both AD and T2D.

Molecules that prevent amyloid self-assembly and cross-seeding interactions of IAPP and Aβ40(42) might thus be promising anti-amyloid drug candidates for both diseases. In previous studies of our group, the IAPP "hot segments" were used to design peptides termed "interaction surface mimics" (ISMs). ISMs consisted of IAPP segments IAPP(8-18) and IAPP(22-28) covalently linked to each other by different tripeptide units. The nature of the linker dictated the conformation of the ISMs and their ability to inhibit the amyloid self-assembly of IAPP or Aβ40(42). Thereafter, several rounds of optimization of one of the ISMs, including shortening, cyclisation, and substitutions of L- with D-amino acids, yielded 17-residue long macrocyclic peptides termed "macrocyclic inhibitory peptides" or MCIPs. MCIP **2e** was a potent inhibitor of Aβ40(42) and, in addition, it exhibited high proteolytic stability in human plasma *in vitro* and BBB permeability in a human cerebral endothelial cell model.

In this work, the sequence of MCIP **2e** and related analogs was further shortened. "Head-to-tail" cyclization and D-amino acids were used for optimizing conformational rigidity, proteolytic stability and BBB permeability. In total, four cyclic hexapeptides termed "minimized IAPP mimics" or MIMs (**2f**, **2g**, **2h** and **2i**) and four linear control peptides (**2f linear**, **2g linear**, **2h linear** and **2i linear**) were synthesized and studied.

Biophysical and functional studies indicated that cyclisation stabilized a conformation which confers potent inhibitory activity towards both IAPP and Aβ42. In fact, MIMs were found to bind with high affinity both IAPP and Aβ42 and were potent inhibitors of their amyloid self-assembly and cytotoxicity whereas linear control peptides showed very weak binding and no anti-amyloidogenic activity. Furthermore, **2i** effectively suppressed self- and cross-seeding events of both IAPP and Aβ42.

Various methods were used to characterize the interactions of MIMs and their linear controls with IAPP and Aβ42 and the sequence parts of IAPP and Aβ42 which were involved in their interactions were identified. In addition, an experimental approach in which different methods were combined to follow the formation of cytotoxic amyloid oligomers was developed. This approach was used to study inhibitory effects of both MIMs and of the so-called "amyloid core mimics" (ACMs), another class of amyloid inhibitors recently developed in our laboratory. The results of the biophysical and biochemical studies showed that despite their minimum size and their minimal IAPP-derived elements, MIMs are able to interact with various species of the amyloidogenic pathways of IAPP and Aβ42 and suggested that their interactions might interfere with the structural organization of amyloid core regions of IAPP and Aβ42 and contribute to their potent anti-amyloid effects.

Importantly, *ex vivo* electrophysiological studies in mouse brains (in collaboration) showed that MIMs **2i** and **2g** ameliorated the inhibition of hippocampal synaptic long-term potentiation (LTP) caused by Aβ42 aggregates. Furthermore, **2i** and **2g** were found to have strongly improved proteolytic stabilities in human plasma *in vitro* in comparison to their template peptide **2e**, and **2i** exhibited a good BBB permeability in a human cerebral endothelial cell model (in collaboration) as well. These two cyclic hexapeptides could thus be promising leads for the development of novel anti-amyloid drugs in AD, T2D or both diseases.

Zusammenfassung

Die Proteinfehlfaltung und -selbstassoziation in Amyloidfibrillen ist für zahlreiche Proteine und Polypeptide dokumentiert worden. Etwa 40 von ihnen werden mit verheerenden zelldegenerativen Krankheiten in Verbindung gebracht, wie zum Beispiel das β-Amyloidpeptid (Aβ40(42)) und das Insel-Amyloid-Polypeptid (IAPP), die an der Entstehung der Alzheimer-Krankheit (AD) bzw. am Typ-2-Diabetes (T2D) beteiligt sind.

Zugleich gibt es immer mehr Hinweise auf Gemeinsamkeiten und Zusammenhänge zwischen AD und T2D. Darüber hinaus deuten mehrere Untersuchungen darauf hin, dass IAPP und Aβ42 im Gehirn und in der Bauchspeicheldrüse von AD- und T2D-Patienten kolokalisieren. Die Sequenzen von IAPP und Aβ40(42) sind zu 25 % identisch und zu 50 % ähnlich und frühere Untersuchungen unserer Gruppe haben gezeigt, dass Aβ40(42) und IAPP mit hoher Affinität miteinander interagieren. Wir haben auch gezeigt, dass ihre Interaktion durch spezifische kurze "*hot-spot*"-Peptidregionen vermittelt wird, und dass dieselben Segmente auch für die Selbstassoziation der beiden Peptide entscheidend sind. Zusätzlich zu den oben genannten Erkenntnissen haben verschiedene *in-vitro*- und *in-vivo*-Studien nahegelegt, dass Kreuznukleations-Wechselwirkungen zwischen IAPP und Aβ40(42) die Amyloidbildung sowohl bei AD als auch bei T2D beschleunigen könnten.

Daher könnten Moleküle, welche die Amyloidogenese und die Kreuznukleations-Wechselwirkungen von IAPP und Aβ40(42) verhindern, vielversprechende Leitstrukturen für die Entwicklung von Anti-Amyloid-Medikamenten bei beiden Krankheiten sein. In diesem Zusammenhang wurden in früheren Arbeiten unserer Gruppe die „*hot-spot*"-Regionen von IAPP verwendet, um Peptide, die "*interaction surface mimics*" (ISMs) genannt wurden, zu entwerfen. Die ISMs bestehen aus den IAPP-Segmenten IAPP(8-18) und IAPP(22-28), die durch verschiedene Tripeptideinheiten kovalent miteinander verbunden sind. Dabei bestimmt die Art des Tripeptid-Linkers die Konformation der ISMs und ihre Fähigkeit, die amyloide Aggregation von IAPP oder Aβ40(42) zu hemmen. Mehrere Optimierungsrunden an einem der ISMs, einschließlich der Verkürzung, der Zyklisierung und des Ersetzens von L- durch D-Aminosäuren, führten anschließend zu makrozyklischen Peptiden, welche aus 17 Aminosäuren bestehen und "*macrocyclic inhibitory peptides*" oder MCIPs genannt wurden. Das MCIP **2e** erwies sich dabei als ein potenter Inhibitor der Amyloidogenese von Aβ40(42), der sich darüber hinaus aus einer hohen proteolytischen Stabilität in menschlichem Plasma in vitro und eine gute Blut-Hirn-Schranke-Permeabilität in einem humanen zerebralen Endothelzellmodell auszeichnet.

In dieser Arbeit wurde die Sequenz von MCIP **2e** und verwandten Analoga weiter gekürzt. "*Head-to-tail*"-Zyklisierungen und D-Aminosäuren wurden zur Optimierung der Konformationseinschränkung, der proteolytischen Stabilität und der Blut-Hirn-Schranke-Permeabilität eingesetzt. Insgesamt wurden vier zyklische Hexapeptide (**2f**, **2g**, **2h** und **2i**), die "*minimized IAPP-mimics*" oder MIMs genannt wurden, und vier lineare Kontrollpeptide (**2f linear**, **2g linear**, **2h linear** und **2i linear**) synthetisiert und untersucht.

Biophysikalische und funktionelle Studien weisen darauf hin, dass die Zyklisierung eine Konformation stabilisiert, die sowohl gegenüber IAPP als auch gegenüber Aβ42 eine starke hemmende Wirkung entfaltet. Tatsächlich stellte sich heraus, dass die MIMs mit hoher Affinität sowohl an IAPP als auch an Aβ42 binden und deren Amyloidogenese und Zytotoxizität stark hemmen. Im Gegensatz dazu zeichnen sich die linearen Kontrollpeptide durch eine sehr schwache

Bindung und keine anti-amyloidogene Aktivität aus. Das MIM **2i** ist darüber hinaus in der Lage, sowohl die Selbst- als auch die Kreuznukleation von IAPP und Aβ42 effektiv zu unterdrücken.

Verschiedene Methoden wurden verwendet, um die Wechselwirkungen von MIMs bzw. ihrer linearen Kontroll-Peptide mit IAPP und Aβ42 zu charakterisieren. Die Sequenzteile von IAPP und Aβ42, die sich an ihren Wechselwirkungen mit den MIMs beteiligen, wurden identifiziert. Darüber hinaus wurde ein experimenteller Ansatz entwickelt, bei dem verschiedene Methoden kombiniert wurden, um die Bildung von zytotoxischen Amyloid-Oligomeren zu verfolgen. Mit diesem Ansatz wurde die hemmende Wirkung sowohl der MIMs, als auch der sogenannten "*amyloid core mimics*" (ACMs), einer anderen Klasse von Amyloid-Inhibitoren, die kürzlich in unserem Labor entwickelt wurden, untersucht. Die Ergebnisse der biophysikalischen und biochemischen Studien zeigen, dass MIMs trotz ihrer geringen Größe und ihrer minimalen von IAPP abgeleiteten Elemente in der Lage sind, mit verschiedenen strukturellen Spezies des amyloidogenen Selbstassemblierungsprozesses von IAPP und Aβ42 zu interagieren. Die Befunde stützen die Hypothese, dass diese Wechselwirkungen die strukturelle Organisation von Amyloidkernregionen von IAPP und Aβ42 stören und zur starken anti-amyloidogenen Funktion der MIMs beitragen könnten.

Elektrophysiologische Untersuchungen in Maushirnschnitten *ex-vivo* (in Zusammenarbeit mit einem kooperierenden Labor) zeigten, dass MIMs **2i** und **2g** die durch Aβ42-Aggregate verursachte Beeinträchtigung der hippocampalen synaptischen Langzeitpotenzierung (LTP) unterbinden können. Darüber hinaus wurde festgestellt, dass **2i** und **2g** im Vergleich zu ihrem Templatpeptid **2e** eine stark verbesserte proteolytische Stabilität in humanem Plasma *in vitro* aufweisen. Weiterhin zeichnete sich **2i** auch durch eine gute Durchlässigkeit in einem menschlichen zerebralen Endothelzellmodell der Blut-Hirn-Schranke aus (Arbeiten in Zusammenarbeit mit einem kooperierenden Labor). Zusammenfassend könnten diese beiden zyklischen Hexapeptide vielversprechende Ansatzpunkte für die Entwicklung neuer Anti-Amyloid-Medikamente gegen Alzheimer, T2D oder beider Krankheiten sein.

Abbreviations

α	Alpha
Å	Angstrom
AA	Amino acid
Aβ	β-Amyloid peptide
Aβ40	β-Amyloid peptide (sequence [1-40])
Aβ42	β-Amyloid peptide (sequence [1-42])
ACM	Aβ core mimics
ACN	Acetonitrile
AC_2O	Acetic anhydride
AD	Alzheimer's disease
APP	Amyloid precursor protein
β	Beta
BCA	Bicichoninic acid
Boc	Tert-butyloxycarbonyl
BSA	Bovine serum albumin
C	Concentration
CD	Circular dichroism
Cryo-EM	Cryogenic electron microscopy
CSF	Cerebrospinal fluid
DB	Dot blot
DCM	Dichloromethane
DIEA	Diisopropylethylamine
DMF	Dimethylformamide
DMSO	Dimethylsulfoxide
Eq.	Equivalent
FCS	Fetal calf serum
fAβ42	Aβ42 fibrils
fIAPP	IAPP fibrils
FITC Aβ42	FITC-βAla-Amyloid-β-protein(1-42) (ammonium salt)
Fluos	5(6)-Carboxyfluorescein
Fmoc	9-Fluorenylmethoxycarbonyl
Gdn	Guanidinium
h	Hour
HCl	Hydrochloric acid
HFIP	1,1,1,3,3,3-Hexafluoro-2-propanol
HATU	2-(7-Aza-1H-benzotriazole-1-yl)-1,1,3,3-tetramethyluroniumhexafluorophosphate
HBTU	(2-(1H-benzotriazol-1-yl)-1,1,3,3-tetramethyluronium hexafluorophosphate
HOBt	1-Hydroxybenzotriazole
IC_{50}	Half maximal inhibitory concentration
ISM(s)	Interaction surface mimics peptides
IAPP	Islet amyloid polypeptide (human)
IAPP-GI	[(N -Me)G24, (N -Me)I26] -IAPP
M	Molar
MALDI	Matrix-assisted laser desorption ionization mass spectrometry
mAβ42	Monomeric Aβ42
MCIP(s)	Macrocyclic inhibitor peptides

mg	Milligram
mIAPP	Monomeric IAPP
MIM(s)	Minimized IAPP mimics
min	Minutes
mM	Millimolar
mL	Milliliter
μg	Microgram
μM	Micromolar
μL	Microliter
MTT	3-(4,5-dimethylthiazol-2-yl)-2,5-diphenyltetrazolium bromide
Mtt	4-Methyltrityl
MW	Molecular weight
nm	Nanometer
nM	Nanomolar
NaOH	Sodium hydroxide
NMR	Nuclear magnetic resonance
oAβ42	Oligomeric Aβ42
oIAPP	Oligomeric IAPP
Pbf	2,2,4,6,7-Pentamethyldihydrobenzofuran-5-sulfonyl
PC-12	Rat-pheochromocytoma cell-line
POD	Peroxidase
rIAPP	Rat IAPP
RIN-5mf	Mice pancreatic β cells
RP-HPLC	Reverse phase-high performance liquid chromatography
t_R	Retention time
$t_{1/2}$	Half-life time
SD	Standard deviation
SDS	Sodium dodecyl sulfate
SEC	Size exclusion chromatography
ss-NMR	Solid-state nuclear magnetic resonance
SPPS	Solid phase peptide synthesis
TBS	Tris buffer saline
TEM	Transmission electron microscopy
TFA	Trifluoroacetic acid
TFE	Trifluoroethanol
ThT	Thioflavin-T
TIS	Triisopropylsilan
T2D	Type 2 diabetes
UV	Ultraviolet

Contents

1 Introduction

1.1 Protein misfolding and human diseases

To ensure the normal functioning of cells and organisms in physiological conditions, the correct activity of a network of proteins is essential. The function of a protein depends on its three-dimensional structure, which is determined by its amino-acid sequence. Protein folding is regulated by chaperones, which remove malfunctioning proteins. However, increasing evidence indicates that protein misfolding and aggregation is the most likely cause of various neurological and systemic diseases [1–3]. The hallmark feature of conformational disorders is that a particular protein can fold into a stable alternative conformation, which in most cases results in its aggregation and accumulation in tissues as fibrillar deposits. Eventually, these fibrils form deposits known as "plaques" and display pathogenic effects by misbalancing the physiological conditions of the tissues in which they form (Figure 1). These deposits are mainly extracellular, although more rarely also intracellular, and consist of the largest part of the specific protein subjected to the folding failure. Histological studies have shown that the plaques also contain other biological components, including metal ions, glycosaminoglycans, serum amyloid P component, apolipoprotein and E, and collagen [2,3].

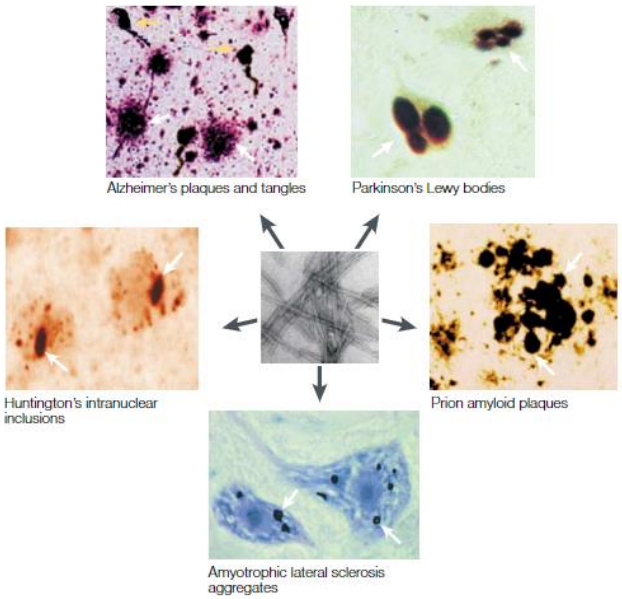

Figure 1. Cerebral aggregates in neurodegenerative diseases. Extracellular amyloid plaques (white arrows) and intracytoplasmic neurofibrillary tangles (yellow arrows) are pathological features of Alzheimer's disease. Intracytoplasmic aggregates are typically present in neuronal cells of patients affected by Parkinson's disease and amyotrophic lateral sclerosis. Intranuclear deposits of huntingtin are observed in Huntington's disease patients. Extracellular prion amyloid plaques that form in different brain regions are present in some cases of transmissible spongiform encephalopathy. Figure taken from reference[1].

More than 37 diseases are associated with the formation of amyloid plaques (Table 1). It is also generally accepted that the pathogenic effect of amyloids is not mediated exclusively by the fibrils but also by toxic oligomeric intermediates [3], especially in the case of central nervous system (CNS)-related diseases. The diseases can be broadly grouped into a) neurodegenerative conditions, in which the amyloid deposition is localised in the CNS, as in

Alzheimer`s disease or Parkinson`s disease b) neuropathic localised amyloidoses, as in Type 2 diabetes, in which amyloid plaques form in the pancreas, and c) non-neuropathic systemic amyloidoses, involving several compartments of the organism, as in senile systemic amyloidosis[2]. Misfolding diseases can be further classified as sporadic (85%), like Alzheimer's and Parkinson's disease; hereditary (10%), such as lysozyme and fibrinogen amyloid; or transmissible (5%) in humans as well as in other mammals, as spongiform encephalopathies[2].

Table 1. Amyloid proteins and some clinically relevant diseases. Table modified from reference [2].

Clinical syndrome	Amyloid protein	Number of residues	Native structure
Alzheimer`s Disease Inclusion body myositis (orphan)	Amyloid-β peptides (1-40, 1-42)	40 or 42	Natively unfolded
Type 2 diabetes	Amylin or Islet amyloid polypeptide (IAPP)	37	Natively unfolded
Dialysis-related amyloidosis	β_2-Microglobulin	99	All-β, Ig like
Parkinson`s disease	α-Synuclein	140	Natively unfolded
Transmissible spongiform encephalopathies (CJD)	Prion protein	253	Natively unfolded (residues 1–120) and α-helical (residues 121–230)
Fronto-temporal dementias	Tau	352-441	Natively unfolded
Huntington disease	Huntingtin (polyQ expansion)	3144	Largely natively unfolded
Amyotrophic lateral sclerosis	Superoxide dismutase	153	All-β, Ig like
Senile systemic amyloidosis Familial amyloidotic polyneuropathy	Transthyretin	127	All-β, prealbumin like
Cataract	γ-Crystallin	Variable	All-β, γ-crystallin like
Primary systemic amyloidosis	Ig light chains	~90	All-β, Ig like
Secondary systemic amyloidosis	Serum amyloid A	76–104	All-α, unknown fold

1.2 Amyloidogenesis in Alzheimer`s disease

Alzheimer`s disease (AD) is the primary cause of dementia in the developed world and it is ranked as the fifth most common cause of death worldwide[2]. The last 30 years of research

identified the brain accumulation of amyloid plaques as the leading cause of AD development. These deposits consist mainly of Aβ40(42) peptides, and their formation is usually followed by the spreading of tau, neuronal degeneration, and ultimately clinical manifestation, taking up to 20–30 years[4].

Neuropathological studies and quantitative neuroimaging investigation indicate a spatial-temporal evolution of Aβ40(42) accumulation that initiates in neuronal clusters with high metabolic activity (such as association cortices) and propagates to the allocortex and the brain stream, eventually reaching the cerebellum (Figure 2) [5].

Experimental pathomechanistic and proof-of-concept studies indicate that Aβ40(42) misfolding, aggregation and increasing accumulation in plaques are caused by the imbalance between neuronal production and extracellular clearance [6].

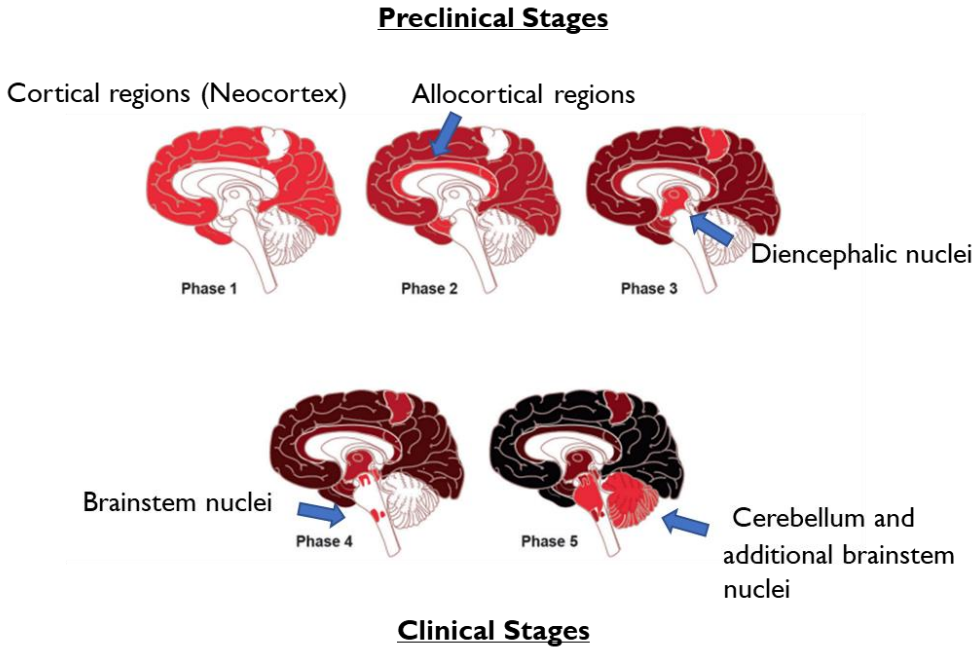

Figure 2. Traditional neuropathological phases of amyloid-β deposition in Alzheimer's Disease. Red areas indicate the regions of CNS affected by Aβ40(42) deposit during the different stages of the pathogenesis. During phase 1, early Aβ accumulation occurs in the neocortical and the association cortices. Additional accumulation is observed in allocortices regions and midbrain (phases 2 and 3), with the cerebellum and brain stem affected by the formation of Aβ40(42) plaques in the late phase of clinical stages. The change to darker shading indicates the continuous accumulation of Aβ. Figure modified from references [4,5].

1.3 Physiological functions of Amyloid β

Aβ40 is a 40-residues in length enzymatic product of the amyloid precursor protein (APP). APP is widely produced by neurons, vascular and blood cells, and, in astrocytes by smaller amounts. In addition to the brain, the precursor and enzymatic complex involved in synthesizing Aβ40(42) are co-expressed in the pancreas, appendix, gastrointestinal tract, and both male and female reproductive organs[7]. The physiological role of APP family members is still emerging, however, they were found to modulate a wide range of functions, such as dendritic spine remodelling, molecular pathways of neurotransmission, and synaptic

homeostasis[8]. Two-steps proteolytic cleavages of APP by β-secretase (β-APP-cleaving enzyme-1 (BACE1)) at the ectodomain and γ-secretase at intra-membranous sites generate Aβ40. 60-70% of the vertebrates share the human sequence of Aβ40, and this is an evidence for its physiological relevance[7]. Noteworthy, the presence of additional Ile^{41} and Ala^{42} at the C-terminus dramatically increases the aggregation propensity of the sequence compared to the 40-residues in length peptide. Increased Aβ42 production is a common feature of familial and sporadic AD[7].

Despite its physiological role is still unclear, Aβ40(42) has been proposed to regulate memory formation[9]. Studies on long-term potentiation (LTP), an indicator of synaptic strengthening, revealed that picomolar concentrations of Aβ might enhance LTP, whereas nanomolar concentrations might suppress it[10]. Furthermore, it has been observed that the extracellular concentration of Aβ40(42) rises after neuronal stimulation, whereas both APP knockout and BACE1 knockout *in vivo* induce cognitive deficits and impair LTP [7]. Early studies have shown that Aβ40(42) peptides may impart a neurogenic effect, as at low concentrations, Aβ40(42) promotes the survival of primary neurons and stimulates neural progenitor cells[11]. However, despite showing neurogenic properties, Aβ40(42) is generally considered an antagonist to the formation of new synapses, as nanomolar concentrations of oligomeric Aβ40(42) induce synapse loss[7]. Furthermore, *in vitro* studies have also shown that low concentrations of Aβ40(42) promote endothelial cell proliferation, induce the formation of capillary-like structures and increased vessel density in brain slice cultures[12]. In contrast, at nanomolar concentrations, Aβ40(42) promotes pathological angiogenesis, resulting in hypervascularisation and anomalies in the blood flow. Further studies showed that Aβ40(42) plays another role in the vascular system and is involved in repairing leaks in the Blood-Brain Barrier (BBB) [7].

Together, this evidence suggests that the concentration of Aβ40(42) is a crucial factor between physiological functions and pathological effects. In this sense, Aβ40(42) peptides may act in a "hormonetic fashion" [7], meaning that low concentrations of Aβ40(42) are involved in a pool of functions of physiological relevance. In contrast, a concentration increase is linked to peptide misfolding and the development of pathology.

Three main proteases α-, β- and γ-secretases—are responsible for APP cleavage, and their activity leads to "amyloidogenic" and "non-amyloidogenic" pathways[4]. Outside the CNS, APP is preferentially cleaved by α-secretase, which is responsible for the amyloidogenic pathway[13], as it cleaves APP in positions 16 and 17 of the Aβ42 sequence. The final enzymatic products, upon lysosomal degradation or γ-secretases activity, are short and hydrophobic peptides, collectively called p3 fragments. APP processing by α-secretases is believed to be protective in AD because this enzymatic pathway competes with production of full length Aβ40(42) [13].

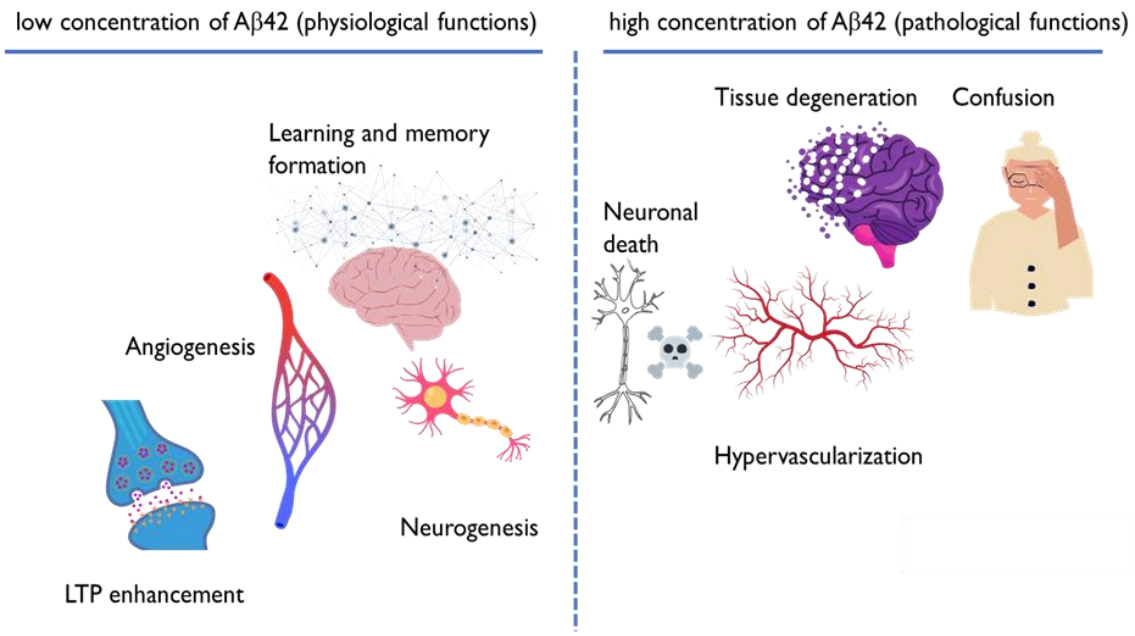

Figure 3. The effects of Aβ40(42) are concentration dependent. Aβ40(42) monomers are involved in a wide range of functions, including learning and memory, angiogenesis, neurogenesis, and repair leaks in the blood–brain barrier. Pathogenic increase in Aβ40(42) concentration leads to peptide misfolding, resulting in neuronal death, hypervascularization, neuronal loss, confusion and loss of memory[7].

β- and γ-Secretases were found to be the main enzymes responsible for forming amyloidogenic species. The β-secretase enzyme (BACE1) cleaves the extracellular juxta membrane region of APP (β-cleavage)[4], thus producing the soluble N-terminus of APP (sAPPβ), while the C-terminal fragment (CTF-β or C99) remains bound to the membrane. The CTF-β fragment is cleaved again by β-secretase, releasing Aβ40(42) into the extracellular space[14]. Of note, BACE1 is involved in metabolism of several other proteins in addition to APP; therefore, it cannot be used as a „druggable“ target[13].

γ-Secretase complex is heterogeneous with respect to its protein composition and expression and exhibits a wide range of enzymatic activity involving a pool of different substrates. The catalytic elements of γ-secretase are presenilins 1 and 2. These intramembrane-cleaving proteases generate the Aβ carboxyl terminus from APP through sequential substrate cleavage. Mutations in presenilins genes have been shown to increase the rate of Aβ40(42) production[13]. In cognitively healthy adults, the average fraction of Aβ40(42) production and clearance rates are estimated to be around 8% per hour[16]; thus, Aβ40(42) is unlikely to reach the concentration necessary to trigger its amyloid formation under physiological conditions. Notably, previous studies suggested that at the CNS level, an impairment of Aβ clearance has an higher impact in amyloid formation rather than increased Aβ40(42) synthesis [17]. Clearance of Aβ40(42) peptides occurs through enzymatic and non-enzymatic pathways, involving several mechanisms, including the enzyme neprilysin (NEP), uptake by microglial or astrocytic phagocytosis.

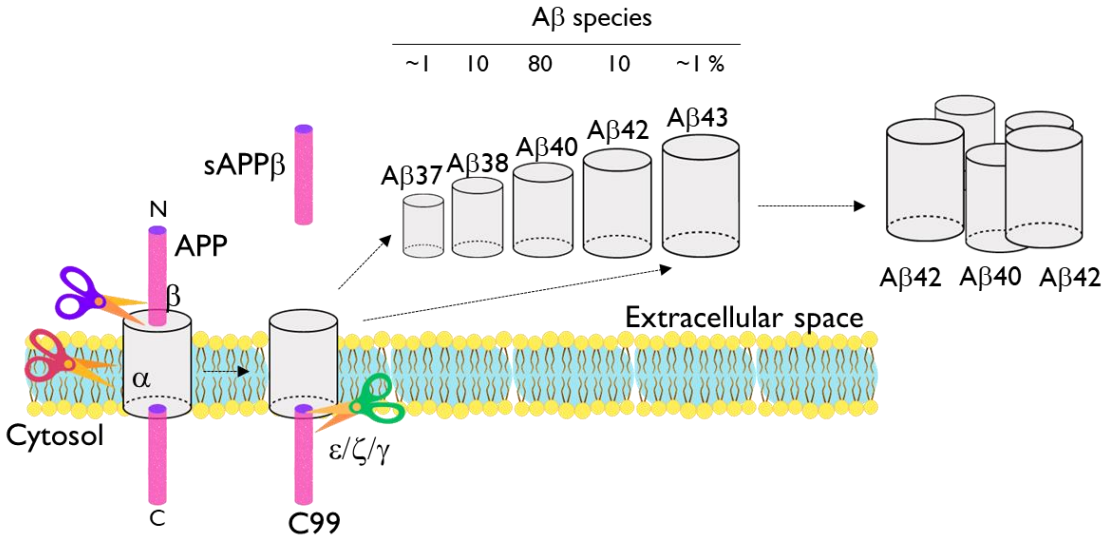

Figure 4. APP processing and generation of Aβ40(42). At first, APP is first cleaved by β-secretase (β) in its ectodomain close to the extracellular/luminal membrane border, thus generating a 99 amino acid C-terminal APP fragment (C99). Next, the cleavages of C99 by γ-secretase at ε-, ζ-, and γ-sites release the APP intracellular domain (AICD) into the cytosol, together with several Aβ species, which are between 37 and 42 residues in length. Alternative cleavage of APP by α-secretase (α) in the Aβ domain prevents formation of Aβ. Pathogenic APP FAD mutations that have been shown or are likely to cause relative increases in the generation of Aβ42 species are located in the γ-secretase cleavage region of the APP TMD and the AICD. Figure modified from reference[15].

1.4 Amyloidogenesis in type 2 diabetes (T2D)

Type 2 diabetes is a metabolic disease associated with progressive β-cell failure, resulting in decreased insulin secretion, and increasing hyperglycaemia. T2D currently affects over 400 million people worldwide, and is estimated to grow to over 700 million by the year 2045[2]. Amyloid deposits in the pancreatic islets of Langerhans were observed in most individuals with T2D and are correlated with a reduction in β-cell mass and as well al the failure of graft and islet cell transplants[18,19].

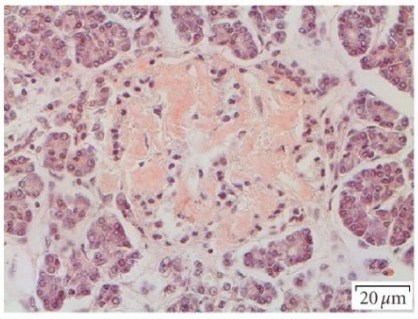

Figure 5. Islet β-cells in a type-2 diabetic patient. In their study, Westermak G.T. and Westermark P.[20] found that all diabetic individuals had very pronounced islet amyloidosis, showing some islets with little remaining endocrine cells. The islet amyloid had typical staining properties with Congo red and was strongly labelled with antiserum against IAPP; Congo red, bar 20 μm. Figure taken from reference [20].

The main protein component of such deposits is islet amyloid polypeptide (IAPP), and a possible strategy to reduce T2D onset is to inhibit amyloid formation and the induced toxicity.

As T2D is a multifactorial disease, the cytotoxicity mediated by IAPP aggregation on β cells cannot be considered the only cause of this pathology. However, IAPP aggregation has been

linked to β cell dysfunction and death; thus, any potential mechanisms to prevent human IAPP (IAPP) misfolding into amyloid fibrils and its depositions into plaques are of great interest to the T2D field[20].

The initiation site for islet amyloid formation in vivo still needs to be clarified, and there is conflicting evidence in the literature. Amyloid deposits detected in T2D appear to be extracellular, and initial studies with transgenic mice were consistent with extracellular deposition. However, other studies with rodent models in which IAPP is overexpressed are more consistent with an intracellular origin[6].

1.5 Biological function of IAPP

hIAPP has been found to modulate several physiological functions, mainly regarding the regulation of glucose homeostasis[6]. This function is fulfilled by inhibiting insulin secretion, controlling gastric emptying, and suppressing glucagon release [21,22]. Furthermore, IAPP is also involved in central functions, such as controlling satiety at the area postrema of the CNS and acting as an adiposity signal.

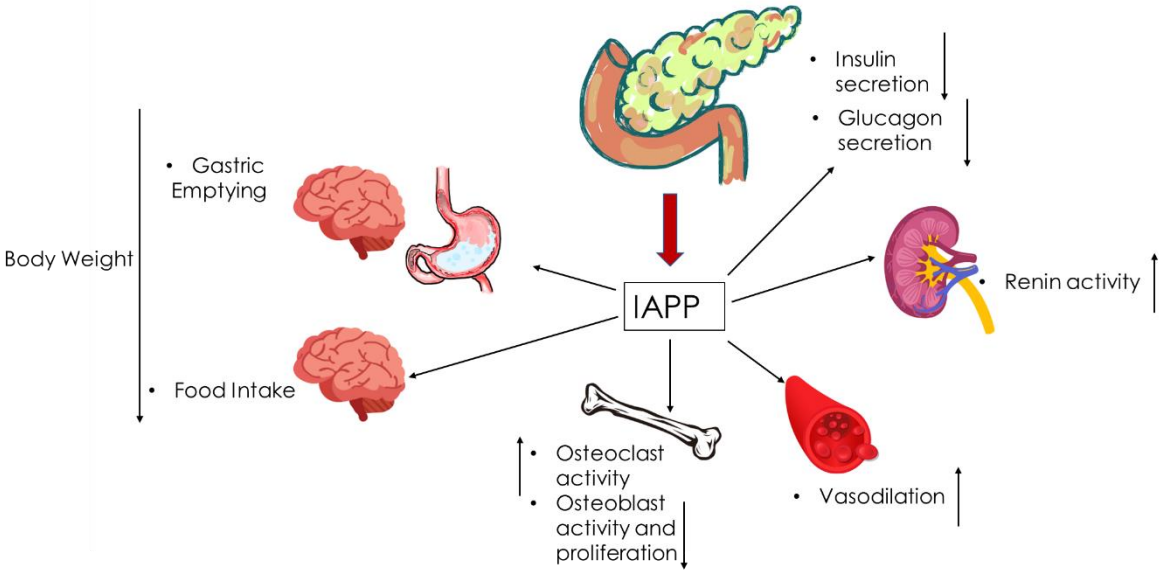

Figure 6.The physiological role of IAPP. IAPP is a polypeptide, 37-residues in length and has endocrine and auto-/paracrine functions. It is involved in slowing down gastric emptying and reducing food intake by acting in the brain and likely at the gastric level, consequently decreasing body weight. For this aspect, amylin also works synergistically with other hormones, such as leptin[23]. Due to its similarity to calcitonin-gene-related peptide, it also affects bone metabolism by decreasing osteoclast activity. Additionally, amylin influences vasodilation and the renin-angiotensin system. Figure modified from reference [23].

IAPP effects are not fully understood, but it has been shown that they are mediated by interaction with six different subtypes of IAPP receptors; consisting of complexes formed between two Calcitonin (CT) receptors and three receptor activity-modifying proteins (RAMS). However, the receptor subtypes active in the peripheral tissue or the CNS[6] are unknown, and no approved small molecule agonists exist.

IAPP is synthesized as an 89-residue long preproform, consisting of a 22-residue long signal sequence and by pro-IAPP. Pro-IAPP is cleaved by the prohormone convertases PC2 and PC1/3 and further processed in the Golgi and the insulin secretory granules to the 37-residue

mature peptide[22,23]. The sequence undergoes subsequent post-translational modifications, including the amidation of the C-terminus through a multi-step process and the formation of an intramolecular disulphide bridge between residues 2 and 7 [6]. IAPP is stored in the insulin secretory granules and represents 1-2% of insulin concentration. Of note, in these conditions, IAPP concentration is higher than that promoting aggregation *in vitro,* and the low pH of the granules could explain why IAPP does not aggregate under these conditions[6].

1.6 Molecular link between Alzheimer`s disease and Type 2 diabetes

AD and T2D share similar features. Both diseases are multifactorial and characterised by tissue degeneration and neuronal or. in the case of T2D, pancreatic β-cell death[24]. In both diseases, the pathogenesis is linked to the accumulation of insoluble amyloid deposits, mainly formed by misfolded Aβ40(42) peptides or IAPP. Protein aggregation is believed to start years before disease onset and worsens with their progression. Furthermore, both diseases are characterized by hyperglycaemia and insulin resistance, to the extent that some authors call AD as "type 3 diabetes"[24].

Several studies also revealed the deposition of IAPP in the brains of patients with AD and brain vessels of T2D patients. In contrast, high levels of Aβ40(42) were observed in the pancreas of type 2 diabetic patients[25,26]. Furthermore, inoculation of pancreatic IAPP aggregates into the brains of transgenic mice with AD resulted in memory deficits (29). Studies demonstrated that IAPP and Aβ40(42) oligomers share a similar cytotoxic mechanism, as they both induce β-cell and neuronal apoptosis. Additionally, IAPP oligomers were found to damage the membrane permeability in neurons, induce ROS production, and alter calcium homeostasis[24].

IAPP and Aβ40(42) sequences are 25% identical and 50% similar, and the degree of identity and similarity increases in the hydrophobic regions that drive the fibril assembly[27]. *In vitro* studies revealed that Aβ42 and IAPP bind each other with high affinity and that their interaction is mediated by the "hot segments" Aβ(19-22), Aβ(27-32), Aβ(35-40) and IAPP(8-18) and IAPP(22-28)[28]. These binding regions include residues that are important for self-assembly. Based on this evidence, several studies have suggested that, at the molecular level, the co-localization and cross-interaction between IAPP and Aβ peptides contribute to, or accelerates, the onset of AD and T2D [29–32].

1.7 Mechanism of amyloid formation

It is widely accepted that amyloids form through a process made of different energetic states. These states include low molecular weight assemblies, such as dimers and trimers, soluble oligomers and protofibrils, and, eventually, fibrils that accumulate in plaques[33]. Obtaining a mechanistic understanding of protein aggregation is crucial for blocking, redirecting, or modifying this pathogenic process. However, elucidating the critical phases of amyloidogenesis is complicated by the complex nature of the aggregation steps. Furthermore, the factors

triggering the misfolding of amyloidogenic peptides, such as IAPP and Aβ40(42), remain unknown.

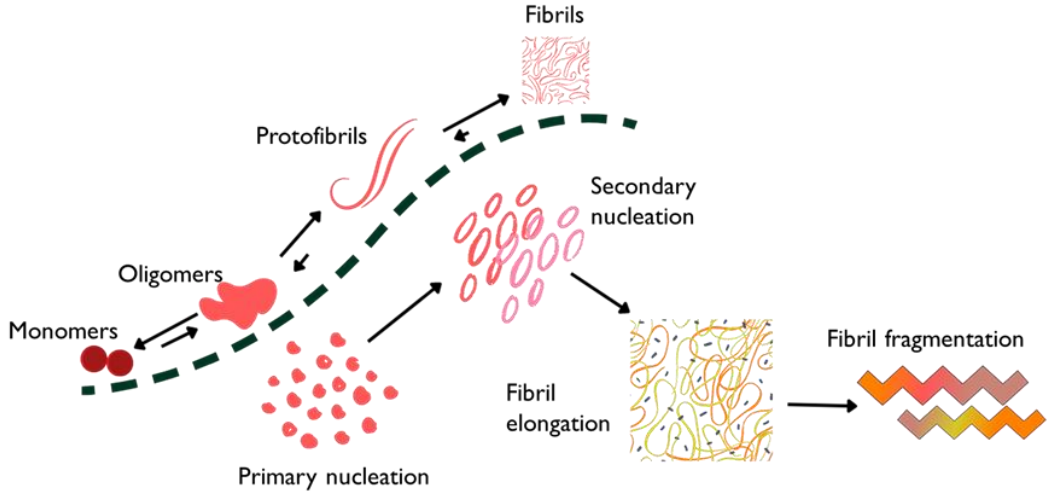

Figure 7. Schematic illustration of an aggregation reaction network. The kinetics of aggregation can be described through a series of microscopic steps in equilibrium with each other. In this scheme, the steps of the aggregation mechanism of an amyloidogenic protein (pink) are shown. Figure modified from reference[33].

The kinetics of amyloid formation can be divided into four micro steps: The first step is primary nucleation, which consists of the self-assembly process into nuclei through spontaneous associations of monomers without the contribution of preformed aggregates[33,34]. This way, monomers, aggregation-competent units, assemble into increasingly stable nuclei, defined as aggregates that grow faster by monomer addition than they dissociate.

The second step is known as secondary nucleation. This step consists of the association of monomers on a preformed fibril surface, which is composed of the same monomeric building blocks (homologous)[34] or by monomers of other amyloidogenic proteins (heterologous). In this step, the fibril, or seed, acts as a catalyser of the aggregation process. Finally, the secondary nucleation rate depends on two parameters: the concentration of monomers and the concentration of seeds[34].

After the nucleation steps, fibrils elongate through a dock-lock mechanism called “fibril elongation”, in which, at first, monomers dock quickly to fibril tips; then in a locking step, they undergo a structural conversion to adopt fibril morphology and structural characteristics, likely with preformed fibrils acting as templates[35].

Finally, fibril growth drastically accelerates by generating new reactive surfaces enabling a further elongation step upon fragmentation[36]. This effect, which alters the fibrils` size and their amyloid-competent surface, modifies their ability to interact with biological surfaces, such as cellular membranes and other fibril particles. The combined effects of decreasing length of individual fibrils and increasing number of fibrillar particles caused by fibril fragmentation could enhance the cytotoxic potential of fibrillar material.

1.8 Structural properties of different amyloid species

Identifying the target's structure is a significant challenge for developing inhibitors of amyloid assembly. The transient nature of the species involved complicates this task. Here, I will briefly report some evidence regarding the structures and properties of amyloid monomers, oligomers, and fibrils.

1.8.1 Properties of amyloid monomers

Soluble and unordered monomers are the physiological and native forms of various amyloidogenic peptides. Due to the lack of a stable secondary structure, monomers are generally classified as "intrinsically disordered", and the transition from an unfolded state into secondary structures rich in β-hairpins is considered important for oligomerisation of amyloidogenic peptides and proteins[37]. β-Hairpins consist of two β-strands adjacent in primary structure, oriented in an antiparallel direction, and linked by a short loop of two to five amino acids. The importance of β-hairpin structures in the amyloidogenic process is due to their propensity to form bulky and compact assemblies, their twisted shapes and their highly hydrophobic surfaces[37]. The role of these structures has been elucidated in the work of Härd and Hoyer, who reported solution-phase NMR spectroscopy studies of monomeric IAPP and Aβ42 in complex with affibodies to stabilise the β-hairpin structures[37,38]. Furthermore, Kayed et al. and Dupuis et al. showed that IAPP monomers could adopt an β-hairpin-rich structure on-pathway to the amyloid formation[39,40].

1.8.2 Properties of amyloid oligomers

Special attention has been dedicated to the properties of amyloid oligomers, which are generally defined as such based on their size (*e.g.* 2 to 20-mers or other), growth rate (lower than fibrils), structure (less organised than amyloid fibrils) and toxicity[34].

Characterization via NMR, FTIR and EPR spectroscopies revealed additional biophysical and biochemical properties, such as the presence of β-sheet-rich structures, a transient and polymorphic nature, and structural features shared by oligomers of proteins with a different primary sequence[41].

The secondary nucleation step is thought to generate the most significant amount of oligomeric species, which can be described as smaller than the mature fibrils, with a less organised structure and a lower growth rate. Once generated, the oligomers undergo a structural reorganisation into grow-competent species. However, due to their transient nature, solving their structure remains challenging.

Strong evidence underlines the toxic potential of soluble amyloid oligomers and their generation process [42,43]. Studies on the neurotoxicity of Aβ peptides showed that soluble, low-number oligomers, such as dimers-dodecamers of naturally secreted human Aβ injected in the rodent hippocampus, could impair both synaptic strength and long-term depression.

Furthermore, Aβ oligomers can inhibit critical mechanisms of synaptic plasticity which result into synaptic loss, as assessed by the decrease of dendritic spine density (3).

The biophysical and biological properties of amyloid oligomers do not depend on their primary sequences. Low-order, partially structured and soluble oligomeric species of h-IAPP were found to be toxic and to upregulate oxidative stress, inflammation and apoptosis in rat INS-1 β-cells and murine pancreatic islets[45]. The proposed mechanism of their cytotoxicity involves disruption or formation of pores in cell membranes by forming ion-leaking pores[46–48], leading to increased membrane fluidity, calcium dysregulation, and decreased cell viability [25,49]. IAPP oligomers have also been found within disturbed mitochondrial membranes in transgenic hIAPP mice and T2D patients, which was linked to the overproduction of oxygen-reactive oxygen species (ROS)[25].

Soluble oligomers that adopt an elongated morphology are called protofibrils. Protofibrils are transient species formed during the lag phase of spontaneous amyloid growth when the amyloidogenic peptide or protein is at a relatively high concentration[50]. Contrary to mature fibrils, Aβ protofibrils incubated in buffer tend to dissociate and do not bind ThT[51]. Kayed and coworkers reported that soluble protofibrils are immunoreactive towards A11, an oligomers-specific antibody[52].

Aβ40(42) protofibrils were found to inhibit LTP-mediated synaptic plasticity in mouse hippocampus and accumulate in glial cells[53]. Protofibrils of both Aβ40(42) and IAPP have also been reported to disturb membrane integrity by inducing reactive oxygen species (ROS)[54], resulting in decreased membrane fluidity, intracellular calcium dysregulation, depolarisation, and impaired long-term potentiation (LTP)[55]. In addition, the damaging effects of protofibrils were significantly greater than those of low molecular weight oligomers of Aβ42[56].

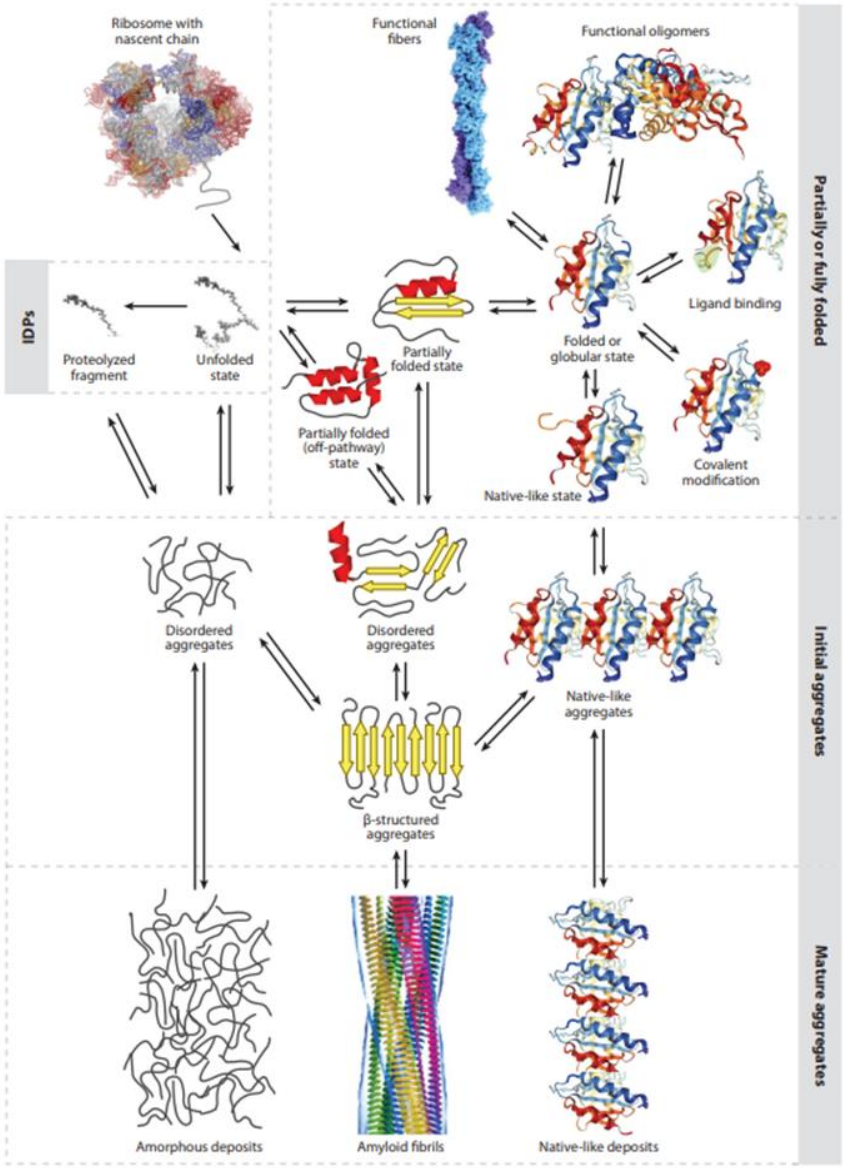

Figure 8: Schematic representation of the amyloidogenic pathway. At first, species formed during the aggregation are clusters of a small number of molecules, which retain a structural memory of their monomeric state. These early oligomers are unstable and can be unfolded, partially ordered, or ordered depending on the structure of their initial monomeric species. When aggregation proceeds, such aggregates reorganise into more structured species, rich in β-sheet content, and usually grow in compactness and size. The β-sheet oligomers can grow further via self-association or by adding monomers to form well-defined fibrils with a highly organised cross-β structure. This figure is taken from reference[3].

1.8.3 Properties of amyloid fibrils

Amyloid fibrils are typically 7-13 nm in diameter, organised in 2-8 protofilaments that often twist around each other or associate in lateral ribbons 2-7 nm high and up to 30 nm wide[3]. A characteristic feature of the amyloid assemblies is the morphological and structural similarity of fibrils formed by different peptides. This phenomenon might be explained by similar structural elements, such as the formation of β-strands, the low degree of twist in the β-sheets, and the fact that short peptides can assemble into three-dimensional crystals[2].

In *in vitro* systems, amyloid fibril formation is generally quantified by binding dyes, such as thioflavin-T (ThT) and Congo red (CR) [57].

Fluorescence enhancement upon binding to fibrils is the most defining and thoroughly studied property of ThT. It is widely believed that the increase in ThT fluorescence results from selective immobilisation of a subset of ThT conformers[58,59]. Several experimental data and quantum mechanical predictions suggest that ThT behaves as a "molecular rotor" [58,59]. A low energy barrier allows the benzylamine and benzathiole rings of ThT to rotate freely about their shared carbon-carbon bond. This rotation rapidly quenches excited states generated by photon excitation, causing low fluorescence emission for free ThT. In contrast, rotational immobilisation of ThT preserves the excited state, resulting in a high quantum yield of fluorescence[58]. By extension, amyloid fibrils are likely to present a ThT-binding site that sterically "locks" the bound dye, thus leading to an enhancement of ThT fluorescence[58].

The fibrillar morphology, β-sheet content, and reactivity to binding dyes are the three characteristics that are generally accepted to define protein aggregates as amyloid structures.

Structural analysis performed via X-ray fiber diffraction, Fourier transform infrared spectroscopy, solid-state magnetic resonance (ssNMR), X-ray crystallography and Cryo-EM[60–64] revealed that fibrils fold into a cross-β structures, in which β-strands are positioned perpendicularly to the axis of the fibrils and are organised into β-sheets that run through the length of the fibrils.

Aβ40 fibrils

Tycko and co-workers established methods for producing two types of homogeneous fibrils from chemically synthesised Aβ40, which have been characterised via ssNMR (Figure 10)[65–67]. One fibril structure consists of 3-fold symmetrical fibrils with twisted morphology and arranged triangularly; the other contains 2-fold symmetrical fibrils with a striated ribbon morphology which stack on top of each other to create four layered β-sheets [66,68]. The structures of the protofilaments of both fibril types are very similar and consist of extended networks of layered, in-register parallel β-sheets. The N-terminal region Aβ(1-10) is unstructured, whereas the central segment Aβ(11−22) and the C-terminal residues Aβ(30−39) are organised in two β-strands connected by a loop consisting of Aβ(23−29) (Figure 9). In 2019, Fändrick and coworkers [60] solved the Cryo-EM structure of Aβ40 fibrils isolated from the meninges of AD patients, containing low levels of Aβ42 fibrils[69]. Overall, these fibrils revealed a twisted morphology that resembles that observed in *in vitro* experiments, with the remarkable difference that fibrils obtained *ex vivo* were right twisted. The Cryo-EM structure revealed that each Aβ40 peptide stack contains four cross-β sheets, termed β1–β4, comprising residues 2–8, 10–13, 15–19 and 32–34. Remarkably, the organisation of the regions 10-19 and 30-37 into β-strands was supported by the Cryo-EM model proposed by Murzin, Peak-Chew, Goedert and coworkers[61].

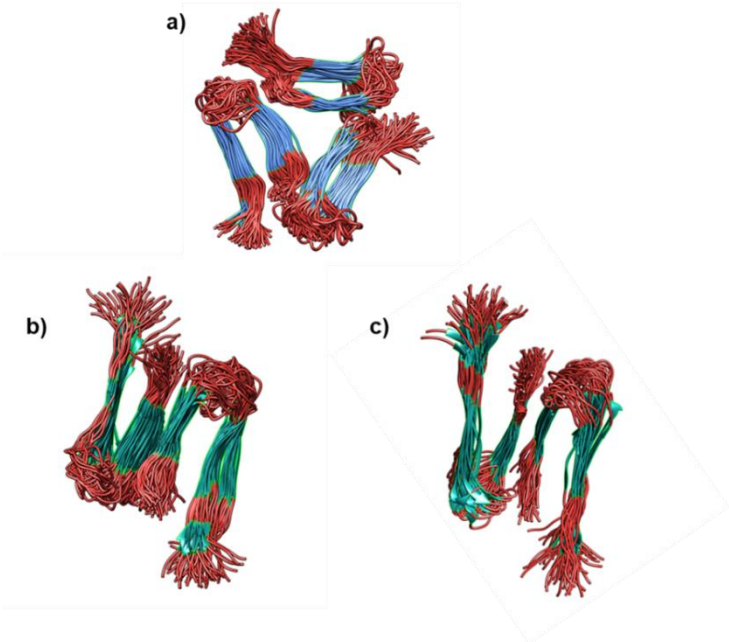

Figure 9: ssNMR structures of Aβ40 fibrils. Tycko and coworkers resolved the structures of two types of Aβ40 fibrils via ssNMR.[65,66]. The first type (a) is formed by 3-fold symmetrical fibrils with twisted morphology and arranged triangularly; the second one (b-c) contains 2-fold symmetrical fibrils characterised by a striated ribbon morphology stacking on top of one another to create four layered β-sheets. In both models, segments Aβ(11-22) and Aβ(30-39) are structurally organised into β-strands (highlighted in blue). This second model sees an additional variable, the "staggering" of the internal quaternary contacts[66], consisting of the organisation of the β-sheets along the direction of the long fibril axis. The staggering can be negative (b) or positive (c). The structures were downloaded from the PDB, (2LMP(a)[65], 2LMPO(b) and 2LMN(c)[66]) and the Figures were generated with Chimera[70] software package.

The β-sheets run parallelly to the orientation of the hydrogen-bonded β-strands relative to one another. In contrast to what was found in the ssNMR model, the peptide fold is C-shaped and not U-shaped. The central contact site, which occurs close to the main fibril axis, is formed by residues 24–26.

Aβ42 fibrils

The ssNMR structure of the same Aβ42 fibril polymorph was solved independently by the research groups of Riek[71], Ishii[72], and Griffin[73]. Their studies showed that the protofilaments composing Aβ42 fibrils fold into a convoluted S-shape, which differs from the shape of the protofilament subunits in the Aβ40 fibrils solved via ssNMR[65,66]. The fibril identified by Riek and Griffin consists of two protofilament subunits, which are 2-fold symmetrical (Figure 10). The inner part of each protofilament is formed by packed hydrophobic residues organised in two cores, one containing residues Ile^{31}, Val^{36}, Val^{39}, and Ile^{41}, and the other having Leu^{17}, Phe^{19}, Phe^{20}, Val^{24}, Ala^{30}, and Ile^{32}[73]. The surface exposed to the solvent contains mainly charged and polar residues, including Lys^{16}, Glu^{22}, Asp^{23}, Ser^{26}, and Lys^{28}, and forms the main turn/loop between the three main β-strands, spanning between Aβ(10-40) [73]. Additional structural stability is given by a salt bridge formed between the side chain of Lys^{28} and the Ala^{42} carboxylic group.

In 2017, Schröder, Willbold, and co-workers determined the structure of a different Aβ42 fibril polymorph using cryo-EM(64). Although the C-terminus resembles the ssNMR structure, the cryo-EM structure indicates that the N-terminus is ordered and part of the fibril's cross-β structure.

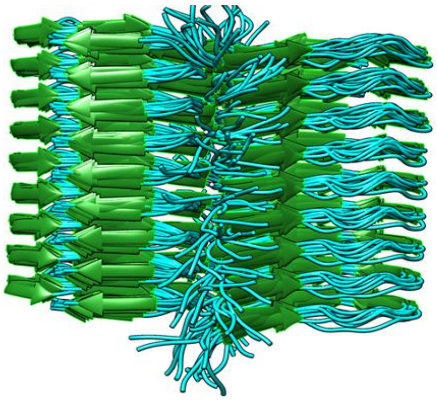

Figure 10: ssNMR structures of Aβ42 fibrils. Colvin et al. [73] solved the structure of a dimer formed from two S-shaped monomers, with most hydrophobic residues buried in the fibril core. The hydrophilic residues are solvent-exposed and include the main turn/loop between the three main β-strands (in green). The structure was downloaded from the PDB (5KK3(a)) [73], and the figure was generated with Chimera[70] software package.

IAPP fibrils

Studies revealed that while human IAPP (hIAPP) is strongly amyloidogenic, rat IAPP (rIAPP) is not[74,75]. The primary sequences of the two peptides differ only in six positions, five of which are located in regions 20 to 29. This evidence suggested that IAPP(20-29) is the amyloidogenic core of hIAPP[74]; moreover, in rIAPP, three of these AA residues (Ala^{25}, Ser^{28} and Ser^{29}) are substituted by proline, a well-known β-sheet breaker [74,76]. Studies on short peptide fragments covering hIAPP(20-33) revealed that pentapeptides and longer segments form amyloid fibrils *in vitro*. High-resolution X-ray crystallography studies of short peptides hIAPP(22-27) and hIAPP(28-33) [74,77]. revealed that while the segment hIAPP(28-33) forms an extended β-strand, the segment hIAPP(22-27) folds into a backbone turn[74]. Tycko and coworkers[78] reported the solid-state NMR structure of full-length IAPP fibrils, revealing the presence of parallel, in-register alignment of β-strands, which suggested a hairpin structure of two β-sheets, not including the central region IAPP(18-27). In 2016, Weirich et al.[79] reported the ssNMR structure of recombinant and non-amidated IAPP fibrils. This study revealed the presence of up to four β-strands per monomer present in fibrillar $IAPP_{COOH}$ that were in the segments IAPP(8-20), IAPP(23-28), IAPP(30-32), and IAPP(35-36).

In 2020, Schröeder[62], Eisenberg[63], and Radford and Ranson groups[80] reported cryo-EM structures of IAPP amyloid fibrils within 4.2 Å and 3.6 Å resolution. The IAPP fibril polymorphs studied by all three groups comprise two helically twisted protofilaments, each consisting of a stack of monomers arranged in the cross-β-sheet structure typical for amyloids. Both Röder et al[62], and Gallardo et al.[80] reported an S-shaped protofilament composed of three short β-strands, formed by segments IAPP(14–19(20)), IAPP(26–31(32)) and IAPP(35–36(37)) and linked by short loops. By contrast, Cao et al. [63] reported an I-shaped fold containing short β-strands formed by similar segments to those in the S-shaped folds suggested by the other authors [81].

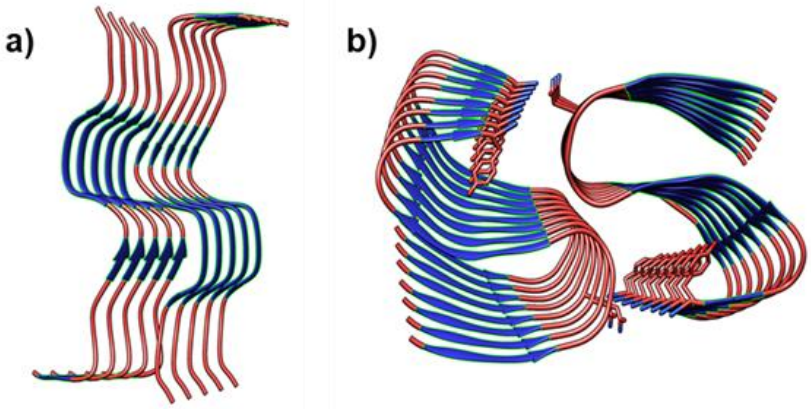

Figure 11: Cryo-EM Structures of IAPP fibrils. Eisenberg`s (a) [63] and Schröder`s (b)[62] groups solved the cryo-EM structures of two different polymorphs of IAPP fibrils. Both fibrils consist of two helically twisted protofilaments, each formed by a stack of monomers arranged in a cross-β-sheet structure. In both polymorphs, the segments IAPP(14–19)(20)), IAPP(26–31(32)) and IAPP(35–36(37) form short β-strands (in blue). The structure of the fibril resolved by Cao et al.[63] is "I" shaped (a), whereas the cryo-EM mapping of the structures identified by Röder et al.[62] is "S" shaped (b), by what is also reported by the groups of Radford and Ranson [80]. The structures were downloaded from the PDB (6VW2 (a)[63], and 6Y1A(b) [62]), and the figure was generated with Chimera[70] software package.

1.9 Peptide inhibitors of amyloid formation

Until now, only very few anti-amyloid drugs have reached the market[10]. The development of amyloid inhibitors faces significant challenges, like the transient kinetics of the amyloid assembling and the necessity of high-affinity interaction between the inhibitor and the target, as toxic self-assembly often occurs at low nanomolar protein concentration[10]. On top, drug candidates must fulfil other pharmacological properties like target specificity, solubility in body fluids, and permeability of physiological membranes, especially if targeting the CNS.

In the last two decades, the three most exploited approaches to develop anti-amyloid inhibitors were: antibodies/proteins, small organic molecules, and peptides and peptidomimetics[10], each presenting unique advantages and disadvantages. The main drawbacks of monoclonal antibodies concern four crucial points: a) their effectiveness at slowing cognitive decline is mixed, b) the higher risk of developing vasogenic cerebral oedema and cerebral micro-haemorrhages, also known as amyloid-related imaging abnormalities (ARIA)[82] c) their low membrane permeability, requiring intravenous administration which limits patient compliance and d) the limited coverage due to their high production costs.

Small molecules may have the advantage of higher stability in biological fluids and tissues, the potential to cross physiological barriers, including the brain-blood and gastrointestinal barriers, and immunological tolerance[84].

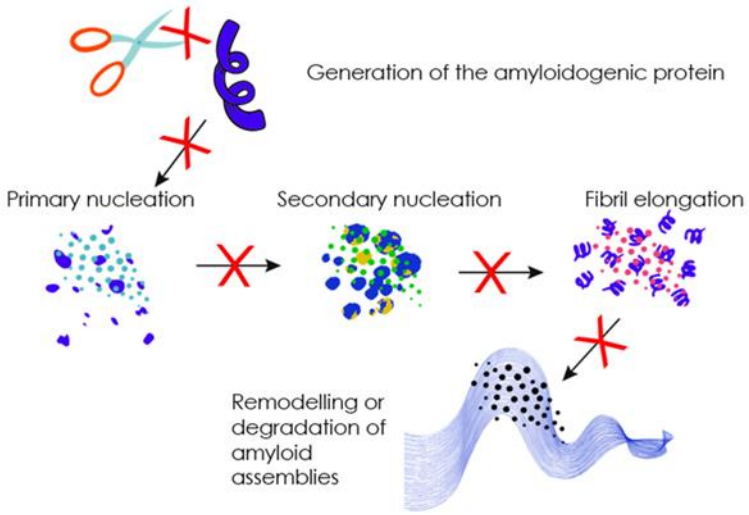

Figure 12: Schematic representation of the molecular strategies to interfere with amyloid formation. An anti-amyloid candidate should target one or more steps of the amyloid formation, such as the generation of the amyloidogenic proteins (i.e., inhibitors of γ- and β-secretases), blocking the nucleation mechanisms and/or remodel, disassemble or degrade preformed fibrils. Figure based on references[10,83].

On the other hand, small molecules lack specificity, leading to off-pathway side effects, long half-life, and low efficacy of interfering with protein-protein interactions due to their small surfaces. Up to now, only the small molecule "Tafamidis" among anti-amyloid drug candidates has reached the clinic for treatment of transthyretin (TTR micro-haemorrhages (familial amyloid polyneuropathy (FAP) treatment)[85].

Peptides may show optimal pharmacodynamic properties, such as high efficacy, selectivity, and potency[10]. Nevertheless, the main disadvantages of peptide drug candidates concern their limited pharmacokinetics, especially low proteolytic stability, rapid clearance, and poor bioavailability/oral availability. In the last years, development and optimisation of macrocyclic peptides have overcome some of these significant drawbacks. Macrocyclic peptides often combine enhanced proteolytic stability and membrane permeability with increased surface areas, which is critical in modulating the protein-protein interactions involved in amyloid formation [74,78]. The development of peptide amyloid inhibitors is obtained in several steps, which can be summarised in Figure 13. Head-to-tail cyclised, and N-methylated hexapeptides are an appealing scaffold for designing bioactive compounds. In fact, several cyclic hexapeptides from natural sources are marketed for medicinal and veterinary applications. This includes the antibacterial vancomycin[10,83], the antifungal caspofungin, the immunosuppressant cyclosporine, the anticancer agent FK228 and the anthelmintic emodepside[86]. Head-to-tail cyclised, and N-methylated hexapeptides are an appealing scaffold for designing bioactive compounds. Multiple chemical tools have been developed to circumvent peptide degradation by plasma proteins and their low membrane permeability, including cyclisation, the introduction of D-amino acids, unnatural amino acid substitution and the use of peptidomimetics such as peptide bond isosteres and peptoid formation[87]. Of these, peptide backbone cyclisation is by far the most straightforward technique, as it may provide better metabolic stability and introduce conformational constraints to the peptide backbone, thus dictating spatial arrangement of the pharmacophores[86].

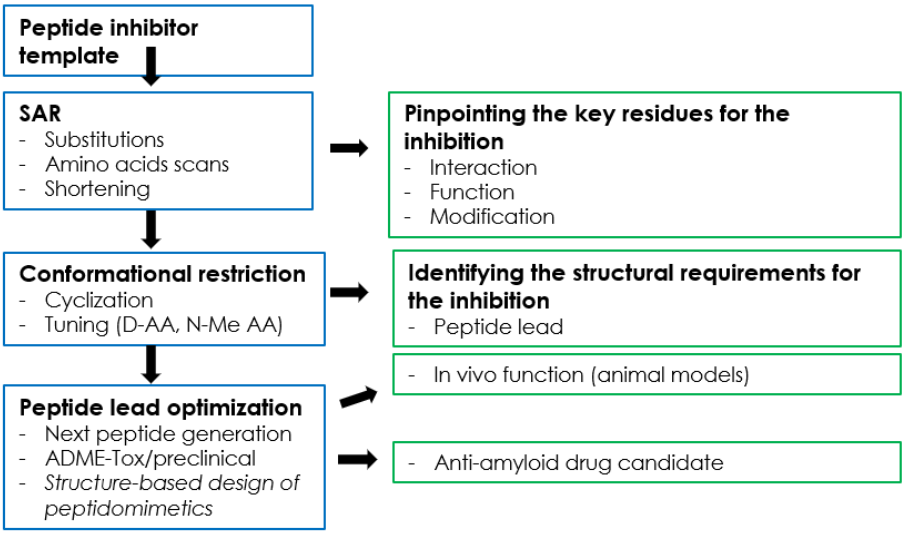

Figure 13: Schematic representation of anti-amyloid peptide drug design, optimisation, and discovery based on hierarchical strategies. Scheme adapted from references [10,83].

Cyclic peptides with a ring size of 3-7 present some appealing characteristics for drug development. They fold into preferred conformations, and their structural constraint can be further modulated by the insertion of N-methylations in specific positions(79). Furthermore, they usually present optimal characteristics to act as cell-penetrating peptides (CPPs), such as a molecular weight below one kilodalton, five hydrogen bond donor groups, and a polar surface area smaller than 250 Å[88]. Such characteristics make them potential candidates for cytosolic delivery through the blood–brain or the gastrointestinal barrier[88] [89].

Kanai and Sohma groups reported a novel class of small cyclic peptides showing anti-amyloidogenic properties against Aβ42 self-assembly. The head-to-tail cyclised inhibitors were designed using the amyloidogenic core of Aβ(15-20) as a template[90] and were further optimised by applying enantio- and retro-enantio approaches and decorated with fluorescent probes. This class of peptides class was further found to inhibit Aβ42 fibrillogenesis.

Gadhiri and coworkers reported the design, synthesis and characterization of organic nanotubes based on rationally designed cyclic octapeptides[91], alternating D-and L- amino acids. When protonated, these compounds crystallise into tubular structures hundreds of nanometres long, with internal diameters of 7-8 Å. The similarities between the structural and biochemical characteristics of the nanotubes and amyloids[91,92] were used as a basis by Rahimipour and coworkers for synthesising a library of hexacyclic peptides, also alternating D-and L- amino acids[93]. This class displayed anti-amyloidogenic properties, and the lead compound, CP-2, suppressed amyloidogenesis of Aβ40(42), α–syn, and the tau amyloid core hexapeptide AcPHF6[94]. Inhibition was likely mediated by the ability of CP-2 aggregates to bind amyloidogenic oligomers and penetrate cell membranes.

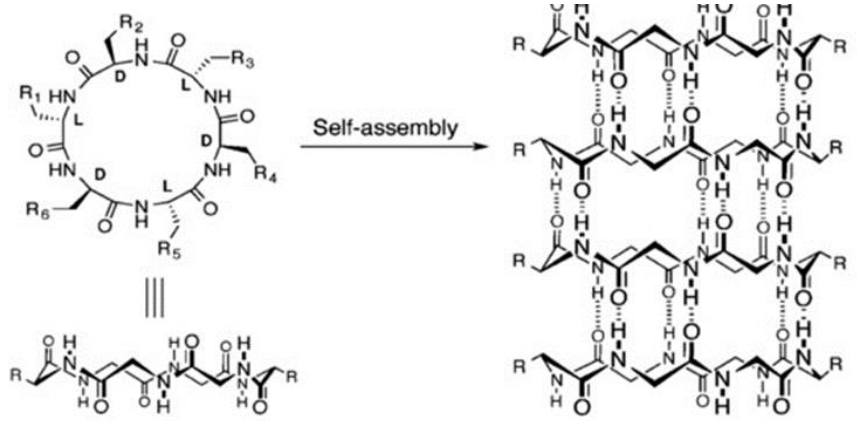

Figure 14. Schematic representation of a nanotube assembly from cyclic D, L-a-peptides. Cyclic peptides with an even number of alternating d- and l- a-amino acids form flat ring-shaped conformations that stack on top of each other through an intermolecular hydrogen-bonding network to form hollow and cross β-sheet-like tubular structures. Figure taken from reference[93].

1.10 Peptide inhibitors designed based on the IAPP-Aβ cross-interaction

Increasing evidence supports the hypothesis that AD and T2D might be linked, as clinical studies suggest that patients suffering from T2D might be at risk of AD and vice versa. On the pathophysiological level, both diseases are characterised by localised deposition of amyloid material extracellularly. Thus, the high affinity and structural similarity between IAPP and Aβ has been suggested as a possible molecular link between the two misfolding diseases[27–29,31]. Indeed, in both AD and T2D, two short, linear, and conformationally flexible polypeptides can be subjected to folding failure and become amyloidogenic. Notably, both polypeptides self-assemble into cytotoxic aggregates at nanomolar concentrations.

At the molecular level, the sequences of Aβ40 and IAPP are 25% identical and 50% similar. At the same time, high degrees of identity and similarity are shared between the short sequences Aβ(15–21) and IAPP(10–16) or Aβ(26–32) and IAPP(21–27), which were found to participate in Aβ40 or IAPP self-assembly (Figure 15)[95]. Our group has successfully designed and developed IAPP/Aβ amyloid inhibitors by identifying the “hot segments” of the IAPP/Aβ cross-interaction[28]. The design strategy’s molecular basis was that selectively N-methylated IAPP analogues, inhibiting IAPP amyloid self-assembly by impairing the H-bonding between the β-strands formed during the amyloid formation, were found to be nanomolar inhibitors of the cytotoxic self-assembly of Aβ40[28,88–90, 96]. In addition, IAPP-GI, ([(N -Me)G24, (N -Me)I26] -IAPP) was the first reported nonfibrillar/nontoxic cross-amyloid inhibitor redirecting Aβ40 amyloid assembly to form non-toxic and non-fibrillar hetero-oligomers. IAPP-GI and related analogues [96] were also found to remodel preformed Aβ40 fibrils[96].

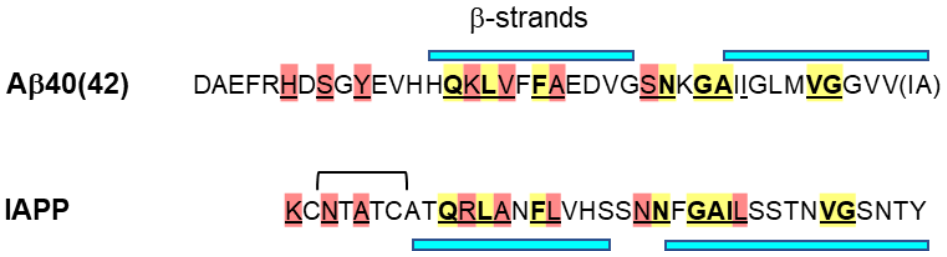

Figure 15. Primary structures of Aβ and IAPP. The identical amino acids shared by both Aβ40(42) and IAPP sequences are highlighted in yellow, and similar amino acids are marked in red. The blue bars indicate the region of both sequences arranged in β-strand, based on the ssNMR models. Figure based on reference [28].

The next round of optimisation consisted of the design of (cross)amyloid inhibitors called "interaction surface mimics" or ISMs[97]. ISMs were 21-residue long peptides that mimic putative IAPP self-and/or Aβ cross-interaction surfaces. Notably, some of them were found to also block cross-seeding of IAPP by Aβ40 fibrils, which has been suggested as a possible link between the two diseases[27,29,31].

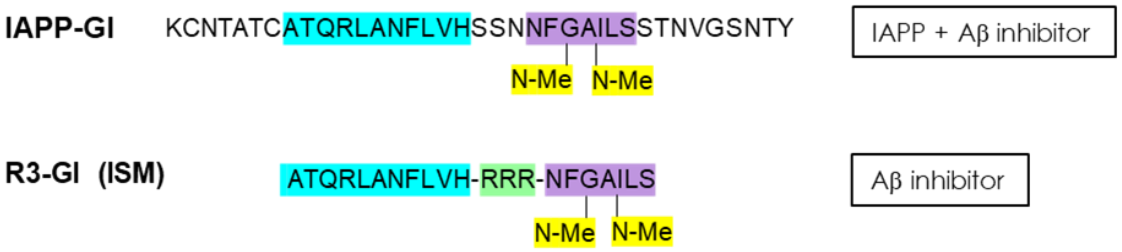

Figure 16. Primary structures of IAPP-GI and R3-GI. The N-methylations in positions 24 and 26 of the IAPP sequence are highlighted in yellow. In contrast, the segments of the IAPP sequence conserved in the **R3-GI** design are marked in blue (IAPP(8-18)) and purple (IAPP(22-28)). The linker inserted in the **R3-GI** sequence to stabilise preferred conformations is highlighted in green. Figure based on reference [98].

The design of inhibitors was based on the finding that IAPP self-assembly is mediated by the same two hot segments involved in cross-assembly with Aβ40(42)[28]. ISMs were generated by connecting "hot spots" (in the native or N-methylated form) through tripeptide linkers that could influence the secondary structures of peptides, thus modulating their potency and selectivity[98]. The high-affinity binding of ISMs mainly mediated binding affinity and inhibitory potential to prefibrillar Aβ40(42) or IAPP species, which were sequestered into amorphous/nontoxic hetero-aggregates. In the next round of optimisation, the ISM **R3-GI** was used as a template to design novel macrocyclic peptides as potent amyloid inhibitors. These macrocyclic inhibitory peptides (MCIPs) mimic functional (inhibitory) IAPP interaction surfaces while maintaining only four IAPP-derived recognition elements[99], alternated with glycines. Spanopoulou and coworkers[99] reported that the 17-residue **2b** was a nanomolar inhibitor of the cytotoxic self-assembly of both Aβ40(42) and IAPP but was readily degraded by serum proteases. Therefore, a systematic L-/D-residue exchange was used to achieve crucial drug-like properties, such as plasma stability and BBB permeability. This approach led to the design of analogue **2e**, a selective nanomolar inhibitor of Aβ40(42)

with high proteolytic stability in human plasma. As **2e** also crossed the BBB in a human cerebral cell model, it is a promising candidate for AD anti-amyloid drugs.

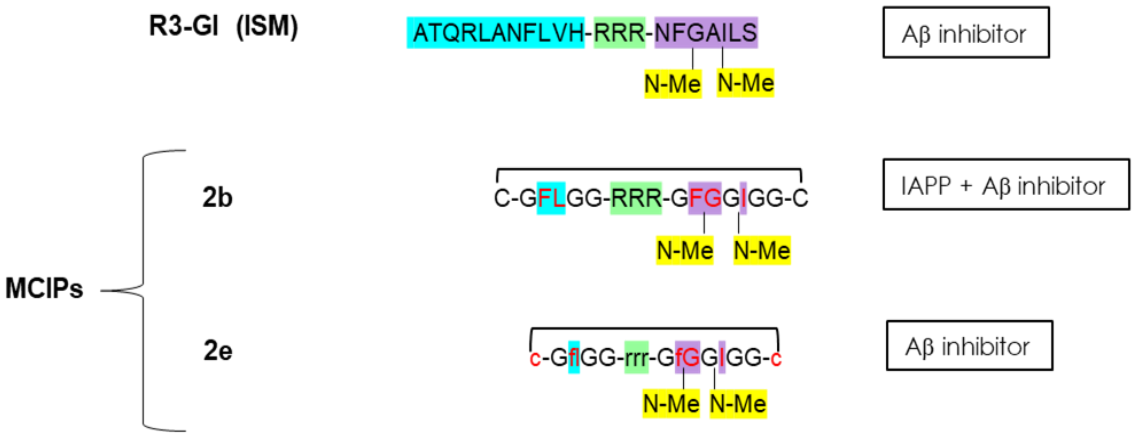

Figure 17. Primary structures of the MCIPs. The first step of the MCIPs design was an N-terminal truncation of the primary sequence of **R3-GI**, which was used as a template. The N-terminal shortening was applied based on the hypothesis that IAPP(14-18) dictates IAPP self- and cross-interactions [28,100,101]. The sequences were cyclised by forming a disulphide bridge between the Cys introduced at the N- and C- termini (**2a**). Aiming to minimise IAPP-derived AA even further, all the residues, except for Phe[15], Leu[16], Phe[23] and (NMe)Ile[26], were substituted with glycines (**2b**). Finally, substituting the critical residues with D-amino acids was applied to enhance the proteolytic stability and the membrane permeability of the sequences. Scheme based on reference[99].

2 Aims of the thesis

As mentioned in the previous chapter, earlier studies of our group showed that the "hot segments" of the IAPP and Aβ42 interaction can be used as templates to design potent inhibitors of amyloid assembly of Aβ42 or IAPP[28,95]. In this context, the previously designed 17-residue long MCIPs containing four IAPP-derived amino acids Phe^{15}, Leu^{16}, Phe^{23} and Ile^{26} (in its N-methylated form) were found to be potent inhibitors of IAPP or Aβ42 amyloid formation[96]. Notably, MCIP **2e** strongly suppressed Aβ40(42) amyloid self-assembly and, in addition, it exhibited a high proteolytic stability in human plasma *in vitro* and was able to cross the BBB in a human cerebral endothelial cell model[96].

In my thesis, I addressed the questions a) whether designed cyclic hexapeptides termed minimized IAPP mimics (MIMs) and consisting of the four above mentioned IAPP-derived key residues, an Arg residue, and a Gly residue would still be able to inhibit amyloid formation and cytotoxicity of IAPP and/or Aβ42, and if yes b) whether MIMs might have favourable properties with respect to proteolytic stability in human plasma and BBB permeability in a human cerebral cell model as found for the MCIP **2e**.

On this basis, my thesis had these specific aims:

1. Design and synthesis of cyclic hexapeptides (MIMs) acting as potent inhibitors of IAPP and/or Aβ42 amyloid self-assembly.
2. Biophysical characterization of MIMs and their linear precursors, including secondary structure and self-association propensity, to determine their structure-activity relationships and learn more about the structural basis of their activity.
3. Characterization of the effects of MIMs on unseeded, self-seeded, and cross-seeded amyloid self-assembly and cytotoxicity of IAPP and/or Aβ42.
4. Characterization of the effects of MIMs on the amyloidogenic character and cytotoxicity of different species of the amyloidogenesis pathway of IAPP and Aβ42, i.e., monomers, oligomers, and fibrils.
5. Development of an experimental approach to follow formation of transient IAPP and Aβ42 oligomeric species based on their intrinsic characteristics (structure, cytotoxicity, morphology, and immunoreactivity).
6. Characterization of the interactions occurring between MIMs and their target polypeptides via CD spectroscopy, cross-linking, peptide arrays, and fluorescence spectroscopic titrations.
7. Characterization of the proteolytic stabilities of selected MIMs and linear precursors in human plasma *in vitro*.
8. Characterization of the BBB-crossing potential of a selected MIM (lead peptide) in a human cerebral endothelial cell model (in collaboration)
9. Studying the effects of selected MIMs on the impairment of the hippocampal synaptic LTP caused by Aβ42 aggregates (in collaboration).

3. Materials and Methods

3.1 Materials

3.1.1 Chemicals

Table 2. Chemicals

Chemicals	Company (city or country)
Acetic Anhydride	Sigma-Aldrich (St. Louis, USA)
Acetonitrile (ACN)	VWR (Radnor, USA)
2-(7-Aza-1H-benzotriazole-1yl)-1,1,3,3-tetramethyluronium) (HATU)	Bachem (Bubendorf, CH)
BSA (Albumin Fraction)	Roth (Karlsruhe, DE)
(2-(1H-Benzotriazol-1-yl)-1,1,3,3-tetramethyluronium-hexafluorophosphat) (HBTU)	Iris Biotech (Marktredwitz, DE)
5(6)-carboxyfluorescein (Fluos)	Sigma-Aldrich (St. Louis, USA)
5(6)carboxytetramethylrhodamine (TAMRA)	(Novabiochem/ Merck) ((Darmstadt, DE)
Chloranil	Fluka (Seelze, DE)
Dichloromethan (DCM)	Roth (Karlsruhe, DE)
2CTC resin	Iris Biotech (Marktredwitz, DE)
Dimethylsulfoxide (DMSO)	Sigma-Aldrich (St. Louis, USA)
N,N-Diisopropylethylamine (DIEA	Roth (Karlsruhe, DE)
3-(4,5-dimethylthiazol-2-yl)-2,5-diphenyltetrazolium bromide (MTT)	Sigma-Aldrich (St. Louis, USA)
N,N-Dimethylformamide (DMF)	CLN (Niederhummer, DE)
Diethyl ether (Et_2O)	CLN (Niederhummer, DE)
1,2-Ethanedithiol (EDT)	Fluka (Seelze, DE)
Dithiothreitol (DTT)	Sigma-Aldrich (St. Louis, USA)
Glycin	Fluka (Seelze, DE)
Glutaraldehyde solution	Sigma-Aldrich (St. Louis, USA)
Hellmanex	Hellma Analytics (Müllheim, DE)
Hydrochloric acid (HCl)	Roth (Karlsruhe, DE)
1,1,1,3,3,3-hexafluor-2-propanol (HFIP)	Roth (Karlsruhe, DE)
1-Hydroxybenzotriazol (HOBt)	Sigma-Aldrich (St. Louis, USA)
Isopropanol	CLN (Niederhummer, DE)
Methanol (MeOH)	VWR (Radnor, USA)
Milk powder (not fat-dried)	VWR (Radnor, USA)
Ninhydrin	Sigma-Aldrich (St. Louis, USA)
NupAGE 4-12% BT Gel	Invitrogen (DE)
Peptide Calibration Standard	Bruker (Billerica USA)
Phenol	Iris Biotech (Marktredwitz, DE)
Piperidine	Roth (Karlsruhe, DE)
Polylysin	Sigma-Aldrich (St. Louis, USA)
Proteinmarker-Multimark TM	Fisher Scientific (Hampton, USA)
Protected amino acids (AA)	Iris Biotech (Marktredwitz, DE)
NP Mes SDS Buffer BMF (20x)	Invitrogen (DE)
SDS page	Invitrogen (DE)
Sodium chloride (NaCl)	Roth (Karlsruhe, DE)
Sodium dihydrogen phosphate (NaH_2PO_4)	Merck (Darmstadt, DE
Sodium dodecyl sulfate (SDS)	Roth (Karlsruhe, DE)
Sodium hydrogen phosphate dihydrate (NaH_2PO_4 x 2 H_2O)	Roth (Karlsruhe, DE)
Sodium hydroxide (NaOH)	Roth (Karlsruhe, DE)
Super signal duration ECL staining solution	Sigma-Aldrich (St. Louis, USA)
NP Transfer Buffer BMF (20x)	Invitrogen (DE)
3-[Bis(dimethylamino)methyliumyl]-3*H*-benzotriazol-1-oxide hexafluorophosphate	Iris Biotech (Marktredwitz, DE)
Thioflavin T (ThT)	Sigma-Aldrich (St. Louis, USA)

Triisopropylsilane (TIS) 99%	Sigma-Aldrich (St. Louis, USA)
Trichloracetic acid (TCA)	Roth (Karlsruhe, DE)
Trifluoracetic acid (>99.5%) (TFA for synthesis)	Iris Biotech (Marktredwitz, DE)
Trifluoracetic acid (>99.5%) (TFA for HPLC)	Sigma-Aldrich (St. Louis, USA)
Trifluoroethanol (TFE)	Roth (Karlsruhe, DE)
Triton X-100	Sigma-Aldrich (St. Louis, USA)
Uranyl acetate	Sigma-Aldrich (St. Louis, USA)

3.1.2 Synthetic peptides (purchased or provided by others)

Table 3. Peptides

Peptides	**Company (city or country)**
TAMRA-Aβ42	Bachem (Bubendorf, CH)
Aβ(1-42)	Synthesis by the group of Prof. Dr. Aphrodite Kapurniotu, purification by Peptide Specialty Laboratories
FITC-βAla-Amyloid-β-protein (1-42) (Ammonium salt) (abbr. FITC-Aβ42)	Bachem (Bubendorf, CH)
hIAPP	Synthesis by K. Hille (group of Prof. Dt Kapurniotu)
Fluos-IAPP	Synthesis by K. Hille (group of Prof. Dr. Aphrodite Kapurniotu)

3.1.3 Assay kits

Table 4. Assay kits

Assay kits	**Company (city or country)**
Micro Bicinchoninic acid (BCA) protein assay kit	Fischer Scientific Pierce (DE)
SuperSignal West Dura extended duration substrate	Fischer Scientific (DE)

3.1.4 Materials and devices

Table 5. Materials

Material	**Company (city or country)**
96 well plate, Cellstar, sterile, F-bottom (cell culture)	Greiner Bio-One (Frickenhausen, DE),
96 well plate, CellGradeTM plus, sterile (cell culture)	B. Braun (Melsungen, DE)
Cellstar® Tubes, 15 mL	Greiner Bio-One (Frickenhausen, DE)
Cellstar® Tubes, 50 mL	Greiner Bio-One (Frickenhausen, DE)
Cuvette, quartz	Hellma Analytics (Müllheim, DE)
Disposable hypodermic needles, 100 Sterican Gr.18	BRAND (Wertheim, DE)
Filter, Millex-FG, 0.2 µm	Filter, Millex-FG, 0.2 µm Merck (Darmstadt, DE)
Glass reaction vessel	CS-Bio Inc (California, USA)
Microtiter plate, 96 well, F-bottom, black	FluoroNunc/Thermo Fisher Scientific
Nitrocellulose membrane	XCell II BlotModule, Thermo Fisher Scientific
Pasteur pipette	BRAND (Wertheim, DE)
Pipette tips, 2-200µl, yellow	BRAND (Wertheim, DE)
Pipette tips, 100-1000µl, blue	BRAND (Wertheim, DE)
Pipette tips, 0.5-10µl	Axygen (Union City, USA)
Pasteur pipettes, glass, 145mm	BRAND (Wertheim, DE)
Reaction vessel, 1.5m	Sarstedt (Nümbrecht, DE)
Syringe, BD Discardit II, sterile, 10 mL	Becton Dickinson (Franklin Lakes, USA)
Syringe, BD Discardit II, sterile, 20 mL	Becton Dickinson (Franklin Lakes, USA)
Syringe, BD Discardit II, sterile, 2 mL	Becton Dickinson (Franklin Lakes, USA)
TEM grids, FCF300-Cu, 300 mesh	Electron Microscopy Science

Table 6. Devices	
Devices	**Company (city or country)**
Analytical balance	Denver Instrument Sartorius (Göttingen, DE)
Centrifuge Labofuge AE	Heraeus Sepatech (Osterode, DE)
CO_2 Incubator MCO-17AIC	Sanyo Electric Co
Eppendorf centrifuge 5417C	Netheler-Hinz GmbH (Hamburg, DE)
Jasco FP-6500 fluorescence spectrophotometer	Jasco (Gross-Umstadt, DE)
Heating block neo Block 1	NeoLab (Heidelberg, DE)
HPLC degassing unit DG-2080-53	Jasco (Gross-Umstadt, DE)
HPLC low-pressure gradient unit LG-2080-02S	Jasco (Gross-Umstadt, DE)
HPLC pump PU-2080 Plus	Jasco (Gross-Umstadt, DE)
HPLC UV/Vis detector UV-2077 Plus	Jasco (Gross-Umstadt, DE)
LAS-4000 mini Fujifilm	Fujifilm Europe GmbH (Düsseldorf, DE)
Magnetic stirrer Topolino	Carl Roth (DE)
Microscope model CKX41	Olympus
Multichannel pipette	BRAND (Wertheim, DE)
2030 Multilabel Reader VictorX3 instrument	(PerkinElmer Life Sciences)
pH-Meter	Mettler Toledo (Greifensee, CH)
Shaker CAT S20	CAT (Staufen, DE)
Jasco 715 spectropolarimeter	Jasco (Gross-Umstadt, DE)
SDS X cell sure Lock BIO-RAD	Invitrogen (Carlsbad, USA)
Ultrapure water unit TKA MikroPure	TKA (Niederelbert, DE)
Ultrasonic bath SONOREX	Bandelin (Berlin, DE)
UV-Vis spectrophotometer V630	Jasco (Gross-Umstadt, DE)
Vortex Mixer Vortex Genie 2	Scientific Industries (New York, USA)

3.1.5 HPLC-columns and precolumns

Table 7. HPLC-columns and precolumns	
Instrument	**Company**
SEC column: Superdex 75 10/300 GL column	(GE Healthcare)
Column: Nucleosil 100 C18, 250 mm length, ID 8 mm, 7 µm particle size	Grace/Alltech
Precolumn: Nucleosil 100 C18, 33 mm length, ID 8 mm, 7 µm particle size	Grace/Alltech

3.1.6 Cell culture material

Table 8. Cell culture reagents	
Reagent	**Company (city or country)**
D-Glucose	Sigma-Aldrich (St. Louis, USA)
Fetal Calf Serum (FCS)	Fisher Scientific (Hampton, USA)
L-Glutamine	Fisher Scientific (Hampton, USA)
Horse serum	Fisher Scientific (Hampton, USA)
Non-essential amino acids (NEAA)	Fisher Scientific (Hampton, USA)
Penicillin/Streptomycin	Fisher Scientific (Hampton, USA)
RPMI-1640	Fisher Scientific (Hampton, USA)
Trypsin-EDTA (0.05%)	Fisher Scientific (Hampton, USA)

3.1.7 Antibodies

Table 9. Antibodies

Antibodies	**Company**
Polyclonal Rabbit-Anti-Amylin (Human)	Peninsula Laboratories
Polyclonal (anti-)oligomer A11 antibody	Fisher Scientific (Hampton, USA)
Polyclonal Donkey anti-rabbit-POD	GE-Healthcare

3.1.8 Buffers

Table 10. Buffers

Buffer	**Composition**
HPLC buffer A	0.058% (v/v) TFA in water
HPLC buffer B	0.05% (v/v) TFA in 90% ACN/water
1xb (pH 7.4)	10 mM phosphate buffer (pH 7.4)
IAPP ThT buffer	aqueous 50 mM sodium phosphate buffer, pH 7.4, containing 100 mM NaCl
Aβ42 ThT buffer	aqueous 45 mM ammonium acetate buffer pH 8.5
TBS-T	20 mM Tris/HCl, 150 mM NaCl, and 0.05% Tween-20

3.2 Methods

3.2.1 Synthesis of minimized IAPP mimics and linear precursors

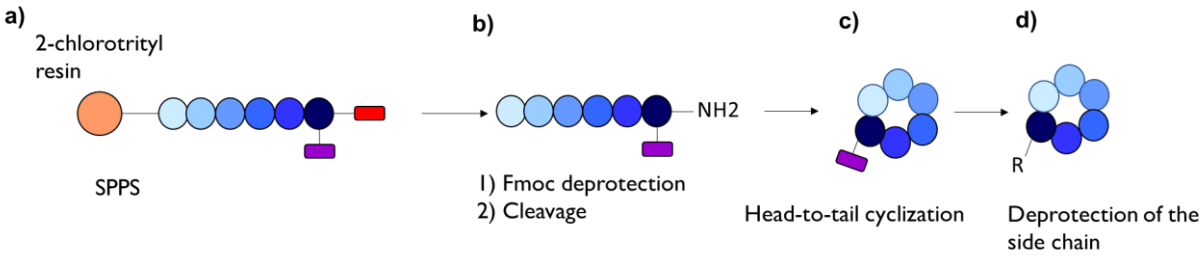

Scheme 1. Steps of the synthesis of MIMs and linear analogues. (a) MIMs and the linear precursors were synthesised on 2-chlorotrityl resin using the Fmoc/tBu strategy. (b) After coupling the last amino acid, the N-terminal Fmoc protecting group was removed, and the peptide was cleaved from the resin while keeping the protecting group for Arg/Lys side chain in situ. (c) The head-to-tail cyclisation was performed in solution. (d) Once the cyclisation was accomplished, the protecting group for the side chain was removed.

3.2.1.1 Fmoc/tBu approach of solid phase peptide synthesis (SPPS)

The linear peptide sequences were synthesised by manual SPPS following the Fmoc/tBu strategy[102–105] (Scheme 1). Accordingly, couplings steps of N-terminally and sidechain-protected amino acids (Table 11) were performed by incubating the pre-treated resin in DMF with a mixture of 3-fold-excess of Fmoc-AA-OH, 3-fold-excess of activator (HBTU or HATU) and 4.5-fold-excess of DIEA, as described in Table 12. The substitution level obtained after coupling the first amino acid was used to calculate the excess of activators, amino acids, and DIEA used for assembling the peptide chain. The yield of the couplings was qualitatively ensured via the Kaiser or chloranil tests to monitor the introduction and deprotection of amino acids and N-methylated amino acids, respectively[106]. The N-terminal

Fmoc protecting group was cleaved in a solution of 25% piperidine in DMF by applying the deprotection cycles described in Table 12.

Table 11. Sidechain-protecting groups of the amino acids used in this work

Amino acid	Protecting group
Arg or (D)-Arg	Pbf (2,2,4,6,7-Pentamethyldihydrobenzofuran-5-sulfonyl)
Lys or (D)-Lys	Boc (tert-butyloxycarbonyl) Mtt (4-Methyltrityl)

Table 12. Steps of 2g synthesis by applying the Fmoc/tBu strategy

N.	Amino acid	Coupling*	Number of couplings	Capping*	Fmoc-deprotection**
6	Fmoc-(D)-Leu-OH	AA (1.25 eq.) DIEA (3 eq.) in DCM (1 h)	2	DCM/MeOH/DIEA (16/3/1) (10 min)	1 x 5 minutes 1 x 10 minutes
5	Fmoc-(D)-Phe-OH	AA (3 eq.) HBTU (3 eq.) DIEA (4.5 eq.) (40 min)	2	Ac_2O (10 eq.) DIEA (10 eq.) (10 min)	1 x 1 minute 1 x 5 minutes
4	Fmoc-Gly- OH	AA (3 eq.) HBTU (3 eq.) DIEA (4.5 eq.) (40 min)	2	AC_2O (10 eq.) DIEA (10 eq.) (10 min)	1 x 5 minutes 1 x 10 minutes
3	Fmoc-Ile-(N-Me)-OH	AA (3 eq.) HBTU/HATU (3 eq.) DIEA (4.5 eq.) (40 min)	3	AC_2O (10 eq.) DIEA (10 eq.) (10 min)	1 x 1 minute 1 x 5 minutes (Chloranil Test)
2	Fmoc-(D)-Phe-OH	AA (3 eq.) HBTU (3 eq.) DIEA (4.5 eq.) (40 min) (Chloranil test)	2	Ac_2O (10 eq.) DIEA (10 eq.) (10 min)	1 x 1 minute 1 x 5 minutes
1	Fmoc-(D)-Arg(Pbf)-OH	AA (3 eq.) HBTU (3 eq.) DIEA (4.5 eq.) (40 min)	2	--	1 x 1 minute 1 x 5 minutes

*The solvent used for the reactions was DMF, if not otherwise specified. Couplings were confirmed via Kaiser test if not otherwise specified.

**The Fmoc-deprotection was performed in 25% piperidine in DMF and monitored via Kaiser test, if not otherwise stated.

3.3.1.2 Substitution level determination

The amount of reagents used for synthesising the peptide was optimised by calculating the substitution level of the resin after coupling the first amino acid. For MIMs syntheses, a low substitution level was desirable to avoid steric hindrance and side reactions, such as diketopiperazine formation [111–115].

3 mg of resin bearing the C-terminal Fmoc-protected amino acid were weighed into a volumetric flask and incubated for 10 min with 10 mL of 25% v/v piperidine in DMF at RT. The deprotonation, cleavage, and rearrangement of the Fmoc group lead to the formation of the dibenzofulvene-piperidine adduct, which exhibits its UV absorbance maximum at 290 nm with ε=5800 $mol^{-1} \cdot L \cdot cm^{-1}$ [104]. 1 mL of the piperidine solution was transferred into a 1-

cm cuvette, and the absorbance was measured at 290 nm (baseline subtracted). This procedure was repeated three times.

Once the absorbance was obtained, the substitution level was calculated by applying the Lambert–Beer's law equation:

$$S.L.= (A * V)/(\varepsilon * m)$$

S.L. = substitution level (mmol/g)
A = absorbance
V= volume (mL)
ε = molar coefficient at 290 nm (=5800 L mol^{-1} cm^{-1})
m = (g)

The substitution level was obtained as a mean of three values and is reported in Table 13.

Table 13. Representative substitution levels of MIMs and linear analogue-resin

Peptide	S.L. (mmol/g)
2f	0.28
2g	0.32
2h	0.51
2i	0.34
2f linear	0.28
2g linear	0.32
2h linear	0.51
2i linear	0.34

3.2.1.3 Coupling of N-methylated amino acids

N-methylated amino acids were coupled by applying the standard coupling method described in Table 12. Due to steric hindrance, coupling the following amino acid usually required a 3rd step performed with a 3-fold molar excess of HATU. The coupling efficiency was qualitatively ensured by the chloranil test[116], which is suitable for assessing the reactivity of secondary amines.

3.2.1.4 Capping Steps

The capping step (Ac_2O/DIEA in DMF, 10-fold molar excess) consisted of an acetylation performed after each coupling confirmed via Kaiser or chloranil tests. This reaction was necessary to avoid the elongation of shorter peptide sequences, which could decrease the yields of the synthesis and the purity of the final products.

3.2.1.5 Kaiser test

The Kaiser test is a colourimetric assay used to monitor the coupling of amino acids, as it can detect the presence of free and primary amino groups[108,117]. A characteristic and intensive blue colour is generated by the reaction of ninhydrin with free primary amines, and it can be considered a positive result [100,102]. Conversely, the presence of colourless and yellow solutions confirms the absence of NH_2 and the completeness of the coupling. This qualitative

assay was performed by incubating few beads of peptide resin in a test tube with three drops of the following solutions:

- Ninhydrin in ethanol (5 g in 100 mL ethanol)
- Phenol in ethanol (40 g in 10 mL ethanol)
- An aqueous solution of potassium cyanide in pyridine (2 mL of aqueous 0.001M KCN in 100 mL pyridine)

The sample tubes were incubated for 5 minutes at 100°C.

3.2.1.6 Acetaldehyde/Chloranil test

The chloranil test is the standard qualitative method used to monitor the presence of secondary amines, such as Pro or N-methylated amino acids. chloranil reacts with secondary amines in the presence of acetaldehyde, resulting in a green-blue benzoquinone derivative[103,105,106]. Tertiary amines (Fmoc-protected N-methylated amino acid) or amide groups (peptide bond) are not nucleophilic enough to generate the reactive intermediate. Therefore the solution and the beads remain colourless [103,105,106]. The test is performed at RT by incubating for a few seconds a small amount of peptide resin in a sample tube with the following solution:

- 2% acetaldehyde in DMF (v/v) (few drops)
- 2% chloranil in DMF (a few drops)

Remarkably, the sensitivity of both the Kaiser and the Chloranil tests decreases while elongating the peptide chain, and their results can eventually be misleading. This was not observed while synthesising Minimized IAPP Mimics due to their small size.

3.2.1.7 Peptide cleavage from 2-chlorotrityl chloride resin

After performing the last Fmoc-deprotection of the N-terminal AA (AA 1) as described previously, the peptides synthesized on 2-chlorotrityl resin were cleaved from the resin in mildly acidic conditions[118]. This way, the protecting groups of the side chains were kept in situ. This strategy was necessary to avoid the formation of side products, involving the C-terminus of the peptide and the side chains of the N-terminal Arg or Lys, during the following head-to-tail cyclization performed in solution.
To cleave the peptide from the 2-chlorotrityl resin, 40 mg of peptide-resin were treated in TFE:DCM (20:80) (1 mL) under agitation for 1 h, and this procedure was repeated 3 times. Thereafter, the collected cleavage solution was evaporated by using a rotary evaporator;. The peptide was redissolved in a solution of 80% B in A and lyophilized.

To obtain the linear sequences, the peptides were cleaved in one step by treating 40 mg of peptide resin in a mixture of TFA/ddH_2O (95/5). The reaction was performed for 3 h and under agitation, to achieve a full cleavage of the peptide sequences from the resin and to remove the side protecting groups from the sequence. Thereafter the cleavage solution was diluted (1/10) in 80% B in A, frozen down and lyophilized.

3.2.1.8 Head-to-tail cyclization

The head-to-tail cyclisation was performed in highly diluted conditions to promote the formation of an intramolecular bond rather than an intermolecular one[119]. The peptides were diluted to 0.8 mM[119] in DMF in the presence of 1.5 eq. of activators (BOP and HOBT, equimolar) and 2.25 eq. of DIEA.

For the head-to-tail cyclisation, 6 mg of crude peptide powder, after cleavage from the resin and lyophilisation, was weighted into a vial together with BOP and HOBT. After that, the peptide powder was dissolved in 2 mL of DMF. The vial containing this solution was placed on ice before adding the DIEA to avoid racemisation [119]. Subsequently, the solution was transferred into the round bottom flask, diluted to the final volume of DMF, and left under vigorous agitation for 12 h at RT.

The kinetics of the cyclisation was followed via analytical RP-HPLC combined with MALDI-TOF. The HPLC analysis was performed with 50 µL of peptide solution (0.8 mM) per time point, including 0 h, 2 h, 4 h, 6 h and 24 h. In all cases, the retention time of the cyclised peptides increased by circa 2 minutes compared to the linear sequences, indicating an increase in hydrophobicity upon cyclisation. Remarkably, the peak assigned to the linear precursor was not observed by the end of the reaction, indicating that the reaction was complete and achieved in quantitative yield. After achieving the cyclisation, the DMF was evaporated entirely using a rotary evaporator. The dried product was redissolved in 80% B in A and lyophilised.

The head-to-tail cyclisation could also be performed in DMSO without variation in the kinetics. Thus, DMF was the solvent of choice due to its lower boiling temperature (153 ºC vs 189 ºC)[120].

3.2.1.9 Side chain deprotection of MIMs

The side chain deprotection was performed by treating the cyclised peptide in solution of 95% TFA in ddH_2O (1 mg/mL) for 120 minutes under vigorous agitation. In these acidic conditions, Boc and Pbf are easily removed [103,104]. After that, the peptide solution in TFA was diluted in 80% B and lyophilised or directly purified via HPLC.

3.2.2 Synthesis of fluorescently labelled 2i (Fluos-2i)

For the fluorescence spectroscopy titrations, the DB studies, and the BBB permeability studies, the sequence of **2i** was labelled with 5(6)carboxyfluorescein (Fluos) on the N^{ε} of the N-terminal (D)-Lysine. Before introducing the Fluos moiety, the side protecting group of ε amino group had to be selectively cleaved while a) keeping the amino group on the N^{α} Fmoc-protected to prevent the formation of side products and b) avoiding the full cleavage of the peptide from the resin. To ensure the orthogonality of the protecting groups, Fmoc-(D)-Lys(Mtt)-OH[117] was used to replace Fmoc-(D)-Lys(Boc)-OH. The synthesis was carried out on Wang resin that withstands conditions used for the -Mtt deprotection (Table 14), contrary to the 2-chlorotrityl chloride resin.

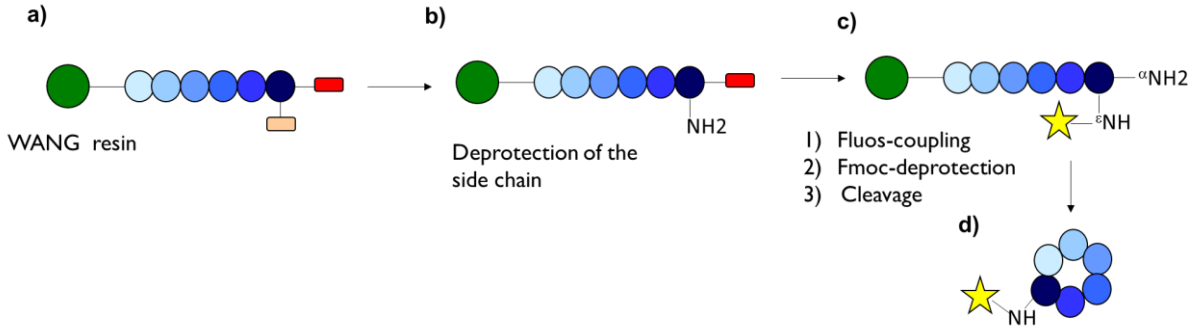

Scheme 2. Synthesis of Fluos-2i. (a) The synthesis of the linear sequence was accomplished by applying the Fmoc/tBu strategy, as described in Table 12. (b) The side protecting group on the on N^{ε} of Fmoc-(D)-Lys(MTT)-OH[1] was selectively removed to avoid side reactions in the solution. (c) After introducing the 5(6)carboxyfluorescein (Fluos) in N^{ε} of (D)-Lys[1], the N^{α} was Fmoc deprotected, and the peptide sequence was cleaved from the resin. (d) after that, the head-to-tail cyclisation was performed in solution.

3.2.2.1 Coupling of the C-terminal amino acid on WANG resin

A mixture of 3 eq. of Fmoc-protected amino acid and 3 eq. of activators (HBTU and HOBT) was dissolved in a small volume of DMF and added to the resin. After that, 4.5 eq. of DIEA were added to the solution, and the mixture was shaken vigorously for 2 h. After determining the substitution level, a capping step was performed by incubating the resin with 10 eq. of Ac_2O and 10 eq. of DIEA in the minimum volume of DMF for 40 min. The substitution level of the resin was 0.24 mmol/g.

3.2.2.2 Mtt deprotection of Fmoc-(D)- Lys(Mtt)-OH

For the synthesis of the fluorescently labelled analogue **Fluos-2i**, Fmoc-D-Lys(Mtt)-OH was used as a building block[117] (Scheme 2). The introduction of the Fluos moiety was usually performed on 30 mg of peptide resin. After the last coupling step and while maintaining the Fmoc protecting group in situ, 30 mg of peptide resin were Mtt-deprotected by treating the resin with the deprotection cycles described in Table 14. Of note, the synthesis of the peptides carrying Mtt- as protecting group could not be performed on 2-chlorotrityl chloride resin due to the acidity of the conditions used for the deprotection[117]. These conditions are sufficient to cleave the peptide from the 2-chlorotrityl resin.

Table 14. Steps of the Mtt deprotection

Step	Conditions	Time
Equilibration	DCM	3 x 3 min
Deprotection	1% TFA, 5% TIS in DCM	2 x 2 min
Deprotection	1% TFA, 5% TIS in DCM	6 x 10 min
Washing	DCM	3 x 3 min
Kaiser test		
Neutralisation	1% DIEA in DMF	2 x 2 min
Washing	DMF	3 x 1 min

% = v/v

3.2.2.3 Coupling of fluorescein

After washing the resin extensively, 5(6)-carboxyfluorescein (Fluos) was introduced on the ε-amino group of (D)-Lys[1] by adding 3 eq. of Fluos, 3 eq. of HBTU and 4.5 eq. of DIEA as described in Table 15. The coupling was performed two times for 2 h;. Notably, the resin was

washed extensively between the two coupling steps to avoid forming a side product carrying two Fluos moieties, as identified via MALDI.

Table 15. Steps of the labelling with Fluos

Step of the labelling	Conditions	Time
Equilibration	DMF	2 x 5 min
Fluos-coupling	Fluos/ HBTU/DIEA (3 eq., 3 eq., 4.5 eq.) in DMF	1 x 2 h
Washing	DMF	6 x 2 min
Fluos-coupling	Fluos/ HBTU/DIEA (3 eq., 3 eq., 4.5 eq.) in DMF	1 x 2 h
Washing	DMF	3 x 2 min

3.2.2.4 Peptide cleavage from WANG resin and head-to-tail cyclisation

After introducing 5(6)carboxyfluorescein (Fluos) on the ε-amino group of (D)-Lys[1] (30 mg of peptide-resin), the α–amino group of (D)-Lys[1] was Fmoc deprotected in 25% piperidine in DMF. After washing extensively in DMF, the resin was dried with Et_2O (1 mL, 10 min) and by employing the desiccator for 30 min. The cleavage mixture consisted of 95% TFA and 5% ddH_2O (1 mL), and the resin was treated with it for 3 h under strong agitation and light protection. The collected cleavage solution was then diluted (1/10) in 80% HPLC buffer B in HPLC buffer A (% v/v) and lyophilised. The head-to-tail cyclisation was performed in the conditions described in paragraph 3.2.2.7, and the solution was protected from the light during the reaction.

3.2.3 Purification of synthesised peptides

Reversed-phase high-performance liquid chromatography (RP-HPLC) is the most applied method for analytical and preparative separations of compounds of interest in chemical, biological, pharmaceutical, food and biomedical applications [121]. This method consists of a stationary phase packed with a non-polar hydrophobic octyl or octadecyl functional group bonded to silica gel [121]. The mobile phase is a polar solvent. The retention time ($\mathbf{t_R}$) of the analyte, peptides, in the case of this work, depends on the affinity for the two phases[121]. The polar compound gets eluted first in this mode, and hydrophobic compounds are retained for longer. The columns used are C18, C8, and C4 (in the order of increasing polarity of the stationary phase). The purification of MIMs, their linear precursors and **Fluos-2i** was performed via RP-HPLC on a NucleoSil 100 C18 column with a length of 25 cm, internal diameter of 8 mm and 7 µm particle size (Grace/Alltech) and a pre-column Nucleosil 100 C18 with a length of 33 mm and 7 µm particle size (Grace/Alltech).

The flow rate was 2 mL/min, and eluting buffers were:

- HPLC buffer A: 0.058% (v/v) TFA in water
- HPLC buffer B: 0.05% (v/v) TFA in 90% ACN/water

Peptides were detected at 214 nm or 214 nm paired with 433 nm if fluorescently labelled. The gradient programs that were used are shown in Tables 16 and 17. The eluted peptide solution was immediately frozen in dry ice and lyophilised.

Noteworthy, one round of purification was sufficient to achieve over 95% yield of purity for the small cyclic peptides, except for **Fluos-2i**, for which a second round of purification was necessary, as described in Table 17.

Table 16. HPLC-gradient applied to purify the synthetic peptides

HPLC program	Flow (mL/min)	Time (min)	Buffer A	Buffer B
10-100% B in 30 min	2.0	0	90%	10%
		1	90%	10%
		20	0%	100%
		30	0%	100%

Table 17. HPLC-gradient was applied for the second round of purification of Fluos-2i

HPLC program	Flow (mL/min)	Time (min)	Buffer A	Buffer B
Langsam Aβ	2.0	0	70%	30%
		7	70%	30%
		37	30%	30%

3.2.4 Matrix-assisted laser desorption/ionisation

Matrix-assisted laser desorption/ionisation (MALDI) mass spectrometry (MS) is one of the most widely used techniques in proteomics to achieve structural identification and characterization of proteins and peptides[122–124]. Matrix-assisted laser desorption/ionisation (MALDI) is an ionisation technique that exploits a laser energy-absorbing crystallised molecule (matrix) to create ions from the embedded analytes while ensuring minimal fragmentation[124]. MALDI is a “soft ionisation” technique that produces rapid and effective ionisation of a wide range of biomolecules using a matrix to absorb laser energy to produce ions with minimal fragmentation[124]. The charged analytes/ions generated by the MALDI source are then detected and measured using different types of mass analysers, such as time-of-flight (ToF), quadrupole (Q), ion trap (IT), quadrupole ion trap (Q-IT), FT-ICR analysers, etc. Coupling a quadrupole and ToF produced high-resolution hybrid mass spectrometers, i.e., Q-TOF tandem mass spectrometric instrument[123,124]. For peptide and protein analysis, a MALDI source is commonly coupled with a ToF detector (MALDI-ToF)[124].

In this thesis, the samples were prepared by dissolving a small amount of the lyophilised peptide into an aqueous solution consisting of aqueous 97% acetone and 0.1% TFA and then mixed (1:1) with a saturated solution of a-cyano-4-hydroxycinnamic acid (HCCA) (matrix) prepared in the same solvent. 0.5 µl of this mixture were spotted on the target. Subsequently, the spots were dried and washed with an aqueous solution consisting of 10 mM $NH_4H_2PO_4$ containing 0.1% TFA to quench the signal of adduct ions. The mass was recorded on positive ion mode, and monoisotopic mass was determined as $[M+H]^+$ or $[M+Na]^+$ or $[M+K]^+$ (M is monoisotopic mass).

3.2.5 Preparation of peptide stocks

Preparation of IAPP stock solution

IAPP was synthesised on RINK amide resin[125] by Kathleen Hille (group of Prof. Dr. Aphrodite Kapurniotu) by applying Fmoc based SPPS. The crude product was subjected to air oxidation, purified via RP-HPLC by members of the Peptide Biochemistry group, and stored at -20°C. IAPP stocks were prepared by dissolving IAPP powder in HFIP (1 mg/mL) and incubating the solution on ice for three h at RT to obtain a homogeneous solution. After that, the stock was filtered through 0.2 µm filters, and the absorbance of Tyr^{37} (274 nm) was measured via UV detection according to previously published protocols[28,95,96,98–100,126,127]. The exact concentration was calculated by applying Lambert-Beer`s[128] law (extinction coefficient ε(274 nm) = 1440 $M^{-1}cm^{-1}$).

$$A = c * \varepsilon * d$$

c : concentration (M)
A: absorbance
ε: molar absorbance coefficient (L mol^{-1} cm^{-1})
d: optical path length (cm)

Preparation of Aβ42 stock solution

Aβ42 was synthesised on Tentagel Resin 4-Hydroxybenzyl Alcohol (R PHB) resin by applying Fmoc-based SPPS by Kathleen Hille, member of the group of Prof. Dr. Aphrodite Kapurniotu. The crude product was purified via RP-HPLC by PSL (Germany), and peptide aliquots were stored at -60 °C. Aβ42 Stocks were prepared by dissolving 500 µg of HPLC-purified Aβ42 (1 mg/mL) in a solution of aqueous 5 M Gdn/HCl in 10 mM TRIS/HCl pH 6.0 and by loading the solutions onto a Superdex 75 10/300 GL column (eluent: 50 mM ammonium acetate pH 8.5, 0.5 mL/min)[127]. The monomeric Aβ42 elution peak was collected on ice, stored at 4°C and used within ten days. The exact concentration was determined by measuring the absorbance at 274 nm (Tyr^{10}) and by applying the Lambert-Beer law (extinction coefficient ε (274 nm) = 1440 $M^{-1}cm^{-1}$).

Preparation of stock solutions of Fluos-peptides and Fluos-IAPP by using UV spectroscopy

HPLC-purified peptides were dissolved in HFIP and filtered through 0.2 µm pores filters. The concentration was obtained by measuring the UV absorbance at the wavelengths at 432 nm by applying the Lambert-Beer law (extinction coefficients: ε(432 nm) = 22770 $M^{-1}cm^{-1}$), according to previously published protocols[98,126,127,129].

Preparation of stock solutions of FITC- Alaβ–Aβ42, TAMRA-Aβ42 using UV spectroscopy

The peptides were dissolved in HFIP, and no filtration was applied. The concentration was obtained by measuring via UV the absorbance at 432 nm (FITC)[99,127] and at 547 nm (TAMRA)[127] and by applying the Lambert-Beer law (extinction coefficients: ε(432 nm) = 22770 $M^{-1}cm^{-1}$[100,126,129], ε (547 nm) = 71391 $M^{-1}cm^{-1}$[127]).

3.2.6 Determination of MIMs concentration via bicinchoninic acid (BCA) protein assay

Bicinchoninic acid (BCA) assay is a copper-based colorimetric assay for protein and peptide quantification. The assay relies on forming a Cu2 +–protein complex in a basic environment,

followed by the reduction of Cu^{2+} to Cu^{+} [130]. The bicinchoninic-Cu^{+} complex formation triggers a colour shift from green to purple, with strong absorbance at 562 nm, proportional to the peptide amount. The assay is performed at 37ºC to increase the amino acids exposure and minimise the differences in amino acid composition in different protein samples. Parameters that might influence the assay are the number of peptide bonds and the presence of amino acids such as cysteine, tyrosine, and tryptophan side[130]. This assay determined amounts of MIMs and linear precursors lower than 1 mg. Due to the short peptide sequences, the incubation at 37ºC was performed for c.a 12 h.

3.2.7 ThT binding assay

Thioflavin-T (ThT) fluorescence[58,59,131,132] is commonly used in *in vitro* systems to follow the kinetics of amyloid formation and to monitor fibril formation in the presence of potential anti-amyloid candidates. Upon binding to the fibril surfaces, ThT gives an intense signal at 486-490 nm when excited at 450 nm.

IAPP self-assembly-related studies

Freshly made IAPP (6 μM) alone and in a mixture with different fold-excess of inhibitors were prepared in IAPP ThT buffer, consisting of aqueous 50 mM sodium phosphate buffer, pH 7.4, containing 100 mM NaCl and 0.5% HFIP. The mixtures of IAPP/inhibitor were made by mixing the IAPP solution in HFIP with the HFIP stock of the peptides (1 mM) and evaporating this solution to obtain an HFIP film. Of note, ThT assays were also performed by mixing IAPP and lyophilised peptide powder, and no difference in the inhibitory effect was observed.

The incubations were prepared in Eppendorf tubes, kept at 20ºCover the time of the experiment, and the kinetics of IAPP fibrillogenesis was followed for seven days. At the indicated time points, 30 μL aliquots of the incubations were mixed with 170 μL of Thioflavin T solution (20 μM ThT in 0.05 M aqueous glycine/NaOH, pH 8.5) in a black microtiter plate. The ThT binding was determined by measuring the fluorescence emission at 486 nm upon excitation at 450 nm using a 2030 Multilabel Reader VictorX3[10,95,98,99,127].

Oligomeric IAPP-related studies

1 h system. IAPP (12 μM) was prepared in IAPP ThT buffer, consisting of aqueous 50 mM sodium phosphate buffer, pH 7.4, containing 100 mM NaCl and 0.5% HFIP. After 1 h of aging, the solution of oIAPP (as shown via DB in Figure 38) was mixed with the HFIP film of the inhibitor, suitable for having 10-fold excess. The incubations were kept at 20ºC, and kinetics of IAPP fibrillogenesis was followed for 24 h by mixing 30 μL aliquots of the incubations with 170 μL of Thioflavin T solution (20 μM ThT in 0.05 M aqueous glycine/NaOH, pH 8.5) in a microtiter plate. The signal was measured by using a 2030 Multilabel Reader VictorX3.

3 h system. IAPP (12 μM) was prepared in IAPP ThT buffer, consisting of aqueous 50 mM sodium phosphate buffer, pH 7.4, 100 mM NaCl and 0.5% HFIP, and aged for 3 h. After that, the solution was mixed with the HFIP film of the inhibitor in 10-fold excess. The solutions

were aged at 20ºC, and kinetics of IAPP fibrillogenesis was followed for 24 h by mixing 30 μL aliquots of the incubations with 170 μL of Thioflavin T solution (20 μM ThT in 0.05 M aqueous glycine/NaOH, pH 8.5) in a microtiter plate. The signal was measured by using a 2030 Multilabel Reader VictorX3.

Fibrillar IAPP disaggregation-related studies

7-day aged IAPP (6 μM) was prepared in IAPP ThT buffer, consisting of aqueous 50 mM sodium phosphate buffer, pH 7.4, containing 100 mM NaCl and 0.5% HFIP. The incubations were prepared in Eppendorf tubes, kept at 20ºC, and the kinetics of IAPP fibrillogenesis was followed for 7 days. After that, the IAPP fibrils were transferred into an Eppendorf tube containing the HFIP film of the inhibitor (20-fold excess), and the solution was mixed. The ThT fluorescence was measured every 24 h for seven days by vortexing vigorously the solution and mixing 30 μL of the peptide solutions with 170 μL of Thioflavin T solution (20 μM ThT in 0.05 M aqueous glycine/NaOH, pH 8.5) in a microtiter plate[126].

IAPP self-seeding-related studies

Preformed IAPP seeds (10%) (confirmed via TEM) were prepared by aging IAPP (128 μM) in IAPP ThT buffer consisting of aqueous 50 mM sodium phosphate buffer, pH 7.4, containing 100 mM NaCl and 0.5% HFIP. 2.34 μL of the incubation-containing seeds were added to 20 250 μL of freshly made IAPP (12 μM) or IAPP/**2i** (1/10) in IAPP ThT buffer. The incubations were kept at 20ºC, and the ThT binding was measured at 0 h, 1 h, 3 h, 6 h, 24 h and 48 h, by mixing 30 μL of the peptide solutions with 170 μL of Thioflavin T solution (20 μM ThT in 0.05 M aqueous glycine/NaOH, pH 8.5) in a microtiter plate[126]. ThT fluorescence was measured by using a 2030 Multilabel Reader VictorX3.

IAPP/Aβ42 cross-seeding related studies

Preformed Aβ42 seeds (10%), ThT and TEM confirmed were prepared by aging Aβ42 (88 μM) in IAPP ThT buffer consisting of aqueous 50 mM sodium phosphate buffer, pH 7.4, containing 100 mM NaCl and 1 % HFIP. 3.4 μL of the solution containing the seeds were added to a freshly made solution containing IAPP (12 μM) or IAPP/**2i** (1/10) in IAPP ThT buffer containing 0.5% HFIP[127]. The incubations were kept at 20ºC, and the kinetics of the seeding effect was followed at the indicated time points by mixing aliquots of the samples with Thioflavin T solution (20 μM ThT in 0.05 M glycine/NaOH, pH 8.5). The ThT binding was measured by using a 2030 Multilabel Reader VictorX3. The ThT binding of the seeds and the buffer signal were subtracted from the data of the assays.

Aβ42 self-assembly related studies

SEC-disaggregated Aβ42 (5 μM), alone and in mixture with the HFIP film of inhibitors (prepared from 1 mM stock solutions), was ready in 180 μL of aqueous ammonium acetate buffer, 45 mM, pH 8.5, in 96-wells MTP plates. The mixtures were incubated with 20 μL of aqueous 100 μM ThT and shaken for the first five h (500 rpm; orbital shaker (CAT S20)) at

37ºC, according to previously reported protocols[127,133]. The incubations were kept at the same temperature but without shaking for the rest of the experiment—the ThT binding of the seeds and the buffer signal were subtracted from the date of the assays. The binding was measured at the indicated time points by using the 2030 Multilabel Reader VictorX3.

Oligomeric Aβ42 related studies

SEC-disaggregated Aβ42 (5 μM) was prepared in 180 μL of aqueous ammonium acetate buffer, 45 mM, pH 8.5, and mixed with 20 μL of aqueous ThT 100 μM in a 96-wells MTP plate. The solution was aged 5 h at 37ºC and under shaking conditions (500 rpm, orbital shaker (CAT S20)). After that, a solution containing oligomeric Aβ42 (confirmed via TEM and DB)[127] was mixed with the HFIP film of the inhibitor in 5-, 10- or 20-fold excess, according to previously published protocols[127]. The ThT binding of Aβ42/**2i** mixtures was measured every 30 minutes for the first 5 h and after 24 h, 48 h, 144 h and 168 h using a 2030 Multilabel Reader VictorX3.

Fibrillar Aβ42 disaggregation studies

SEC-disaggregate Aβ42 (5 μM) was prepared in 180 μL of aqueous ammonium acetate buffer, 45 mM, pH 8.5, and mixed with 20 μL of aqueous ThT 100 μM in a 96-wells MTP plate. The solution was aged for 5fiveh at 37ºC and under shaking conditions (500 rpm, orbital shaker (CAT S20)), and without shaking but at the same temperature for 6 days. The presence of fAβ42 was confirmed via ThT binding assay and TEM. After 6 days of aging, the solution containing fibrillar Aβ42 was mixed with the HFIP film of the inhibitor (20-fold excess) and prepared from a 1 mM stock. The plate was kept in steady conditions throughout the experiment and the binding was measured at the indicated time points by a 2030 Multilabel Reader VictorX3.

Aβ42 self-seeding related studies

Preformed Aβ42 seeds (10%), which presence was confirmed via TEM and ThT fluorescence, were prepared in Eppendorf tubes by aging solutions (88 μM) in IAPP ThT buffer consisting of aqueous 50 mM sodium phosphate buffer, pH 7.4, containing 100 mM NaCl and 1% HFIP for 7 days at 20ºC. Afterwards, Aβ42 seeds were mixed with monomeric Aβ42 (5 μM) or Aβ42/inhibitor mixtures prepared in 180 μL of aqueous ammonium acetate buffer, 50 mM, pH 8.5, containing 20 μL of aqueous ThT 100 μM in a 96-wells MTP plate. The incubations were kept at 37ºC under shaking conditions (500 rpm, orbital shaker (CAT S20)) for the first 5 h. The incubations were held at the same temperature but without shaking for the rest of the experiment. The kinetics of the seeding were followed for 48 h by measuring the ThT binding using a 2030 Multilabel Reader VictorX3. The ThT binding of the seeds and the buffer signal were subtracted from the data of the assays.

Aβ42/IAPP cross-seeding-related studies

Preformed IAPP seeds (30%) were prepared in Eppendorf tubes by aging IAPP (128 μM) in IAPP ThT buffer consisting of aqueous 50 mM sodium phosphate buffer, pH 7.4, containing 100 mM NaCl and 0.5% HFIP. Incubations were aged for 24 h at 20ºC. 2.34 mL of IAPP seeds solution were added to the incubations containing Aβ42 (5 μM) or Aβ42/peptide-

mixtures (1/10) prepared in 180 μL of aqueous ammonium acetate buffer, 50 mM, pH 8.5, containing 20 μL of aqueous ThT 100 μM in a 96-wells MTP plate[127]. The incubations were kept at 37ºC and under shaking conditions (500 rpm orbital shaker (CAT S20)) for the first five h of the experiment. In contrast, they were incubated without shaking but at the same temperature for the rest of the experiment. The kinetics of the seeding effect was followed for 48 h, and the ThT fluorescence was measured using a 2030 Multilabel Reader VictorX3. The ThT binding of the seeds and the buffer signal were subtracted from the data of the assays.

3.2.8 MTT reduction assay

The MTT reduction assay is widely applied to quantify cell viability [91,94,95,116,118]. Reduction of MTT (3-(4,5-dimethylthiazol-2-yl)-2,5-diphenyl-2h-tetrazolium) occurs at the mitochondrial level and results in a redox chemical reaction which yields the formation of formazan, a violet-blue water-insoluble molecule[134]. The absorbance of the homogenised formazan solution can be measured at 570 nm. In this work, the MTT reduction assay is combined with the ThT binding assay and TEM to characterise the effect of the peptide inhibitors on the cytotoxicity mediated by IAPP and Aβ42 different species.

IAPP related studies

IAPP cytotoxicity studies were performed on RIN-m5F cells using previously established protocols[135]. Cells were cultured in RPMI 1640 medium containing 10% (v/v) heat-inactivated calf serum, L-glutamine (2 mM), penicillin/streptomycin (25 U/mL), not essential amino-acid (NEAA) (0.1 mM), glucose (1mg/1mL) and sodium pyruvate (1 mM). RINm5f cells were trypsinated, plated at a 7×105 cells/mL density in 96-well plates and cultured for 24 h. Aliquots of the peptide incubations prepared for the ThT assays and aged 24 h or 7 days, were diluted with cell culture medium and added to the cells at the indicated final concentrations.[96,99,127,129] After 20 h of incubation (37°C, humidified atmosphere, 5% CO_2), the cells were treated with MTT (0.5 mg/mL) and incubated for 120 minutes in the same conditions. Afterwards, the entire solution was removed, and 100 μl of HCl (0.04 M) in isopropanol were added. After 10 min of shaking, 100 μl of ddH_2O was added and mixed. The absorbance of the formazan was measured at 570 nm with a 2030 Multilabel Reader VictorX3.

Aβ42 related studies

Aβ42 cytotoxicity studies were performed on PC-12 cells, a cell line derived from rat pheochromocytoma (88). PC-12 cells were cultured in RPMI 1640 medium containing 10% (v/v) heat-inactivated horse serum, 5% (v/v) fetal calf serum and penicillin/streptomycin (25 U/mL). 24 h before the experiment, the cells were detached from the flask and plated at a 1×105 cells/mL density in 96-well plates. The flask and the plates were coated with polylisine[98,99,127]. Stepwise dilution of the peptide incubation prepared as described for the ThT studies, without ThT[127] and aged for six days, was prepared in cell medium and added to the cells at the indicated final concentrations. After that, cells were lysed by adding (10% SDS (w/v) in ddH_2O, pH 4.5) and incubated for 12 h under shaking conditions (300 rpm,

orbital shaker (CAT S20)) at RT. The absorbance of formazan was measured at 570 nm with a 2030 Multilabel Reader VictorX3.
To normalise the data, the absorbance value of cells treated with 0.1% Triton X-100 in H_2O was set as a standard for complete inhibition of metabolic ability (0% cell viability), whereas 100% MTT reduction was defined as the absorbance value obtained in wells containing untreated cells[96,99,126,127,129,135,136]. The effect of the buffer was also tested but not used for normalisation. To analyse the results of the assay, the absorbance values were normalised according to the following formula:

$$\%MTTreduction = \frac{\big(Abs(sample) - Abs(0.1\%\ Triton)\big)}{(Abs(medium) - Abs(0.1\%\ Triton))} * 100$$

Abs: absorbance at 570 nm

To determine IC_{50} values, IAPP (100 nM) or Aβ42 (500 nM) were titrated with mixtures of various amounts of peptides under the conditions of the ThT assays (without ThT in the case of the Aβ42 related studies)[99,127]. Cell-damaging effects were determined using 7 d-aged solutions (IAPP-related products) or 6 d-aged solutions (Aβ42 related results) by the MTT assay as described above.

3.2.9 Transmission electron microscopy (TEM)

Transmission electron microscopy (TEM) was performed to verify fibril formation and its inhibition. 10 µl aliquots of solutions of the ThT binding and MTT assays were applied on carbon-coated grids at indicated time points, washed with distilled water and stained with aqueous 2% (w/v) uranyl acetate as described[126,127,136,137]. Grids were examined using a JEOL JEM 100CX (at 100kV) or a JEOL 1400 Plus electron microscope (at 120kV).

3.2.10 Spectroscopic methods of analysis

UV/Vis spectroscopy

Peptide absorbance was determined by UV spectroscopy with a Jasco V630 spectrophotometer, as described in paragraph 3.2.6. Peptide concentrations were calculated according to the Lambert-Beer law.

Fluorescence spectroscopy studies

Fluorescence spectroscopic titrations were performed using a JASCO FP-6500 fluorescence spectrophotometer based on previously established protocols[95,99,100,129]. For the titrations of Fluos- and FITC-labelled peptides, the excitation wavelength was set at 492 nm, whereas the fluorescence emission spectra were recorded between 500 and 600 nm. App. K_Ds of interactions were obtained by titrating freshly prepared solutions of Fluos-IAPP, FITC-Aβ42 or **Fluos-2i** (5 nM), which were found to be mostly monomeric at this concentration[98,99,129,137] with an increasing amount of peptides, as previously described [98,99,129,137]. Briefly, stepwise dilutions of peptide titrants were prepared in HFIP. 2.5 µL of each dilution were transferred into a 1 cm quartz cuvette containing 495 µL of 1xb, covering a final range of concentrations between 0.5 nM and 5 µM (Fluos-IAPP/titrant: 1/0.1-1/1000).

2.5 µL of a freshly prepared HFIP stock of Fluos-IAPP (1 µM) were mixed with the titrant solution in 1xb. The final concentration of HFIP in the solution was 1% (v/v). Measurements were performed at room temperature within 2-5 min after the preparation of the solutions. App. K_Ds were estimated using 1/1 binding models as previously described [95,96,127]. Of note, due to the high self-assembly propensity of the peptides, more complex binding models may also apply[138]. The obtained app. K_Ds are means (±SD) from three binding curves and were estimated using 1/1 binding models. Sigmoidal curve fittings and estimation of affinities of interactions (app. K_D) were done with the Origin software package by applying the formula:

$$F = F_0 + \frac{(F_{max} - F_0)}{1 + 10^{[(\log K\_D - L) * m]}}$$

F: fluorescence intensity
F_0: fluorescence intensity of the fluorescently labelled specie
F_{max}: maximal fluorescence intensity
Log K_D: logarithm of the dissociation constant
L: ligand concentration
m: the slope of the curve

3.2.11 CD-spectroscopy studies

Circular dichroism (CD) is an analytical spectroscopy technique widely used to assign peptide secondary structures through their optical activity[138–142]. This method is based on the differential absorption of optically active molecules' left and right circularly polarised light [139]. The result is that different structural elements have characteristic CD spectra, as summarised in Table 18.

Table 18. Characteristic CD spectra of different secondary structures[142]

secondary structure	maximum (nm)	negative bands (nm)
α-helix	193	208 and 222
β-sheet	195	216
β-turn	195	230
random coil	210 (weak)	195

CD measurements were performed with a Jasco 715 spectropolarimeter. Spectra were measured at room temperature, in a range between 195 and 250 nm, at 0.1 nm intervals and with a response time of 1 sec. Each spectrum was obtained from the average of three consecutive measurements. The baseline of the buffer was subtracted.

The secondary structures of MIMs were characterised via CD spectroscopy. Notably, establishing robust conditions for recording the spectra was challenging, likely due to the strong self-assembling propensity of the peptides, as confirmed later. Applying standard protocols[98,129,137], such as peptide stocks preparation in HFIP (peptide concentration, 1 mM or 0.5 mM) followed by dilution in aqueous buffer (1xb (pH 7.4)) to the final concentrations (5-100 µM) resulted in strong signal scattering which could be due to peptide oligomerisation. Eventually, the spectra were successfully recorded by preparing the peptides as a lyophilised powder, readily dissolving them in the HFIP amount necessary for having

1% in the final volume, and then adding 1xb (pH 7.4). Of note, the assay buffer consisting of 1xb (pH 7.4) and 1% HFIP has been previously used for the far-UV CD characterization of peptide inhibitors of IAPP and Aβ40(42) [28,98,129,137].

The raw data, expressed as ellipticity, was converted to mean residue ellipticity (MRE) by applying the formula:

$$MRE\left[\frac{deg * cm^2}{dmol}\right] = \frac{(100 * \theta)}{(c * d * n)}$$

MRE: mean residue ellipticity (deg·cm^2 ·dmol^{-1})
q: ellipticity
c: concentration
d: optical path length
n: number of amino acids

CD concentration studies on MIMs and linear precursors

Concentration dependence studies were performed by preparing increasing amounts of peptide powder and dissolving them in the HFIP necessary for a final 1% in the total volume of 1xb (pH 7.4). The incubations were kept on ice for 10 minutes to allow complete dissolution and measured afterwards. Measurements were performed in 1 cm cuvettes, or 0.5 cm cuvettes for the 50 μM concentration. The concentrations range was between 5 μM and 50 μM.

TFE studies of **2f** and **2g**

Amounts of **2f** and **2g** peptide powders, suitable for having a final concentration of 20 μM, were dissolved in 1xb (pH 7.4) and mixed with increasing amounts of TFE, indicated as % (v/v) of the final volume. The CD spectra were recorded in 1 cm cuvettes.

pH studies of **2g** and **2i**

Studies on the secondary structure of **2g** (100 μM) in the presence of aqueous HCl 5 (mM, pH 2.5) or NaOH (5 mM, pH 9.8) were performed to characterise the oligomerisation state of the peptides at different pH than the native one. Briefly, the samples were prepared by dissolving the peptide powder suitable for having a concentration of 100 μM. in the amount of HFIP corresponding to 1% of the final volume of 1xb buffer (pH 7.4). Amounts of aqueous HCl (5 mM) or NaOH (5 mM) were added at the indicated % (v/v). The CD measurements were performed in a 0.2 cm cuvette.

CD characterization of the interaction between IAPP, **2g**, **2i** and **2g linear**

To characterise the effects of **2g**, **2i** and **2g linear** on monomeric IAPP misfolding, far-UV CD spectra of IAPP (5 μM), inhibitor (25 μM), and the IAPP/inhibitor mixture (1/5) were measured at various time points, according to previously established methods[127,129,136]. To test the effect of equimolar **2i**, the peptide alone and in a mixture with IAPP was prepared at

5 μM. Incubations containing IAPP were prepared by diluting IAPP (1 mM, HFIP) in 1xb (pH 7.4) containing 1% HFIP to the final concentration (5 μM).

The inhibitors' incubation was prepared with lyophilised powder, as described for the CD concentration studies. For the IAPP/peptide mixtures, the peptide powder was mixed with the IAPP stock in HFIP and diluted in 1xb (pH 7.4). All incubations were prepared on ice, and the spectra were recorded in 1 cm cuvettes. The baseline was subtracted.

3.2.12 Dot Blot studies (DB)

DB assays to assess the binding of MIMs to IAPP monomers, oligomers, and fibrils

IAPP (12 μM) was prepared in IAPP ThT buffer, consisting of aqueous 50 mM sodium phosphate buffer, pH 7.4, 100 mM NaCl and 0.5% HFIP, and incubated at 20ºC. At the indicated time, 10 μL (0.5 μg) of the solution was spotted on a DB membrane. After two h of incubation with 5% milk in TBS-T (blocking step) and three washing steps (5 min each) in TBS-T, the membrane was incubated for 12 h at 10ºC with a solution of **Fluos-2i** (2 μM, for monomers and oligomers, 1 μM for fibrils). This solution was prepared by dissolving a suitable amount of peptide powder in IAPP ThT buffer containing 0.5% HFIP. Membranes containing identical amounts of incubations were incubated in parallel with buffer only to control for fibril autofluorescence. Bound peptides were visualised using a LAS-400mini instrument equipped with a fluorescence filter.

DB assays to assess the binding of MIMs to Aβ42 monomers (mAβ42), oligomers (oAβ42) and fibrils (fAβ42)

According to previously published protocols[127], monomeric Aβ42 (11 μM) was prepared with SEC-disaggregated Aβ42 as described for the ThT binding conditions (w/o ThT) and deposited onto nitrocellulose membranes (Aβ42: 1 μg). The deposition was performed either directly following their preparation (for mAβ42) or after 2 h and 4 h (for oAβ2) or 2 days of aging (for fAβ42; confirmed by ThT binding and TEM). After blocking (5 % milk in TBS-T w/v, 2 h, RT), the membrane was washed three times for 5 minutes with TBS-T and IAPP ThT buffer, consisting of 50 mM sodium phosphate buffer, pH 7.4, with 100 mM NaCl containing 1% HFIP. After that, the membranes were incubated with **Fluos-2i** at 2 μM for 12 h (10°C) in IAPP ThT buffer containing 1% HFIP. To control for fibril autofluorescence, membranes containing m-, o- or fAβ42 were incubated in parallel with buffer only. Bound peptides were visualised using a LAS-400mini instrument with a suitable fluorescence filter.

DB assays reveal the formation of oligomeric IAPP species and the effects of the inhibitors

IAPP (12 μM) was prepared in IAPP ThT buffer (pH 7.4, 0.5% HFIP) and incubated at 20ºC. At the indicated time, 10 μL (0.5 μg) of the solution were spotted on a DB membrane. To characterise the effect of **2i** on the formation of the oligomers, aliquots of IAPP aged 0 h, 1 h or 3 h were mixed with the HFIP film of the inhibitor and spotted after 0 h, 3 h, 6 h or 24 h

of incubation. After blocking it for 2 h in 5% BSA in ddH_2O, the membrane was incubated for 12 h with the (anti-)oligomer A11 polyclonal antibody in 5% BSA in ddH_2O (1:1000). Membrane spotted with the same peptide incubations, in the same amount, were tested with anti-IAPP antibody (1:1000) in 5% milk in TBS-T, to confirm the presence of IAPP. After three washing steps in TBS-T (5 min each), the DB membrane was incubated for 2 h with the secondary antibody donkey anti-rabbit Ig-POD in 5% BSA in ddH2O (1:5000). Finally, the membrane was developed with ECL SuperSignal West Dura Extended Duration Substrate, and the signal was measured via LAS mini.

DB assays to reveal the formation of oligomeric Aβ42 and TAMRA-Aβ42 species.

The presence of oligomers of Aβ42 or TAMRA-Aβ42 (5 μM) in solutions at various time points of incubations were performed as reported by Taş et al.[127]. Briefly, Aβ42 incubations were prepared for the ThT binding assay but without ThT or as for the MTT reduction assay, and the presence of oligomeric species was studied by DB. At the indicated time points, Aβ42 (4.5 μg) or TAMRA-Aβ42 (4.9 μg) was spotted onto a nitrocellulose membrane. After blocking (5% BSA in ddH2O, 2 h, RT) and three washing steps with TBS-T (5 min each), membranes were incubated overnight (10 °C) with (anti-)oligomer A11 polyclonal antibody (1:1000 in 5% BSA in ddH2O). The primary antibody was combined with donkey anti-rabbit-POD (1:5000). The membrane was developed with ECL SuperSignal West Dura Extended Duration Substrate, and the signal was measured via LAS mini.

3.2.13 Cross-linking studies

Hetero-complex cross-linking studies combined with NuPAGE and WB were performed using a previously developed assay system to characterise IAPP homo- and hetero-assemblies. Briefly, IAPP (30 μM) and IAPP/**2i** mixtures (1/1, 1/5 and 1/10) were incubated in 1xb (pH 7.4). After 30 minutes, aliquots were cross-linked for 2 min with 25% aqueous glutaraldehyde and treated with a 2 M $NaBH_4$ solution (in 0.1 M NaOH) for 20 min. Following precipitation with aqueous trichloroacetic acid (10% v/v) on ice and centrifugation (12000 g) for 10 minutes [99]. The pellets were dissolved in 20 μL of NuPAGE sample buffer, boiled (95°C) for 5 min and subjected to NuPAGE gel electrophoresis as described[127]. Peptides were transferred onto nitrocellulose membranes. The membranes were blocked for 12 h (10°C) with 5 % milk in TBS-T (20 mM Tris/HCl, 150 mM NaCl and 0.05 % Tween-20). Finally, the membranes were washed thrice in TBS-T, each for 5 minutes.

To reveal the presence of homo-/hetero-assemblies, membranes were incubated (2 h) with rabbit polyclonal anti-IAPP antibody (Peninsula; 1:1000) for IAPP-containing assemblies, combined with suitable peroxidase (POD)-coupled secondary antibodies (donkey anti-rabbit-POD (1:5000). Homo-/hetero-assemblies were detected with SuperSignal West Dura Extended Duration Substrate. Prestained protein size markers ranging from 3.5 to 260 kDa (Fisher Scientific) were electrophoresed in the same gels.

3.2.14 Peptide arrays

Peptide array n.5 contains IAPP and Aβ42 decamers between the N- and the C- terminus of the peptide's full sequences. Decamers are positionally shifted by one residue and were synthesised on a modified cellulose membrane support. The synthesis was performed by Kathleen Hille, Dr. Christos Kontos, Dr. Valentina Armiento and Dr. Karin Taş (Peptide Biochemistry Group, Prof. Dr. Aphrodite Kapurniotu) using stepwise SPOT synthesis protocols and a MultiPep Rsi peptide synthesiser [28]. According to the manufacturer's instructions, the decamers were immobilised on a glass slide by Dr. Christine Krammer (ISD, Prof. Dr. Jürgen Bernhagen). After that, the membrane was blocked by using 1% BSA in TBS-T for 4 h at RT. The arrays were incubated for circa 12 h at 10°C with **Fluos-2i** (1 μM in TBS-T containing 1% BSA), followed by washing with TBS-T. Visualisation of bound **Fluos-2i** was performed with a LAS-4000mini instrument.

3.2.15 Human plasma peptide stability studies

Proteolytic stability in human plasma is essential for peptide leads for drug development. Thus, the resistance of **2i**, **2g** and their linear precursors towards plasmatic proteases was analysed *in vitro* by reversed-phase (RP) HPLC combined with MALDI-TOF MS.

20 μg of lyophilised peptide powder were dissolved in 44 μL of human blood plasma (obtained from voluntarily healthy patients) and incubated at 37°C for different time points. After quenching with aqueous trichloroacetic acid (10%) in ddH2O (1/1)[99], the incubations were kept on ice for 10 minutes, and the plasmatic proteins were precipitated through centrifugation (20200 g; 4 min). The supernatants were separated and mixed (1/2) with a solution of 80% HPLC buffer B and 20% HPLC buffer A (v/v). Supernatants were analysed via RP-HPLC (detection at 214 nm) by using a Nucleosil 100 C18 column (Grace/Alltech) (length 33 mm length, ID 8mm, 7 μm particle size) with a flow rate of 2.0 mL/min and eluting buffers A, 0.058% (v/v) TFA in water, and B, 0.05% (v/v) TFA in 90% (v/v) ACN in water.

The elution gradient is described in Table 19.

Table 19. HPLC-gradient applied for the proteolytic stability studies[99]

HPLC program	Flow (mL/min)	Time (min)	Buffer A	Buffer B
Schnell Schnell Aβ	2.0	0	90%	10%
		1	10 %	90%
		8	10%	10%

The peaks were collected, frozen down, lyophilised and analysed via MALDI-TOF. MALDI samples were prepared using 97% acetone in ddH_2O + 0.1% TFA as a solvent and α-Cyano-4-hydroxycinnamic acid (HCCA) as a matrix[99].

The % of intact amounts of **2g** and **2i** was calculated by taking as reference a calibration curve obtained by the HPLC analysis of aliquots of lyophilised peptide powder without plasma (20 μg, 10 μg and 5 μg).

The % intact amount of **2e** was calculated by taking the area of the peak of the **2e**`s plasma incubation at 0 h as 100% intact peptide [99].

3.2.16 Blood-Brain Barrier (BBB) crossing studies

These studies were performed by Dr. Yuan Tian from the group of Prof. Dr Jürgen Bernhagen, ISD (LMU), as described below. The text is adapted from reference[99]:

Human cerebral microvascular endothelial (hCMEC/D3) cells were grown in coated dishes coated with rat tail collagen type I in EndoGro-MV complete culture media kit. The Transwell permeability assay was performed based on a previously established assay[99] using 24-well plates containing 6.5 mm Transwell inserts (0.4 µm pore polycarbonate membrane [99]). hCMEC/D3 cells were cultured on the membranes of the Transwell inserts ($2x10^5$ cells/insert) (37°C and 5% CO2) until full confluency. The medium was removed from the upper and lower chambers and then reconstituted with 200 µl (180 µl and 20 µl 100 µM peptides) and 800 µl of the medium, respectively. As a positive control, the N-terminal fluorescein-labelled 12 amino acid-long peptide THRPPMWSPVWP-amide (Transferring receptor binder, **Fluos-Tfrb**), known to readily cross the BBB via binding to the transferrin receptor[143,144], was included in the experimental design. Similarly, **LY** (Lucifer yellow), which does not cross the BBB, was included in the experiments to ensure the tightness of the cell monolayer. **Fluos-2e** (10 µM), **Fluos-2i** (10 µM), **Fluos-Tfrb** (10 µM), or Lucifer yellow (20 µM) were added to the upper (donor) chamber of the Transwell device. For quantification of fluorescently labelled peptides present in the acceptor chamber, 100 µl of medium (3 replicates) were transferred from the lower chamber to the wells of a 96-well black polystyrene plate, and the fluorescence at 519 nm (excitation at 495 nm) was measured with a fluorescence microplate reader (Perkin Elmer Enspire). Lucifer yellow in the lower chamber was quantified by measuring the fluorescence at 530 nm (excitation at 485 nm)[145–148]. To calculate the relative permeability, the following equation was applied:

$$Papp\ (\mathrm{cm/s}) = (\mathrm{dQ/dt})(1/\mathrm{A})(1/\mathrm{C0})(\mathrm{cm/s})$$

(dQ/dt): the number of peptides or LY in the lower chamber after 2 h of incubation (nmol/s)
A: membrane area of the upper chamber (0.33 cm^2)
C0: initial concentration in the upper chamber (nmol/mL)

Of note, studies on the transport rate of Lucifer yellow were performed in parallel to the studies on peptide transport. They were consistent with a good tightness or integrity of the hCMEC monolayer, confirming the TEER measurements. Of note, confluent hCMEC monolayers in Transwell filters represent a suitable model of the human blood-brain-barrier (BBB) with good transendothelial electrical resistance (TEER) values of 30-100 Ωcm^2 [99]. Briefly, this cell model has been extensively characterised and found to maintain a brain endothelial phenotype; despite lower complexity due to lack of co-cultured astrocytes/pericytes or application of flow-based shear stress, hCMEC monolayers have suitable barrier characteristics with high junctional integrity, restricted permeability to paracellular tracers, and good transendothelial electrical resistance (TEER) values of 30-100 $\Omega\ cm^2$ [99].

3.2.17 Studies on Long Term Potentiation (LTP)

These studies were performed by Markus Ballmann, group of Prof. Dr. Gerhard Rammes, at the Department of Anaesthesiology and Intensive Care at TUM Klinikum Rechts der Isar, as previously described in ref. [55,98,99,127]. Text adapted from references [99].

Sagittal hippocampal slices (350 μm) were obtained from C57BL/6N mice (6–8 weeks of age, male (Charles River Laboratories)) in ice-cold Ringer solution bubbled with a mixture of 95% O_2 and 5% CO_2. The animals were treated according to protocols approved by the ethical committee on animal care and use of the government of Bayern. (Regierung von Oberbayern, ROB), Germany. The extracellular recordings were performed using artificial cerebrospinal fluid (ACSF)-filled glass microelectrodes (2–3 MΩ) at room temperature. ACSF consisted of 125 mM NaCl, 2.5 mM KCl, 25 mM $NaHCO_3$, 2 mM $CaCl_2$, 1 mM $MgCl_2$, 25 mM D-glucose, and 1.25 mM NaH_2PO_4 (pH 7.3) and was bubbled with 95% O_2 and 5% CO_2. Field excitatory postsynaptic potentials (fEPSPs) were evoked in the hippocampal CA1 dendritic region using two independent inputs that stimulated the Schaffer collateral commissural pathway (Sccp). For LTP induction, high-frequency stimulation (HFS, 100 Hz/100 pulses) conditioning pulses were delivered to the same Sccp inputs. Both stimulating electrodes were used to gain the input specificity of LTP. Aβ42 (50 nM), Aβ42/MIMs mixtures (1/10) or MIMs alone (500 nM) were freshly dissolved in ACSF and applied 60–90 min before high-frequency stimulation, and the responses were measured for 60 minutes after HFS[127].

4 Results

4.1 Design of the Minimized IAPP Mimics (MIMs)

For the minimized IAPP mimics (MIMs) design, the previously reported macrocyclic inhibitor peptides (MCIPs)[99] were used as templates. Briefly, the MCIPs are 17-residue-long peptide inhibitors of IAPP and/or Aβ40(42) self-assembly, designed to mimic IAPP interaction surfaces while maintaining only minimal IAPP-derived self-/cross-recognition elements[99]. The molecular basis for their "cross-amyloid" inhibitory function was the interaction between IAPP and Aβ40(42); in fact, our group and others [28,95,100], showed that prefibrillar Aβ40(42) and IAPP species interact with nanomolar affinity and that IAPP suppresses Aβ42 amyloidogenesis *in vitro*[126]. Also, seed amounts of Aβ40(42) fibrils can cross-seed IAPP amyloidogenesis *in vitro* and in animal models *in vivo*[99,149]. Furthermore, we have previously shown that the same IAPP regions act as binding sites for its self- and hetero assemblies with Aβ40(42)[28,100,137]. The "hot spots" of the IAPP sequence were used to design interaction surface mimics (ISM), in which IAPP(8-18) and IAPP(22-28) were linked by different tripeptides units and were found to sequester IAPP and or Aβ42 from the amyloid assembly (Scheme 3). A deeper insight onto the role of the single IAPP-residues involved in the IAPP/Aβ cross-interaction was given by Bakou et al.[100], that reported the pivotal role of Phe^{15}, Ile^{16}, Phe^{23} and Leu^{26} in the self- and cross-assembly of the two amyloidogenic peptides. The MCIPs were optimized analogues of the ISM **R3-GI**, whose sequence was modified by truncation, multiple amino acids substitution with Gly or D-AA, and conformationally constrained by disulphide bridge cyclization[99]. Notably, the selectivity of the MCIPs towards IAPP or Aβ40(42) was modulated by the stereochemistry of the IAPP-derived residues. The lead compound **2e** selectively inhibited Aβ40(42) peptides, had a good stability in human plasma *in vitro*, and displayed an apparent permeability that is in the same range as other BBB-crossing peptides in a human cerebral microvascular endothelial cells model [99].

For the design of the next generation of inhibitors and linear controls, the sequences of the MCIPs **2b** and **2e** and their linear control peptides were shortened to maintain the four key-IAPP residues Phe^{15}, Leu^{16}, Phe^{23} and Ile^{26}, one N-methylation (on Ile^{26}), one Gly, and one Arg from the tripeptide linker of the ISM **R3-GI**[97,98] (**2f linear** and **2g linear**). In the analogs **2h linear** and **2i linear**, the Arg was replaced with a Lys to incorporate a fluorescence moiety on N^{ε}-amino group of Lys, enabling determination of binding affinity and BBB crossing ability.

To confer structural rigidity, the linear sequences were cyclized via head-to-tail lactam bond formation, yielding the cyclic hexapeptide inhibitors MIMs **2f**, **2g**, **2h** and **2i**. As for the MCIPs, the introduction of D-AA was used to increase the proteolytic stability and the BBB permeability of the peptides (**2g** and **2i**).

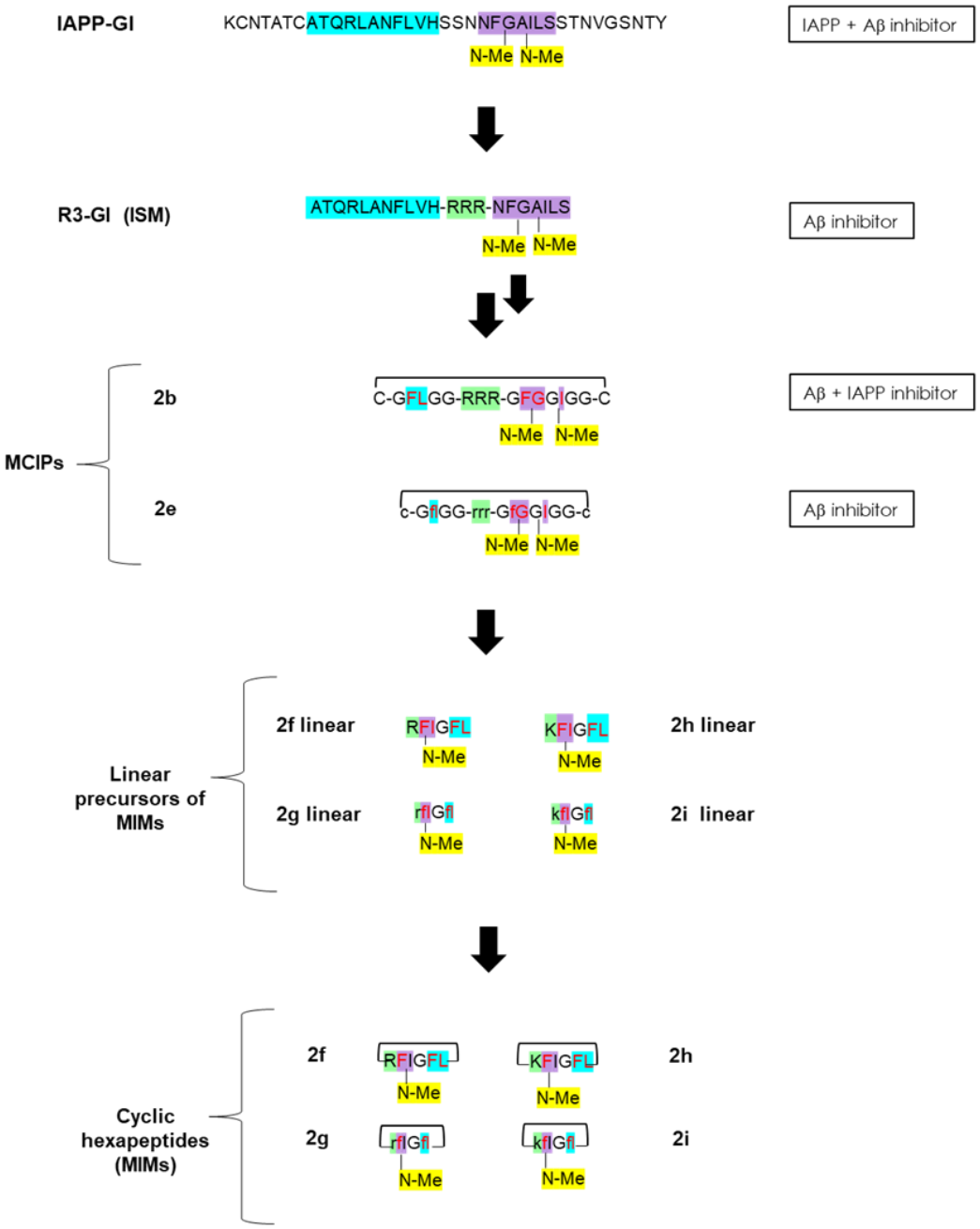

Scheme 3. Design of Minimized IAPP Mimics. The structural determinants of MIMs were identified through several rounds of optimization. The inhibitor **IAPP-GI** was designed by introducing N-methylations in positions 24 and 26 of the IAPP sequence, which enhanced the solubility and conferred inhibitory potential towards both IAPP and Aβ40[98]. In the next round of optimization, IAPP(8-18) (blue) and IAPP(22-28) (purple) were connected through a tripeptide linker stabilising β-sheet structures of the sequence. This class of inhibitors was named interaction surface mimics (ISMs), and the nature of the linker dictated the selectivity towards IAPP or Aβ40. The ISM **R3-GI** was used as a template to design macrocyclic inhibitory peptides (MCIPs), optimised by Gly substitution, cyclisation and introduction of D-amino acids[99]. The MCIPs **2b** and **2e**, were used as templates to design the linear precursors of minimised IAPP mimics (MIMs) (red-coloured residues: IAPP-derived; D-residues: lower-case (highlighted in blue, green and purple); amide-bond N-methylations: "N-Me" (highlighted in yellow). To confer structural rigidity, the linear sequences were cyclized via head-to-tail lactam bond formation, yielding the cyclic hexapeptide inhibitors MIMs. Scheme modified from ref. [95].

4.2 Peptide Synthesis

The assembling of MIMs was carried out by applying the Fmoc/tBu solid phase peptide synthesis (SPPS)[102–104] on 2-chlorotrityl resin. The synthetic strategy included cycles of coupling steps and N-terminal Fmoc deprotections as described in Scheme 4. Briefly, the major challenge of the MIMs` synthesis is the presence of an N-methylation on the Ile^3 in the proximity of Gly^4, which might increase the rate of diketopiperazine formation[150,151]. Due to the bulky structure of its linker, the 2-chlorotrityl resin[107,108,118,152] was the resin of choice for reducing the occurrence of side reactions while synthesising these short and sterically hindered peptides[115,153].

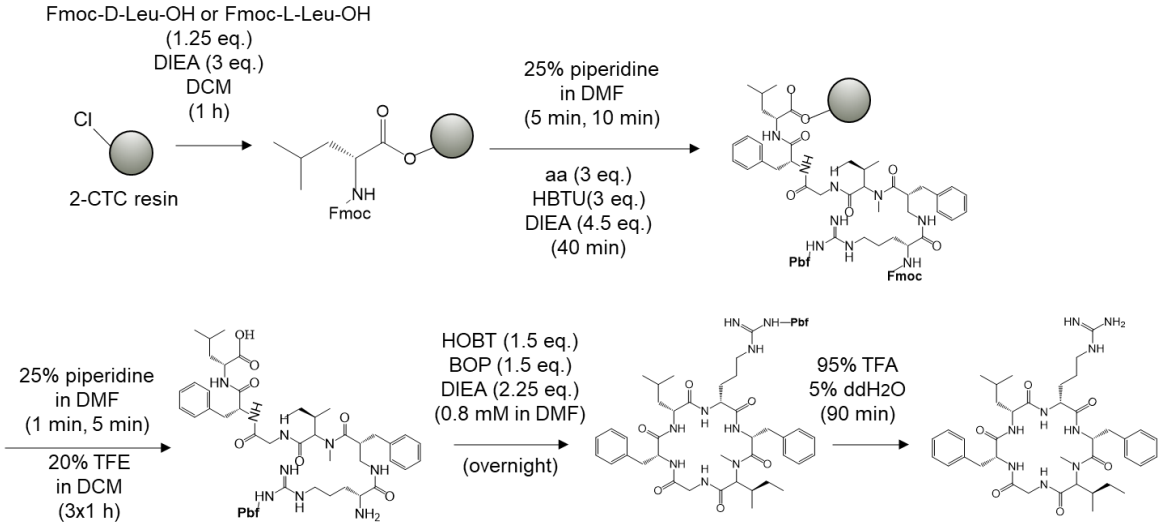

Scheme 4. Synthesis of MIMs. The linear precursors were synthesised on 2-chlorotrityl resin[107] by applying the Fmoc/tBu method. For the coupling steps, double couplings performed with the indicated molecular equivalents of amino acids, DIEA and activators were used, as previously reported[98,99,136,154]. The Fmoc deprotection was achieved by treating the peptide resin with 25% piperidine in DMF. For coupling (NMe)Ile^3 on Gly^4, a third coupling step was performed by using 3 eq. of HATU instead of HBTU, and shorter Fmoc-deprotection steps were used to avoid diketopiperazine formation[111,113,115]. After the last Fmoc-deprotection step, the peptide chain was cleaved in a mixture of TFE/DCM (20/80) to keep the side-protecting groups in situ. The head-to-tail lactam bond formation was performed in highly diluted conditions to avoid the formation of intermolecular bonds[119]. Once the cyclisation was accomplished, the protecting groups on the side chains were removed in a mixture of TFA/ddH_2O (95/5).

For the same reason, shorter Fmoc deprotection steps were applied after introducing the N-methylated amino acid, as described in Table 12.

After synthesising the linear sequences, the side chains-protected peptides were cleaved from the resin in a mixture of TFE/DCM (20/80, 3h). The intramolecular head-to-tail lactam bond formation was performed in highly diluted conditions to avoid intermolecular side reactions[119]. With this purpose, the lyophilised and crude peptides (6-10 mg) were dissolved in DMF (0.8 mM) in the presence of DIEA (2.5 eq.) and HOBT/BOP (1.25 eq. each) (Scheme 4). The kinetics of the cyclisation was monitored via RP-HPLC and confirmed by MALDI-TOF analysis. After accomplishing the reaction, the solvent was removed with a rotary evaporator, and the side-protecting groups were cleaved in a mixture of TFA/ddH_2O (95/5) (Table 20).

The linear analogues of MIMs were obtained by cleaving fully assembled peptides from the resin in a mixture of TFA/ddH2O (95/5). This way, the side-protecting groups were readily cleaved from the peptide sequences (Scheme 5, Table 20).

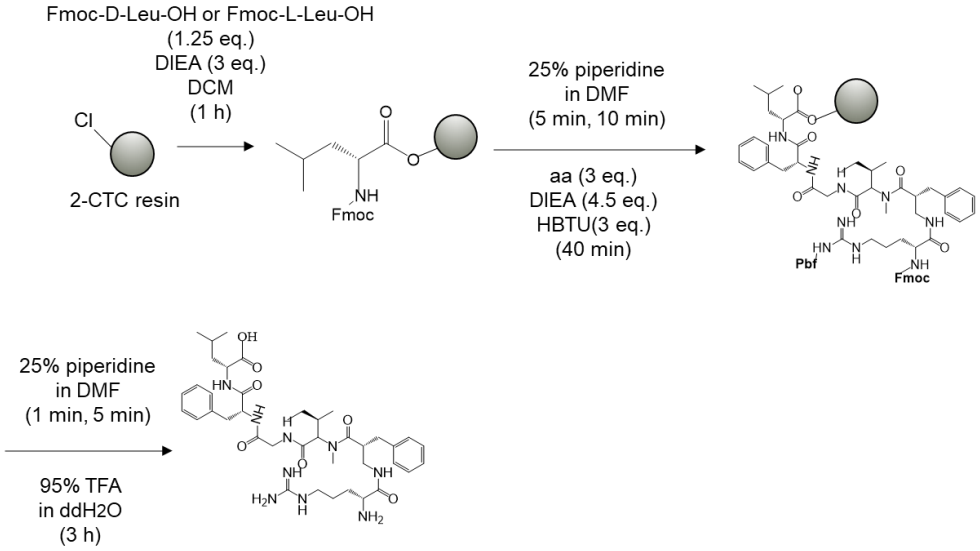

Scheme 5. The synthetic strategy of the linear sequences. The synthesis of the peptide chains was accomplished on 2-chlorotrityl resin by applying the Fmoc/tBu strategy. Coupling steps were performed with the indicated molecular equivalents of amino acids, base, and activators. Each coupling step was repeated twice. The Fmoc deprotection was achieved by treating the peptide resin in a mixture of 25% piperidine in DMF. After the last Fmoc-deprotection, the peptide and the side-protecting groups were cleaved in a mixture containing 95% TFA in ddH_2O.

Different conditions were applied to synthesise the fluorescently labelled analogue of **2i** (**Fluos-2i**) (Scheme 6). The peptide sequence of **2i** was synthesised by performing the same steps of the Fmoc/tBu strategy as described before but with two significant differences: the use of WANG resin and the introduction of Fmoc-D-Lys(Mtt)-OH as N-terminal amino acid. Thus, the side protecting group on the ε–amino group of (D)-Lys[1] could be removed by applying mild acidic conditions [152,155] avoiding a) the deprotection of the Fmoc- α-amino group, which was necessary to exclude the formation of side products during the cyclisation in solution and b) the cleavage of the peptide from the resin.

For these reasons, the WANG resin [104,156] was used, as the 2-chlorotrityl resin could not withstand the acidic conditions used for the Mtt-cleavage[104,107,118] due to its high pH sensitivity. After cleaving the Mtt protecting group, the Fluos moiety was introduced in two coupling steps, performed accordingly to previously published protocols[28,100,127,129,136].

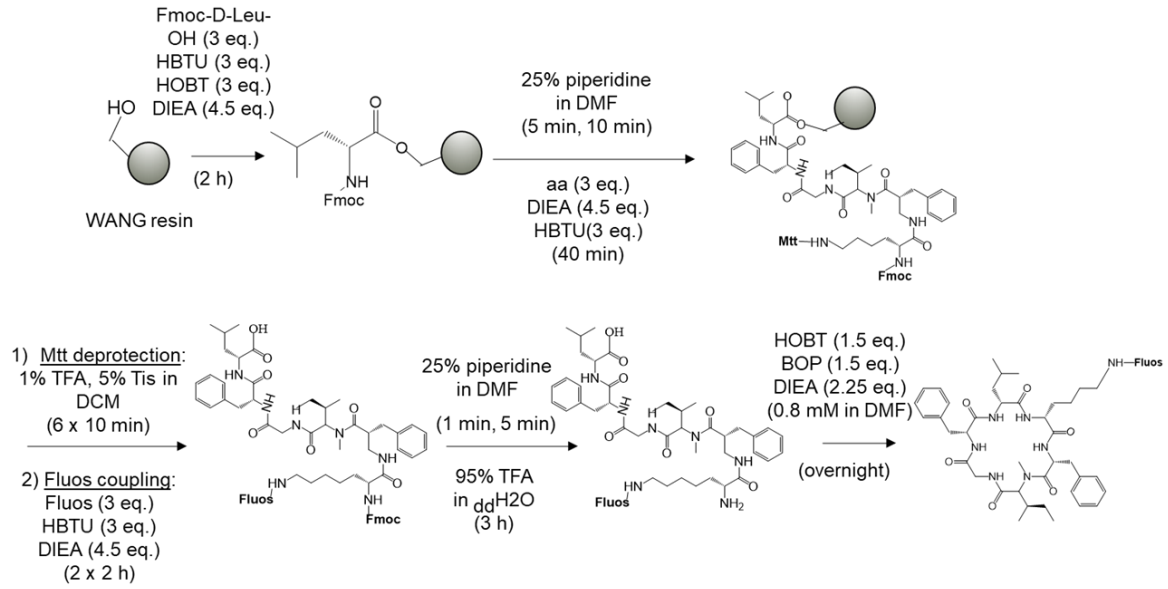

Scheme 6. Synthesis of fluorescently labelled 2i (Fluos-2i). The peptide sequence of **2i** was synthesised on WANG resin to introduce 5(6)carboxyfluorescein on the ε-amino group of (D)-Lys[1]. The synthesis was accomplished by applying the Fmoc/tBu strategy, as described above, and by incorporating Fmoc-(D)-Lys(Mtt)-OH as N-terminal amino acid, ensuring an orthogonal protection of the two amino groups. The Mtt-group was removed in a mixture of 1% TFA and 5% triisopropylsilane (TIS) in DCM[117]. Of note, these conditions were not sufficiently acidic to cleave the peptide from the resin. The fluorescent dye was introduced in two coupling steps, performed with a mixture of Fluos (3 eq.), HBTU (3 eq.) and DIEA (4.5 eq.)[28,100,129,136,137]. The N-terminal Fmoc deprotection was performed in 25% piperidine in DMF. The cleavage of the peptide from the resin was performed with a mixture of 95% TFA with 5% ddH_2O. The head-to-tail cyclisation was performed for 12 h in solution, in a mixture of peptide (0.8 mM), activators (1.5 eq.) and DIEA (2.25 eq.) in DMF[119].

Table 20. Sequences and abbreviations of synthesised and tested MIMs and linear controls. The sequence of the inhibitors (MIMs, grey background) and linear sequences (green background) are shown. The presence of the D-amino acids is indicated with small letters, whereas the N-methylated residues are shown in bold. All linear peptides have a free N-terminal amino group (NH_2-) and are C-terminal carboxylic acids (-COOH), whereas the cyclic analogues are constrained via head-to-tail lactam bond formation.

Peptide Sequence	Abbreviation
cyclo-[RF**(N-Me)Ile**GFL]	**2f**
cyclo-[rf**(N-Me)Ile**Gfl]	**2g**
cyclo-[KF**(N-Me)Ile**GFL]	**2h**
cyclo-[kf**(N-Me)Ile**Gfl]	**2i**
RF**(N-Me)Ile**GFL	**2f linear**
rf**(N-Me)Ile**Gfl	**2g linear**
KF**(N-Me)Ile**GFL	**2h linear**
kf**(N-Me)Ile**Gfl	**2i linear**

The cyclised and deprotected peptides and their linear precursors were purified via RP-HPLC using the gradient described in Table 21. Overall, the head-to-tail lactam bond formation increased the retention time of all the cyclised peptide sequences by circa 2 min. Noteworthy, one round of purification was sufficient to achieve over 95% purity yield for the peptides, except for **Fluos-2i**, for which a second round of purification and a different gradient was necessary. The degree of purity of the peptide products was confirmed via MALDI-TOF

(Table 21). As reported in Table 21, the yield of the peptide purification spanned between 24% and 30% (Table 22).

Table 21. Molecular weights (M) of synthetic peptides used in this study as determined by MALDI-TOF-MS.

Peptide	$[M+H]^+$ ($[M+Na]^+$) calculated (g/mol)	$[M+H]^{+[a]}$ or $[M+Na]^{+[b]}$ found (g/mol)
2f	748.44 (770.65)	748.54[a] and 770.51[b]
2g	748.44 (770.65)	748.48[a] and 770.62[b]
2h	720.44 (742.65)*	742.51[b]
2i	720.44 (742.65)	720[a] and 742.57[b]
2f linear	766.44 (788.52)	766.46[a] and 788.78[b]
2g linear	766.44 (788.52)	766.48[a] and 788.52[b]
2h linear	738.44 (760.52)	738.50[a] and 760.57[b]
2i linear	738.44 (760.52)	738.59[a] and 760.57 [b]
Fluos-2i	1078.23 (1100.76)	1100.71[b]
Fluos-2e	2053.20 (2075.65)	2076.31[b]
Fluos-Tfrb	1847.75 (1869.93)	1848.88[a]
Fluos-IAPP	4260.16 (4282.14)	4260.48[a]
Aβ42	4512.28 (4534.26)	4512.12[a]
IAPP	3901.86 (3923.84)	3902.41[a]
2e	1694.88 (1716.88)	1694.78[a]

M, monoisotopic mass; $[M+H]^{+[a]}$; $[M+Na]^{+[b]}$

Table 22. Yields, HPLC-chromatograms and MALDI spectra of MIMs and linear precursors

Peptide abbreviation	Yield of synthesis (%)*	Yield of purification (%)**	Expected Mass $[M+H]^+$ ($[M+Na]^+$)	Chromatograms of HPLC purified peptide	MALDI-MS of HPLC purified peptide
2f	63	24	748.44 (750.65)	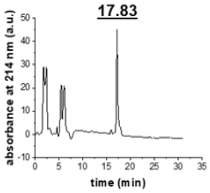	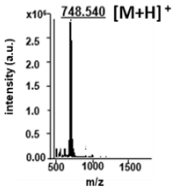
2g	58	25	748.44 (750.65)	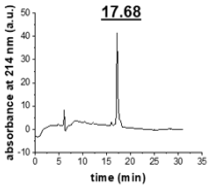	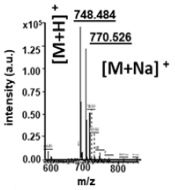
2h	58	24	720.44 (742.65)	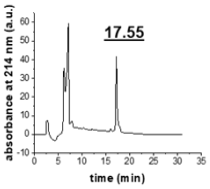	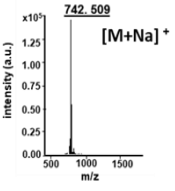
2i	64	26	720.44 (742.65)	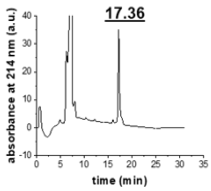	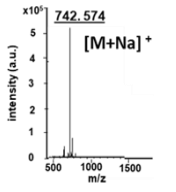
2f linear	64	26	766.44 (788.52)	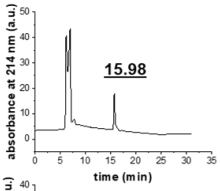	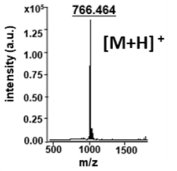
2g linear	63	28	766.44 (788.52)	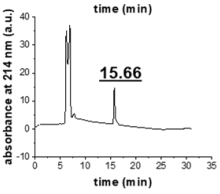	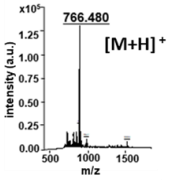
2h linear	58	29	738.44 (760.52)	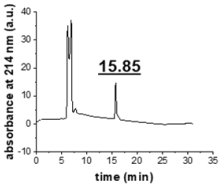	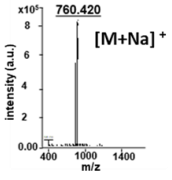
2i linear	64	29	738.44 (760.52)	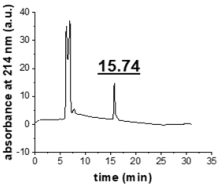	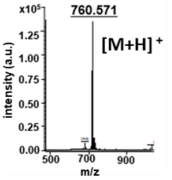

The HPLC injections were performed by dissolving 500 μg of peptide powder in 20% TFA and 80% B. Solutions compositions are described in 3.1.8. Peptide were eluted in the gradient described in Table 16.

* Calculated as $Y_{synthesis} = (W_p/Y_{theor}) \times 100$ (W_p= weight of lyophilized peptide, Y_{theor}= theoretical yield, obtained as M_R x R_L x MW of peptide (M_R= mass of the resin, R_L= resin loading)[157].**Calculated as $Y_{purification} = (W_p/W_{crude}) \times 100$ (W_p= weight of HPLC-purified peptide, W_{crude}= weight of crude peptide).

4.3 Biophysical characterization of CD structures and self-assembly of MIMs and linear precursors

4.3.1 CD spectroscopy studies

4.3.1.1 CD characterization of MIMs

Circular dichroism is the unequal absorption of left-handed and right-handed circularly polarised light, and it is a straightforward method for determining the secondary structure of peptides and proteins[59,138,139,142]. This is because diverse structural elements have characteristic far-UV CD spectra, therefore, CD spectroscopy studies, performed in physiological conditions, can be a valid technique to elucidate the conformation of a protein or a peptide in the biological environment[140–142].

The secondary structures of MIMs were characterised by this method. Notably, establishing robust conditions for recording the spectra was not a straightforward process, likely due to the peptides' strong self-assembling propensity, as confirmed in later studies (4.3.1.6 and 4.3.2). Applying standard protocols[98,129,137], such as peptide stocks preparation in HFIP (peptide concentration, 1 μM or 0.5 μM) followed by dilution 1xb (pH 7.4) to the final concentrations (5-100 μM) resulted in strong signal scattering which could be due to peptide oligomerisation[97–99]. The conditions tested to overcome this problem include the addition of different cosolvents, such as aqueous solution HCl (1 mM) and trifluoroethanol (TFE), and trying different cuvette path lengths.

Eventually, the spectra were successfully recorded by preparing the peptides as lyophilised powder and dissolving them in the necessary amount of HFIP to reach a final concentration of 1% in 1xb (pH 7.4).
CD spectroscopy studies of MIMs (10 μM) performed in these conditions revealed a negative band with a minimum at 228 nm and a positive band with a maximum at 195 nm, indicating the presence of β-sheet/β-turn structures (Figure 18). Of note, the spectrum of **2f** showed a blue shift of the minimum to 225 nm and a red shift of the maximum to 205 nm. (Figure 18a).

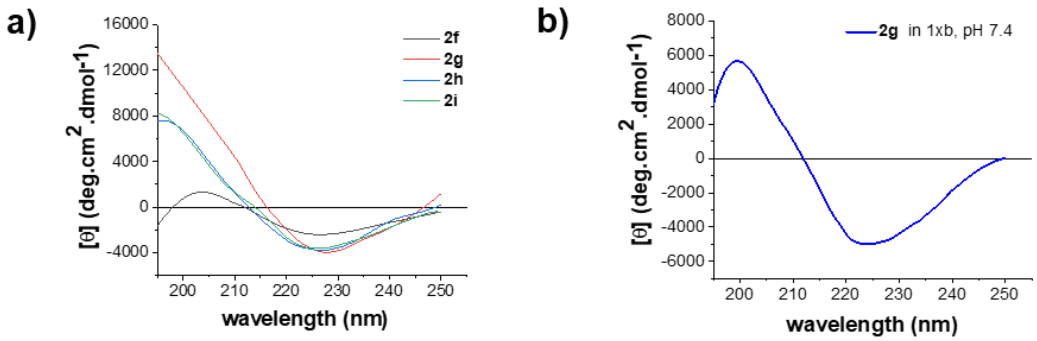

Figure 18. CD studies on MIMs conformations. (a) CD studies of **2g**, **2h** and **2i** (10 μM) prepared as peptide powder and dissolved in 1xb (pH 7.4) containing 1% HFIP revealed a minimum at 228 nm and a maximum at 198 nm. The spectrum of **2f**, prepared in the same condition, showed a minimum at 225 nm and a maximum at 205 nm. (b) The far-UV CD profile of **2g** prepared in 1xb (pH 7.4) without HFIP showed the same structure. Baselines were subtracted from the spectra.

Next, the effect of HFIP on **2g** secondary structure was studied (Figure 18b). HFIP is widely used to disaggregate amyloidogenic peptides and proteins due to its remarkable solvent properties[135,136,158,159]. However, fluorinated alcohol can strongly influence the secondary structure of peptides and proteins [160–162]. Thus, CD studies on **2g** were performed in 1xb without HFIP to understand whether its presence influenced the peptide conformation (Figure 18b). The results revealed that the spectra recorded with or without HFIP are very similar, suggesting that the cosolvent does not affect the secondary structure.

4.3.1.2 CD characterization of the linear precursors

The secondary structure adopted by a peptide is a crucial feature for determining its biological activity[98,99,139,163]. The head-to-tail cyclisation is a widely exploited approach to modulate and stabilise the conformation of short peptides [86,164]. Thus, CD studies were performed on the linear precursors to understand the cyclisation`s effect on the conformation of the primary sequences. CD studies were performed in the same conditions described in paragraph 4.3.1.2. The spectra of **2g linear**, **2h linear** and **2i linear** showed a minimum at 224 nm and a maximum at ~205 nm. In contrast, the **2f linear** spectrum revealed a minimum at ~230 nm and a maximum at ~200 nm. When compared to the structures of MIMs, the spectra of the linear analogues revealed a blue shift of the minimum observed at 230 nm for the cyclic peptides and a red shift of the maximum observed at 198 nm (Figure 19). Taken together, the results indicate the presence of an ordered structure containing β-sheet/β-turn features and a clear difference between the conformation of MIMs and linear analogues, except for **2f linear**.

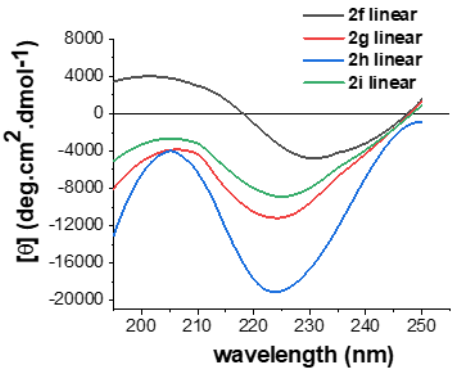

Figure 19. CD studies on linear precursors. Solutions of linear analogues (10 μM) were prepared in 1xb (pH 7.4) containing 1% HFIP and analysed via CD spectroscopy. The CD spectra of **2g linear**, **2h linear** and **2i linear** showed a minimum at 224 nm and a maximum at 205 nm, whereas the spectrum of **2f linear** showed a red shift of the minimum to 230 nm and a positive signal at 198 nm. Baselines were subtracted from the spectra.

4.3.1.3 CD concentration dependence studies of MIMs

CD concentration dependence studies were performed to investigate the self-assembly propensity of MIMs. Previous studies showed that this property is essential for the mode of action of the peptide templates ISMs[97,98], as this process might contribute to sequestering Aβ or IAPP into non-fibrillar/non-toxic hetero assemblies[97–99]. CD spectra were recorded with peptide solutions of concentrations ranging between 5 and 100 μM. Peptide solutions were prepared by dissolving the lyophilised powder in 1% HFIP in 1xb (pH 7.4), and the cuvette path

length was either 1 cm (5-20 μM) or 0.5 cm (50-100 μM). Spectra measurements revealed no variation of the mean residue ellipticity of **2f** in response to the increased peptide concentration (Figure 20a). Conversely, a strong self-assembly propensity was observed for **2g** (Figure 20b), as the signal intensity of the negative band with a minimum at 230 nm diminished in response to the increased peptide concentration. Similarly, a decrease of the mean residue ellipticity of the maximum at 198 nm was observed for peptide concentrations higher than 20 μM. The correlation between self-assembly propensity and reduction in signal intensity was supported by TEM analysis of **2g** solution (Figure 20e), indicating that the assemblies' structural organisation and size increased with the peptide concentration. CD spectra of **2h** (Figure 20c) revealed similar characteristics as **2f**, as the signal intensity did not change in response to the concentration. Finally, CD studies on **2i** (Figure 20d) showed that the peptide oligomerises, as indicated by the decrease of mean residue ellipticity observed at 198 nm in response to the increased concentration.

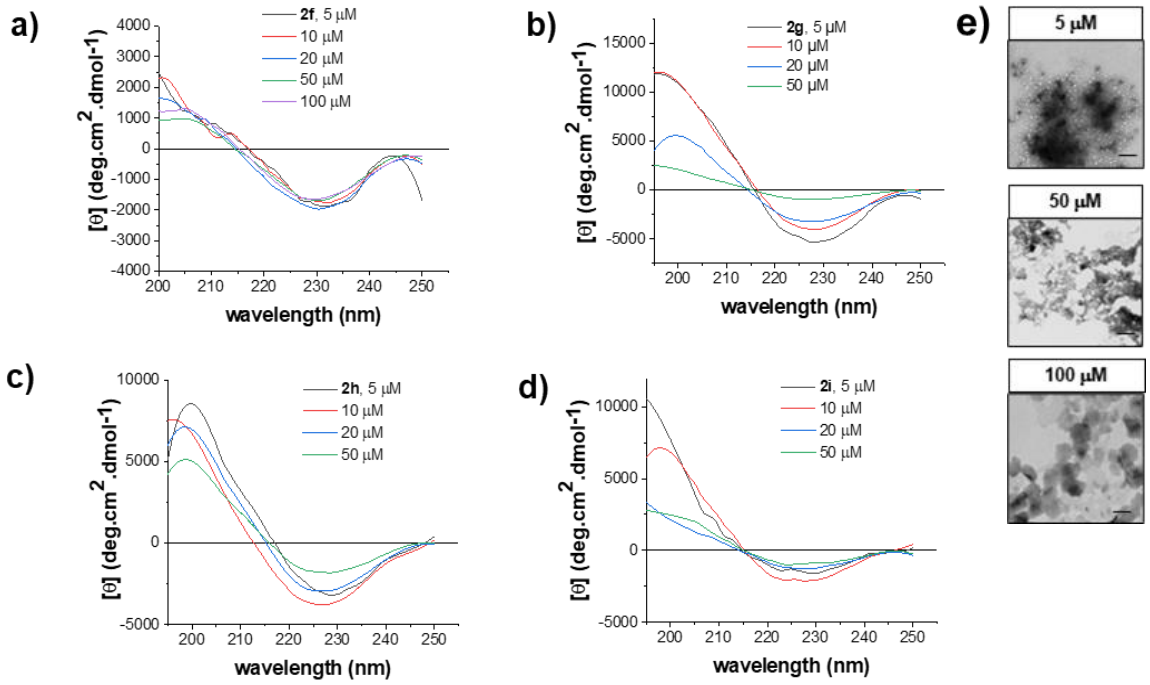

Figure 20. CD concentration dependence studies of MIMs. Spectra of peptide concentrations ranging 5 and 50 μM for **2f** (a), **2g** (b), **2h**, (c) and **2i** (d) are shown. Measurements were performed in 1×b (pH 7.4) containing 1% HFIP. The signal of the buffer was subtracted from the spectra. (e) TEM analysis of solutions containing increasing concentrations of **2g** was performed by depositing aliquots of the incubations used for the CD measurements on TEM grids (bars, 100 nm).

4.3.1.4 CD concentration dependence studies of the linear analogues

To understand whether the head-to-tail cyclisation might influence the self-assembly propensity of MIMs, CD concentration dependence studies were performed on the linear precursors in concentrations between 5 and 50 μM. The peptide solutions were prepared by dissolving the peptide powder into the HFIP amount necessary for having 1% in the final volume of 1xb (pH 7.4), as described in 4.3.1.1.

CD spectroscopy studies revealed that all the linear precursors form oligomers at low concentrations (Figure 21). The signal intensity of the characteristic minima observed at 230 nm for **2f linear** (Figure 21a) and at 224 nm for the other precursors (Figure 21b-d) decreased at concentrations higher than 10 μM.

Taken together, the results indicate that the primary sequences of the peptides are highly prone to aggregation, independently of the head-to-tail cyclisation. HPLC characterization suggested that the linear sequences are less hydrophobic than their cyclised version, as shown by the shorter retention time in the HPLC gradient (Tables 22). This result was expected, as the formation of a lactam bond between the N- and the C- termini decreased the net charge of the sequences. However, the higher degree of hydrophilicity did not result in a weaker aggregation tendency.

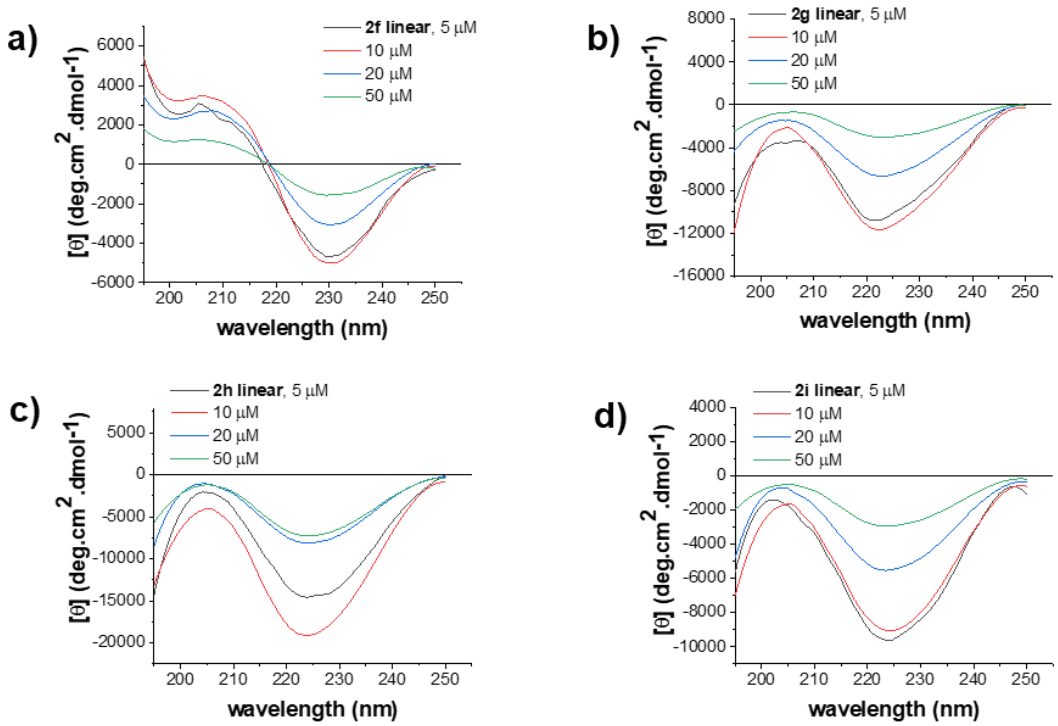

Figure 21. CD concentration dependence studies of the linear precursors. CD spectra of (a) **2f linear**, (b) **2g linear**, (c) **2h linear** and (d) **2i linear** were recorded. Peptide solutions were prepared in 1xb (pH 7.4) containing 1% HFIP, concentrations as shown. The signal of the buffer was subtracted from the measurements.

*4.3.1.5 TFE studies of **2f** and **2g***

The solvent trifluoroethanol (TFE) induces the formation of α-helical and β-hairpin structures in peptides, depending on the specific amino acid sequences[115]. Among several mechanisms, this fluorinated alcohol acts through the enhancement of polypeptide internal hydrogen bonding, by the perturbation of water structure, by decreasing the hydrophobic effect, and by solvating certain groups of the polypeptide chain [161,165]. TFE titration is a useful tool to determine the helical propensity of a peptide sequence, as for helical-prone peptides, a smaller amount of TFE induces the transition and stabilization of their structure[161].

For the TFE titrations, the amounts of **2f** and **2g** peptide powders, suitable for having a final concentration of 20 µM, were dissolved in the indicated amount of TFE, corresponding to the % (v/v) of the final volume and diluted in 1xb (pH 7.4). The CD spectra were recorded in 1 cm cuvettes.

Mixing the peptide solutions with increasing amounts of TFE did not lead to a conformational transition of the β-turn structures of **2f** and **2g** to α-helices (Figure 22). In fact, the same secondary structure was observed for all CD measurements, and no shift of the minimum at 230 was detected. Even for peptide solutions containing 80% TFE (v/v), the typical structural elements of α-helices, including the two characteristic minima at 208 and 222 nm were not observed.

Together with the results shown in Figure 18b, the findings indicate that the presence of fluorinate alcohols does not influence the structure of MIMs. Thus, the results suggest that the head-to-tail cyclisation increases structural rigidity of the conformation of the peptides.

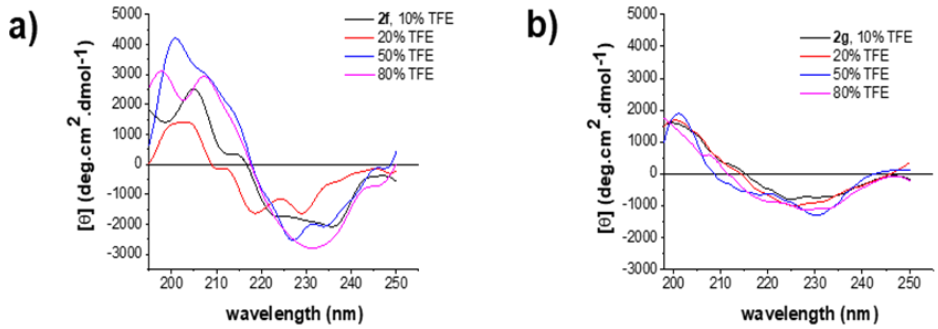

Figure 22. TFE studies of 2f and 2g. CD spectra were recorded by analysing (a) **2f** and (b) **2g** (20 µM each) prepared in 1xb (pH 7.4) with increasing amounts of TFE (%,v/v). The signal of the buffer was subtracted from the spectra.

*4.3.1.6 CD spectra of **2g** and **2i** at different pH*

Oligomerisation states are highly influenced by the H-bond networking between a solute molecule and the solvent [166–168]; thus, pH dependence studies were performed to characterise further the oligomeric structures formed by MIMs in aqueous conditions.

CD spectra were recorded with peptide solutions of **2g** and **2i** (100 µM each) prepared by dissolving the peptide powder in 1xb (pH 7.4) containing 1% of HFIP and mixed with amounts of aqueous protic cosolvents HCl (5 mM in ddH_2O), and NaOH (5 mM in ddH_2O).

CD spectroscopy studies of **2g** (100 µM) in 1xb (pH 7.4) containing more than 40% HCl (v/v, pH 6) revealed an enhancement of the β-turn structure compared to the spectrum recorded at neutral pH (Figure 23a), as indicated by the increase in signal intensity at 230 nm and 198 nm. Figure 23b shows that the maximum value of the mean residue ellipticity at 195 nm and 228 nm was observed for peptide solution containing 80% HCl (v/v, pH 3). TEM analysis of the peptide solutions used for the far-UV CD studies revealed the presence of aggregates with different morphologies at different pH: spherical aggregates were observed for the peptide

prepared at native pH, whereas unordered structures were detected in acidic conditions (Figure 23c).

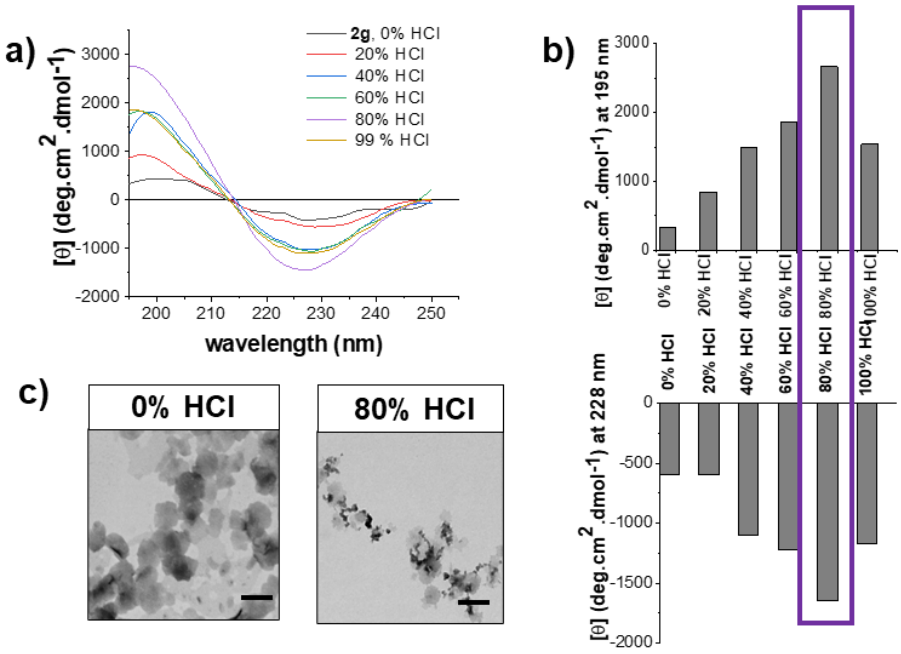

Figure 23. CD spectroscopy studies of 2g in the presence of aqueous HCl (5 mM). (a) CD studies were performed by treating **2g** (100 µM) in 1xb (pH 7.4) with increasing amounts of aqueous HCl (5 mM) (v/v). The signal of the buffer was subtracted from each spectrum. (b) Mean residue ellipticity of incubations of **2g** from (a) at 195 nm and 228 nm. The maximum signal increase is highlighted in purple (c) TEM imaging of **2g** solutions at 0% HCl (v/v) (pH 7.4), and 80% HCl (v/v) (pH 3) revealed the presence of spherical aggregates (scale bar, 100 nm).

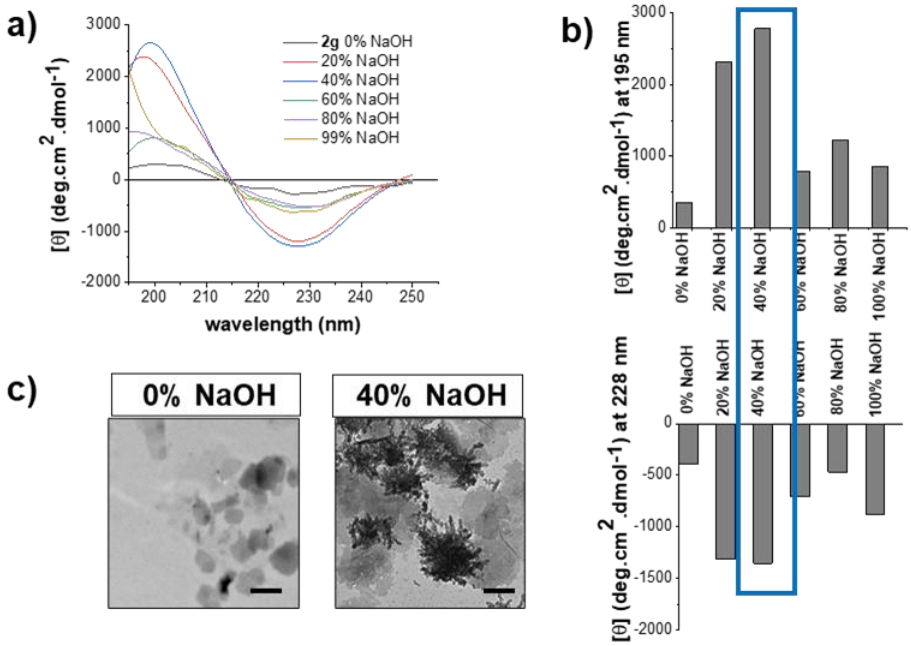

Figure 24. CD spectroscopy studies of 2g in the presence of amounts of aqueous NaOH (5 mM). (a) CD studies of **2g** solutions (100 µM) in 1xb (pH 7.4) mixed with aqueous NaOH (5 mM) are shown. The signal of the buffer is subtracted from the spectra. (b) Mean residue ellipticity of incubations of **2g** from (a) at 195 nm and 228 nm. The maximum increase is highlighted in blue. (c) TEM imaging revealed the presence of diverse morphologies at different pH: roundish structures were observed at neutral pH and unordered morphologies at acidic pH (scale bar, 100 nm).

CD spectroscopy studies of **2g** solutions (100 μM) prepared in the same conditions and titrated with NaOH (5 mM) showed similar behaviour. An increase in signal intensity was observed for peptide solutions containing either 20% or 40% of NaOH (v/v) (Figure 24a). The mean residue ellipticity at the characteristic minimum (228 nm) and maximum (195 nm) was circa three times higher than that observed at neutral pH. TEM analysis of peptide solution at basic pH (Figure 23c) revealed the presence of different structures than the roundish ones observed at pH 7.4.

These observations confirm that **2g** assemblies undergo a pH-dependent structural rearrangement in the presence of protic cosolvents, possibly shifting from oligomeric structures to their monomeric form.

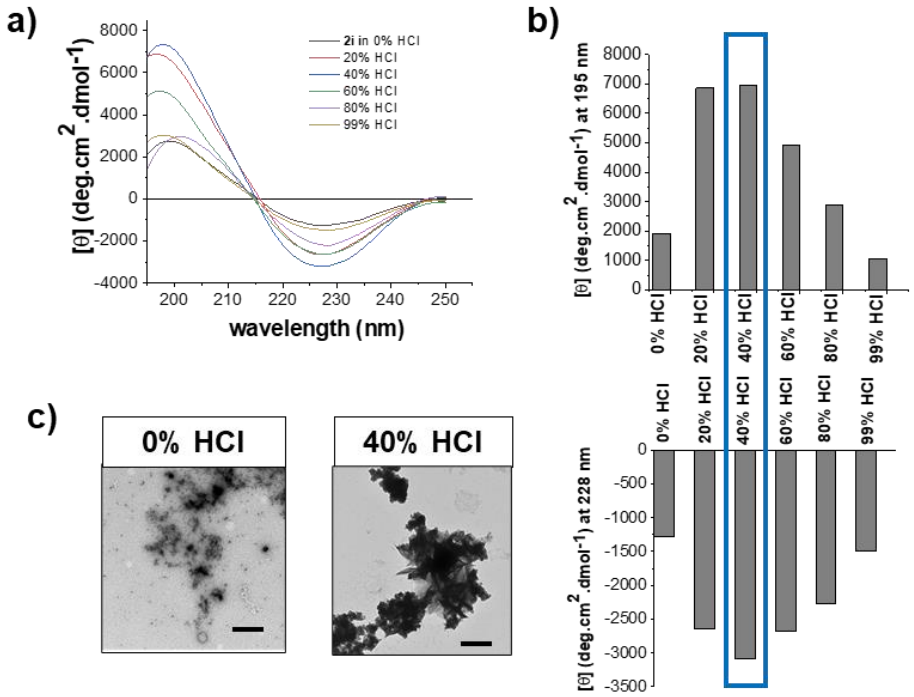

Figure 25. CD studies of 2i at acidic pH. (a) CD studies performed by treating **2i** (100 μM) in 1xb (pH 7.4) with increasing amounts of aqueous HCl (5 mM) (v/v) are shown. Baselines are subtracted from the CD spectra. (b) Mean residue ellipticity of incubations of **2i** from (a) at 195 nm and 228 nm. The maximum value is highlighted in blue. (c) TEM characterization of **2i** solutions containing 0% HCl (v/v) (pH 7.4) or 40% HCl (v/v) (pH 6) (scale bar, 100 nm).

4.3.2 Determination of 2i self-assembly propensity via fluorescence spectroscopy

Fluorescence spectroscopy was used to quantify the affinity of self-association, as done previously for other amyloid inhibitors showing strong self-assembly propensity [28,95,97,98]. Fluorescence spectroscopy titrations were performed by incubating HFIP stocks of N^{ε}-amino-terminal fluorescein-labelled **2i** (**Fluos-2i**) at 5 nM with increasing amounts of **2i**, in 1xb (pH 7.4) containing 1% HFIP. The binding of a 100-fold molar excess resulted in a fluorescence enhancement of 44 % (Figure 26a). The obtained sigmoidal titration curve was consistent with cooperative self-assembly, and the determined apparent affinity (app. K_D) was 34.43 (± 10.28)

nM. Results were in agreement with the self-assembly propensity observed via CD concentration dependence studies (Figure 20d) and previous results on ISMs and MCIPs[98,99].

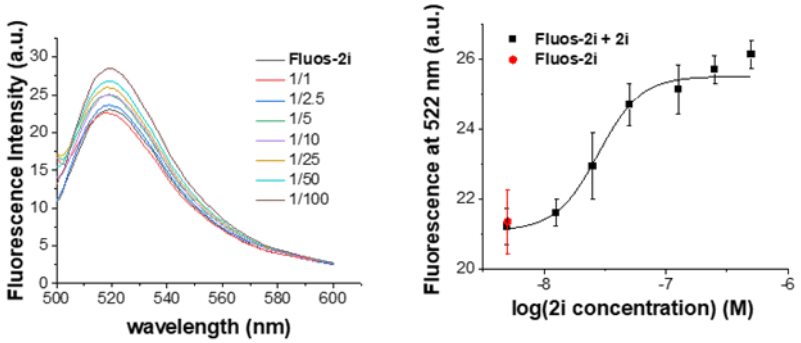

Figure 26. Self-assembly of 2i as studied via fluorescence spectroscopy titrations. Fluorescence emission spectra of N$^{\varepsilon}$-terminal fluorescein-labelled **2i** (**Fluos-2i**; 5 nM) alone and after titration with **2i** at the indicated molar ratios. Peptide incubations were prepared in 1xb (pH 7.4) containing 1% HFIP. On the right, the binding curve is shown. The estimated app. K_D value for **2i** self-association is 34.43 (± 10.28) nM. Data are means (±SD) from three binding curves.

4.4 Effect of MIMs and linear precursors on IAPP fibrillogenesis and cytotoxicity

One of the first questions assessed in this work was whether MIMs maintain the inhibitory function of the template **R3-GI**. It was answered by testing the activity of **2f**, **2g**, **2h**, and **2i** on IAPP amyloid formation via ThT binding assay and TEM imaging. Furthermore, the MTT reduction assay was used to characterise the cytotoxicity of the heterocomplexes formed between IAPP and MIMs after 24 h and 7 days of aging.

These methods are widely applied to characterise the formation and the cytotoxic effects of amyloid assemblies[90,93,94,98,99,127,129]. ThT is a small molecule commonly used to monitor the formation of amyloid *in vitro*. Its fluorescence enhancement and shift upon binding to fibrils is its most defining and thorough property [131]. In fact, it is widely accepted that the increase in ThT fluorescence results from the selective immobilisation of a subset of ThT conformers[132,170] and that amyloid fibrils are likely to present a ThT-binding site that sterically "locks" the bound dye[58]. ThT emits at 482-490 nm upon binding to amyloid fibrils when excited at 450 nm [131].

The MTT (3-(4,5-dimethylthiazol-2-yl)-2,5-diphenyl-2h-tetrazolium bromide) reduction assay is widely used to test cellular metabolic activity. This molecule can cross the cell and mitochondrial membranes and is reduced to formazan by metabolically active cells [134].

ThT studies performed by titrating amyloidogenic IAPP with increasing concentrations of **2f**, **2g**, **2h** and **2i** revealed that MIMs could effectively inhibit IAPP fibrillation in a concentration-dependent fashion (Figure 27). Full suppression of IAPP fibril formation was observed when the inhibitors were added in 5 and 10-fold excess, as shown by the lack of fluorescence increase compared to the control (Figure 27a-d, left panels and Figure 28a). Of note, **2i** was the only analogue that showed full inhibition of IAPP in 2-fold excess (Figure 27d). Conversely, incubating IAPP with lower folds of inhibitors did not significantly change its kinetics.

Titrations of cytotoxic IAPP with MIMs at 24 h and 7 days showed full amyloid-mediated cytotoxicity suppression (Figure 27a-d, right panels, and 28b). The MTT studies supported the ThT finding, confirming that the inhibition of the cytotoxicity occurs in a concentration-dependent manner. The cytotoxicity studies yielded the IC_{50}s in the nanomolar range (Figure 28d-g, Table 24), indicating that MIMs are potent inhibitors of IAPP amyloid formation.
TEM analysis of incubations of IAPP/MIMs in 5-fold excess and aged for 7 days (Figure 28c) revealed the presence of amorphous aggregates. In contrast, typical elongated amyloid fibrils were observed for samples containing IAPP alone. These findings suggested that IAPP/MIMs hetero complexes are non-amyloidogenic and non-cytotoxic.

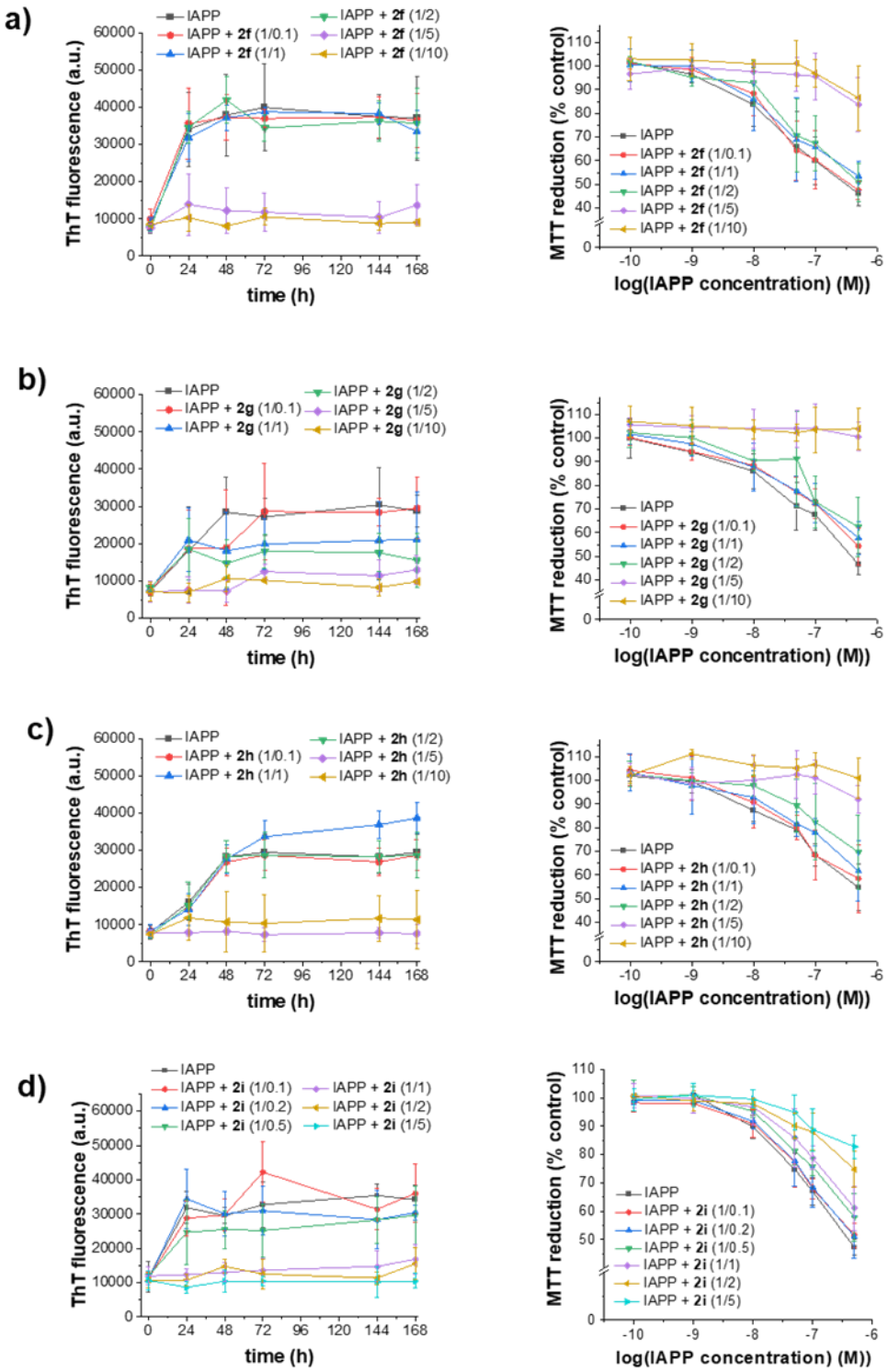

Figure 27. Effects of MIMs on IAPP amyloidogenesis and cytotoxicity. (a-d, left panels) The effects of MIMs on IAPP self-assembly as determined by the ThT binding assay (IAPP/MIMs, 1/0.1-1/10) (means (±SD) 3 assays)) re shown. For the single assays, see Appendix Figures A4, A10, A16, and A22. (a-d, right panels) **2f**, **2g**, **2h** and **2i** suppress IAPP cytotoxicity (7-day-aged solutions) on RIN-5mf cells as determined by the MTT reduction assay (IAPP/MIMs, 1/0.1-1/10) (means (±SD) 3 assays) (n=3 each). For the single assays, see Appendix Figures A5, A11, A17, and A23. Peptide solutions were prepared in IAPP ThT buffer containing 0.5% HFIP (IAPP, 6 μM) and incubated at 20ºC.

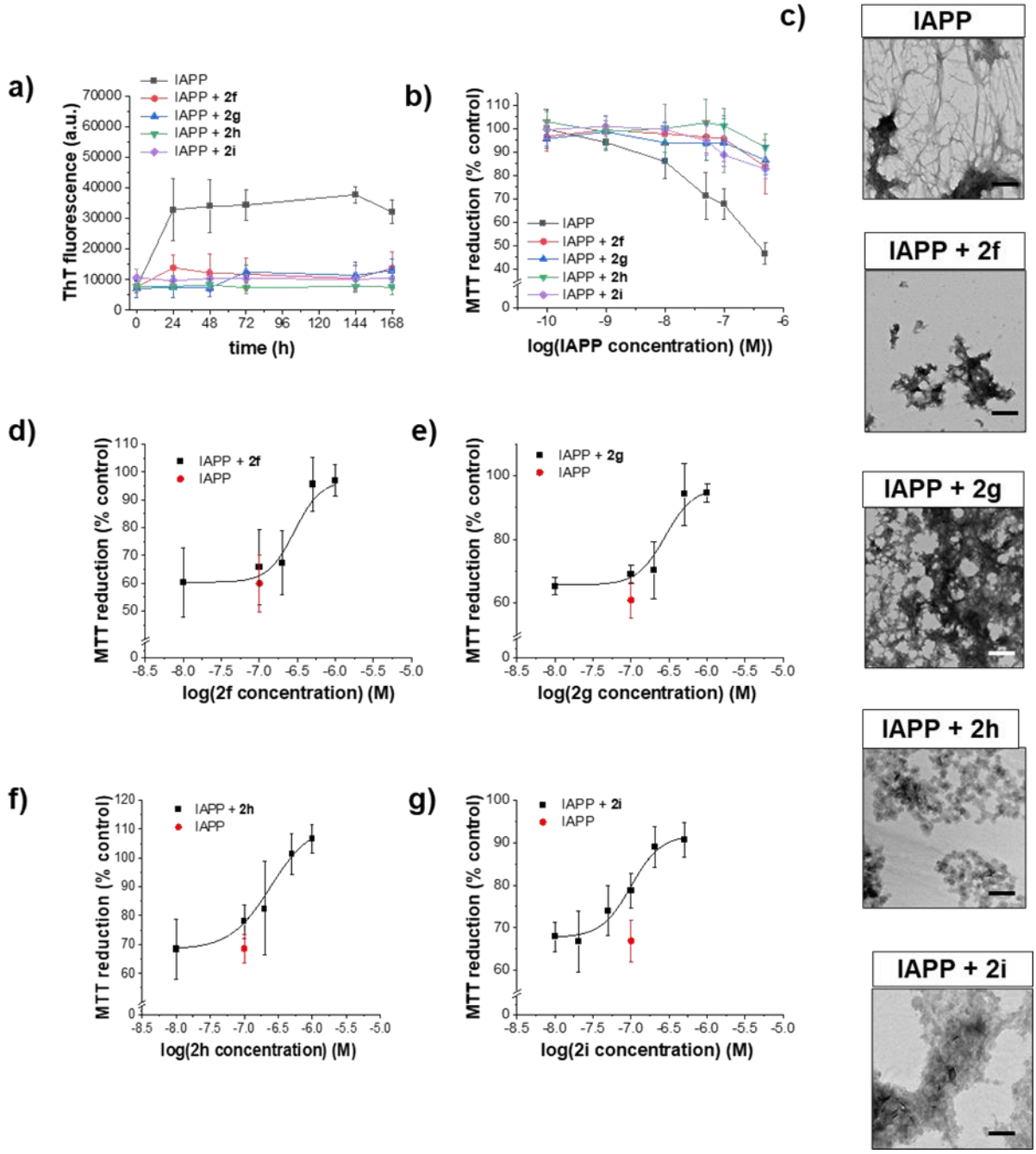

Figure 28. MIMs inhibit IAPP amyloidogenesis and cytotoxicity in 5-fold excess. (a) Effects of MIMs on IAPP amyloid self-assembly as determined by the ThT binding assay (IAPP/peptide, 1/5) (means (±SD), 3 assays). Peptide solutions were prepared in IAPP ThT buffer containing 1% HFIP (IAPP, 6 μM) and kept at 20ºC. (b) **2f**, **2g**, **2h** and **2i** suppress IAPP cytotoxicity on RIN-5mf cells (7-day-aged solutions) as determined by the MTT reduction assay (IAPP/MIMs (1/5)) (means (±SD) 3 assays (n=3 each)). The MTT assays were performed with peptide aliquots from (a). (c) Incubations from (a) were morphologically characterised via TEM (scale bars, 100 nm). (d-g) IC_{50} curves of inhibitory effects of MIMs on cell damaging IAPP fibrils formation. Aged solutions (7 d) of IAPP alone (100 nM) or its mixtures with different amounts of MIMs were added to RIN5-fm cells. Cell damage was determined by the MTT reduction assay for mixtures of IAPP with **2f** (d), **2g** (e), **2h** (f), and **2i** (g), as indicated. Cytotoxicity of IAPP alone is included in each graph for comparison (red symbol). Data and determined IC_{50} values are means (±SD) from 3 independent assays (n=3) (Table 23). For the single assays, see Appendix Figures A6, A12, and A24.

Next, the effect of the head-to-tail cyclisation was investigated by testing the inhibitory potential of the linear precursors. ThT studies performed by incubating IAPP with linear

precursors up to 50-fold excess revealed that IAPP fibril formation was not influenced by their presence (Figure 29). Mixtures of IAPP/linear precursors assembled into ThT-binding fibrils after 24 h, as observed for IAPP alone (Figure 29a-c). Notably, it was excluded that the increase of the ThT was due to the high concentration of the peptides by incubating **2i linear** alone in the corresponding concentration (Fig. 29c).

Table 23. IC_{50} values of inhibitory effects of MIMs on IAPP-mediated damage. Effect of 24 h or 7 days aged IAPP/MIMs mixtures on cultured RIN-5fm cells [a]

MIMs	IC_{50} (±SD) (nM) (aged 24 h) [b]	IC_{50} (±SD) (nM) (aged 7 d)
2f	240.44 (±46.76)	300.65 (±67.87)
2g	178.54 (±57.35)	307.76 (±24.18)
2h	608.58 (±525.43)	287.55 (±143.43)
2i	65.54 (±17.45)	95.33 (±25.66)

[a] IC_{50}s, means (±SD) from 3 titration assays (n=3 each; IAPP, 100 nM) (Figure 28).
[b] For the single assays, see Appendix Figures A1-3 (**2f**), A7-9 (**2g**), A13-15 (**2h**), A19-21 (**2i**).

TEM analysis of the samples containing IAPP and **2g linear** in 50-fold excess revealed the presence of typical amyloid fibrils, to the same extent and morphology as in controls containing IAPP alone (Figure 29d).

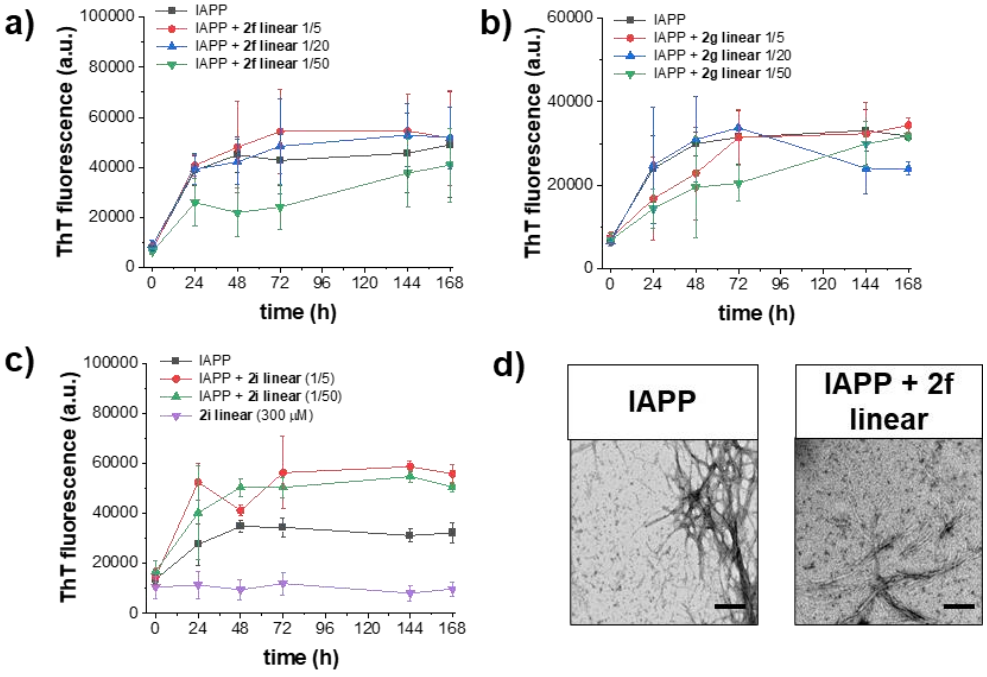

Figure 29. Inhibitory potential of 2f linear, 2g linear, and 2i linear towards IAPP amyloid formation. Effect of (a) **2f linear,** (b) **2g linear** and (c) **2i linear** on IAPP self-assembly as determined by the ThT binding assay (IAPP/MIMs, 1/5-1/50) (means (±SD) 3 assays). Incubations were prepared in IAPP ThT buffer containing 0.5% HFIP (IAPP, 6 µM) and kept at 20ºC. (d) TEM images of incubations of (b) revealed the presence of amyloid fibrils (scale bar, 100 nm).

The results suggest that the cyclic peptide compounds are at least ten times more potent than their linear precursors. This confirms the hypothesis that head-to-tail cyclisation is critical

for stabilising specific conformations enabling high-affinity amyloid inhibitory interactions with IAPP amyloidogenic species.

4.5 Determination of IAPP binding affinities of MIMs and linear precursors

According to previously established protocols, the apparent affinities of the interaction between MIMs for monomeric IAPP were quantified by fluorescence spectroscopy [28,100,127,129,136]. Titrations of synthetic N^{α}-terminal fluorescein-labelled IAPP (Fluos-IAPP) (5 nM) with MIMs revealed high-affinity interactions, as most of the app. K_Ds fell in the low nM range (Fig. 30a-d, Table 24). Our group previously reported that freshly made solutions of Fluos-IAPP at 5 nM consisted mainly of monomers[28,100,136]. Titrating Fluos-IAPP with **2g** amounts higher than 125 nM resulted in a decreased signal that could be explained by the aggregation of the complexes (fig. 30b). Sigmoidal titrations curves were obtained and were consistent with a cooperative self-assembly process[28,136].

To investigate the effect of the head-to-tail cyclization, the affinities of the interaction between the linear precursors and monomeric IAPP were also quantified (Figure 31). Fluorescence spectroscopy studies were performed in the same conditions described above.

Titrations of synthetic Fluos-IAPP (5 nM) in 1xb (pH 7.4), containing 1% HFIP, with increasing amounts of the linear sequences revealed no binding affinity, or weak binding in the case of **2i linear** (Figure 31c). These results are in accordance with the ThT findings (Figure 29), that revealed that the linear precursors are at least 10-times weaker than their cyclized analogues.

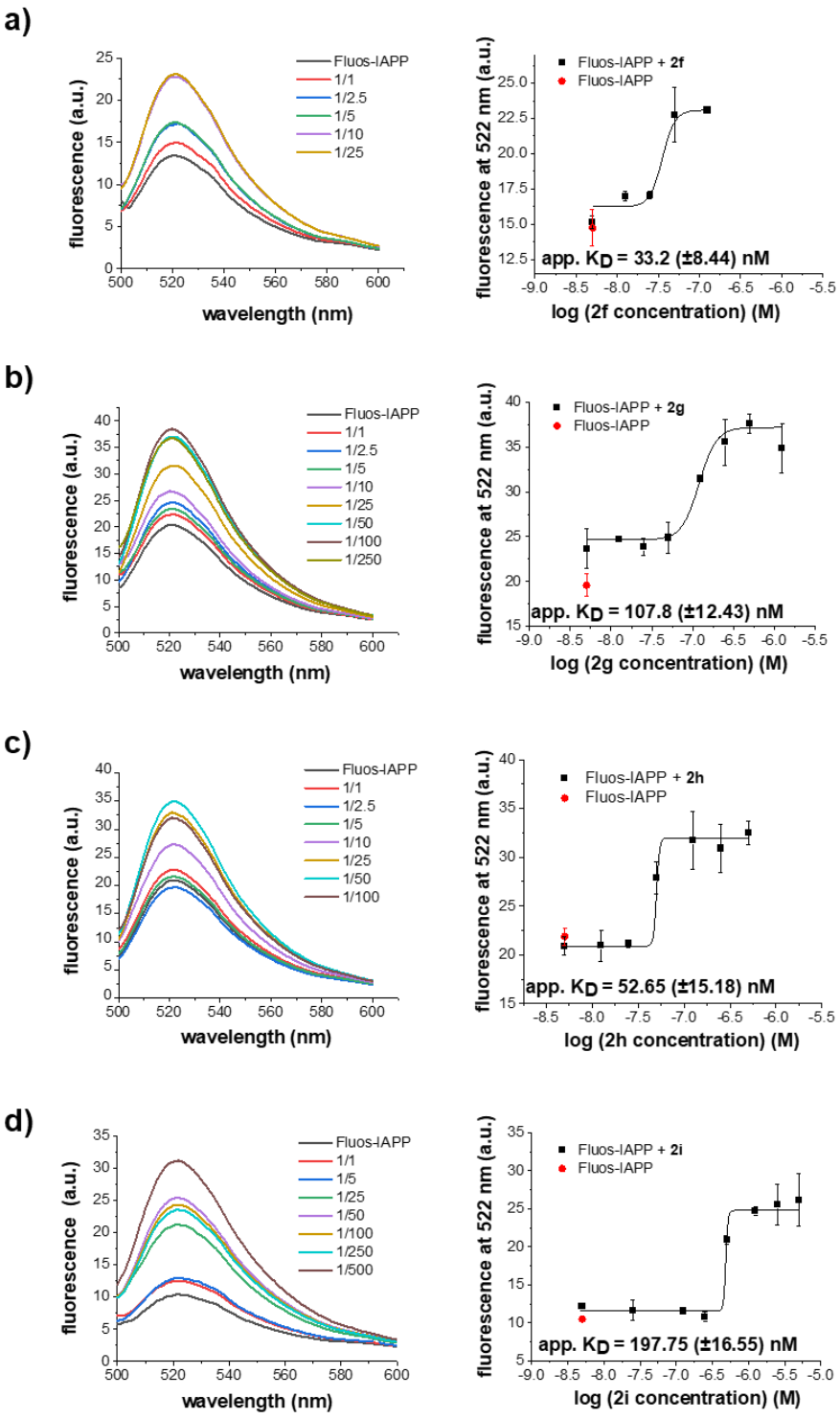

Figure 30. Determination of app. K_Ds of interaction of MIMs with IAPP by fluorescence titrations. Left panels (a-d) show fluorescence emission spectra of Fluos-IAPP (5 nM) alone or with various amounts of (a) **2f**, (b) **2g**, (c) **2h**, and (d) **2i**. The molar excess of Fluos-IAPP/MIMs are indicated. Right panels (a-d) show the binding curves of (a) **2f**, (b) **2g**, (c) **2h** and (d) **2i**. App. K_Ds are means (±SD) from 3 binding curves. Measurements were performed in 1×b (pH 7.4) containing 1% HFIP.

Table 24. IC_{50} values of inhibitory effects of MIMs on IAPP-mediated cell damage after 7 days of co-incubation[a], app. K_Ds of MIMs/IAPP interactions[b][c] and % of fluorescence increase[d]

MIMs	IC_{50} (±SD) (nM)[a]	app. K_D(±SD) (nM)[b][c]	Fluorescence increase (%)[d]
2f	300.13 (±67.32)	33.2 (±8.44)	52
2g	307.47 (±24.33)	107.8 (±12.43)	52
2h	287.12 (±143.76)	52.65 (±15.18)	53
2i	95.82 (±24.84)	197.75 (±16.55)	75

[a] IC_{50}s, means (±SD) from 3 titration assays (n=3 each; IAPP, 100 nM).
[b] Determined by titrations of N-terminal fluorescein-labeled IAPP (5 nM; pH 7.4) with MIMs (Figure 30).
[c] App. K_Ds are means (±SD) from 3 binding curves.
[d] Compared to % of Fluos-IAPP alone.

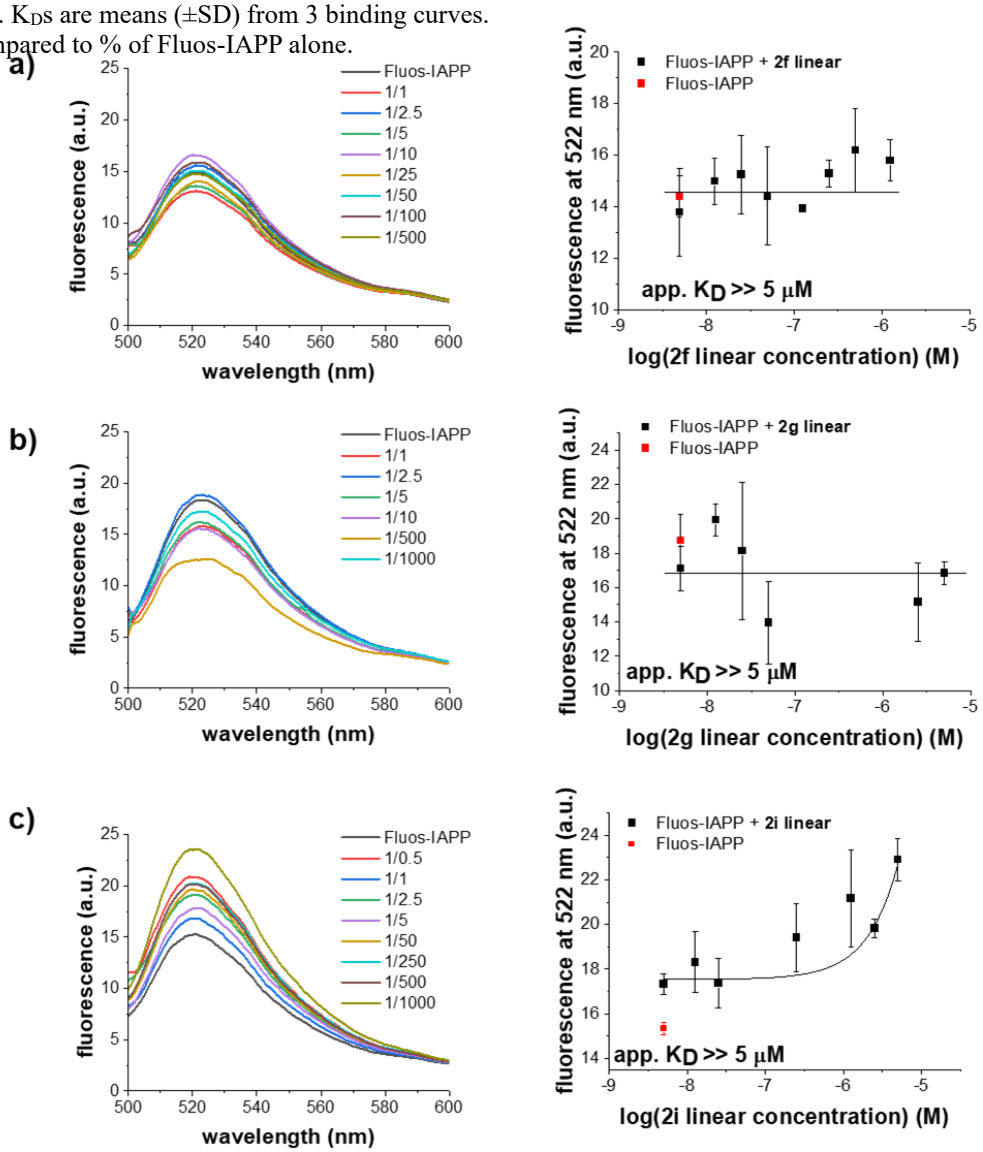

Figure 31. Determination of app. K_Ds of the interaction of linear precursors with IAPP via fluorescence titrations. Left panels (a-c) show fluorescence emission spectra of Fluos-IAPP (5 nM) alone or with various amounts of (a) **2f linear**, (b) **2g linear** and (c) **2i linear** in 1xb (pH 7.4) containing 1% HFIP. The molar excess of Fluos-IAPP/linear precursors is indicated. Right panels (a-c) show representative binding curves of (a) **2f linear**, (b) **2g linear**, and (c) **2i linear** (mean of 3 binding curves).

4.6 Effects of MIMs on IAPP conformational transition followed via CD spectroscopy

4.6.1 Effect of 2g in 5-fold excess to IAPP

To study the effects of **2g** on the conformational transition of IAPP misfolding, far-UV CD spectra of IAPP (5 µM), **2g** (25 µM), and the IAPP/**2g** mixture (1/5) were measured at various time points (Figure 32). As previously reported[98,127,129], the spectrum of monomeric IAPP at time 0 h consisted of large amounts of unordered structures (Figure 32a). In contrast, the spectrum of **2g** in 5-fold excess indicated significant quantities of β-turn structure, with a minimum at 228 nm and a maximum at 195 nm (Figure 32a).

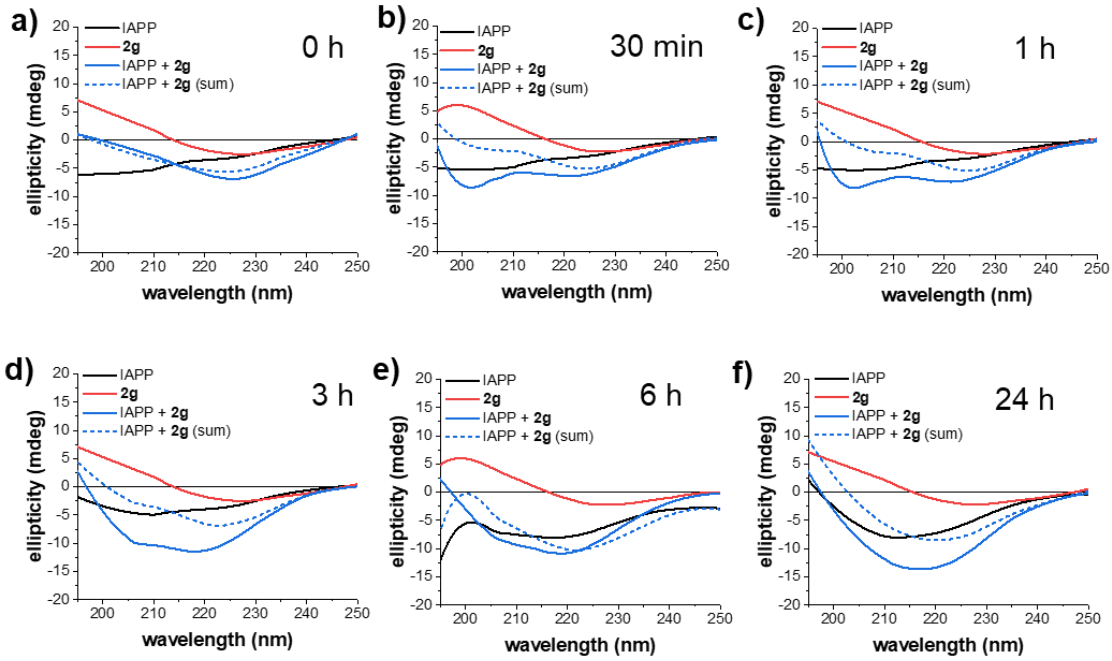

Figure 32. Characterization of IAPP/2g interaction via CD spectroscopy. CD spectra of IAPP (5 µM), IAPP + **2g** (1:5; 5 µM and 25 µM) and **2g** alone (25 µM) are shown at (a) 0 h, (b) 30 minutes, (c) 1 h, (d) 3 h, (e) 6 h, and (f) 24 h of incubation. Peptide solutions were prepared in 1xb (pH 7.4), containing 1% HFIP. The sums of the spectra of **2g** and IAPP are also shown in dashed lines. A difference between the measurement and the sum of the spectra was observed after 30 minutes of incubation, as shown by the presence of two minima at 202 and 222 nm. After 24 h of aging, the solution containing the mixture was clear, whereas precipitation into insoluble aggregates was observed for IAPP alone. After 24 h, the incubation containing IAPP was measured after mixing to redissolve the precipitate. The signal of the buffer was subtracted from the spectra.

After 30 min of incubation and for each time point, the CD spectrum of the mixture revealed the presence of minima at 202 and 222 nm (Figure 32b). Of note, the difference in wavelengths between the two minima decreased over time and indicated significant amounts of β-sheet/turn structures(Figure 32c-f). This profile differed from the sum of the spectra of IAPP and **2g** alone, confirming that IAPP interacts with **2g**. After 24 h (Figure 32f), the far-UV CD spectrum of IAPP indicated a conformational change into β-sheet-rich assemblies, resulting in aggregation into insoluble species due to the fibril formation process. Notably, the precipitated aggregates were resuspended by vigorously mixing, allowing the far-UV CD

measurements. By contrast, no precipitation was observed in the mixture, suggesting that the interaction between **2g** and IAPP in the inhibitory 5-fold-excess yielded soluble hetero-assemblies that suppressed IAPP fibrillogenesis.

4.6.2 Effect of 2i in 5-fold excess to IAPP

The interaction between **2i** and monomeric IAPP was characterised via CD spectroscopy, as previously described for **2g**.CD spectra of IAPP (5 µM), IAPP/**2i** (1/5), and **2i** (25 µM) were recorded at different time points (Figure 33). CD spectroscopy studies of **2i** alone revealed the presence of well-defined β-sheet/β-turn structures, with a minimum at 228 nm and a maximum at 200 nm (Figure 33a). The mean residue ellipticity remained stable over the experiment, indicating that the peptide stayed in solution. In contrast, time-dependence studies of IAPP alone showed a conformational shift from a largely unordered structure to β-sheet-rich and insoluble species, which were resuspended to allow the measurement at 24 h (Figure 33f). The mixture of IAPP and **2i** showed one minimum at circa 202 nm until 3 h (Figure 33d) and red-shifted to 222 nm after 24 h of incubation (Figure 33f).

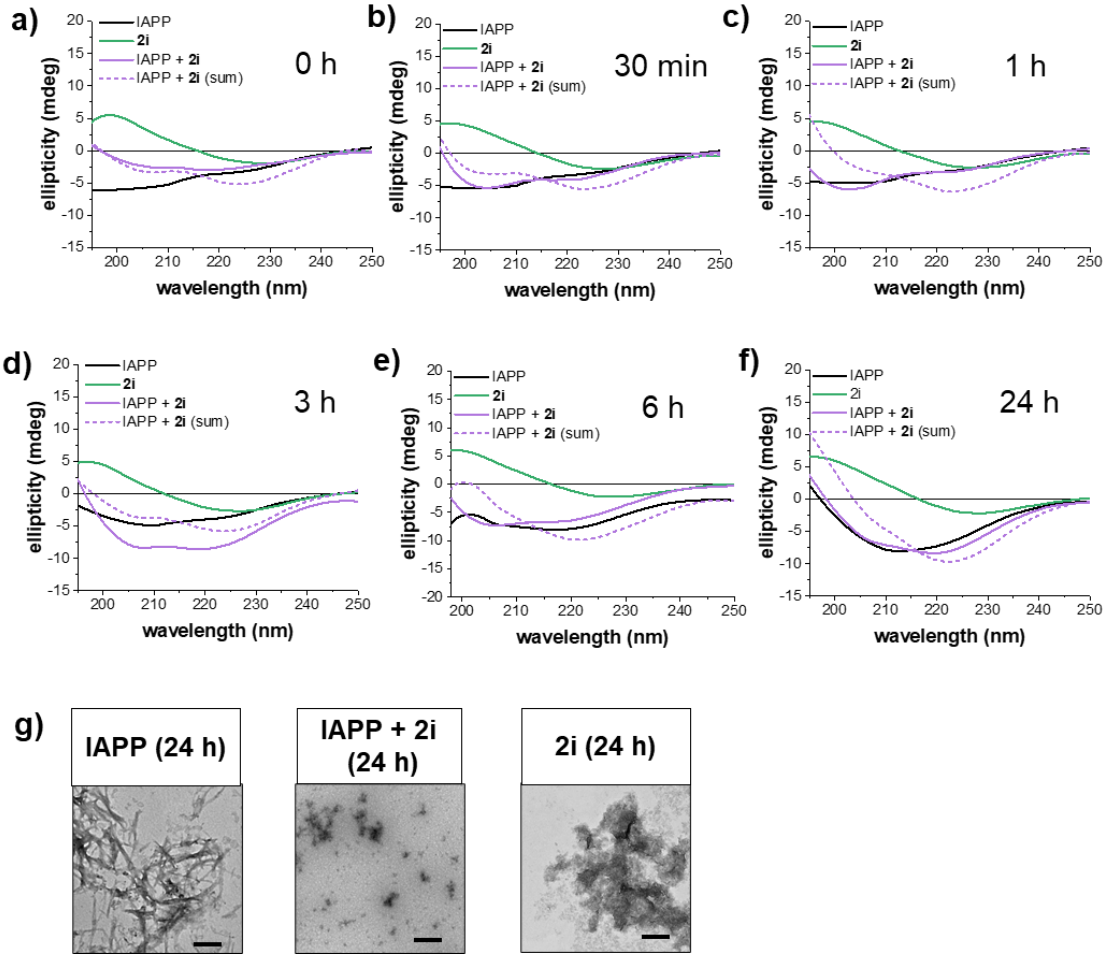

Figure 33. CD characterization of the interaction between IAPP and 2i followed over time. CD spectra of IAPP (5 µM), IAPP + **2i** (1:5; 5 µM and 25 µM) and **2i** alone (25 µM) prepared in 1xb (pH 7.4) containing 1% HFIP) were measured at (a) 0 h, (b) 30 min, (c) 1 h, (d) 3 h, (e) 6 h, (f) 24 h. (g) TEM analysis of peptide solutions aged 24 h confirmed that the IAPP/**2i** co-assemblies are non-fibrillar but amorphous (scale bar, 100 nm).

This result is consistent with a structural transition to higher amounts of β-sheet structures. However, the solution remained transparent and homogeneous for 24 h, and the peptide mixture differed from the sum of the spectra at each time point of incubation. Such findings confirmed the occurrence of the interaction between IAPP and **2i.** As observed for the **2g**/IAPP mixture**,** the sum of the spectra of the single peptides differed at each time point from the spectra of the IAPP mixture.

4.6.3 Effect of an equimolar amount of 2i on IAPP misfolding

The effect of equimolar amounts of **2i** on the conformational transition of IAPP misfolding was characterised via CD (Figure 34) to compare the results with the ThT and MTT findings showing no inhibitory properties in these conditions (Figure 27). As described above, far-UV CD spectra of IAPP (5 μM), IAPP/**2i** (1/1), and **2i** (5 μM) were recorded at different time points. Spectra of the mixture of IAPP and **2i** revealed the characteristic minimum at 202 nm observed for the 5-fold excess incubation only at time 0 h (Figure 34a). At later time points, the mixture showed a minimum at 228 nm, which indicates an increase of β-turn structures (Figure 34b-d). Overall, the structure of the mixture resembles that of the peptide alone. After 6 h (Figure 34e), the signal intensity of the mixture decreased, indicating the development of aggregates. After 24 h of aging (Figure 34f), the formation of insoluble species was observed in the IAPP solution, as expected, and in the mixture, indicating that **2i** in equimolar amount could not suppress IAPP misfolding. After resuspension, the signal of the mixture was the same as the sum of the spectra of the single peptides. These results suggest that the equimolar complex formed between **2i** and IAPP at 1/1 was not stable enough to block IAPP misfolding into fibrils.

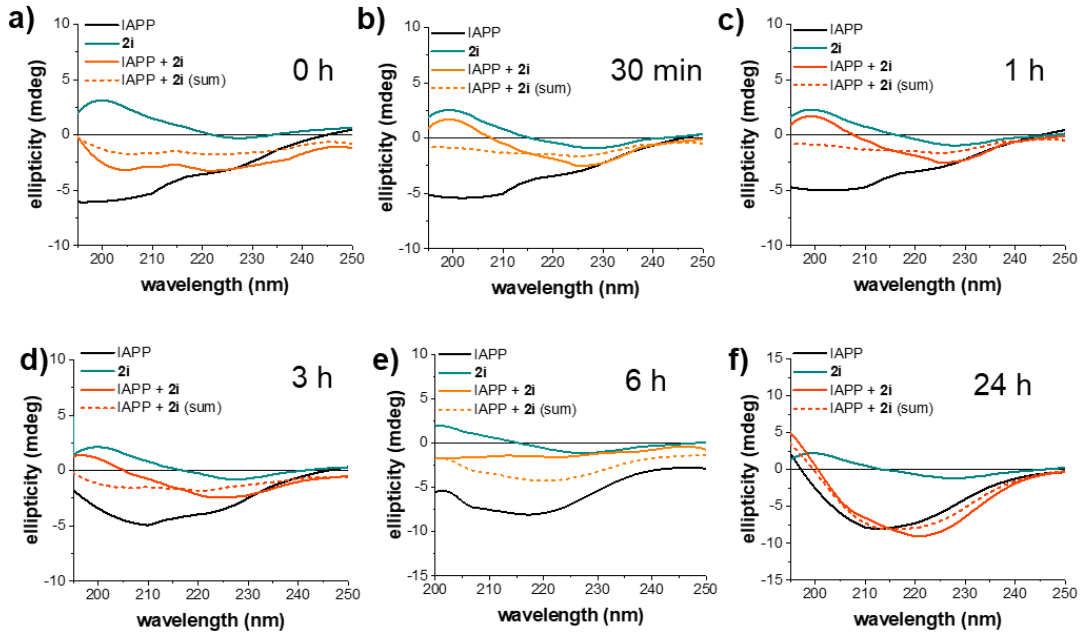

Figure 34. Far-UV CD characterization of the interaction between IAPP and equimolar 2i followed over time. CD spectra of IAPP (5 μM), IAPP + **2i** (1:1; 5 μM) and **2i** alone (5 μM) were recorded on solution prepared in 1xb (pH 7.4) containing 1% HFIP at (a) 0 h, (b) 30 min, (c) 1 h, (d) 3 h, (e) 6 h and (f) 24 h. The sums of the spectra of **2i** and IAPP are also shown in dashed lines. After 24 h of aging, both the solutions containing IAPP and IAPP/**2i** were turbid, indicating the formation of insoluble aggregates and far-UV CD measurements were performed after vigorous resuspension.

4.6.4 Effect of 2g linear on IAPP misfolding

As a proof of concept, the effects of **2g** and **2i** on IAPP misfolding were compared to that of **2g linear** in 5-fold excess. Based on the design concept of the class, an interaction between the linear precursors and IAPP was expected. However, studies on the inhibitory potential (Figure 29) and binding affinity (Figure 30) of the linear sequences revealed that neither inhibit IAPP fibrillation nor bind it in the nanomolar range.

The incubations containing IAPP (5 μM), **2g linear** (25 μM), and the IAPP/ **2g linear** mixture (1/5) were prepared as described above, and far-UV CD spectra were recorded at various time points (Figure 35a–f).

Of note, higher peptide concentrations were not tested, as it was observed that the linear analogues, such as MIMs, readily assembled into oligomers at low concentrations (Figure 19). The results indicate that a transient interaction between IAPP and the linear precursor occurs within 1 and 6 h of incubation (Figure 35c-e). This result is shown by the signal intensity difference but not the structure observed between the sum and the mixture within this time frame. After 24 h of aging (Figure 35f), the spectra of the mathematical sum and the mixture were the same in profile and intensity. These results support the hypothesis that head-to-tail cyclisation is a critical feature in conferring affinity and inhibitory potential to the sequences of MIMs.

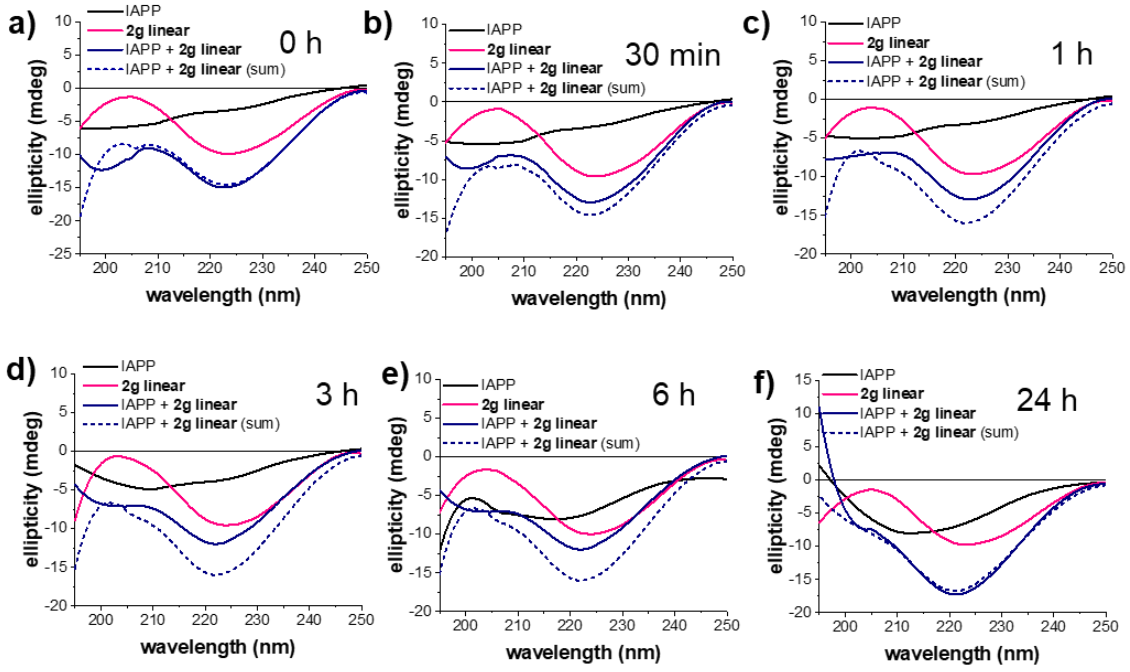

Figure 35. Characterization of IAPP/2g linear interaction via CD studies. Spectra of IAPP (5 μM), IAPP + **2g linear** (1:5; 5 μM and 25 μM), and **2g linear** (25 μM) were recorded at (a) 0 h, (b) 30 min, (c) 1 h, (d) 3 h, (e) 6 h, (f) 24 h. Peptide solutions were prepared in 1xb (pH 7.4) containing 1% HFIP. In dashed lines, I show the sums of the spectra of **2g linear** and IAPP at the corresponding incubation time. After 24 h of aging, precipitation was observed in both solutions containing IAPP and IAPP/**2g linear**, and the insoluble aggregates were resuspended to allow the CD measurements.

4.7 Interaction between 2i and IAPP followed via crosslinking

The characterization of hetero-complex formed between IAPP and **2i** was performed via cross-linking studies in combination with NuPAGE and WB by following a previously developed assay system to detect IAPP homo- and hetero-assemblies[98,127,129]. Briefly, for characterising IAPP homo-/hetero-assemblies, IAPP and IAPP/**2i** mixtures (1/1, 1/5 and 1/10) were incubated for 30 minutes, cross-linked via glutaraldehyde, and analysed via the SDS page.

At this time point, IAPP alone contained monomers and low MW oligomers (dimers, hexamers), as indicated by the bands observed at c.a 3 and 6 kDa[98] (Figure 36). In contrast, multiple hetero bands corresponding to low MW co-assemblies were observed for the excess IAPP/**2i** mixtures in the inhibiting folds. Analysis of the IAPP/**2i** mixture in 1/5 and 1/10 revealed the presence of bands between 3.5 and 10 kDa that could correspond to a hetero-dimer[127,129] or a hetero-trimer formed by one molecule of IAPP and two of **2i**. A second band was detected at circa 12 kDa, which could correspond to a heterotetramer, possibly formed by an IAPP dimeric structure stabilised by two inhibitor molecules. Bands at higher MW (15 kDa and 20 kDa) might indicate the presence of diverse multimers.

The results support the hypothesis that the interaction of **2i** with monomeric IAPP, might redirect IAPP misfolding to the formation of soluble and non-toxic heteroaggregates[98,127,129].

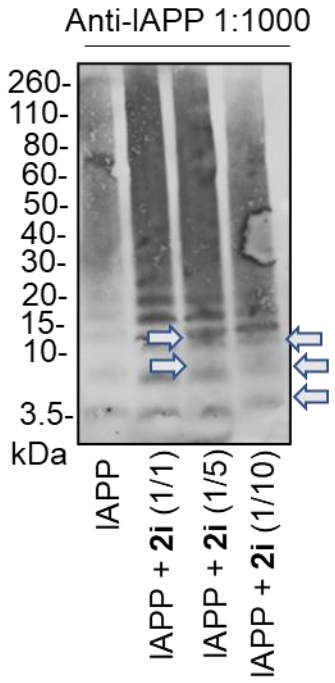

Figure 36. Characterization of hetero-assemblies of IAPP with 2i via cross-linking with glutaraldehyde, NuPAGE, and Western blot (WB) with anti-IAPP antibody. Characterization of 30 minutes aged IAPP with various molar ratios of **2i** was characterised via cross-linking, NuPAGE and Western blot with anti-IAPP antibody. Incubations of IAPP (30 μM) and IAPP/**2i** (1/1; 1/5, 1/10) were prepared in 1xb (pH 7.4) containing 1% HFIP. A representative gel (n=3) is shown, see Appendix Figure A25.

4.8 Identification of IAPP regions that mediate its interaction with 2i

To identify the IAPP regions involved in its interaction with **Fluos-2i**, peptide arrays consisting of glass slides containing 10-residue IAPP peptide sequences were used. The decamers covered full-length IAPP and were positionally shifted by one residue, as previously done by Andreetto et al. (34).

Incubation with **Fluos-2i** revealed one cluster of 5 consecutive IAPP binding segments, corresponding to IAPP(7-20) (Figure 37). The "binding core", corresponding to the common sequence of all five binding segments, was IAPP(11-16) or RLANFL, which is one of the regions suggested to be involved in IAPP self-assembly and cross-talking with Aβ40(42)[28,98,100,137].

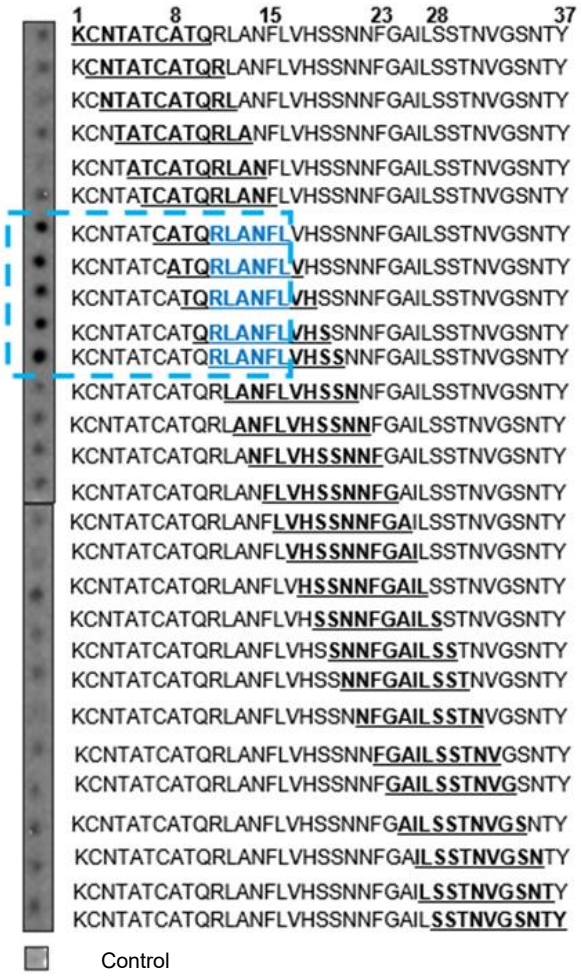

Figure 37. Identification of IAPP segments that bind Fluos-2i using peptide microarrays. Glass slides with synthetic IAPP decamers (bold) consisting of overlapping IAPP sequences (bold) incubated for 12 h at 8° C with **Fluos-2i** (1 µM) prepared in 1% BSA in TBS-T (w/v) are shown; the visualisation was performed by fluorescence. Dashed blue line frames underline identified **Fluos-2i** binding clusters; IAPP "binding cores", or common residues between consecutive binding regions, are indicated as blue letters (results representative from 3 membranes, see Appendix Figure A26).

4.9 Interactions and effects of 2i on IAPP oligomers (oIAPP) and fibrils (fIAPP)

4.9.1 Identification of oIAPP

The amyloid formation process, also in the case of IAPP, can be described as a sequence of transitions through different conformational states in equilibrium with each other[33,57]. At first, a relatively small number of monomers form highly disordered, unstable clusters that may easily dissociate, as only weak intermolecular interactions are involved in their formation. However, when the association and the growing phase continue, these aggregates can form more bulky, compact, and stable species that reorganise in β-sheet structures, eventually developing into mature, well-defined, and highly structured fibrils[33,34,171–173].

Notably, several recent studies underlined how early-stage amyloid oligomers could mediate a higher cytotoxic effect when compared to already-formed fibrils, indicating these species as an essential target for inhibiting amyloid pathogenic development [46,47,53,174–177].

In this work, the facts that IAPP oligomers do not bind ThT[178], are immunoreactive towards the specific antibody A11[52], are cytotoxic and non-amyloid-like[177] were used to establish a method to detect their presence through a combination of different techniques, including dot blot (DB) analysis with (anti-)oligomer A11 polyclonal antibody, MTT reduction assay, ThT binding assay and TEM imaging[127].

ThT studies confirmed that IAPP species bind only weakly ThT in the first 6 h of aging (Figure 38a). This result suggests that IAPP aggregates formed within these time points lack the typical β-sheet structure characteristic of amyloid fibrils, which binds ThT[58,131,132]. The development into amyloid fibrils occurs after 24 h of aging, as indicated by the increase of ThT fluorescence at this time point (Figure 38a). MTT studies revealed that the species formed during the IAPP lag phase are more cytotoxic than IAPP monomers (Figure 38b), even though the fibrils displayed the highest cell-damaging effect.

DB studies revealed that the IAPP population changes over time. Strong A11 immunoreactivity was observed in IAPP incubations aged for 1 h and 3 h (Fig.38c), whereas only a weak signal was observed in incubations of IAPP at 0 h or later time points. The results suggest that monomeric IAPP (0 h) contains only tiny amounts of A11-reactive IAPP species, at their maximum between 1 and 3 h. The lack of signal observed for the following time of incubations suggests that at later time points, the A11 reactive IAPP oligomers develop into insoluble amyloid fibrils, which are not recognised by the antibody.

TEM analysis (Figure 38d) confirmed that IAPP monomers (0 h) and A11 reactive IAPP aggregates identified within 1 and 3 h are structurally unordered. In contrast, the presence of typical amyloid fibrils was confirmed at later time points.

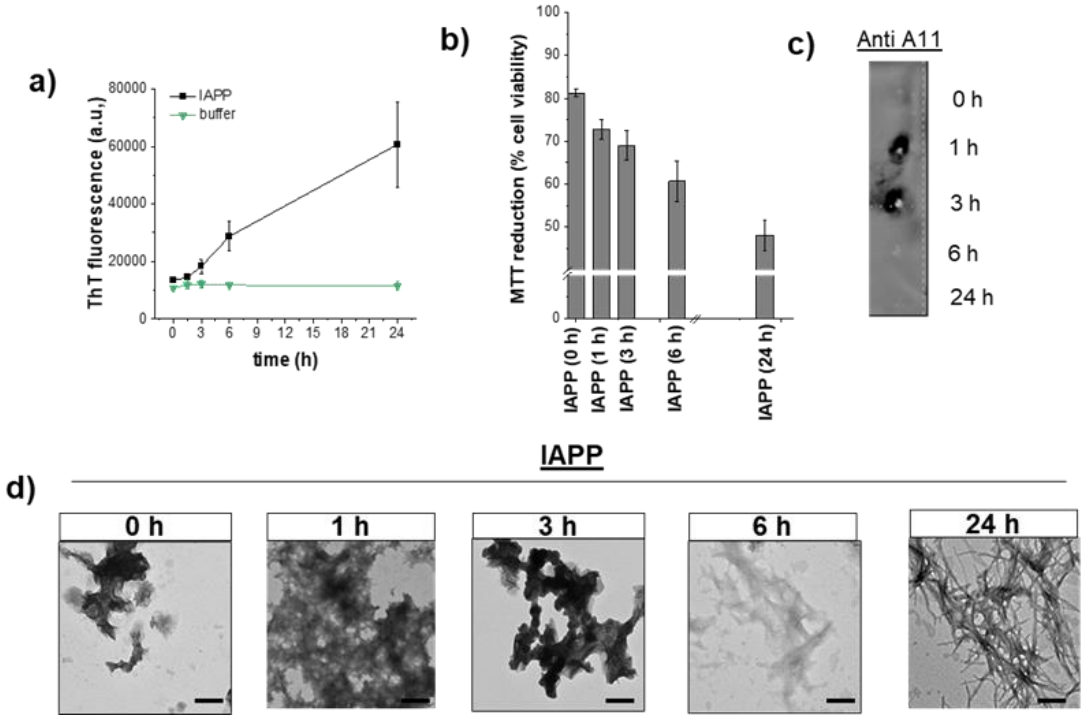

Figure 38. Identification of oligomeric IAPP species based on their amyloidogenicity, cytotoxicity and A11 immunoreactivity. IAPP (12 μM) incubations were prepared in IAPP ThT buffer containing 0.5% HFIP and aged at 20ºC. (a) The kinetics of the amyloid assembly was followed via ThT assay, and no or limited binding was detected in the first 3 h (means (±SD) 3 assays). (b) MTT reduction assays performed with aliquots from (a) on RIN-5mf (1 μM on the cells, (means (±SD) 3 assays n=3 each)) revealed increased cytotoxicity over time. (c) DB analysis of IAPP solutions aged for different time points (oIAPP, 0.5 μg) with (anti-)oligomer A11 polyclonal antibody confirmed the presence of immunoreactive species between 1 and 3 h of aging. A representative membrane (n=4, see Appendix Figure A27) is shown. The presence of IAPP on the membrane was confirmed by anti-IAPP antibody detection (n=3, see Appendix Figure A28). (d) The IAPP assemblies were morphologically characterised via TEM imaging (scale bars, 100 nm).

4.9.2 Comparison of the affinity of 2i for mIAPP, oIAPP and fIAPP

DB studies were used to characterise the binding affinities of **Fluos-2i** to monomeric (mIAPP), oligomeric (oIAPP), or fibrillar IAPP (fIAPP). Of note, evidence of the binding affinity of **Fluos-2i** for monomeric IAPP was previously given by the fluorescence spectroscopy studies, as shown in Figure 29.

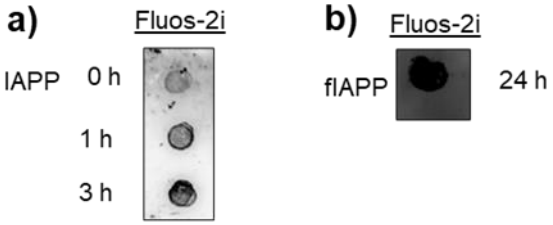

Figure 39. DB analysis shows that Fluos-2i binds to different aggregate states of IAPP. (a) IAPP incubations (12 μM) were prepared in IAPP ThT buffer containing 0.5% HFIP and aged at 20ºC. At the indicated time points, peptide aliquots were spotted on a DB membrane (1 μg). **Fluos-2i** solution was prepared in IAPP ThT buffer containing 0.5% HFIP (2 μM). Membranes were incubated in **Fluos-2i** solutions for 12 h at 8ºC. **Fluos-2i** binds monomeric (0 h), oligomeric (1 and 3 h) and fibrillar IAPP (24 h). A representative membrane is shown ((a) n=2, see Appendix Figure A29, (b) n=3, see Appendix Figure A30). The autofluorescence of fIAPP was controlled before incubation with **Fluos-2i** (see Appendix Figure A31).

The experiments were performed by aging IAPP solutions for the indicated time points, allowing the formation of monomers (0 h), oligomers (1 and 3 h) and fibrils (24 h). Aliquots

of the incubations were spotted on cellulose membranes and then incubated with a solution of **Fluos-2i**.

As shown in Figure 39, the results indicate that **Fluos-2i** binds IAPP monomers, oligomers, and fibrils with increasing affinity. Noteworthy, the affinity for IAPP fibrils was stronger than for the other species; thus, the analysis was performed on two different membranes (Appendix Figure A33).

4.9.3 Effects of 2i on the formation of oIAPP

To answer the question of whether **2i** inhibits the formation of oligomeric IAPP, the presence of oIAPP in mixtures of IAPP and **2i** in 10-fold excess was investigated by DB analysis with (anti-)oligomer A11 polyclonal antibody detection, MTT reduction assay, ThT binding assay and TEM imaging (Figure 40).

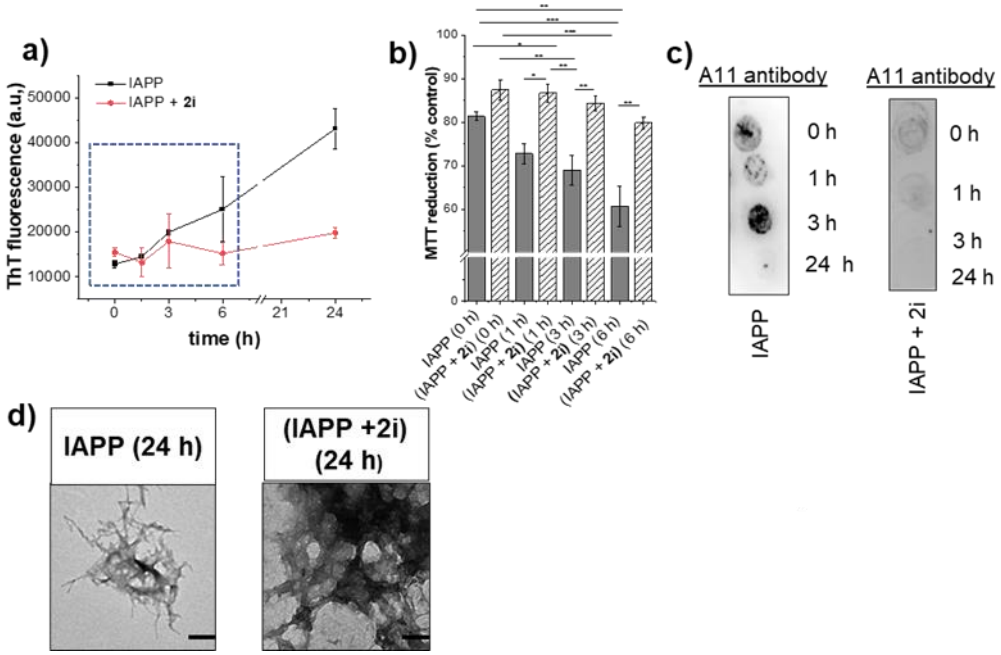

Figure 40. Effect of 2i on oIAPP formation. IAPP (12 µM) was prepared in IAPP ThT buffer containing 0.5% HFIP and aged at 20ºC. (a) The kinetics of IAPP self-assembly in the presence of **2i** (IAPP/**2i,** 1/10) was followed via ThT binding (means (±SD) 3 assays). (b) Cytotoxicity studies on RIN-5mf cells revealed that **2i** effectively suppresses the cell damage mediated by oIAPP (1 µM on the cells (means (±SD) 3 assays, n=3 each). (c) Dot blot analysis of peptide aliquots from (a) shows that **2i** suppresses the immunoreactivity of oIAPP. A membrane showing oIAPP reactivity in the same conditions is shown for comparison. Representative membranes (**2i**/IAPP n=3, see Appendix Figure A32, IAPP n=4, see Appendix Figure A27) are shown. The presence of IAPP in membranes containing IAPP/**2i** mixtures was assessed via DB with anti-IAPP detection (n=3, see Appendix Figure A33). (d) TEM pictures of peptide aliquots from (a) aged 24 h are shown (scale bar, 100 nm).

As expected from the studies on the effect of **2i** on mIAPP amyloid formation and cytotoxicity (Figure 27d and Figure 28b,c), the ThT binding assay confirmed that the mixture of mIAPP and **2i** is not amyloidogenic (Figure 40a). Cytotoxicity studies performed with mIAPP/**2i** mixtures aged between 0 h and 6 h showed that cell damage was significantly reduced in the presence of the inhibitor (Figure 40b). The DB studies indicated that **2i** in 10-fold excess either inhibits the formation of oIAPP or shields the antibody's binding site, as no immunoreactivity was detected (Figure 40c). Finally, TEM imaging of IAPP/**2i** mixtures

aged 24 h revealed the presence of highly structured aggregates, which do not resemble IAPP fibrils (Figure 40d).

4.9.4 Effects of 2i on preformed oIAPP

A combination of ThT, MTT, DB and TEM studies revealed the presence of cytotoxic and A11-immunoreactive oIAPP within 1 and 3 h of aging (chapter 4.9.1, Figure 38). Further studies on the development of oIAPP upon incubation of monomeric IAPP with **2i** revealed that the MIM effectively suppresses oIAPP formation and cytotoxic effect (Chapter 4.9.3, Figure 40). These observations raised two questions: a) Does **2i** block the development of preformed oIAPP? And if so, b) is there any difference in its inhibitory potential depending on the oligomerisation state of IAPP?

Effect of 2i on oIAPP formed after 1 h of aging.

To study whether **2i** influences the growth of IAPP oligomers, 1 h aged IAPP was incubated with **2i** in 10-fold excess. The effects of **2i** on oIAPP cytotoxicity and development into fibrils were characterised by ThT binding assay combined with DB with (anti-)oligomer A11 polyclonal antibody detection, MTT reduction assay and TEM (Figure 41).

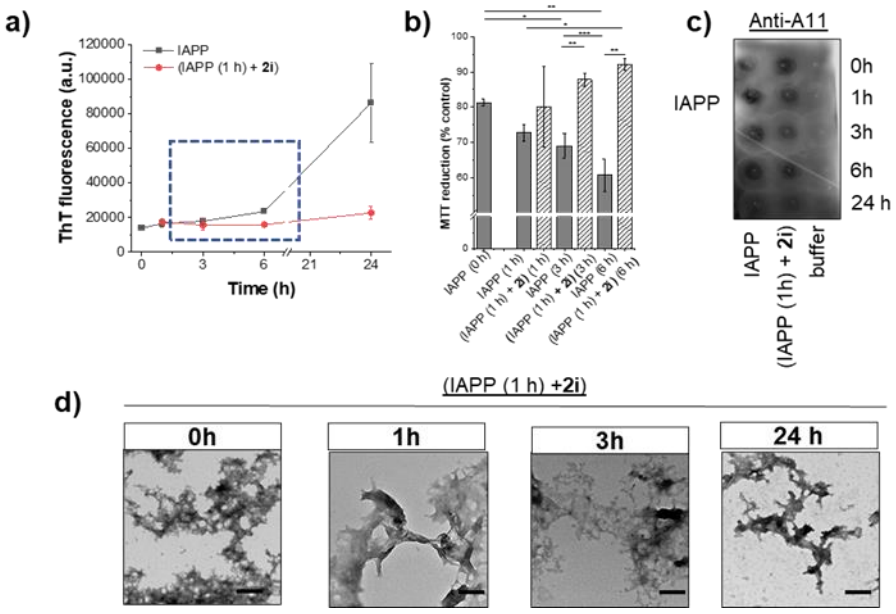

Figure 41. Effect of 2i on oIAPP species formed at early steps of the nucleation process. IAPP (12 µM) was prepared in IAPP ThT buffer containing 0.5% HFIP and aged at 20ºC. (a) The effect of **2i** (10-fold) on IAPP fibrillation when added to preformed oIAPP (1 h) as determined by ThT binding assay (means (±SD) 3 assays) is shown. (b) Cytotoxicity studies performed with incubations from (a) revealed that **2i** effectively suppresses the cytotoxicity mediated by oIAPP aged 1 h (1 µM on the cells, (means (±SD) 3 assays, n=3 each)). (c) DB analysis with (anti-)oligomer A11 polyclonal antibody of peptide aliquots from (a) shows that **2i** reduces the immunoreactivity of oIAPP. A representative membrane (n=2, see Appendix Figure A34) is shown. The presence of IAPP in IAPP/**2i** mixtures was confirmed via anti-IAPP detection (n=2, see Appendix Figure A35). (d) TEM pictures of aliquots from (a) show the complex's morphology formed at different incubation times (scale bar, 100 nm).

ThT binding studies revealed that the heterocomplexes formed between oIAPP solution aged for 1 h and **2i** do not bind ThT. In contrast, the increase in ThT fluorescence confirmed that oIAPP alone self-assembled into amyloid fibrils within 24 h (Figure 41a). This result suggests that **2i** might dissolve preformed oIAPP or redirects its amyloid assembly to off-pathway

species Cytotoxicity studies showed that oIAPP/**2i** mixtures were non-cytotoxic (Figure 41b), indicating that the interactions between the two peptides suppressed the cell damage mediated by oIAPP. DB studies revealed that hetero-complexes formed between oIAPP (1 h) and **2i** (10-fold) were less A11-immunoreactive than oIAPP alone (Figure 41c).

Effect of 2i on 3 h-aged IAPP

To confirm the previous findings, the effect of **2i** was tested on oIAPP formed in a later aggregation stage. In this case, IAPP oligomers aged for 3 h were mixed with **2i** in 10-fold excess. The effect on IAPP amyloid self-assembly and cytotoxicity were monitored via ThT binding assay, MTT reduction assay and TEM (Figure 42).

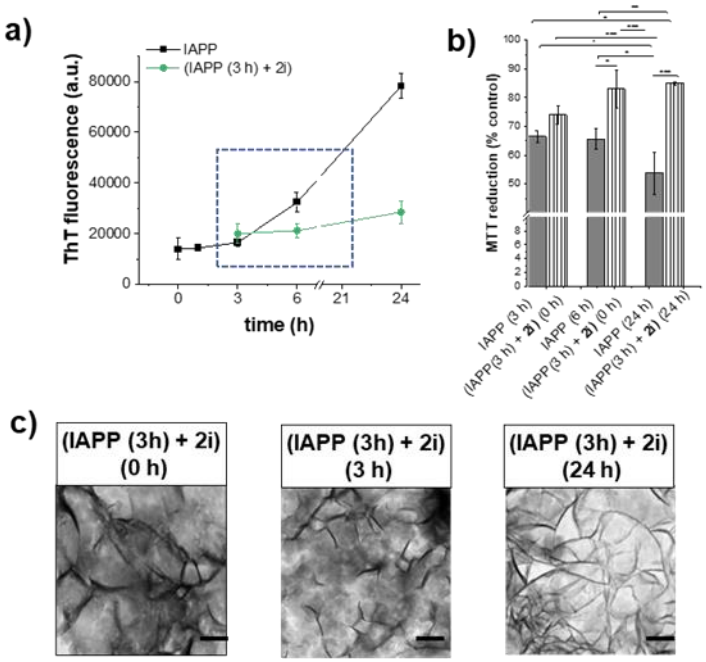

Figure 42. Effects of 2i on oIAPP species aged for 3 h. IAPP (12 μM) was prepared in IAPP ThT buffer containing 0.5% HFIP and aged at 20ºC. (a) The effect of **2i** (10-fold) on IAPP fibrillation when added to preformed oIAPP (3 h) as determined by ThT binding assay (means (±SD) 3 assays) is shown. (b) Cytotoxicity studies performed on RIN-5mf with incubations from (a) revealed that **2i** effectively blocks the cytotoxicity mediated by oIAPP aged 3 h (1 μM on the cells, (means (±SD) 3 assays, n=3 each)). (c) TEM pictures of peptide aliquots from (a) imaged after different time points of incubation (scale bar, 100 nm).

ThT studies revealed that mixtures of oIAPP (3 h) with **2i** do not bind ThT until 24 h (Figure 42a). This result suggests that adding **2i**, even at a late stage of IAPP oligomerisation, interferes with its development into amyloid fibrils. In good accordance, MTT studies revealed that mixtures of oIAPP (3h) with **2i** are significantly less toxic than oIAPP (Figure 42b). Of note, DB studies were not performed, as the A11-immunoreactivity of IAPP decreased after 3 h of aging. Surprisingly, TEM studies on incubations containing mixtures of 3 h aged oIAPP and **2i** aged for 24 h, revealed the presence of a network of highly organised fibrillar structures (Figure 42c); interestingly, these hetero-fibrils, or "needles-like structures", did not bind ThT and were not cytotoxic (Figure 42 a,b).

4.9.5 Effects of 2i on preformed IAPP fibrils (fIAPP)

To answer whether **2i** dissolves preformed IAPP fibrils, as observed for other peptides[136], IAPP fibrils (6 days aged IAPP) were incubated with **2i** in 10-fold excess. The possible effects of **2i** were followed via the ThT assay, the MTT reduction assay and TEM (Figure 43).

Figure 43a shows that the ThT binding of fIAPP after co-incubation with **2i** decreases steadily within 7 days of incubation. However, an unexpected increase of ThT binding was observed in incubations containing IAPP alone, and this might be due to the vigorous agitation that was applied to collect the fibrils. For this reason, the ThT results can be considered only preliminary. MTT reduction assays performed 7 days after co-incubating fIAPP and **2i** revealed that the cytotoxicity observed in cells treated with IAPP fibrils was significantly reduced in the presence of the inhibitor (Figure 43b). Finally, the analysis of TEM grids prepared at the end of the experiment confirmed the presence of typical amyloid fibrils for the sample containing IAPP alone and showed amorphous aggregates mixed with fibrils for the IAPP/**2i** mixture.

These findings support the hypothesis that **2i** might effectively interact with different IAPP species and remodel or disaggregate preformed IAPP fibrils and cytotoxic oligomers. These results indicate that **2i** might disaggregate, remodel, or coat preformed IAPP fibrils, diminishing their cytotoxic potential[136].

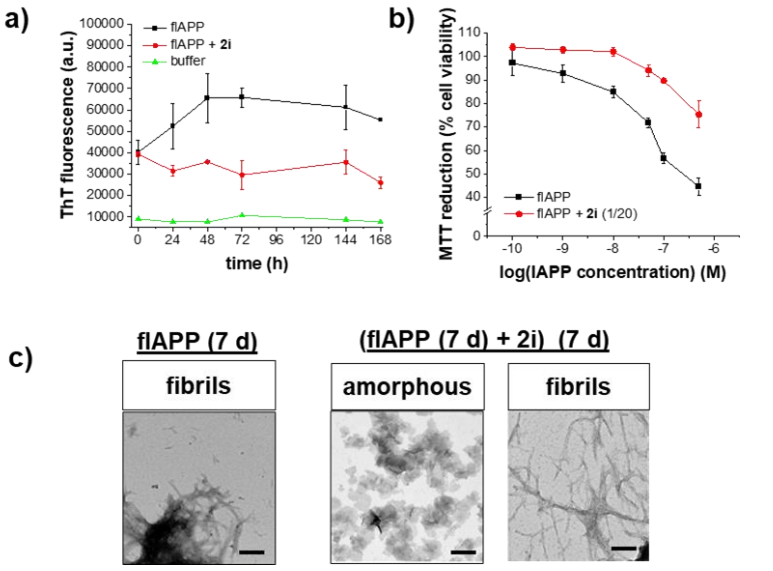

Figure 43. Effect of 2i on preformed IAPP fibrils. IAPP (12 µM) was prepared in IAPP ThT buffer containing 0.5% HFIP, aged at 20ºC for 6 days and mixed with **2i**. (a) Effect of **2i** (20-fold) when added to preformed fIAPP (6 d) as determined by ThT binding assay (means (±SD) 3 assays). (b) Cytotoxicity studies performed on RIN-5mf with incubations from (a) after 7 days of aging (means (±SD) 3 assays, n=3 each)). (c) TEM pictures of peptide aliquots from (a) after 7 days of incubation (scale bar, 100 nm).

4.10 Activity of MIMs and linear precursors on Aβ42 fibrillogenesis and cytotoxicity

After studying the effects of MIMs on IAPP fibrillation and cytotoxicity, their possible effects on Aβ42 amyloid formation and cell damage were investigated. These studies aimed to understand whether the minimal IAPP elements, included in self- and cross-interaction regions of IAPP full sequence, are sufficient to suppress Aβ42 amyloid formation. This effect was previously observed for other classes of amyloid inhibitors based on this concept design[98,99].

The first question addressed in this part was whether MIMs could inhibit the amylogenesis of Aβ42 monomers (mAβ42). As done for IAPP-related studies (Chapter 4.4), the formation of amyloid fibrils in incubations prepared with mAβ42 alone and in a mixture with the inhibitors was followed via ThT binding assay (Figure 44a-d, left panels)[127]. The formation of Aβ42 amyloid was detected after a lag phase of 90 minutes, as indicated by the strong increase in fluorescence observed after this time point[127]. Similarly, ThT studies on incubations containing Aβ42/MIMs mixture (1/0.1-1/2) revealed an increase of ThT fluorescence comparable to that of Aβ42 alone and no effects on its lag phase (Figure 44a-d, left panels). Conversely, ThT studies on incubations of Aβ42 and MIMs in 5- and 10-fold excess revealed suppression of Aβ42 fibrillation until 6 days (Figure 44a-d, left panels, and Figure 45a). The results indicate that MIMs inhibit Aβ42 fibril formation in a concentration-dependent fashion, as observed for IAPP.

Cytotoxicity studies were pursued by performing the MTT reduction assay, carried out by administering stepwise dilutions of peptide incubations to PC-12 cells (Figure 44a-d, right panel). To the ThT findings, the cell-viability studies confirmed the concentration-dependent inhibitory effect of MIMs. In fact, incubations of mixtures of Aβ42/MIMs (1/5 and 1/10) entirely suppressed Aβ42 cytotoxicity. In contrast, no or weak effect was observed for mixtures of Aβ42/MIMs at lower molar ratios (Figure 44a-d, right panels, and Figure 45d-g). To determine IC_{50} values, Aβ42 (500 nM) was titrated with various amounts of peptides and the cell-damaging effects were determined using 6 d-aged solutions (Figure 45d-e). The cytotoxicity studies yielded IC_{50} values in the sub-micromolar range (Table 25). The results suggest that even if their inhibitory activity towards IAPP is stronger, MIMs are potent suppressors of Aβ42 amyloid formation and cytotoxicity.

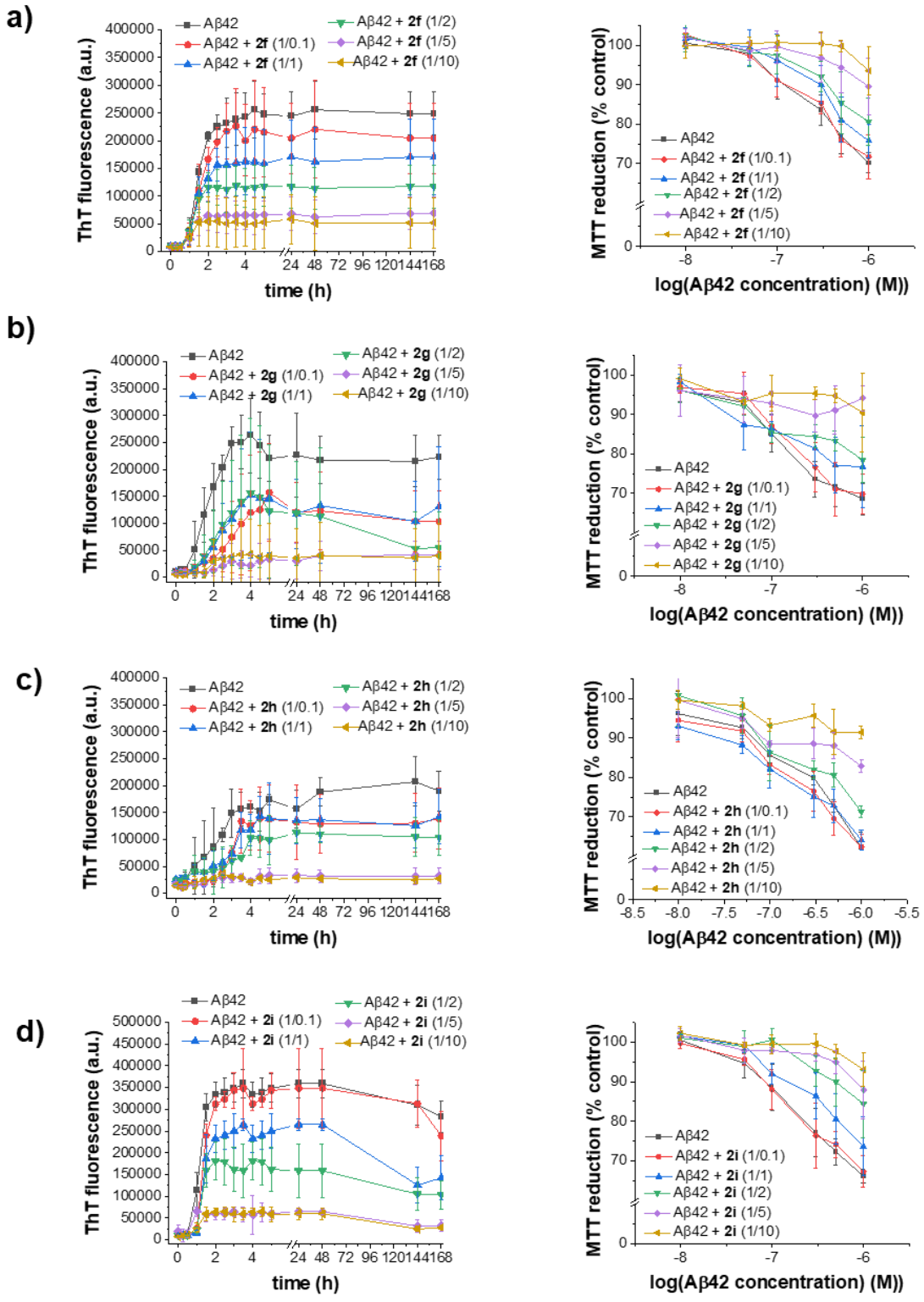

Figure 44. Concentration-dependent effect of MIMs on the amyloid self-assembly and mediated cytotoxicity of Aβ42. Left panels (a-d) effects of (a) **2f**, (b) **2g**, (c) **2h**, and (d) **2i** on Aβ42 self-assembly as determined by ThT binding assay (Aβ42/MIMs 1/0.1-1/10) (means (±SD) 3 assays (n=3 each), see Appendix Figures A36, A39, A42, A45). Incubations were prepared using SEC-disaggregated Aβ42 (5 μM) in Aβ42 ThT buffer and aged at 37ºC under shaking conditions for the first 5 h. The incubations were kept at the same temperature and without shaking for the rest of the experiment. Right panels (a-d) show the effect of MIMs on Aβ42 mediated cytotoxicity on PC-12 cells after 6-days of incubation, as determined via MTT reduction assay (Aβ42/MIMs (1/.01-1/10)) (means (+SD), 3 assays (n=3 each); for single assays see Appendix Figures A37, A40, A43, A46).

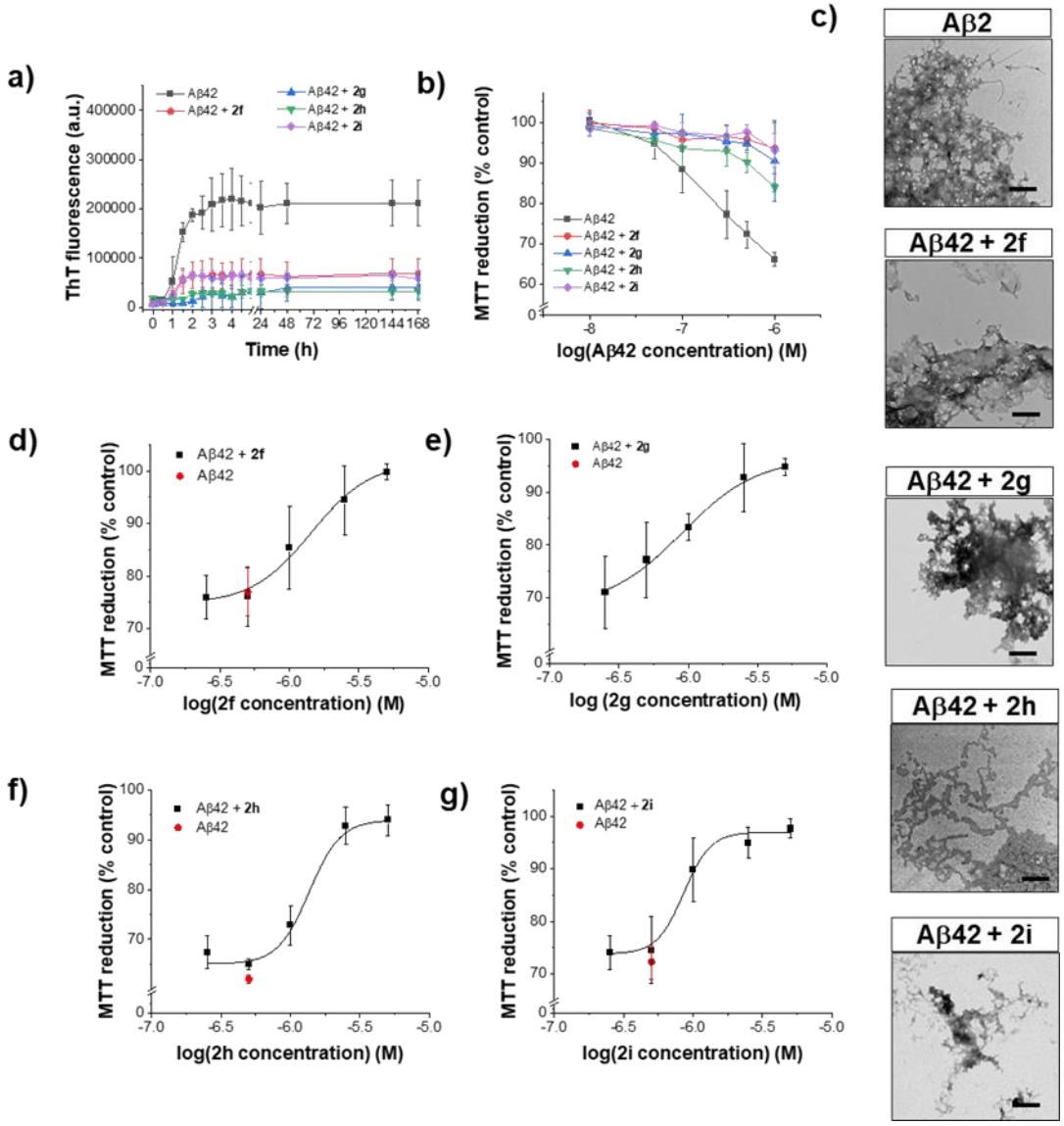

Figure 45. MIMs suppress Aβ42 amyloid self-assembly and cytotoxicity. (a) Aβ42 fibrillation was followed by ThT binding assay (Aβ42/peptide 1/5) (means (±SD), 3 assays). Peptide mixtures were prepared using SEC-disaggregated Aβ42 (5 μM) in Aβ42 ThT buffer and aged at 37ºC under shaking conditions for the first 5 h. (b) **2f**, **2g**, **2h** and **2i** blocked the cell-damage of Aβ42 fibrils (6-day-aged solutions) on PC-12 cells as determined by the MTT reduction assay (Aβ42/ MIMs (1/5)) (means ((±S D), 3 assays (n=3 each)). (c) Incubations from (b) were morphologically characterised via TEM (scale bars, 100 nm). (d-f) IC_{50} values of inhibitory effects of MIMs on the formation of cell-damaging Aβ42 amyloid assemblies were obtained by administering to PC12 cells aged solutions (6 d) of Aβ42 alone (500 nM) or in mixtures with different amounts of MIMs. Cell damage was determined by the MTT reduction assay for mixtures of Aβ42 with **2f** (c), **2g (d)**, **2h** (e), and **2i** (f), as indicated; cytotoxicity of Aβ42 alone is included in each graph for comparison (red symbol). Data and determined IC_{50} values (Table 25) are means (±SD) from 3 independent assays (n=3). For the single assays, see Appendix Figures A38, A41, A44, and A46.

Next, the linear precursors' possible activity on Aβ42 amyloid self-assembly was investigated. These studies were pursued to understand the contribution of the head-to-tail cyclisation and whether the primary sequences of MIMs, containing the four IAPP-residues critical for its self- and cross-interaction, was sufficient to display an inhibitory effect towards

Aβ amyloid assembly. ThT results revealed that the precursors **2f linear**, **2g linear** and **2i linear** did not suppress Aβ42 amyloidogenesis up to 50-fold excess (Figure 46a,c,d).

Table 25. IC_{50} values of inhibitory effects of MIMs on Aβ42-mediated cell damage after 6 days of co-incubation[a]

MIMs	IC_{50} (±SD) (nM)[a]
2f	1060 (±208)
2g	998 (±119)
2h	1361 (±347)
2i	678 (±157)

[a] IC_{50}s, means (±SD) from 3 titration assays (n=3 each, Aβ42, 500 nM).
For the single experiments, see Appendix Figures A38 (**2f**), A41 (**2g**), A44 (**2h**), A47 (**2i**).

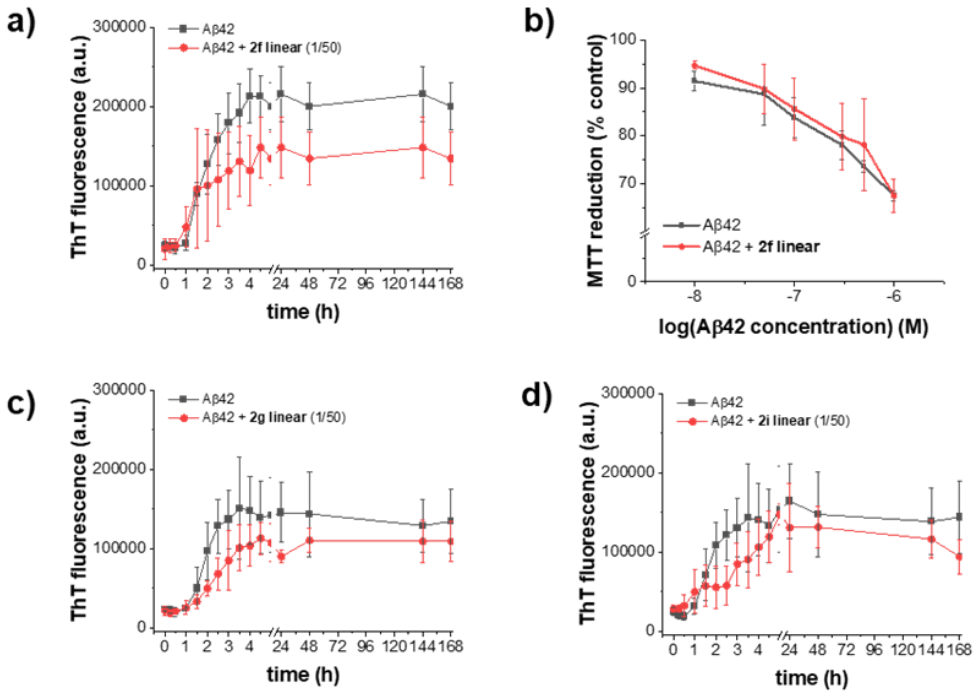

Figure 46. Inhibitory potential of 2f linear, 2g linear, and 2i linear towards Aβ42 fibrils formation 50-fold excess. Effect of (a) **2f linear**, (c) **2g linear** and (d) **2i linear** on Aβ42 amyloid assembly, as determined by ThT binding assay (Aβ42/peptide 1/50) (means (±SD), 3 assays (n=3 each)). Peptide incubations were prepared using SEC-disaggregated Aβ42 (5 µM) in Aβ42 ThT buffer and aged at 37ºC under shaking conditions for the first 5 h. (b) Cell viability studies were performed with Aβ42/**2f linear** incubations on PC-12 cells after 6 days of incubation (means (± SD), 3 assays (n=3 each)).

By these findings, MTT reduction assays performed after 6 days of incubation showed that **2f linear** in 50-fold excess did not interfere with Aβ42 cell damage (Figure 46b). Taken

together, the results confirmed that the cyclisation confers to the class 10 times more potency, possibly stabilising a specific conformation able to interfere with Aβ42 amyloid assembly.

4.11 Determination of binding affinities towards monomeric Aβ42 (mAβ42)

Fluorescence spectroscopy studies were performed to understand whether MIMs may display their potent anti-amyloidogenic activity towards Aβ42 by interacting with Aβ42 monomers. Such a hypothesis was supported by the findings obtained from characterising the mIAPP/MIMs interaction (Figure 30).

According to previously established protocols[28], monomeric N^{α}-FITC-labelled Aβ42 (5 μM) was titrated with increasing MIMs amounts (Figure 47). Increased amounts of titrants resulted in enhanced fluorescence intensity at 522 nm (Figure 30a-d, left panels) triggered by the binding interaction. The fluorescence increased between 59% and 85% of FITC-Aβ42, as reported in Table 26. Sigmoidal titration curves were obtained and were consistent with the cooperative self-assembly process[28,136]. However, due to the strong self-assembly propensity of the peptides, other models than a monomer-monomer interaction might be applicable as well[28,98]. As reported in Table 26, the app. K_D values fell in the mid- to the low-nanomolar range, indicating that MIMs bind monomeric FITC-Aβ42 with high affinity.

As a proof of concept, the binding affinities of the linear precursors to FITC-Aβ42 were also quantified. Based on the ThT studies (Figure 46) showing a lack of inhibitor potential, lower binding affinities were expected. Figure 48 shows titrations of synthetic FITC-Aβ42 (5 nM) with increasing amounts of **2g linear** and **2i linear.** As expected, the study revealed weak binding, as no upper plateau of the titration curve was reached. This result indicates that the app. K_Ds of Aβ42/linear precursors interaction might fall within 1 and 5 μM. The increase in fluorescence observed when the titrants were added in 250- or 500-fold excess indicates that the linear precursors are between 25- and 50- times weaker ligands than their cyclised analogues.

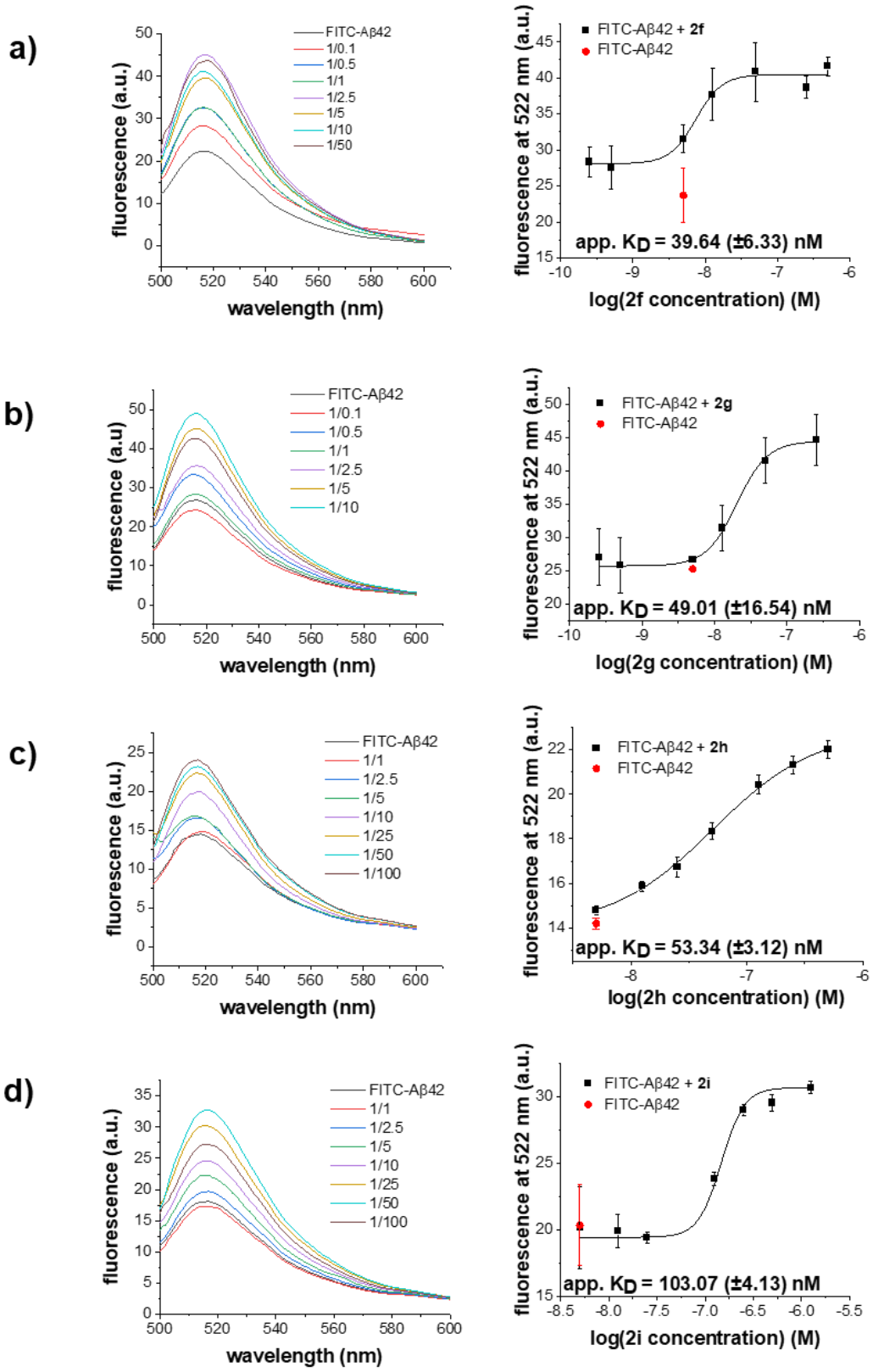

Figure 47. Determination of app. K_Ds of the interaction of MIMs with Aβ42 by fluorescence titrations. Left panels (a-d) show fluorescence emission spectra of FITC-Aβ42 (5 nM) alone or with various amounts of (a) **2f**, (b) **2g**, (c) **2h**, and (d) **2i**. The molar excess of FITC-Aβ42/MIMs is indicated. Right panels (a-d) show the binding curves of (a) **2f**, (b) **2g**, (c) **2h** and (d) **2i**. App. K_Ds are means (±SD) from 3 binding curves (FITC-Aβ42, 5nM). Measurements were performed in 1×b (pH 7.4) containing 1% HFIP.

.

Table 26. IC_{50} values of inhibitory effects of MIMs on Aβ42-mediated cell damage[a] after 6 days of co-incubation, app. K_Ds of MIMs/Aβ42 interactions and % of Fluorescence increase[b][c] [d].

MIMs	IC_{50} (±SD)(nM)[a]	app. K_D (±SD) (nM)[b][c]	Fluorescence increase (%)[d]
2f	1060 (±208)	39.64 (±6.33)	85
2g	998 (±120)	49.01 (±16.54)	66
2h	1361 (±347)	53.34 (±3.12)	54
2i	678.14 (±157)	103.07 (±4.13)	59

[a] IC_{50}s, means (±SD) from 3 titration assays (n=3 each, Aβ42, 500 nM)
[b] Determined by titrations of N-terminal FITC-labelled Aβ42 (5 nM; pH 7.4) with MIMs (Figure 47).
[c] App. K_Ds are means (±SD) from three binding curves
[d] compared to the values of FITC-Aβ42 alone

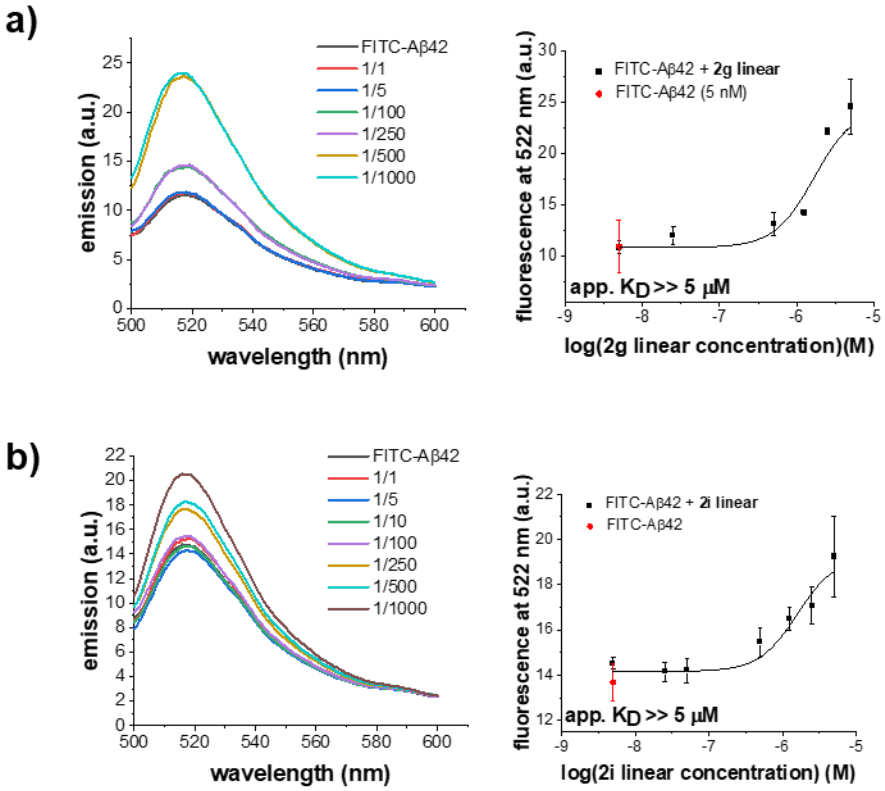

Figure 48. Determination of app. K_Ds of the interaction of linear precursors with FITC-Aβ42 via fluorescence titrations. Left panels (a-b) show fluorescence emission spectra of FITC-Aβ42 (5 nM) alone or with various amounts of (a) **2g linear** and (b) **2i linear** in 1xb (pH 7.4) containing 1% HFIP. The molar excess of FITC-Aβ42/linear precursors is indicated. Right panels (a-b) show the binding curves of (a) **2g linear** and (b) **2i linear** (mean of 3 binding curves).

4.12 Identification of Aβ42 regions that mediate its interaction with MIMs

To address which regions Aβ42 bind **Fluos-2i**, membrane-bound peptide arrays consisting of Aβ42 decamers were used [28]. The synthetic decamers covered full-length Aβ42 and were

positionally shifted by one residue (Figure 49). Incubations with **Fluos-2i** revealed two clusters of Aβ42/MIMs binding regions. The first included 3 consecutive Aβ binding segments covering Aβ(11-21). The cluster comprises a "binding core" including the segments Aβ(12-19), or VHHQKLVF. The second cluster consisted of 4 consecutive Aβ binding segments, including Aβ(25-36). The "binding core" consisted of the commonly shared sequence among the four segments Aβ(28-34) or KGAIIGL. Of note, unspecific binding due to the self-assembly of **Fluos-2i,** might have induced the strong background signal, possibly hindering additional binding regions (i.e., Aβ(35-40)). Therefore, the assay was performed with a lower peptide concentration (0.5 µM vs 1 µM) (see Appendix Figure A48b) that did not reveal significant differences.

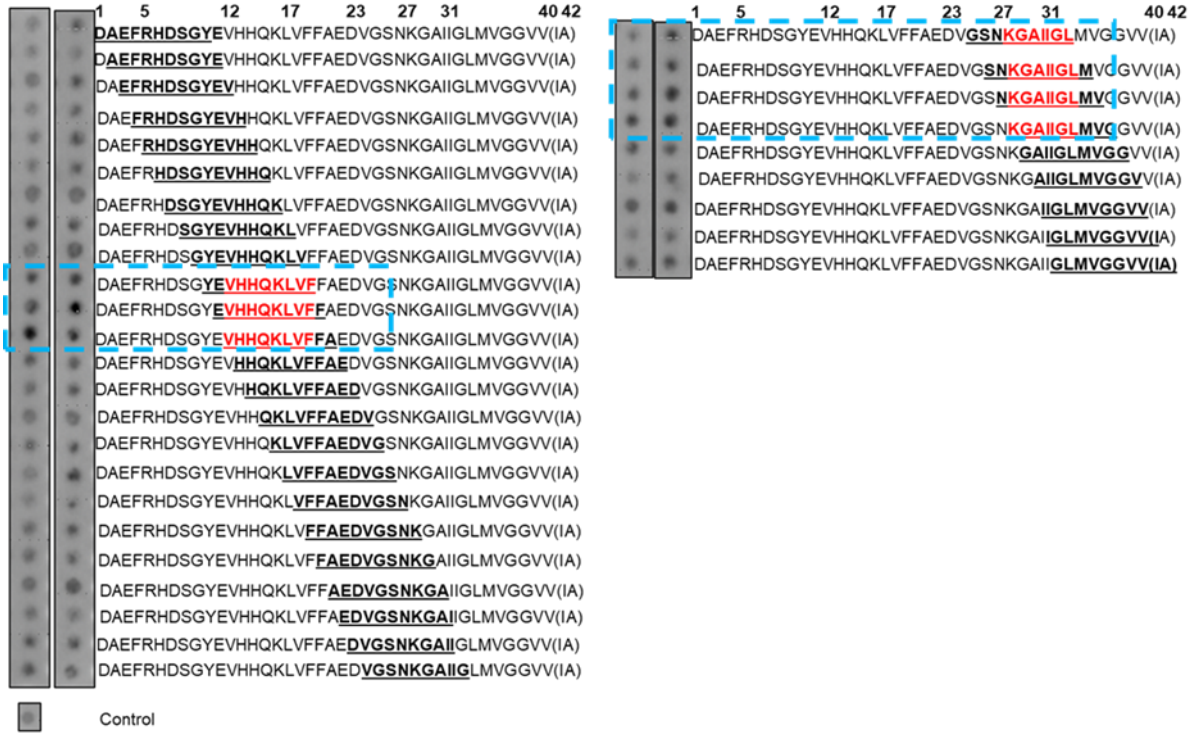

Figure 49. Identification of the regions of Aβ40(42) interacting with Fluos-2i using peptide microarrays. Glass slides with decamers consisting of overlapping Aβ42 sequences (bold) were incubated for 12 h at 8ºC with **Fluos-2i** (1 µM), prepared 1% BSA in TBS-T (w/v). Dashed blue line frames underline the identified **Fluos-2i** binding cluster, whereas the Aβ42 "binding cores" are indicated as red letters and correspond to the shared residues between binding segments (results representative from 3 assays, see Appendix Figure A48).

4.13 Interaction between MIMs and Aβ42 oligomers(oAβ42) and fibrils (fAβ42)

4.13.1 Characterization of oAβ42 and TAMRA-oAβ42

Soluble oligomers are common to most amyloids and may represent the primary neurotoxic species of Aβ40(42) in AD[52,53,55,56,177,179]. Kayed et al.[52] previously suggested that soluble amyloid oligomers from different proteins have a similar structure, which became recognized by the developed antibody A11.

In fact, Aβ42 and IAPP oligomers share some important properties, as they are mainly unordered, immunoreactive towards A11 and highly cytotoxic[41,52,127,180].

On this basis, the development of monomeric Aβ42 into cytotoxic oligomers was followed by applying the same concept and method described in 4.9.1[127]. The characterization of oAβ42 was pursued via DB analysis, TEM characterization, ThT binding and MTT reduction assays[127].

Additionally, the aggregation of N^a-terminal-5-carboxytetramethylrhodamine-Aβ42 (TAMRA-Aβ42) into cytotoxic oligomers was characterised to study whether the dye affects the amyloidogenesis of Aβ42. These experiments were carried out to understand the effect of another class of peptide inhibitors, the so-called Aβ core mimics (ACMs), on oAβ42 cytotoxicity, oAβ42-mediated impairment of hippocampal LTP, and on phagocytosis of oAβ42[127].

ThT binding studies revealed that the lag time of Aβ42 amyloid assembly is circa 90 minutes (Figure 50a), suggesting that after this time point, Aβ42 is at least partially fibrillar. The Identification of A11 immunoreactive oligomers was pursued via DB analysis (Figure 50b) and revealed the presence of oligomers in solutions containing Aβ42 or TAMRA-labelled Aβ42 within 2 and 6 h of incubation. Due to the transient nature of the species involved in the amyloidogenic process, the results of the ThT and DB studies are not in contrast[33,34,171]. MTT results confirmed that the oligomers identified via A11 detection were cytotoxic, and the cell damage mediated by Aβ42 increased with its amyloid self-assembly (Figure 50c). The cytotoxic effect of TAMRA-Aβ42 was comparable to that of unlabelled Aβ42 (Figure 50d), confirming that the label does not influence Aβ42 mediated cell damage. Finally, TEM analysis of solutions containing oligomers of TAMRA-Aβ42 and unlabelled Aβ42 (Figure 50e) confirmed the presence of largely amorphous structures after **2h** and 6 h of incubation. As expected, incubations of Aβ42 and TAMRA-Aβ42 aged for 24 h contained branched and tangled fibrillar structures.

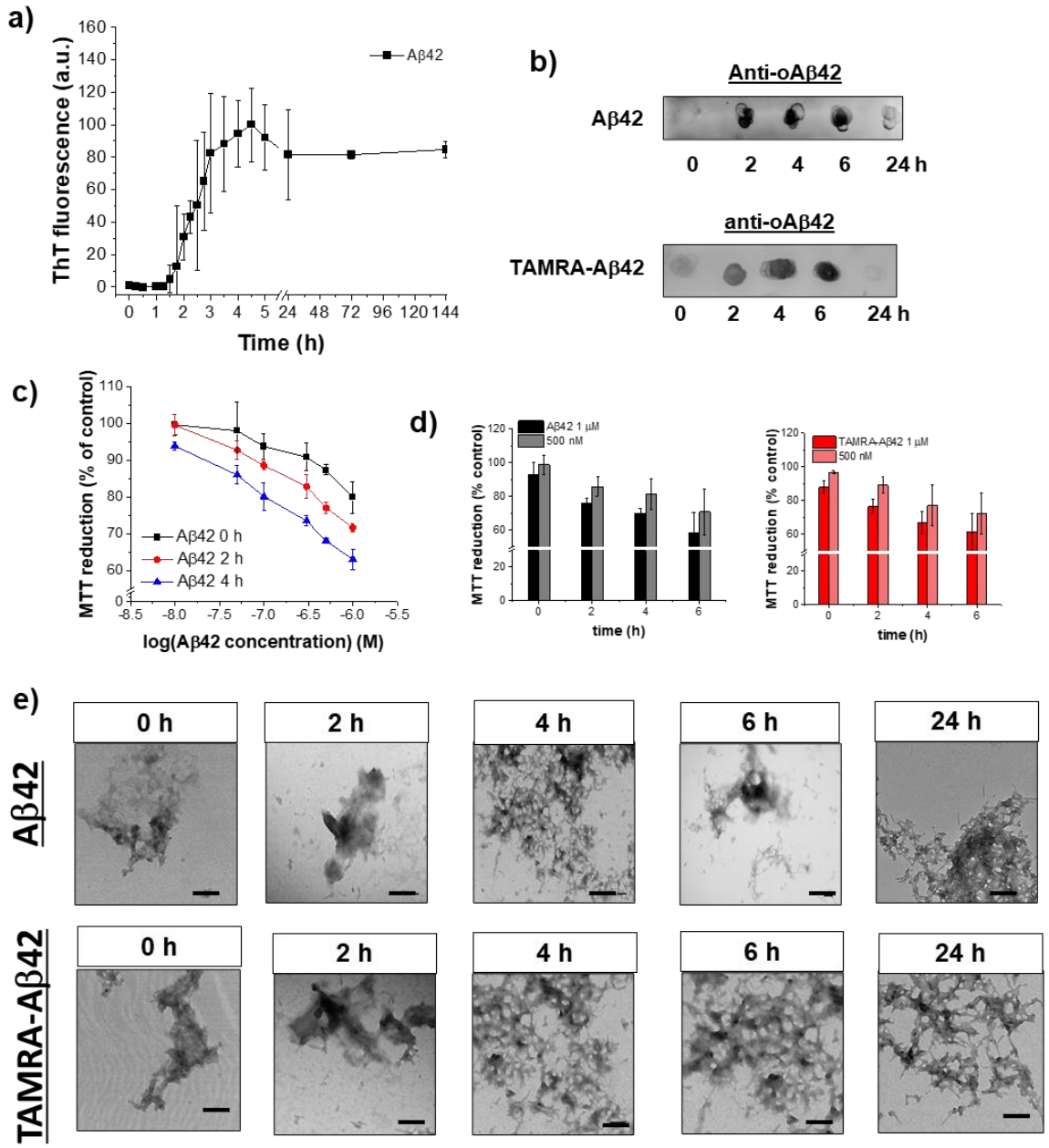

Figure 50. Identification of Aβ42 and TAMRA-Aβ42 oligomeric species through ThT binding assay, MTT reduction assay, A11 immunoreactivity, and TEM imaging. (a) The kinetics of Aβ42 amyloid assembly was followed via ThT assay, and no or limited binding was detected in the first 2 h of incubation (means (±SD), 3 assays, n=3 each) of note, monitoring the ThT binding of TAMRA-Aβ42 was not possible due to a quenching effect occurring between the dies. SEC-disaggregated Aβ42 (5 μM) was prepared in Aβ42 ThT buffer and incubated at 37°C under shaking conditions for the first 5 h of incubation. (b) DB analysis of Aβ42 with (anti-)oligomer A11 polyclonal antibody confirmed the presence of immunoreactive species between 2 and 6 h of aging, independently of the presence of the TAMRA label. One membrane per assay (n=3 for TAMRA-Aβ42, see Appendix Figure A49 n=2 for Aβ42, see Appendix Figure A50) is shown. Aβ42 Incubations were prepared as described above, whereas solutions containing TAMRA-Aβ42 were prepared in IAPP ThT buffer containing 1% HFIP and aged at 37°C under shaking conditions for the first 5 h. (c-d) MTT studies performed on PC-12 cells (means (±SD) n=3 each) revealed increased cytotoxicity of the oligomers and no effect mediated by the TAMRA label (c-d). (d) Effect of the TAMRA label on the cytotoxic effect of Aβ42 (1 μM on the cells, (means (±SD) 3 assays, n=3 each)). (d) TEM analysis shows an increased organisation of the species, shifting from amorphous assemblies to typical amyloid fibrils (scale bar, 100 nm). Part of this Figure is included in Taş et al.[127].

4.13.2 Binding of Fluos-2i to mAβ42, oAβ42, and fAβ42, as detected by DB

As the binding of MIMs to mAβ42 was confirmed via fluorescence spectroscopy titrations (Figure 47), the binding affinity of **2i** for other Aβ42 species was also assessed (Figure 51). Similarly, as for the IAPP corresponding studies (Figure 39), DB analysis was the method of choice to determine this question.

Incubations containing monomeric Aβ42 were aged for the indicated time points, allowing the development of monomers (mAβ42), oligomers Aβ42 (oAβ42) and fibrils Aβ42 (fAβ42). Aliquots of the solutions were spotted on the DB membrane at the indicated time points (Figure 51) and probed with **Fluos-2i**. The results suggest that **2i** binds Aβ42 oligomers and fibrils with increasing affinity, as observed in the case of IAPP (Figure 39).

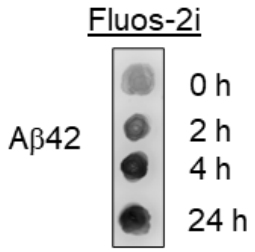

Figure 51. DB analysis shows that Fluos-2i binds to mAβ42, oAβ42 and fAβ42. SEC-disaggregated Aβ42 (11 μM), was prepared in Aβ42 ThT buffer and aged at 37°C under shaking conditions for the first 5 h. At the indicated time points, aliquots of the incubations were spotted on a DB membrane (1 μg) and probed with **Fluos-2i** (5 μM), prepared in IAPP ThT buffer containing 1% HFIP (incubation for 12 h, 8°C). The visualisation was performed by fluorescence, and one representative membrane (n=3 each, see Appendix Figure A51) is shown.

4.13.3 Effect of 2i on preformed oAβ42

Once the affinity of MIMs for oligomeric Aβ42 was confirmed, the effect of **2i** on oAβ42 cytotoxicity and fibrillation was studied. ThT binding, MTT reduction assays and TEM were used to follow Aβ42 fibrillogenesis and cell damage in the presence of **2i**.

The ThT findings indicated that **2i** (10-fold) strongly suppressed the development of preformed Aβ42 oligomers into fibril, as revealed by the lack of fluorescence increase upon **2i** addiction (Figure 52a). Interestingly, a decrease of ThT signal was observed when oAβ42 was incubated with **2i** in 20-fold excess. These results, and the lack of effect of **2i** in 5-fold effect, suggest that the inhibition occurs in a concentration-dependent fashion.

MTT studies revealed that the cytotoxicity mediated by oAβ42 after 6 days upon incubation with **2i** were entirely suppressed (Figure 52b).

Two possible scenarios can explain these findings: a) **2i** interacts with oligomeric Aβ42 and redirects it to forming off-pathway hetero-assemblies, which are non-cytotoxic and non-amyloidogenic or b) the interaction reverses the conformational transition of oAβ42, shifting the equilibrium to its monomeric state.

TEM imaging of the incubations prepared at the end of the experiment revealed the presence of highly organised structures that do not resemble either fAβ42 or mAβ42 (Figure 52c).

Such results suggest that **2i** interacts with oAβ42 and redirects its aggregation to forming non-toxic and off-pathway heteroassemblies.

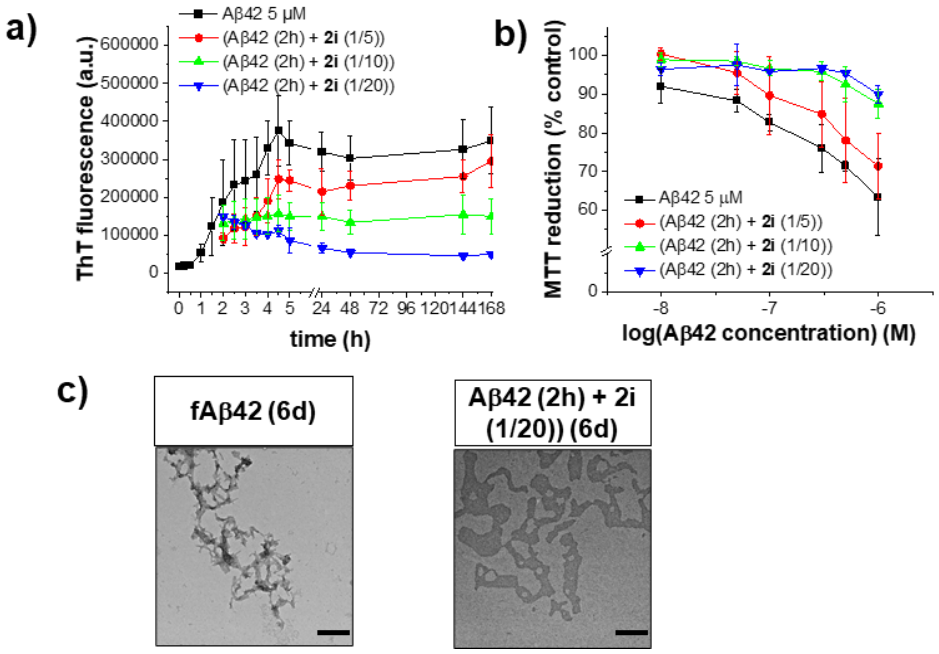

Figure 52. Effect of 2i on the amyloid assembly of Aβ42 oligomers followed via ThT binding assay, MTT reduction assay and TEM imaging. (a) Effect of **2i** addition in 5-, 10- and 20-fold excess on oAβ42 as determined via ThT binding assay ((means (±SD), 3 assays, n=3 each). SEC-disaggregated Aβ42 (11 μM) was prepared in Aβ42 ThT buffer and aged at 37°C under shaking conditions for the first 5 h. (b) Cell viability studies were performed on PC-12 cells with solutions from (a) (6-days-aged-solutions) (means (±SD)), 3 assays, n=3 each). (c) TEM images of incubations aged 6 days revealed that the hetero-complex formed between oAβ42 and **2i** in 20-fold excess is amorphous (scale bar, 100 nm).

4.13.4 Effect of 2i on preformed fAβ42

The effect of **2i** on preformed Aβ42 fibrillar species was investigated via the ThT binding assay, the MTT reduction assay, and TEM.

Aβ42 Fibrils were prepared according to the ThT protocol, and the kinetics of their formation was followed by ThT binding assay. After 6 days of aging, the fibrils were mixed with **2i**, and the possible fibril disaggregation effect was monitored via ThT. In fact, a decrease in ThT binding could correlate with a reduced fibril amount mediated by the incubation with **2i** and its disaggregation/remodelling properties. Furthermore, the effect of **2i** on fAβ42 cytotoxicity was characterised via MTT assay at different time points of incubation, whereas the effect on fAβ42 morphology was characterised via TEM.

Incubation of preformed Aβ42 fibrils with **2i** resulted in a significant decrease of ThT signal until 6 days (Figure 53a). However, the suppression of fAβ42 cell damage was observed only after 24 h of incubation and not at later time points (Fig. 53b)), as shown by the increase in cytotoxicity of fAβ42/**2i** mixtures aged for 48 h and 6 d. Taken together, this result suggests that the cytotoxic effect was possibly mediated a) by the releases of cytotoxic Aβ42 oligomers

due to the disaggregation of fAβ42 upon interaction with **2i** or b) by a further fibril elongation process, occurring after a transient interaction between fAβ42 and **2i**.

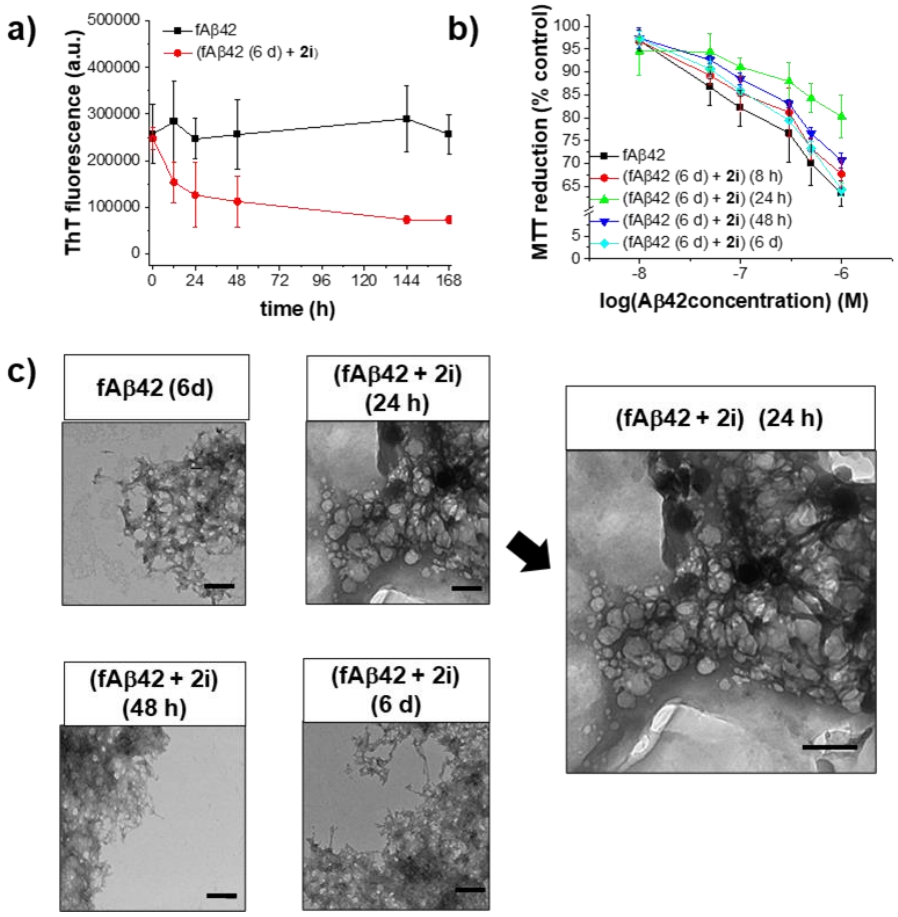

Figure 53. Effects of 2i on preformed fAβ42 as revealed via ThT and MTT assays. SEC-disaggregated Aβ42 (5 μM) was prepared in Aβ42 ThT buffer and aged for 6 days at 37°C (shaking conditions for the first 5 h, without shaking afterwards) and mixed with **2i** (20-fold). (a) Effect of **2i** on preformed fAβ42 revealed by ThT assay (means (±SD), 3 assays, n=3 each). (b) MTT assays performed on PC-12 cells at the indicated time points with incubations from (a) (means (±SD), 3 assays, n=3 each)). (c) TEM images of incubations from (a) at the indicated time points (scale bar, 100 nm), including the magnification of the sample aged for 24 h.

Figure 53c shows TEM pictures of the fAβ42 alone and fAβ42/**2i** mixtures prepared at different time points. The imaging revealed the presence of morphologically diverse species. In fact, as expected, directly after mixing fAβ42 and the inhibitor, the samples exhibited mainly the typical Aβ42 branched and highly structured fibrils in a mixture with the amorphous structures observed for **2i** alone in 100 μM (Figure 25). Circa 10% of the incubations showed a complex morphology that could not be assigned to either species (see the magnification of the sample aged for 24 h), indicating that this organised network might result from the interaction between **2i** and fAβ42. After 24 h of co-incubation, these structures increased to approximately 30% of the total analysed population, suggesting that the formation of these species is linked to decreased cytotoxicity.

4.14 Effect of MIMs on IAPP/Aβ42 self- and cross-seeding events

The interaction occurring between amyloid monomers and a fibrillar surface is a process known as secondary nucleation. This process depends a) on the presence of fibrils, which provide a catalytic template enhancing the nucleation rate, and b) on the concentration of monomers in the system, forming the nuclei on the surface of an already existing aggregate[33]. Secondary nucleation is a process responsible for a large generation of oligomers[34,56,171]. In simplified *in vitro* mechanistic studies, this phenomenon can be partially reproduced in seeding systems, in which preformed seeds catalyse the aggregation of the monomers. This event reduces the amyloid-formation process's lag phase [171].

After observing and characterising the high-affinity interactions of MIMs with diverse amyloid species, the possible effects of **2i** and **2g** on the nucleation of monomeric IAPP and Aβ42 fibrillogenesis mediated by the addition of preformed seeds was investigated. This inhibitory effect could occur through two possible mechanisms that do not exclude each other: by sequestrating the monomers, redirecting them to soluble and non-toxic heterocomplexes, and/or interacting with the preformed seeds, hence making them incompetent to act as a catalytic template.

Figures 43 and 53 showed that **2i** effectively interacts with preformed amyloid fibrils and suppresses their amyloidogenicity and cytotoxicity. These results suggested that **2i** can effectively coat or partially disaggregate preformed fibrillar species. Thus, the work to understand the effect of **2g** and **2i** on the seeding events concerned the formation of a complex formed by amyloidogenic monomeric species and inhibitor seeded by preformed amyloid fibrils.

Effect of 2i on IAPP self-seeding

The effect of **2i** on IAPP self-seeding was investigated by seeding IAPP with preformed IAPP seeds (fIAPP) and followed via ThT binding assay and TEM[127,136]. Adding preformed fibrils to IAPP monomers decreased the lag phase, as shown by the increase of ThT fluorescence observed after 6 h of coincubation (Figure 54) as ThT binding is proportional to the fibril amount in the system, a decreased lag phase accelerates the fibrillogenesis. In contrast, incubations of IAPP alone showed an enhancement of the ThT fluorescence only after 24 h of aging.

Samples prepared by seeding the complex formed between IAPP and **2i** did not bind ThT. This result suggests that **2i** suppresses the nucleation event. TEM analysis confirmed the presence of amorphous and unstructured aggregates at the end of the incubation time. The results indicate that **2i** in 10-fold excess effectively inhibits the acceleration of IAPP self-assembly catalysed by its preformed seeds. Additionally, preliminary results suggest that the peptide in 5-fold excess does not display the same effect, supporting the concentration dependency of its action.

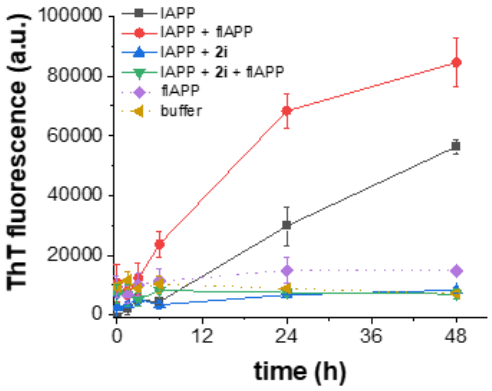

Figure 54. Effects of 2i on IAPP self-seeding. Incubations were prepared in IAPP ThT buffer containing 0.5% HFIP (pH 7.4). IAPP (12 µM) and IAPP/**2i** mixture (1/10) were seeded by adding 24 h-aged IAPP seeds (1.2 µM), prepared in the same buffer. The kinetics of IAPP aggregation was monitored via ThT binding assay (means (±SD), 3 assays). Seeds and buffers, indicated with dotted lines, were subtracted from the incubations to ensure the occurrence of the seeding event.

Effect of 2i on Aβ42 self-seeding

It has been previously reported that Aβ40(42) aggregates through a nucleation-and growth pathway, in which the formation of new aggregates occurs in part through the autocatalytic secondary nucleation on the surface of existing fibrils [181]. This study mimicked the self-seeding event by seeding monomeric Aβ42 (mAβ42) with preformed Aβ42 seeds (fAβ42). The effect of **2i** was studied by forming the mAβ42/**2i** complex and adding the seeds. The kinetics of the amyloid formation was followed via ThT binding assay. The ThT fluorescence of incubations containing monomeric Aβ42 increased after 90 minutes (Figure 55), whereas the lag-phase of samples containing seeded Aβ42 was reduced to one hour. The results indicated that **2i** in 10-fold excess completely suppresses the seeding effect mediated by fAβ42, as the ThT fluorescence was the same as that of the unseeded Aβ42/**2i** mixture. Such an effect was observed until 6 days of incubation, as shown in Figure 55. TEM analysis of incubations aged for 6 days revealed the presence of amorphous and unstructured species.

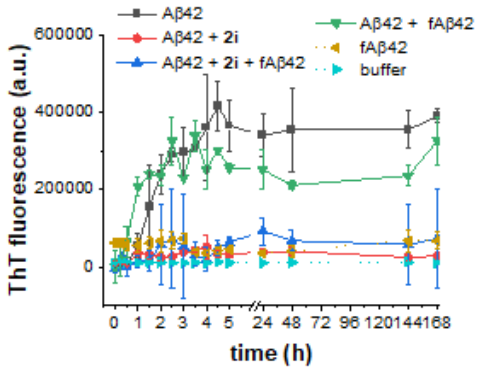

Figure 55. 2i suppresses the seeding of Aβ42 by Aβ42 fibrils. Fibrillogenesis of Aβ42 (5 µM) without or with **Figure 55. 2i suppresses the seeding of Aβ42 by fAβ42.** Fibrillogenesis of Aβ42 (5 µM) without or with fAβ42 seeds (10%) and of fAβ42-seeded Aβ42/**2i** (1/10) was followed by ThT binding (means (±SD), 3 assays). Monomeric Aβ42 (5 µM) was prepared via SEC-disaggregation in Aβ42 ThT buffer, whereas fAβ42 was prepared by aging 80 µM Aβ42 in IAPP ThT buffer containing 1% HFIP. Seeds and buffers, indicated with dotted lines, were subtracted from the incubations to ensure the occurrence of the seeding event.

Effect of 2i on IAPP cross-seeded by fAβ42

Cross-seeding events have been indicated as the molecular link between the onset of AD and T2D [29–32]. Therefore, identifying inhibitors of these pathogenic processes is essential in anti-amyloid drug development against both diseases.

The effect of **2i** on IAPP cross-seeding of fAβ42 was investigated by seeding IAPP with fAβ42 and followed via ThT binding assay and TE microscopy. The ThT binding of incubations containing seeded IAPP rapidly increased within three h of aging, indicating an earlier onset of the fibril formation than IAPP alone (Figure 56). In contrast, the complex formed by IAPP/**2i** could not be seeded by fAβ42, as shown by the lack of increase in ThT fluorescence until 48 h.

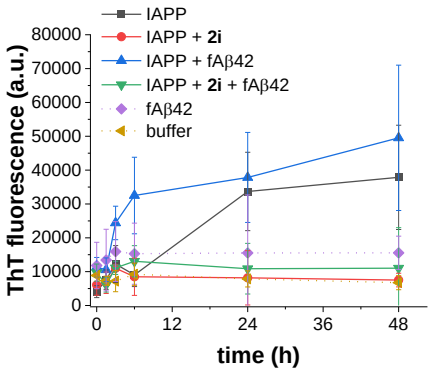

Figure 56. 2i suppresses the seeding of monomeric IAPP mediated by fAβ42. Fibrillogenesis of IAPP (12 μM) without or with fAβ42 seeds (1.2 μM) and of fAβ42-seeded IAPP/**2i** (1/10) was followed by ThT binding (means ±SD, 3 assays). All the incubations containing IAPP were prepared in IAPP ThT buffer (0.5% HFIP), whereas fAβ42 was prepared in IAPP ThT buffer (1% HFIP) at a concentration of 88 μM aged for one week. Seeds and buffers, indicated with dotted lines, were subtracted from the incubations to ensure the occurrence of the seeding event.

Effect of 2g and 2i on Aβ42 cross-seeded by fIAPP

The effect of **2g** and **2i** on monomeric Aβ42 cross-seeded by fIAPP seeds was investigated by incubating Aβ42 (5 μM) with fIAPP and followed via ThT binding assay. The **2g**/Aβ42 seeded complex was imaged via TEM (Figure 57). As expected, adding preformed fibrils to Aβ42 monomers decreased the lag phase, as shown by the increase of ThT reactivity observed after 30 min of co-incubation (Figures 57a (**2g**) and d (**2i**)). In contrast, incubation of monomeric Aβ42 alone showed an increase in ThT binding only after 1.5 h of aging. MTT studies performed after six days of incubation revealed that the presence of **2g** fully inhibited the cytotoxicity observed by fIAPP cross-seeded Aβ42 (Figure 57b).

TEM results were in good accordance with the ThT and MTT findings (Figure 57c), as the analysis of incubations aged for 48 h revealed a network of fibrils for samples containing Aβ42/fIAPP mixture, and unordered species in the presence of **2g.**

The results suggest that **2g** in 10-fold excess effectively suppresses the cross-interaction between mAβ42 and IAPP fibrils.

The effect of **2g** and **2i** on monomeric Aβ42 cross-seeded by fIAPP seeds was investigated by incubating Aβ42 (5 µM) with fIAPP and followed via ThT binding assay. The **2g**/Aβ42 seeded complex was imaged via TE microscopy (Figure 57). As expected, adding preformed fibrils to Aβ42 monomers decreased the lag phase, as shown by the increase of ThT reactivity observed after 30 min of co-incubation (Figure 57a and d). In contrast, incubation of monomeric Aβ42 alone showed an increase in ThT binding only after 1.5 h of aging. MTT studies performed after six days of incubation revealed that the presence of **2g** fully inhibited the cytotoxicity mediated by cross-seeded Aβ42 (Figure 57b).

TEM results were in good accordance with the ThT and MTT findings (Figure 57c), as the analysis of incubations aged for 48 h revealed a network of fibrils for samples containing Aβ42/fIAPP mixture, and unordered species in the presence of **2g.**

The results suggest that **2g** in 10-fold excess effectively suppresses the cross-interaction between mAβ42 and IAPP fibrils.

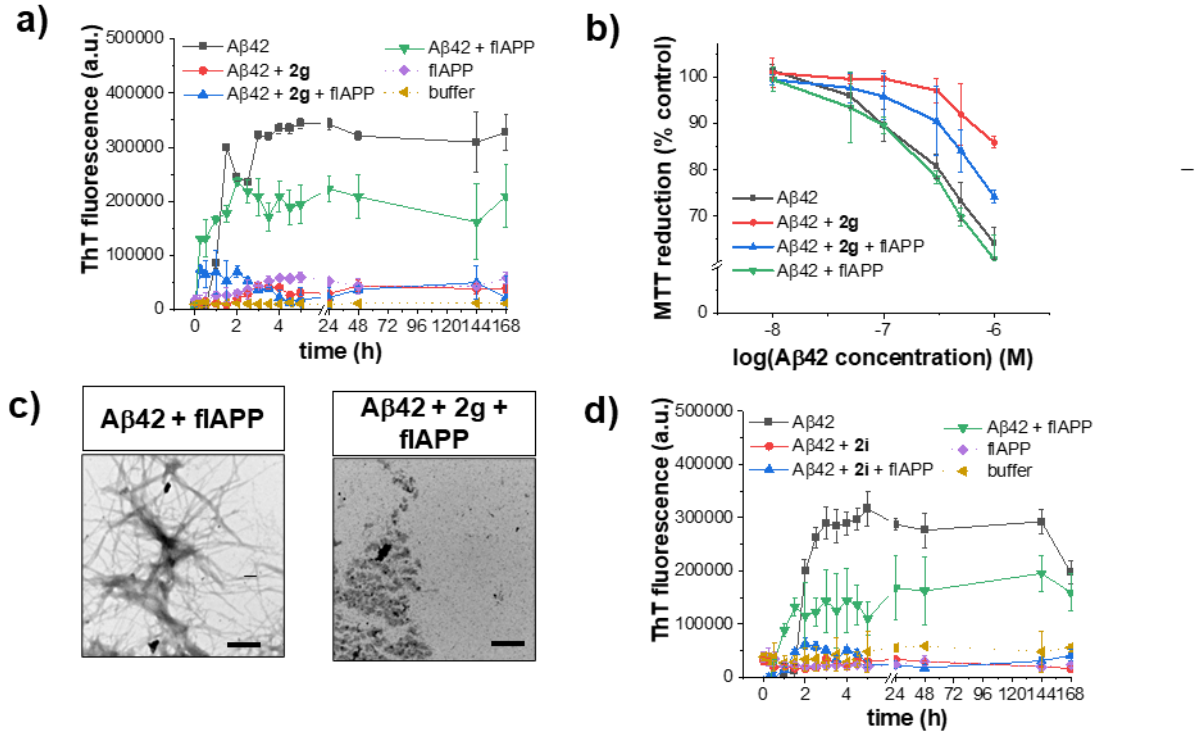

Figure 57. 2g and 2i suppress the fibrillogenesis and cytotoxicity of Aβ42 with or without fIAPP seeds. (a) The amyloid formation of Aβ42 (5 µM) alone or seeded by 30% fIAPP and of the complex of Aβ42/**2g** (1/10) seeded by fIAPP was followed via the ThT binding assay (means (±SD), 3 wells, one representative of 3, see Appendix Figure A52). (b) The effect on the cell-cytotoxicity on PC-12 cells was investigated after six days of aging. (c) TEM pictures of seeded fAβ42 and the complex of Aβ42/**2g** after 6 days of incubation (scale bar, 100 nm) are shown**.** Incubations were prepared with Aβ42 (10 µM), fIAPP (20%), Aβ42/**2g** (1/10) (means (±SD), 3 assays (n=3 each). (d) Fibrillation of Aβ42 (5 µM) alone or seeded by 30% fIAPP and of the complex of Aβ42/**2i** (1/10) seeded by fIAPP was followed via the ThT binding assay (means (±SD), 3 wells, one representative of 3, see Appendix Figure A53). Samples were prepared by incubating SEC-disaggregated Aβ42 (5 µM for the ThT assay and 10 µM for the MTT assay) in Aβ42 ThT buffer. IAPP seeds were prepared by aging IAPP (128 µM) in IAPP ThT buffer containing 0.5% HFIP for 24 h. Seeds and buffers, indicated with dotted lines, were subtracted from the incubations to ensure the occurrence of the seeding event.

4.15 Studies on plasma stability of MIMs and linear controls

Proteolytic stability in human plasma is essential for peptide leads for drug development [87,119,182]. Spanopoulou et al.[99] have previously shown that introducing D-amino acids and cyclisation through a disulphide bridge formation conferred proteolytic stability *in vitro* to the MCIP **2e**. Thus, an essential question of this work was understanding whether the shortening of **2e** sequence would impact the proteolytic stability of the follow-up generation. Furthermore, it has been reported that cyclisation is one of the most straightforward and handful tools to enhance peptide pharmacokinetics [119]. Thus, after studying **2g** and **2i**, the proteolytic stability in human plasma of the linear precursors **2g linear** and **2i linear** was determined.

The proteolytic resistance *in vitro* of **2g** and **2i** in human plasma was determined by HPLC and MALDI-TOF MS (Figures 58, 59 and 60).

Briefly, the peptides were incubated in human blood plasma and in vitro at 37ºC at different intervals. After precipitating the plasma proteins with aqueous trichloroacetic acid (10%) (1/1), the supernatants containing the peptides were separated by centrifugation, and then analysed via HPLC.

Both **2g** and **2i** displayed remarkable resistance toward plasmatic proteases (Figure 58). HPLC chromatograms of **2g** and **2i** incubations after precipitation of plasmatic proteins revealed one peak at $t_R \approx 5.8$ min for both peptides. The MALDI analysis of the collected fractions, as indicated in Figures 59 and 60, showed the molecular weights (MWs) of the intact peptides until 48 h of incubation, whereas no products of digestion were observed.

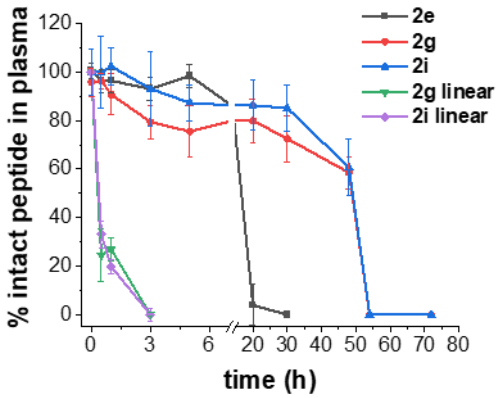

Figure 58. Human plasma stabilities (in vitro) of 2i and 2g compared to the template 2e and the linear precursors. Peptides were incubated in plasma (37ºC) for the indicated time points. Upon precipitation of plasma proteins, their amounts were quantified by RP-HPLC and MALDI-TOF-MS; the remaining intact peptide (% of total) was plotted over incubation time. (**2e**: % of the integrated area of the peak at time 0 h of the incubation in plasma, **2g** and **2i**: % of the integrated area of the peak based on the calibration curve, without plasma). Data are means (±SD) from at least 3 experiments.

To study the linear precursors' proteolytic stability, peptide incubations in human plasma were prepared and treated as described above. HPLC characterization of the supernatants after plasma proteins precipitation revealed that the linear precursors are readily degraded between 30 min and 1 h of incubation (Figure 58). The peak's absorbance and area detected at circa 5 minutes for both peptides readily decreased over time. MALDI-TOF analysis

confirmed the findings, as possible degradation products were identified between 30 min and 1 h of digestion. (Figures 61 and 62).

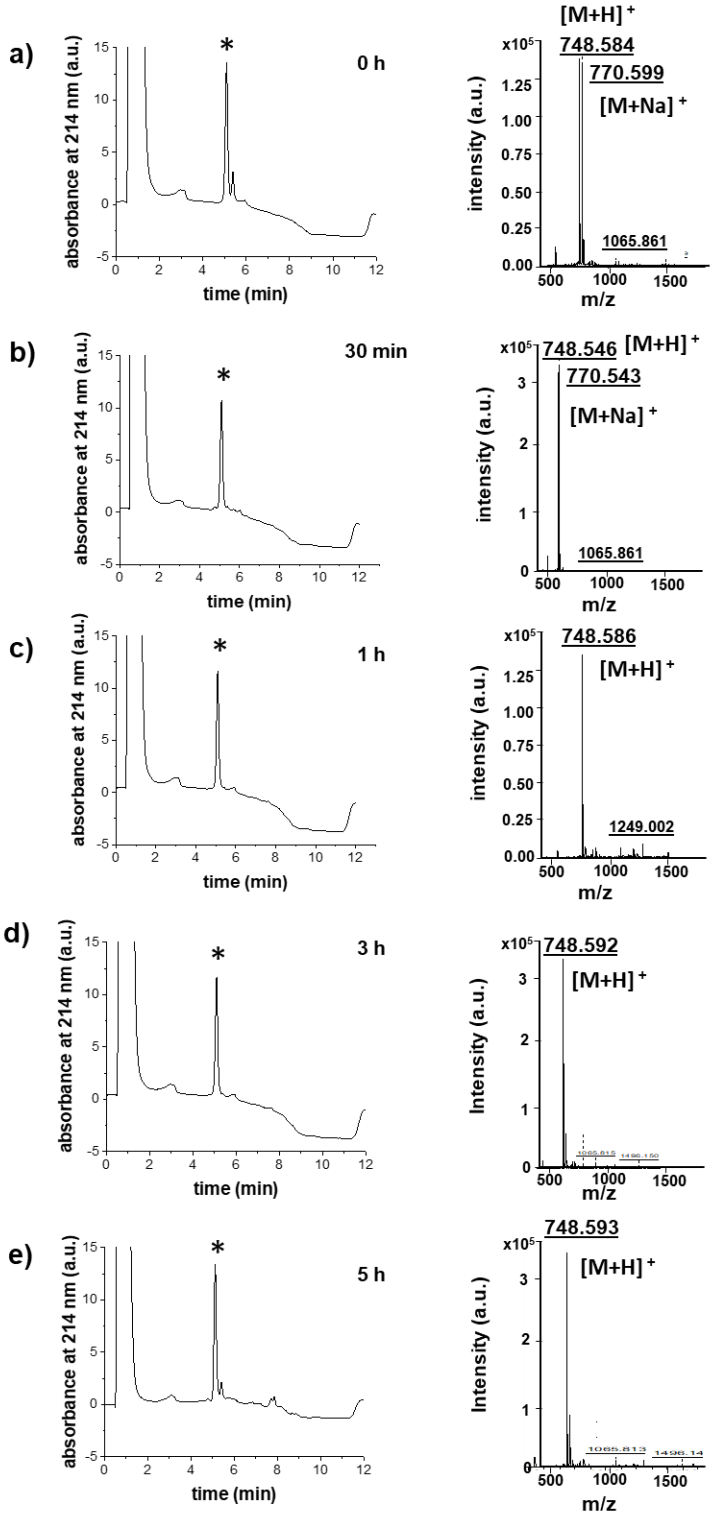

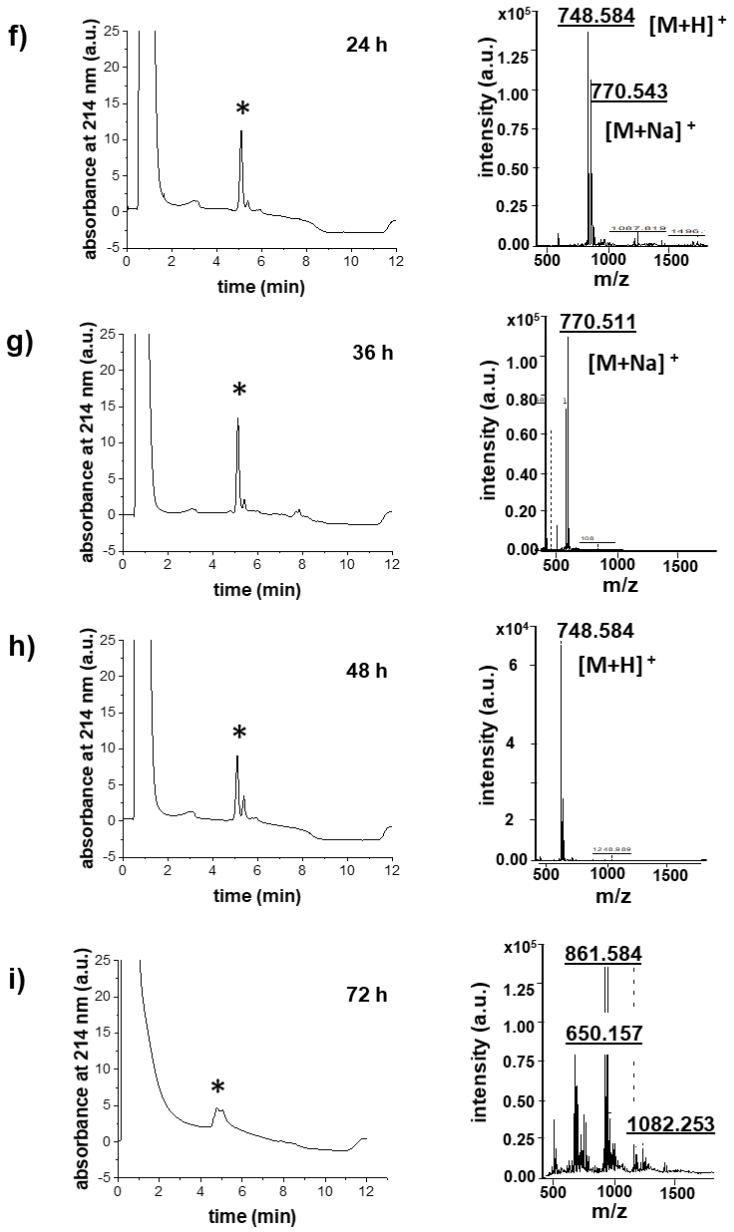

Figure 59. HPLC chromatograms and MALDI-MS spectra of 2g after incubation in human plasma in vitro (37oC) for 0 h (a), 30 min (b), 1 h (c), 3 h (d), 5 h I, 24 h (f), 36 h (g), 48 h (h), and 72 h (i) for proteolytic stability characterization. The left panels show HPLC chromatograms of the supernatant of **2g** after incubation at 37°C in human plasma (in vitro) for the indicated time points. After precipitating the plasma proteins with aqueous 10% TCA, the peptide solutions were analysed via RP-HPLC (214 nm). Right panel show MALDI spectra of the collected peak (*) with $t_R \approx 5.8$ min with the found $[M+H]^+$, $[M+Na]^+$ or $[M+K]^+$ until 48 h. Chromatograms and MALDI spectra are representatives of at least three independent sets of experiments (see Appendix Figures A54 and A55).

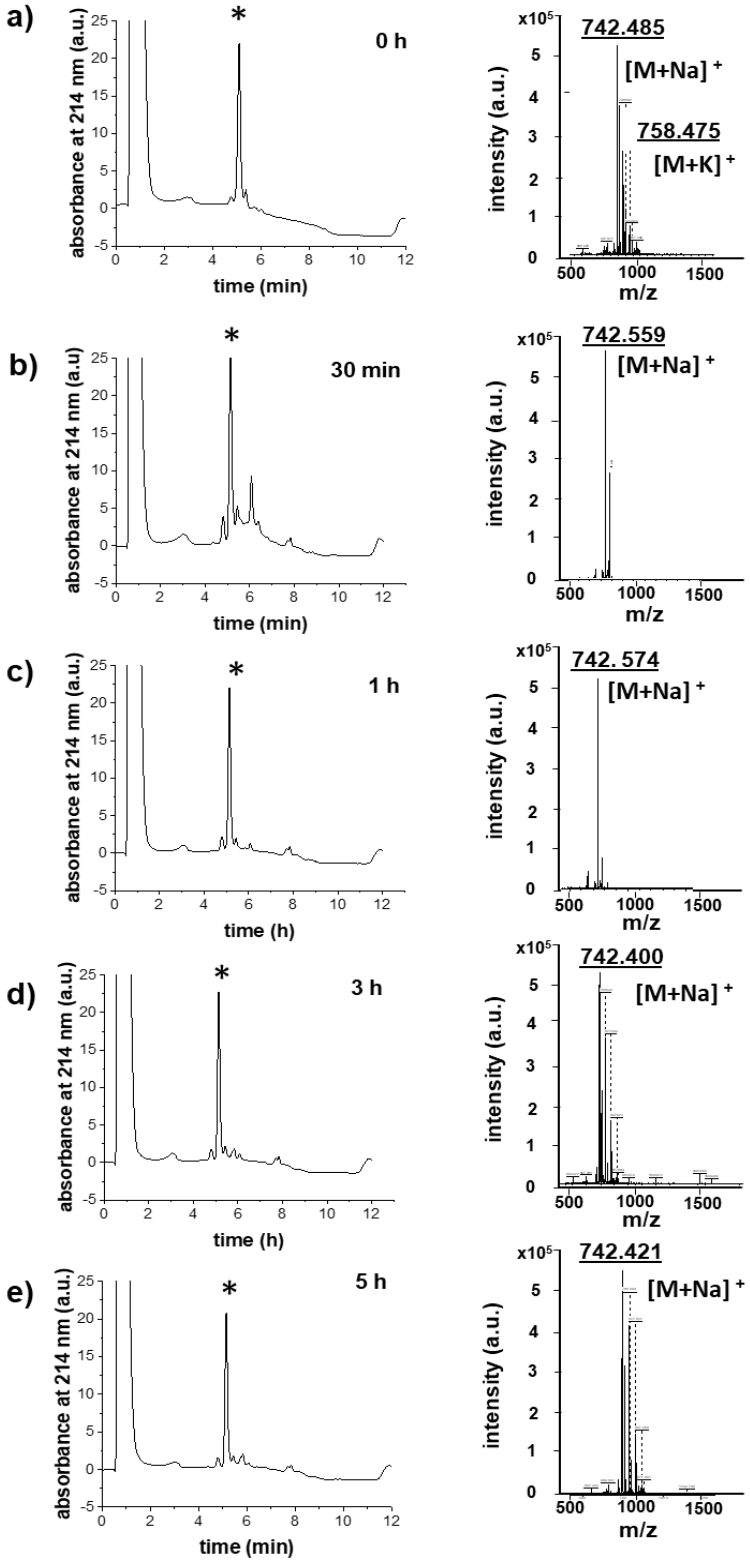
a)
0 h
absorbance at 214 nm (a.u.)
time (min)
742.485
[M+Na] +
758.475
[M+K] +
intensity (a.u.)
m/z
b)
30 min
absorbance at 214 nm (a.u)
time (min)
742.559
[M+Na] +
intensity (a.u.)
m/z
c)
1 h
absorbance at 214 nm (a.u.)
time (h)
742. 574
[M+Na] +
intensity (a.u.)
m/z
d)
3 h
absorbance at 214 nm (a.u.)
time (h)
742.400
[M+Na] +
intensity (a.u.)
m/z
e)
5 h
absorbance at 214 nm (a.u.)
time (min)
742.421
[M+Na] +
intensity (a.u.)
m/z

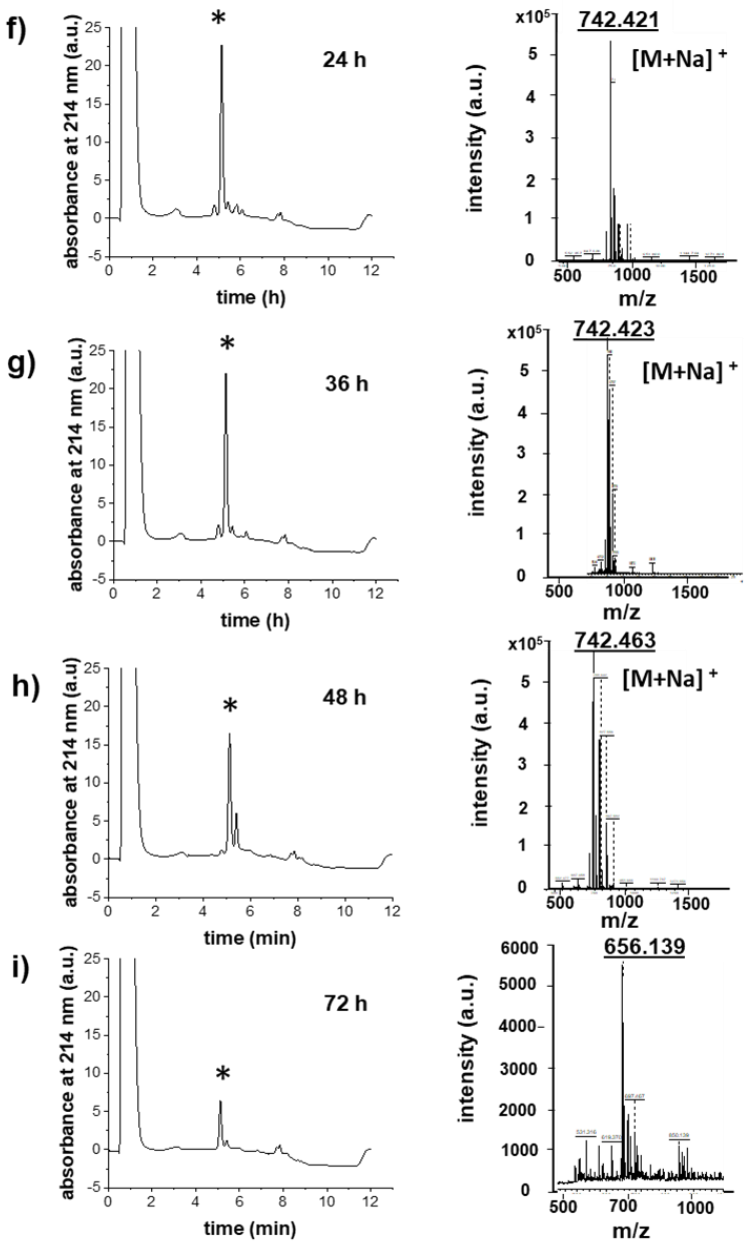

Figure 60. HPLC and MALDI-MS characterization of 2i after incubation in human plasma in vitro (37°C) for the indicated time points. Left panel show HPLC chromatograms of supernatant of **2i** after 0 h (a), 30 min (b), 1 h (c), 3 h (d), 5 h I, 24 h (f), 36 h (g), 48 h (h) and 72 h (i) as detected by RP-HPLC (214 nm). Right panels show MALDI spectra of the collected peak (*) with $t_R \approx 5.8$ min with the found $[M+H]^+$ or$[M+Na]^+$ until 48 h. Chromatogram and MALDI spectra are representatives of at least three sets of independent experiments (see Appendix Figures A56 and A57).

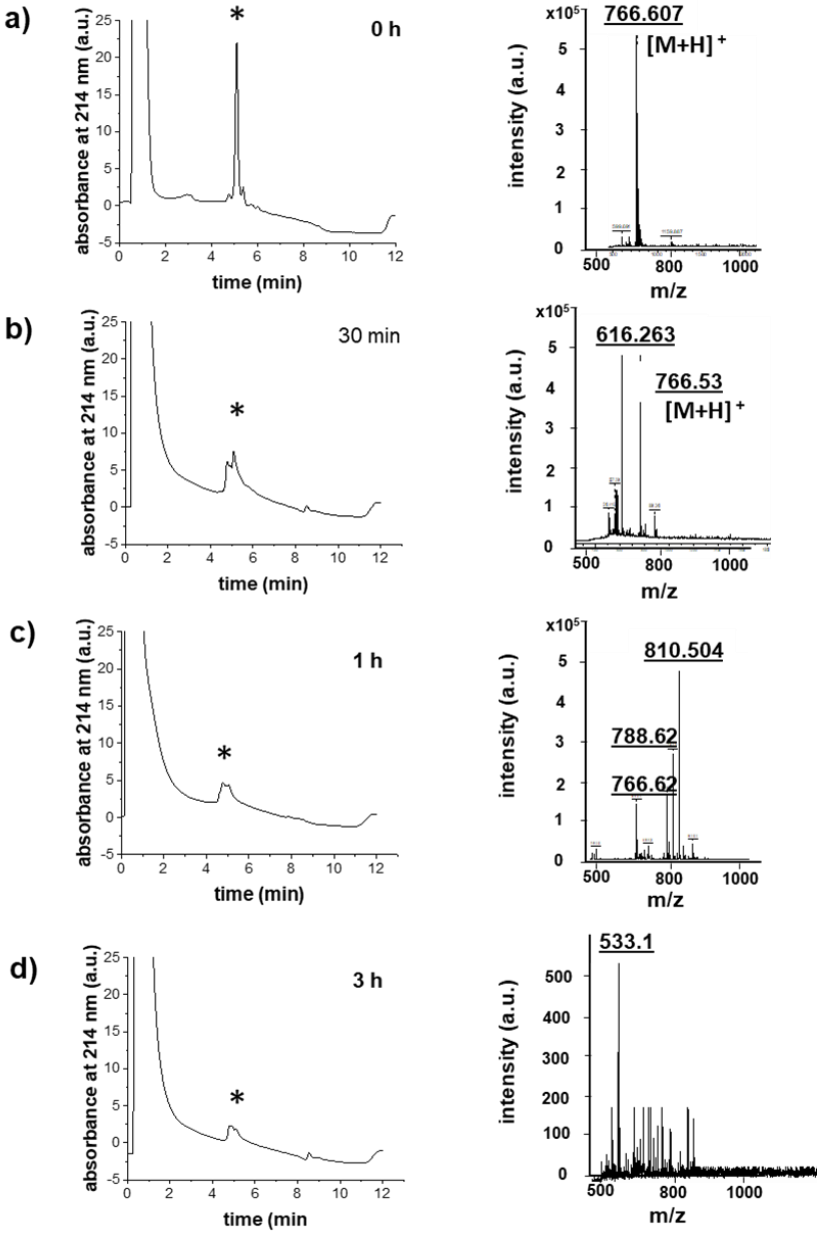

Figure 61. Proteolytic stability of 2g linear determined via HPLC and MALDI-MS. Left panels show RP-HPLC-(214 nm) of **2g linear** after incubation in human plasma in vitro (37°C) at the indicated time points (a-d). Right panels show HPLC MALDI spectra of the collected peak (*) with t_R≈5 min with the found $[M+H]^+$ or $[M+Na]^+$ until 3 h. (MALDI spectra are representatives of at least three sets of independent experiments (see Appendix Figure A58 and A59).

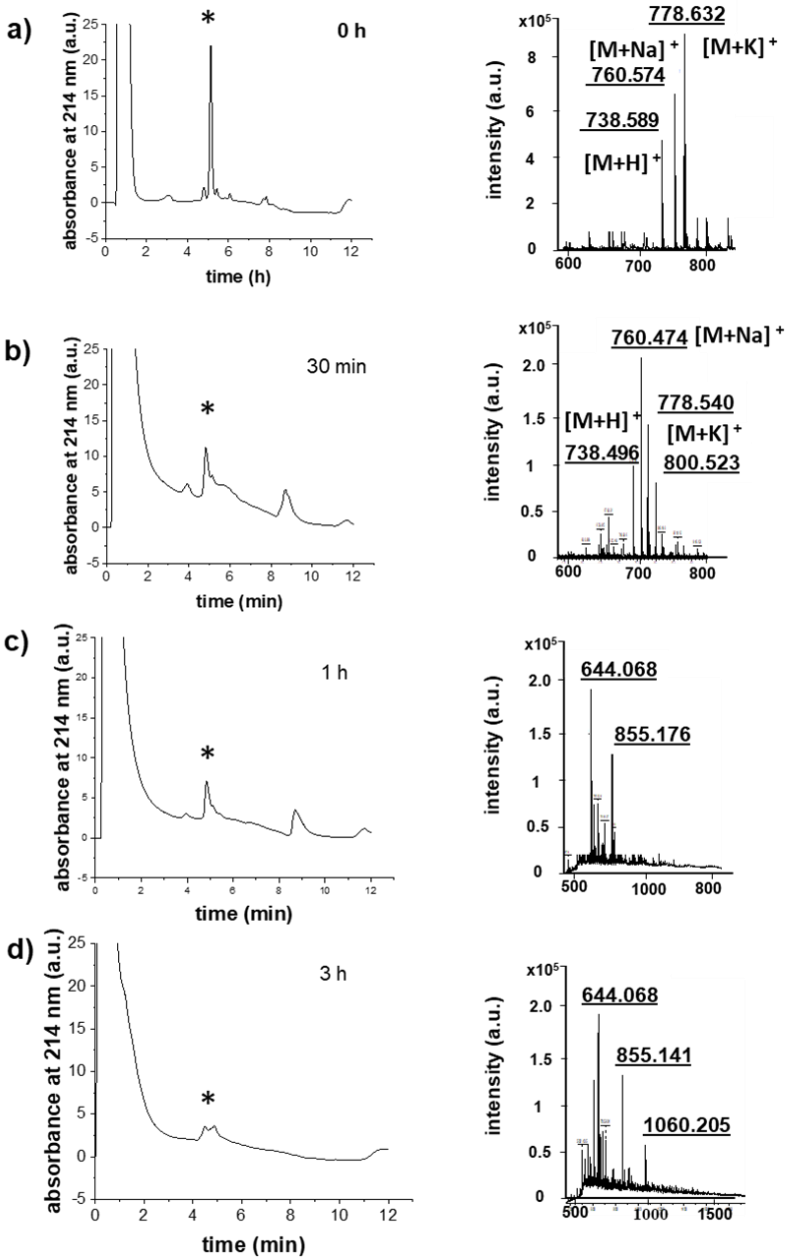

Figure 62. Proteolytic digestion of 2i linear characterized via HPLC and MALDI. Left panels show Incubation of **2i linear** in human plasma in vitro (37°C) for 0 h (a), 30 min (b), 1 h (c), 3 h, and 3 h (d) were analysed via HPLC. Right panels show MALDI analysis of the collected peak (*) revealed the presence of the intact compound until with the found $[M+H]^+$ or$[M+Na]^+$ until 30 minutes. Chromatograms and MALDI spectra are representatives of at least three sets of independent experiments (see Appendix Figures A61 and A62).

4.16 BBB permeability studies of 2i

Penetration of the blood-brain barrier (BBB) is a challenging but critical property of drug candidates targeting disorders of the central nervous system (CNS)[87,146,147]. Due to their intrinsic properties, such as large surface and high polarity, peptide delivery through the BBB is often limited[10]. However, MIMs present some characteristics of other cell-penetrating peptides (CPPs), such as an MW below one kDa and a limited number of hydrogen bond donor groups[88]. These properties might allow them to cross the blood–brain barrier.

Thus, we next studied whether N-terminally fluorescein-labelled **2i** (**Fluos-2i**) could cross the BBB by using a well-established model of human cerebral microvascular endothelial cells (hCMECs) grown as confluent monolayers on Transwell membranes[143,144,148].

Dr. Yuan Tian, from the group of Prof. Dr. Jürgen Bernhagen, ISD (LMU), performed these studies.

Briefly, the experiment was performed by incubating peptide aliquots in the upper chamber of the Transwell membrane for the indicated time points. The medium of both upper and lower chambers was collected and analysed via ELISA to detect the presence of fluorescently labelled peptides which could cross the hCMECs monolayer. The N-terminally fluorescein-labelled Transferrin receptor binding peptide (**Tfrb**) was used as a positive control to ensure the system's functionality. In contrast, Lucifer Yellow (**LY**), which does not cross the BBB, was used as negative control (Figure 63a) [99]. As shown in Figure 63b, the apparent permeability (Paap) of **Fluos-2i** after 2 h of incubation significantly differed from that of **LY**. In fact, **Fluos-2i** crossed the monolayer with an apparent permeability (Papp) at 2 h of 11.99 x 10^{-6} (± 1.41) cms^{-6} (mean (± SEM), which is close to the Papp value of **2e**[99].

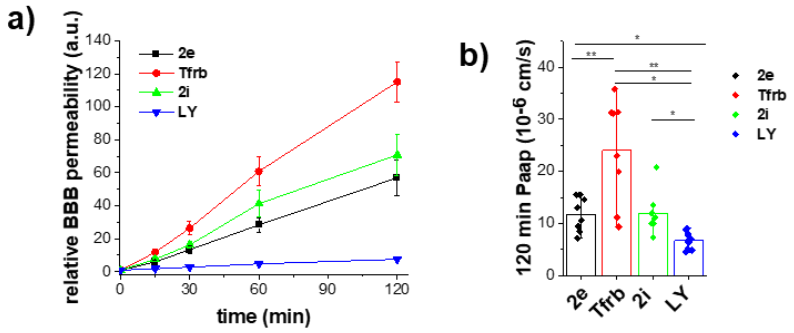

Figure 63. Relative permeabilities of 2i across the BBB cerebral microvascular endothelial cells model. (a) The plot shows the amount of **Fluos-2i** (10 µM) in the acceptor chamber at various time points in comparison to the controls (**Fluos-2e** (10 µM), **Fluos-Tfrb** (10 µM) and **LY** (20 µM). (b) shows the Paap of **2i** and controls after 2 h of incubation (means (±SD) from 8 (**Fluos-2i, Fluos-2e**, & **Fluos-Tfrb**) or 11 assays (**LY**) with each of them performed in 3 technical replicates). Dr. Yuan Tian, from Prof. Dr. Jürgen Bernhagen`s group, ISD (LMU), generated the data.

4.17 Effect of 2i and 2g on Aβ42-mediated inhibition of hippocampal long-term potentiation

Soluble and neurotoxic Aβ oligomers are suggested to mediate the impairment in glutamatergic signalling associated with AD pathology[55]. Oligomeric Aβ42 is thought to affect N-methyl-D-aspartate (NMDA) receptor function and abolish the induction of long-term potentiation (LTP), which is a crucial phenomenon in memory formation (136). Rammes et al.[55] showed that Aβ42 oligomers applied to acute murine hippocampal slices prevented the development of LTP after tetanic stimulation in a concentration-dependent manner. The highest concentration of Aβ42 oligomers (50 nM before oligomerisation) completely blocked LTP. Previous classes of peptide-based amyloid inhibitors have been shown to block Aβ42-mediated inhibition of hippocampal LTP[98,99,127].

These studies were performed by Markus Ballmann, from the group of Prof. Dr. Gerhard Rammes, Department of Anaesthesiology and Intensive Care at TUM Klinikum Rechts der Isar, generated the data.

In this study, we aimed to determine whether the inhibitory activity of **2g** and **2i** towards Aβ42 observed *in vitro* could have physiological relevance in an ex-vivo system.

Figure 64 shows a significant difference between the normalised fESP slope (field excitatory postsynaptic potential) of brain slices treated with Aβ42 alone or the mixture of Aβ42/MIMs. Altogether, the result indicates that in the presence of **2i** and **2g,** the Aβ42-mediated inhibition of hippocampal long-term potentiation (LTP) was entirely blocked. As inhibition of LTP by oAβ42 is linked to loss of memory and cognitive functions in AD, this data supports the physiological relevance of the results found in in vitro studies.

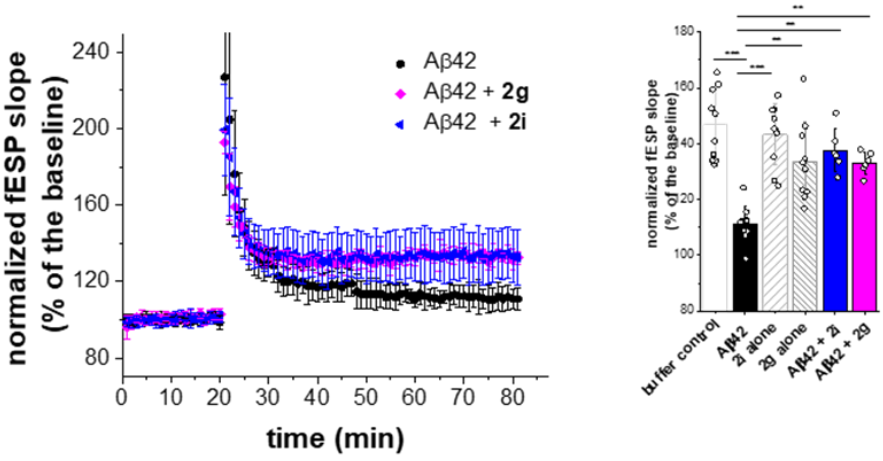

Figure 64. Effect of MIMs of Aβ42 mediated LTP impairment. Amelioration of Aβ42 (50 nM) induced LTP impairment in murine acute hippocampal slices by **2g** and **2i** (500 nM). Time course of synaptic transmission (means (±) SEM (n=6-8 for Aβ42/MIMs (1/10)), n=6-8 (for Aβ42 (50 nM) and buffer controls), and n=6-8 (for MIMs alone (500 nM)). Inset shows LTP values: averages from the last 10 min of recording; data, (means (± SEM) (n, see above); ***P<0.001 *versus* Aβ42 (one-way ANOVA & Bonferroni). Markus Ballman, group of Prof. Dr. Gerhard Rammes, Department of Anaesthesiology and Intensive Care at TUM Klinikum Rechts der Isar generated this data.

5. Discussion

5.1 Design and secondary structure of MIMs and linear analogues

Misfolding and self-assembly into fibrillar structures known as amyloids, have been reported for numerous proteins and polypeptides[2]. Circa forty of them are associated with devastating cell-degenerative diseases, such as the Aβ peptides (Aβ40(42)), which are the main species observed in the amyloid deposits of patients affected by Alzheimer's disease (AD), and IAPP, involved in the development of type 2 diabetes (T2D) [2]. Molecules that prevent amyloid formation are thus promising drug candidates (74).

Rationally designed peptides and peptidomimetics are potential hits for therapeutics in AD and T2D, and several peptide-based inhibitors have been derived from the targeted polypeptides[96,98,99,99,126,127,136,137]. However, designing suppressors of the protein-protein interactions mediating amyloid self-assembly is a significant challenge due to the dynamic nature of the involved structures, the large size of their surfaces and their high-affinity interactions[10].

In this work, the four key residues of the IAPP interaction surfaces with IAPP and Aβ40(42), Phe^{15}, Leu^{16}, Phe^{23} and Ile^{26}, previously nailed down by Bakou and al.[100], were used to design potent inhibitors of amyloid self-assembly of both IAPP and Aβ40(42). This class of inhibitors, named minimised IAPP mimics (MIMs), is currently the last round of optimisation after two generations of inhibitory peptides designed using the surfaces involved in the IAPP/Aβ cross-interaction as a template[98,99].

The first generation of this class of inhibitors was named interaction surface mimics (ISMs) and was designed by linking IAPP(8-18) and IAPP(22-28) through different tripeptide units. The ISMs were found to sequester IAPP and Aβ42 from the amyloid assembly as non-fibrillar and non-toxic aggregates (Scheme 7)[98]. In the next round of optimisation, the ISM **R3-GI** was optimised by sequence truncation, substitutions with Gly, and conformationally constrained by disulphide bridge-mediated cyclisation to yield the macrocyclic *i*nhibitory peptides (MCIPs). While the template **R3-GI** was a selective inhibitor of Aβ40(42) amyloidogenesis, the MCIP **2b** inhibited both IAPP and Aβ40(42)[98,99]. The MCIP **2e**, designed by switching the stereochemistry of the IAPP-derived residues in the sequence of **2b,** displayed a potent and selective inhibitory activity towards Aβ40(42) fibrillation. Furthermore, **2e** had good drug-like properties, such as good proteolytic stability and BBB permeability in in vitro systems.

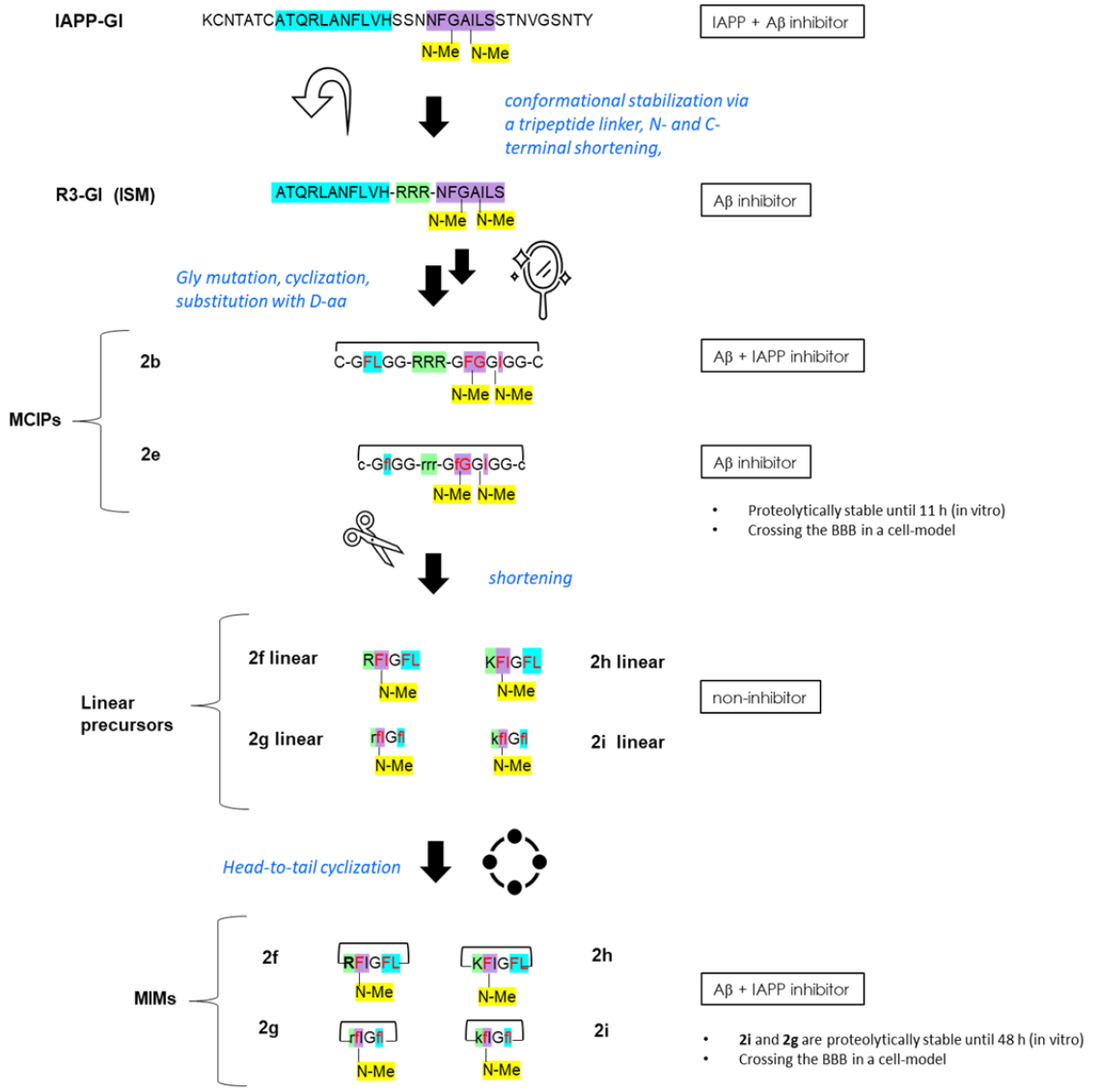

Scheme 7. MIMs are the last round of optimisation of amyloid inhibitors mimicking the potential interaction interfaces of IAPP self- and cross-assembly with Aβ42 (modified from[95]). The first class of inhibitors (ISMs) was designed by connecting IAPP(8-18) (blue) and IAPP(22-28) (purple) through a tripeptide linker stabilising β-sheet structures of the sequence. N-methylation in position 24 and 26 of the IAPP sequence were introduced to enhance solubility and inhibitory potential[98]. The ISM **R3-GI** was used as a template to design the MCIPs, optimised by Gly substitution, cyclisation and substitution with D-amino acids[99]. The minimal elements necessary for the interactions between IAPP and Aβ, which were nailed down by Bakou et al. [100] were maintained in the primary sequence of MIMs (red-coloured residues: IAPP-derived; D-residues: lower-case (highlighted in blue, green and purple); amide-bond N-methylations: "N-Me" (highlighted in yellow).

The primary sequence of MIMs also contains an N-methylation on the Ile, introduced with a double function: improving the solubility of the peptide and impairing the hydrogen bonding involved in the β-strand formation of the amyloids. These properties have been reported also for the previous generations of inhibitors, designed by applying the same strategy[95,98]. Additionally, the sequences of MIMs include a Gly to confer conformational flexibility to the sequence, and an Arg in **2f** and **2g**, which was derived from the tripeptide linker introduced

in **R3-GI** and maintained in **2b**. The Arg could be substituted with a Lys to incorporate a fluorescence moiety on the N^{ε}-amino group (**2h** and **2i**).

As for the MCIPs, cyclisation – in this case via head-to-tail lactam bond formation- and the introduction of D-AA were used to optimize the proteolytic stability and possibly the BBB permeability of the peptides (**2g** and **2i**) [99].

With the ISMs design, our group[98] previously showed that the introduction of β-sheet-structure-propagating tripeptides linking the hot spots regions IAPP(8-18) and IAPP(8-28) could stabilise alternative, amyloid-like-β-sheet folds, relative to the non-inhibitory fold of IAPP(8-28) (Scheme 8). As folding into β-sheet interaction interfaces was identified as an early step in the amyloid cross- and self-assembly and other protein–protein interactions, such property could be effective in developing inhibitors of the early stages of the amyloidogenic misfolding[10].

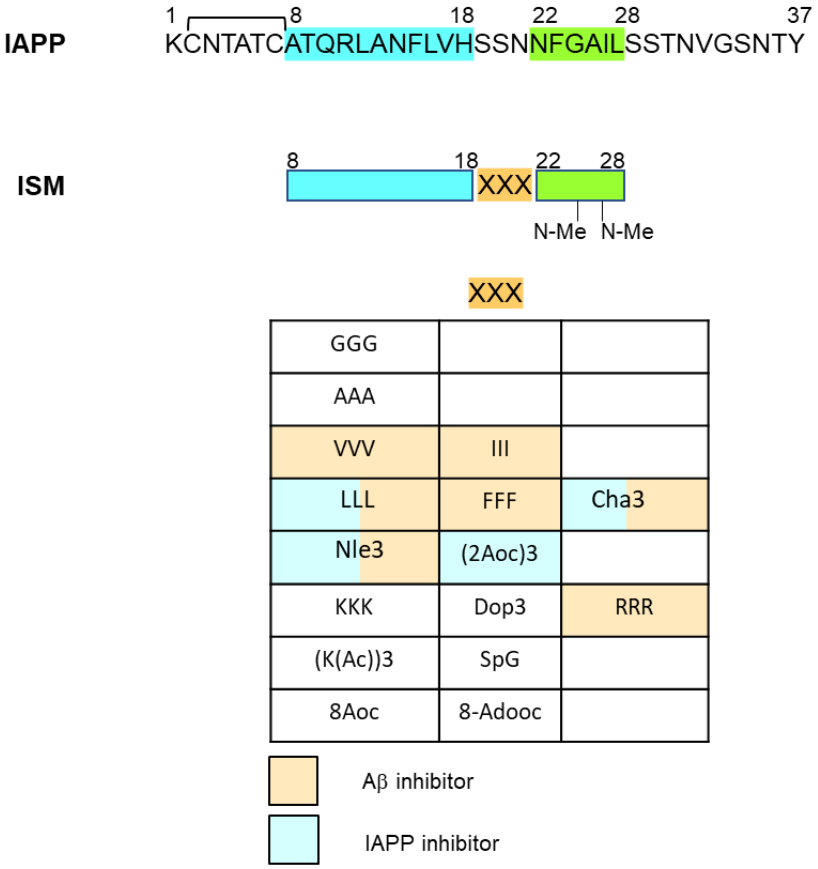

Scheme 8. The nature of the tripeptide in interaction surface mimics (ISMs). Design concept and inhibitory effects of ISMs (2Aoc: 2-Amino-octanoic acid, 8Aoc: 8-Amino-octanoic acid, Cha: cyclohexylalanine, 8-Adooc: 8-amino-3,6-dioxaoctanoic acid[98]. Scheme modified from ref.[10]

The MCIPs **2e** and **2b**, developed based on the ISM **R3-GI** and bearing the same RRR linker, also showed β-sheet/β-turn structural motifs. Interestingly, MD simulations confirmed that some of their topological and structural features might be similar to these of IAPP fibrils[99].

CD studies of **2f**, **2g**, **2h** and **2i** performed in this thesis revealed a high content of β-sheet/β-turn structure, as indicated by the presence of a minimum at 228 nm and a maximum at circa 195 nm (Figure 65). The peptides bearing Lys or D-Lys (**2h** and **2i**) showed a similar CD structure (Figure 65b). In contrast, the spectra of the peptides bearing Arg and D-Arg (**2f** and **2g**) differed in mean residue ellipticity and profile (Figure 65a). In fact, the spectrum of **2f**

showed a maximum at 205 nm, which was blue shifted to 195 nm in **2g** structure (Figure 65a).

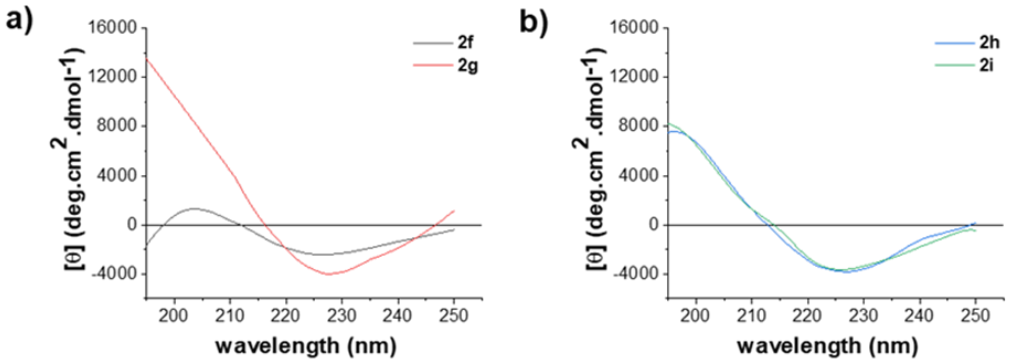

Figure 65. CD spectra of 2f, 2g, 2h and 2i revealed high content of β-sheet/β-turn structures. Comparison between the CD spectra of **2f** and **2g** (a) and **2h** and **2i** (b). These spectra were shown in Figure 20.

The secondary structure of **2g** was highly constrained also in the presence of up to 80% (v/v) of TFE (Figure 66a), a helical-structure inducing cosolvent that acts only within the context of a pre-existing helix-coil equilibrium [157,161]. Furthermore, the oligomerisation state of **2g** was strikingly dependent on the pH, as indicated by the increase of mean residue ellipticity in the presence of amounts of aqueous HCl (5 mM) and NaOH (5 mM) (Figure 66b).

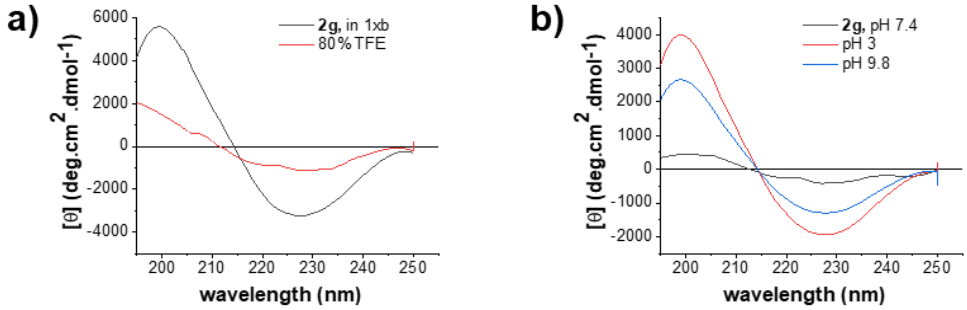

Figure 66. CD spectra of 2g in the presence of TFE and at different pH. Comparison between the CD spectra of **2g** in aqueous conditions (20 µM, 1xb (pH 7.4), 1%HFIP) and in the presence of 80% TFE **(v/v)** (a). CD spectra of **2g** at different pH (100 µM, 1xb (pH 7.4), 1% HFIP) (b). These spectra were shown in Figures 29 and 30.

Both CD spectra of **2g** and **2i**, bearing D-amino acids, revealed a red shift of the minimum at 220 nm observed for the parent peptide **2e** (Figure 67a)[92]. This shift, compatible with an increase of β-turn structure compared to the precursor, was observed for all MIMs. Overall, this feature might explain the loss of selectivity towards Aβ42, as the selectivity of **2e** towards Aβ40(42), compared to IAPP, was linked to a higher contents of β-sheet structural motifs [99]. Like MIMs, the MCIP **2b**, which had a higher content of β-turn than **2e**, was an inhibitor of Aβ42 and IAPP[99] (Figure 67b).

The head-to-tail cyclisation was the most critical feature for dictating the peptide conformation, as shown by the clear difference between the CD spectra of MIMs and their linear precursors (Figure 68b).

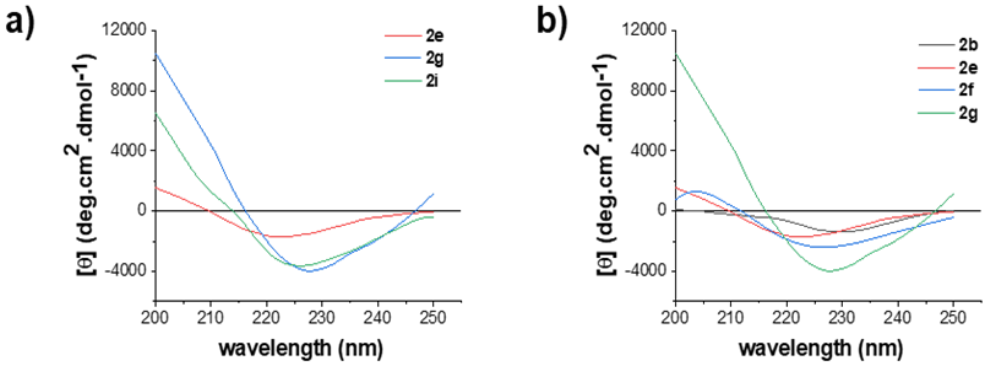

Figure 67. CD spectra of MIMs and the MCIPs revealed different amounts of β-sheet and β-turn structures. (a) CD spectra of peptides bearing D-amino-acids, including **2e, 2g** and **2i.** (b), Comparison between the CD spectra of **2f** and **2g** and the precursors **2b** and **2e.** Spectra were recorded with peptide solutions (10 μM in 1xb (pH 7.4), 1% HFIP). These spectra were shown in Figure 20 and ref. [99].

All CD spectra of the linear precursors presented a blue shift of the minima observed at 230 nm, indicating a partial β-sheet conformation, possibly due to an aggregated state, which is likely dictated by the presence of the N-methylation and by the two phenylalanines. Overall, the profile of **2f linear** resembles its cyclised version **2f**, and it was characterised by a red shift of the minimum observed at 225 nm (Figure 68). Furthermore, bioactivity studies confirmed that the lactam bridge formation between the N- and C-termini caused a 10-fold increase of inhibitory activity on IAPP and Aβ42 fibrillation (Figure 28 and Figure 45).

The high flexibility of short peptides sequence, resulting in a vast range of spatial distribution of functional groups, can affect the peptides' ability to engage in specific interactions with the targets [87,164,183–185]. In this study, the primary sequence of the peptides was designed based on minimal IAPP-derived elements, which were previously found to be essential for IAPP self- and cross-interaction with Aβ40(42)[28,100]. Thus, an interaction between the linear sequences and the targets could be expected; as observed for the linear precursors of the templates MCIPs[99]. In fact, in this work, weak interactions between IAPP or Aβ42 and linear precursors were observed 2**g linear** (Figure 35 and Figure 48) However, due to the small size of MIMs, binding of the linear precursors to IAPP and Aβ42 might be hampered by their structural flexibility.

Conversely, MIMs, have β-sheet/β-turn rich structures as the template MCIPs (Figure 66) and highly constrained conformation. Furthermore, they inhibited IAPP and Aβ42 in 5-fold molar excess, with IC_{50}s in the nanomolar to the sub-micromolar range, as the templates MCIPs[99]. The importance of β-sheet/β-turn structures for the anti-amyloidogenic activity of cyclic D, L-α-peptides were previously underlined by Rahimipour and coworkers[93]. The authors reported that under conditions enhancing hydrogen-bond formation, cyclic D- and L-peptide hexamers could stack on each other to form hollow β-sheet-like tubular structures. The hydrogen bonds in these structural arrangements run parallel to the axis of the nanotubes

and separate the cyclic peptides from each other by ~4.8 Å[87–89]. A similar intermolecular distance is also evident in the β-strands of the amyloids, and the authors suggested that the anti-amyloidogenic activity of the cyclopeptides forming nanotubes might be explained by the structural similarity between the supermolecular assemblies of the amyloids and the peptide inhibitors[91,93,94].

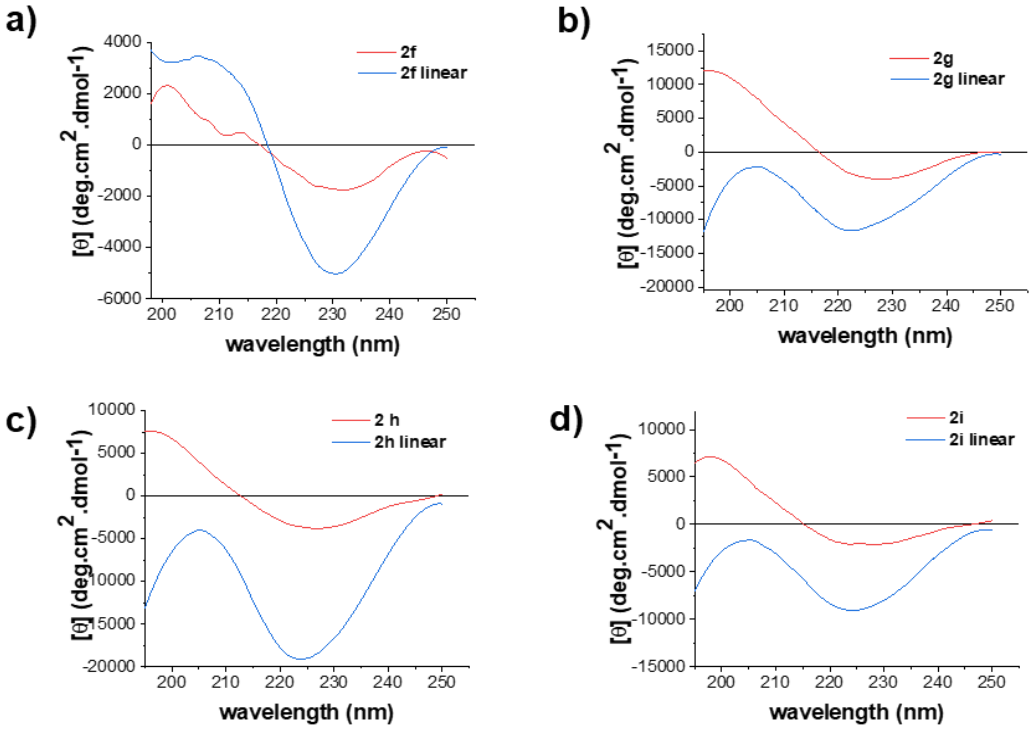

Figure 68. CD spectra of 2f, 2g, 2h and 2i and their linear precursors revealed different secondary structures. Comparison between the CD spectra of **2f** and **2f linear** (a), **2g** and **2g linear** (b), **2h** and **2h linear** (c), and **2i** and **2i linear** (d). Spectra were recorded with peptide solutions (10 µM) prepared in 1xb (pH 7.4), containing 1% HFIP. These spectra are shown in Figures 20 and 21.

However, TEM analysis of high concentrations of MIMs assemblies (100 µM) at physiological pH revealed the presence of globular structures, which were found to be non-amyloidogenic and non-reactive to (anti-)oligomer A11 polyclonal antibody. Such structural differences can be due to a) the higher hydrophobicity of MIMs compared to the sequence of CP-2 and analogues and b) the different order of D-/L-amino acids within the sequences (Figure 69).

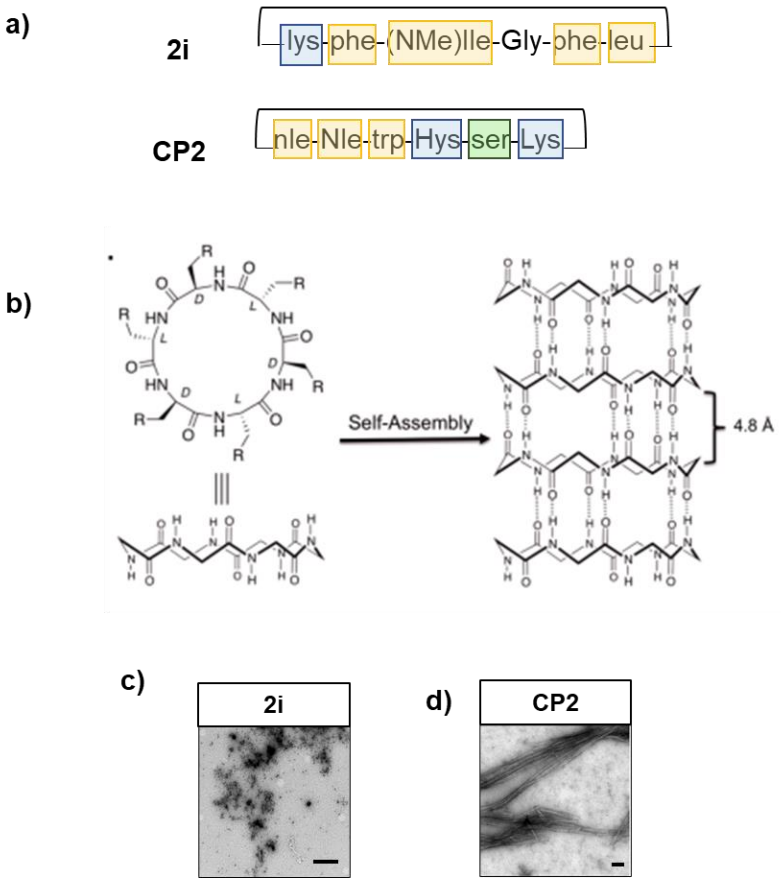

Figure 69. Comparison between MIMs and self-assembly nanotubes consisting of CP-2[93]. Sequences of **2i** and CP-2[93] show hydrophobic residues (yellow), positively charged residues (blue) and polar residues (green). L-Amino acids are indicated with a capital letter. (b) Proposed model of nanotubes self-assembly [93]. (c-d) TEM images of **2i** (100 μM) and CP-2 (100 μM) at neutral pH show amorphous aggregates and amyloid-like structures, respectively (scale bar, 100 nm). The TEM picture of CP-2, its sequence and the self-assembly model were taken from reference [93].

5.2 Self-assembly propensity of MIMs and behaviour at different pH

Results by our group and others have suggested that self-assembly is a desirable property to confer anti-amyloidogenic potential, as it might contribute to sequestering Aβ or IAPP into non-fibrillar/non-toxic heteroassemblies(91,94). The mechanism of action of the ISM **R3-GI** [97], the template for the inhibitor design of the MCIPs and MIMs, was studied in detail by Niu et al., which reported that **R3-GI** could adopt a β-like structure, and oligomerises into colloid-like assemblies[97].

The CD concentration dependence studies presented in this thesis indicated that also **2i** and **2g** self-assemble between 10 and 20 μM (Figure 20). In addition, fluorescence spectroscopic titrations of **Fluos-2i** with **2i** revealed an app. K_D of 34 nM for the self-assembly (Figure 26). Furthermore, TEM imaging of different concentrations of **2g** revealed the presence of increasingly organised assemblies that showed a spherical morphology at 100 μM (Figure 20). CD studies revealed that the signal intensity of **2g** and **2i** increased with amounts of aqueous HCl and NaOH. This observation might suggest that the oligomerised peptides undergo a structural rearrangement mediated by a different H-bonds networking and that at

specific pH, **2i** and **2g** might be in their monomeric form (Figure 23). Novelli et al.[168] reported that the supermolecular assembly of cyclic peptide octamers formed by β- and α-amino acids can be modulated by different pH. The additional amount of protic cosolvents necessary for disaggregating the **2g** and **2i** oligomers might be explained by the different basicity of the guanidinium group of Arg (in **2g**) and the N^{ε} amino group of the Lys (in **2i**). In their protonated state, these two groups differ regarding the hydration-free energy and the spatial organisation of the charge[169] (Figure 70).

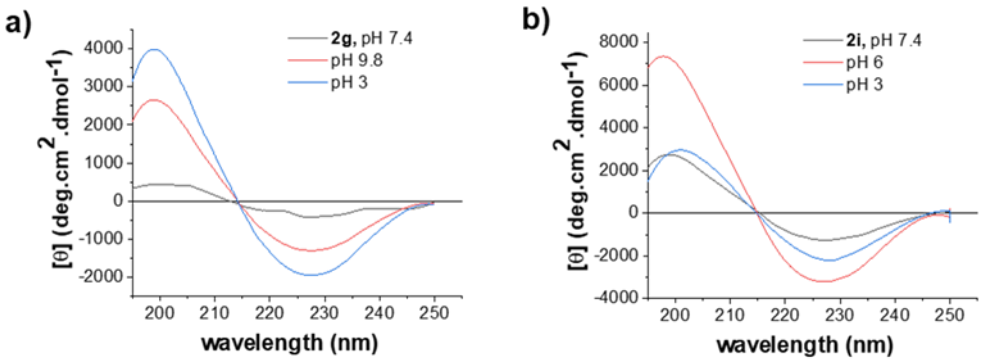

Figure 70. CD spectra of 2g and 2i at different pH. (a) Comparison between the CD spectra of **2g** in aqueous conditions (100 µM in 1xb (pH 7.4), 1% HFIP) and amounts of HCl (5 mM) or NaOH (5 mM). (b) CD spectra of **2i** (100 µM in 1xb (pH 7.4), 1% HFIP) titrated with different amounts of HCl (5 mM).

5.3 Identification of the binding sites of Fluos-2i on Aβ42 and IAPP sequences

Peptide arrays were used to identify the binding sites of **Fluos-2i** on the sequences of IAPP. The findings indicated that MIMs/IAPP interaction site is the segment IAPP(11-16) or RLANFVL (Figure 71), whereas the Aβ "binding cores" of **2i** are Aβ(12-19) or VHHQKLVF, and Aβ(28-34) or KGAIIG (Figure 74).

Interaction between Fluos 2i and IAPP(11-16)

In the last decade, many studies have been conducted to elucidate the structure of IAPP fibrils. Altogether the X-ray diffraction, electron diffraction and cryo-electron microscopy studies performed on synthetic IAPP fibrils agreed on the presence of a cross-β structure with intermolecular β-sheets, in which the β-strands are perpendicular to the fibril axis[76–79,101,186]. Solid-state NMR studies on full-length fibrils confirmed the parallel, in-register alignment of the β-strands and suggested a hairpin structure of two β-sheets, not comprising the region IAPP(18-27)[78]. Despite all the studies agreeing on a parallel in-register alignment of β-strands, their number, position, and relative arrangement enormously vary among these models[79]. In 2020, Schröeder [62], Eisenberg[63], and Radford and Ranson groups[80] reported cryo-EM structures of IAPP fibrils within 4.2 Å and 3.6 Å resolution. The IAPP fibril polymorphs studied by all three groups comprise two helically twisted protofilaments, each consisting of a stack of monomers arranged in the cross-β-sheet structure typical for

amyloids. Both Röder et al. [62] and Gallardo et al.[80] reported an S-shaped protofilament composed of three short β-strands, formed by segments IAPP(14–19(20)), IAPP(26–31(32)) and IAPP(35–36(37)), linked by short loops (Figure 71b and 73).

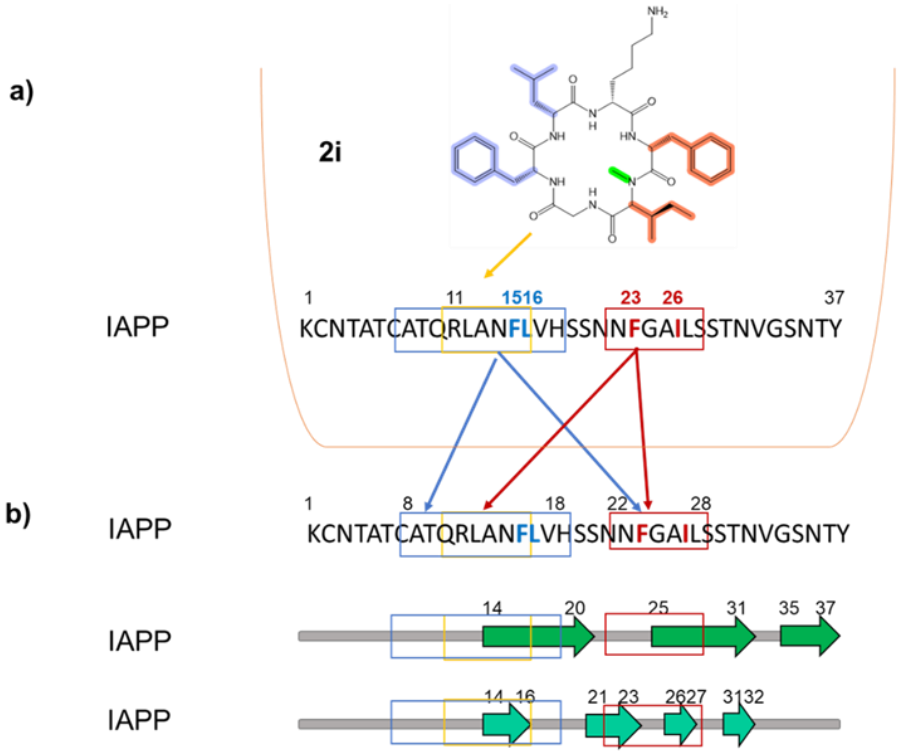

Figure 71. Identification of IAPP segments binding to Fluos-2i. (a) The IAPP "hot-segments" IAPP(8-18) (in blue) and IAPP(22-28) (in red), important for IAPP amyloid self-assembly [28], are shown. The IAPP binding core of **2i**, including IAPP(11-16), is highlighted in orange. The IAPP-derived elements included in **2i** sequence are highlighted in blue (Phe[15] and Leu[16]) or red (Phe[23] and Ile[26]), whereas the N-methylation on Ile is shown in green. (b) The presence of β-strands in fIAPP is reported based on the cryo-EM models of Roeder et al. [62] (upper panel) and Cao et al.[63] (lower panel). IAPP segments involved in IAPP self-assembly or the interaction with **2i** are indicated with the same colour code as in (a). The scheme is modified from ref.[62,63,98].

Of note, "a serpentine fold" was previously reported also by Kajava et al.[71], who characterised the structure of IAPP amyloid fibrils via electron microscopy and scanning transmission electron microscopy (STEM). By contrast, the cryo-EM studies of Cao et al.[63], revealed that hIAPP amyloid fibrils adopt an I-shaped fold containing short β-strands formed by the same regions identified in the other cryo-EM structures[81] (Figure 71b and 72).

Taking these models into consideration, the results of the peptide arrays suggest that the **2i** binding site on IAPP(11-16) might interfere with the formation of the β-strand formed by the segments IAPP(14-19(20)) [62,63,80]. This region is included in IAPP β-hairpin, comprising the residues IAPP(12-28) [187], which is primarily adopted by IAPP monomers[188]. Of note, this region contains the residues Phe[15]and Leu[16], and previous studies from our group revealed that these elements are crucial for IAPP self- and cross- interaction with Aβ42 [28,100]. Hydrophobic and aromatic-aromatic interactions have been detected in monomeric IAPP[189], influence the rate of fibril formation[190], and can play a major role for the inhibition of IAPP aggregation[191]. Mirecka et al. have previously reported the structural characterization of a complex formed between IAPP and the aggregation inhibitor β-wrapin HI18[187]. The

structure of the IAPP:HI18 complex was determined by high-resolution liquid-state NMR spectroscopy and MD simulations. The study revealed that the core of the complex includes IAPP(10-30) , that Phe^{15} and Phe^{23} are in contact and located at the core of the complex, and that H18 is a sub stoichiometric inhibitor of IAPP fibrillation[187].

The interaction between inhibitor and IAPP β-hairpin conformation has been suggested for explaining the mechanism of the MCIPs[99]and other classes of IAPP and Aβ42 inhibitors[37,41,192].The importance of Phe^{15} for IAPP fibrillogenesis has been underlined also by Wiltzius et al.[101]. In their studies, the authors chaperoned IAPP fused to a larger protein, and determined a helical form of IAPP, rarely encountered in vitro due to IAPP strong self-assembly propensity. This transient helical structure, including IAPP(8-18), might dimerize through a π–π stacking interaction occurring between the aromatic groups of two Phe^{15}, orientating the two α-helices in parallel[101]. Of note, the authors reported that mutations at this helical interface affect the rate of fibrillation, suggesting that this dimer is an intermediate on the pathway to fibrillation.

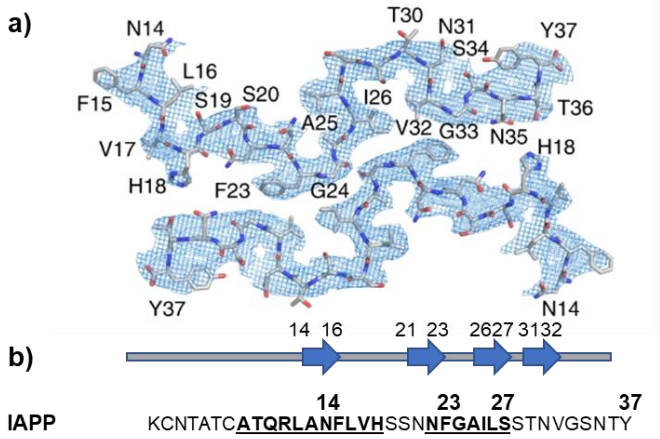

Figure 72. IAPP binding regions of Fluos-2i in the context of the cryo-EM model of Cao et al. The most consistent of the two cryo-EM models of fIAPP proposed by Cao et al. [63], is showed in (a). The visual representation of the IAPP segments organized in β-strands, as proposed by the Cryo-EM structure, is compared to the IAPP cross/self-interaction interfaces nailed down by Andreetto et al (bold, underlined) (b). The Figure was modified from references[63] and [28].

Fluorescence spectroscopy studies indicated that **2i** is a high-affinity ligand of IAPP, and peptide arrays revealed that its binding region is IAPP(11-16). Furthermore, **2i** binds Fluos-IAPP with an app K_D value of 197.75 (±16) nM, that corresponds to a 20-fold weaker binding than the app. K_D, value of IAPP self-assembly (9.7 nM (±0.9)), and it is approximately 4 times worse than the app. K_D value of IAPP cross-assembly with Aβ42 (48.5 nM (±4.2)).

These results might be explained by the lack of binding affinity for IAPP(23–27), or FGAIL, which all three cryo-EM models identified as the 'core' of the protofilaments interaction interface [62,63,80,81].

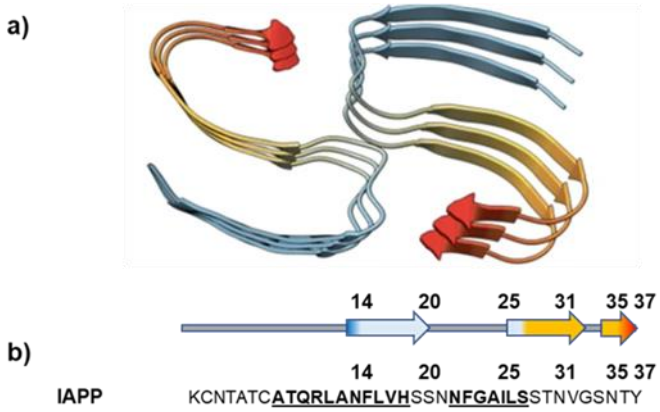

Figure 73. IAPP binding regions in the context of the cryo-EM model of Röder et al. (a) Secondary structure of the fIAPP model according to Röder et al. [62], showing the cross-section of three fibril layers including the three β-sheets showed in (b). The IAPP segments organized in β-sheets are overlayed to the IAPP cross/self-interaction interfaces nailed down by Andreetto et al (bold, underlined) (b) [28] . The Figure is modified from references [28][62].

Interaction between Fluos 2i and Aβ(12-19) and Aβ(28-34)

Peptide arrays revealed two "binding cores" of Aβ42/**2i** interaction, consisting of Aβ(12-19) and Aβ(28-34). Interestingly, these regions correspond to three out of five short Aβ segments previously identified by our group as core regions of the Aβ/IAPP cross-interaction interfaces[28].

In addition to these studies, Tycko and coworkers reported models of fIAPP and fAβ40 obtained via solid-state NMR (55[68]. Together with the results of our group, Tycko`s findings showed that the Aβ sites involved in the formation of β-strands and in its amyloid self-assembly are Aβ(19-22), Aβ(27-32) and Aβ(35-40). Taken together, the results suggested that nearly the same Aβ40 regions adopt β-strands conformations and are involved in the amyloid self-assembly of Aβ40. More recently, the cryo-EM structure of Aβ40 fibrils solved by Kollmer et al. [60], showed that each fAβ40 subunit consists of four cross-β sheets, termed β1–β4, extending between residues 2–8, 10–13, 15–19 and 32–34 (Figure 73). The β-sheets are parallel to each other and to the orientation of the hydrogen-bonded β-strands they form (Figure 73b). Furthermore, the organisation of the regions 10-19 ad 30-37 into β-strands was supported by the cryo-EM model of Aβ42 fibrils proposed by Yang et al[61].

Considering these models, the peptide arrays' results suggest that **2i**, which is conformationally constrained, might affect the β-sheet formation of Aβ(15-19) and Aβ(28-40), which are essential regions for Aβ aggregation. This hypothesis is supported by the observation that **2i** binds monomeric FITC-Aβ42 with an app. K_D value of 103 nM (Table 26), which is in the same range as the app. K_D values of Aβ42 self-assembly (198 nM)[28] and cross-assembly with IAPP (48.5 nM) [28]. Taken together, these results indicate that MIMs might behave as competitors for the binding on the same surfaces involved in Aβ self-assembly, which is consistent with their design concept. Noteworthy, fluorescence spectroscopy and CD studies revealed that **2i** displays a strong self-association propensity

(app.K_D: 34.43 (±10.3) nM) (Figure 26), whereas the concentration of **Fluos-2i** solutions used for the peptide array studies was 0.5 or 1 μM, suggesting that the peptide is not monomeric in the conditions of the experiment. Hydrophobic interactions, occurring between the decamers and aggregated **Fluos-2i**, could hinder binding segments, and this might explain why a large amount of unspecific binding was observed in the peptide arrays (Figure 45).

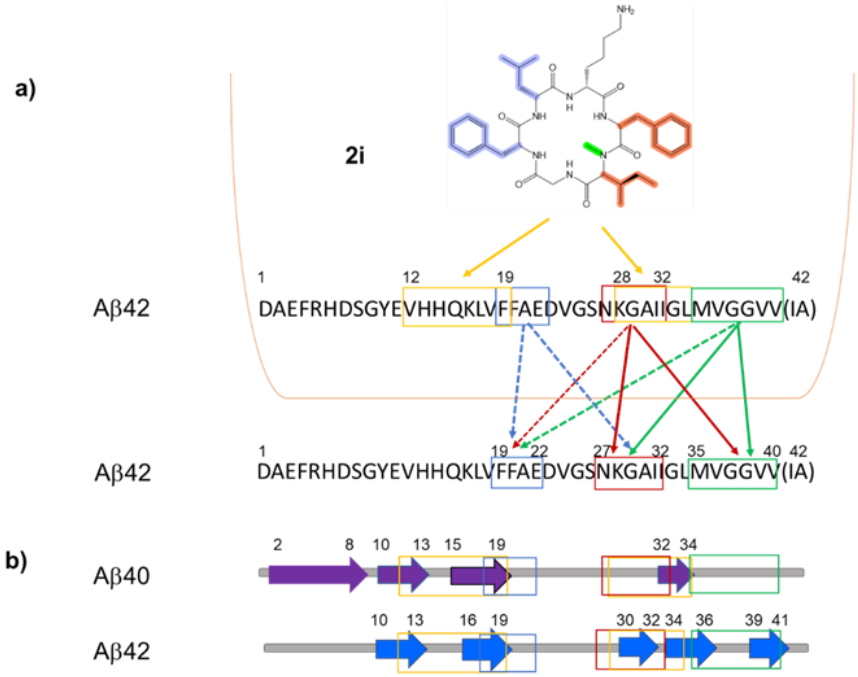

Figure 74. Identification of Aβ42 segments which interact with Fluos-2i. (a) The hot regions Aβ(19-22) (in blue), Aβ(27-37) (in red) and Aβ(35-40) (in green) involved in Aβ42 self-assembly were identified by Andreetto et al.[28] Solid and dashed arrows indicate self-interaction with hot and longer sequences, respectively. The scheme is adapted from ref[28]. The Aβ42 "binding cores" of **2i,** which comprise Aβ(12-19) and Aβ(28-34), are highlighted in orange. The IAPP residues maintained in the **2i** sequence are highlighted in blue (Phe[15] and Leu[16]) or red (Phe[23], Ile[26]). The N-methylation is indicated in green. (b) The β-strands in Aβ40 and Aβ42 fibrils resolved by Kollmer et al.[60] and Yang et al. [61], respectively, are indicated as arrows. Aβ40(42) segments involved in Aβ42 self-assembly or the interaction with **2i** are indicated with the same colour code as in (a). The scheme is modified from references[28,60,61].

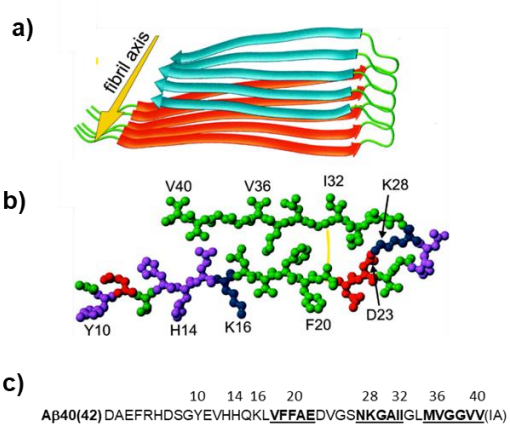

Figure 75. Visual representation of the binding regions of Aβ40 fibrils, according to the ssNMR model of Petkova et al.[68]. (a) Schematic representation of a single molecular cross-β unit of fAβ40, with in-register parallel β-sheets formed by residues 12–24 (orange ribbons) and 30–40 (blue ribbons). (b) single molecular cross-β unit, structured in a double-layer. (c) The Aβ40 binding regions involved in the self/cross-interaction surfaces identified by Andreetto et al. [28] are shown (bold, underlined). The residues of a single molecular cross-β unit reported by Petkova et al. [68] are displayed. (a) and (b) are taken from the reference [68], (c) is adapted from reference [28].

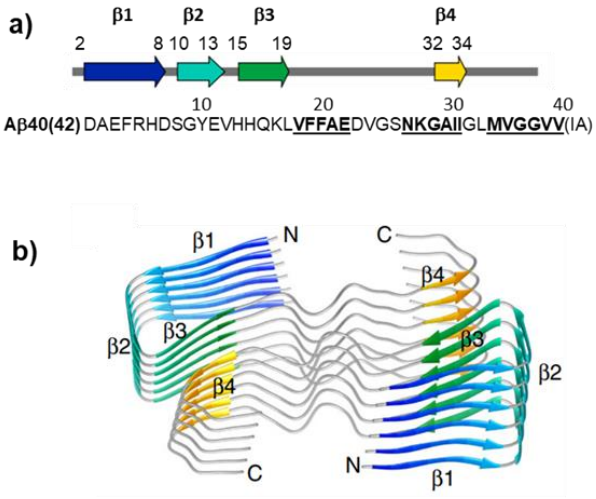

Figure 76. Binding regions in the context of the cryo-EM model of Kollmer et al. (a) the binding regions involved in Aβ self/IAPP-cross-interactions identified by Andreetto et al. [28] are indicated (bold, underlined). The visual representation of the Aβ segments organised in β-strands is based on Kollmer et al. [60]. (b) shows a ribbon diagram of the fibril, indicating the strands according to the colour code used in (a). The upper panel of (a) and (b) are taken from the reference [60].

IAPP and Aβ42 binding sites of Fluos 2i and cross-association

Colocalisation of IAPP and Aβ40(42) has been observed in patients with T2D and AD[28]. The epidemiological link between T2D and dementia might be explained by cross-seeding of IAPP and Aβ aggregation[29–32]. Noteworthy, Schröeder and coworkers suggest that the similar S-shaped polymorphism of IAPP and Aβ fibrils might increase the fibril surface involved in cross-nucleation events[62]. The authors reported that the structural similarity of the backbones of the fibrils is the highest when superimposing the cryo-EM models in an antiparallel arrangement. The interacting interfaces comprise the Gly-Ala-Ile segment at positions 24–26 of IAPP and 29–31 of Aβ40 fibril, solved by Gremer et al. [64]. A similar region was identified by Eisenberg and coworkers [63] when they performed restricted superimposing of their IAPP model with other Aβ structures, including that reported by Kollmer et al. [60,63]. Notably, these segments shared 50% similarity and were identified as cross-seeding cores in previous studies [28,186]. Additionally, Röder et al. [62] reported a further segment that can be superimposed in a parallel arrangement, spanning between the N-terminal strand of the S-fold in IAPP and the LS-shaped $A\beta_{1-42}$ polymorph, corresponding to 14-NFLVHSSNN-22 of IAPP and 16-KLVFFAEDV-24 of Aβ.

The peptide array showed that **2i** is a ligand of close regions of either one -Aβ(29-31) -or two – IAPP(14-22) and Aβ(16-24)- of the segments proposed by the authors in the context of the surfaces involved in IAPP/Aβ cross-nucleation. This evidence might explain the potent inhibitory activity displayed by MIMs against IAPP and Aβ cross-seeding.

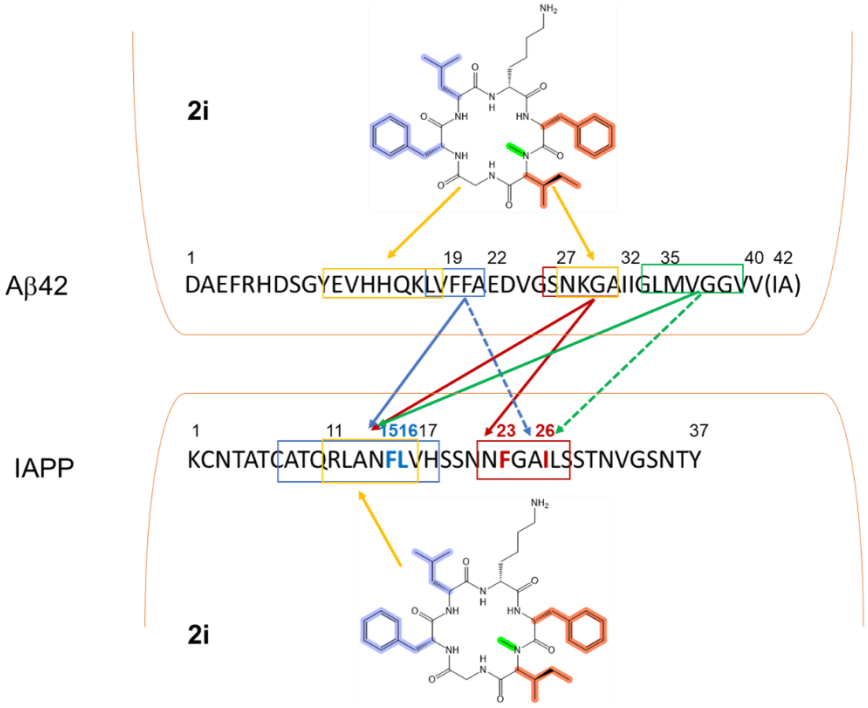

Figure 77. The segments of IAPP or Aβ42 which interact with Fluos-2i in the context of cross-nucleation events. The IAPP and Aβ42 binding segments of **Fluos-2i** (orange) overlap with some of the cross/self-interaction interfaces identified by Andreetto et al. (blue, red and green) [28]. The Figure is modified from reference[28].

5.4 Interaction between MIMs and amyloidogenic monomers

5.4.1 Interaction between MIMs and monomeric IAPP

ThT studies performed by mixing monomeric IAPP species and **2f**, **2g**, **2h** and **2i** revealed that the peptides suppressed completely the amyloid misfolding in 5-fold excess, (Figure 28a and 28b). The results were confirmed by TEM characterization (Figure 28c), which showed unordered structures, morphologically different from the typically tangled and filamentous amyloid fibrils. Cytotoxicity studies showed that these co-aggregates are non-toxic up to 7 days of incubations, and titrations of cell-damaging IAPP (100 nM) yielded IC_{50}s in the low nanomolar range (Figure 28d-g). Interestingly, the IC_{50}s obtained after seven days of aging were comparable to those obtained after 24 h, indicating that the inhibitory potential of the class does not decrease over time (Table 23).

The interaction with the mIAPP was further confirmed by fluorescence spectroscopy titrations, DB, CD interactions and cross-linking studies.

The app. K_D values of the binding affinity of MIMs for mIAPP fell in the same range as the app. K_D obtained for **Fluos-2i** self-assembly. This suggests that the cross-interaction is competing with the self-assembly at the molecular level, and an interaction between MIMs and the substrate might not be equimolar (Table 24). However, cross-linking studies performed on monomeric IAPP and various molar ratios of **2i** revealed the presence of hetero assemblies at low MW, thereby suggesting that the stoichiometry of the (IAPP/MIMs) complex might be 1/1 or 1/2 (Figure 78).

The CD-interaction studies performed by incubating monomeric IAPP and MIMs in an inhibitory fold confirmed that **2i** and **2g** interfered with the misfolding process. Remarkably, in both cases, the CD characterization of the (IAPP/**2g** or **2i**) mixtures aged for 24 h revealed the presence of soluble species with more β-sheet content than that observed for IAPP alone. Contrary to IAPP, no precipitation due to fibrillogenesis was observed, and TEM analysis revealed the presence of amorphous species (Figure 78).

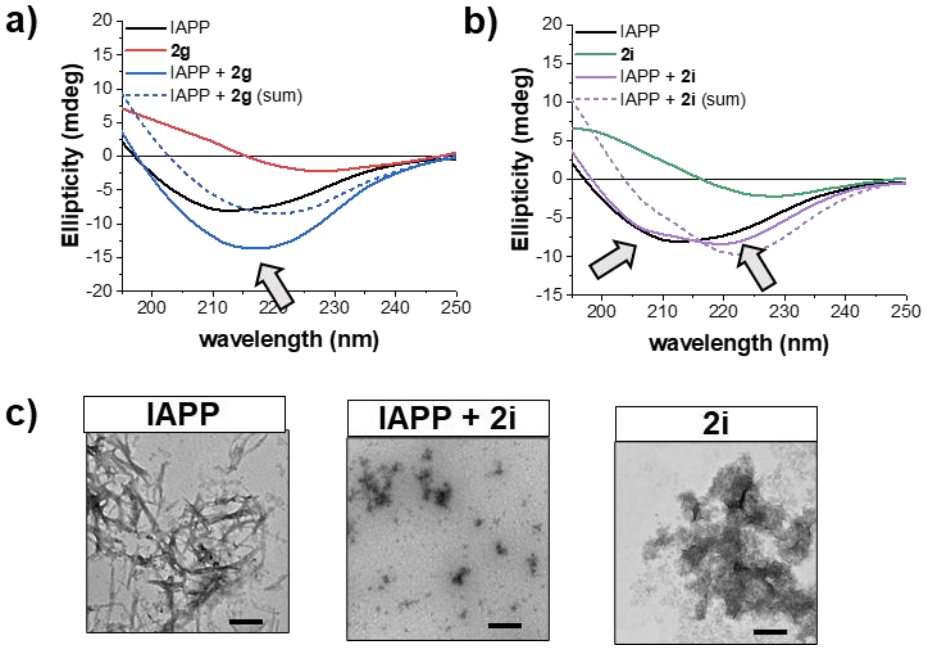

Figure 78. 2g and 2i block monomeric IAPP misfolding into β-sheet rich and insoluble fibrils. (a-b) Far-UV CD spectroscopy studies of incubation of IAPP + **2g**/**2i** after 24 h of aging show different structural elements than IAPP alone after resuspension. The negative bands are indicated with arrows. (c) TEM analysis of incubations from (b) shows the presence of IAPP fibrils and amorphous aggregates in the samples containing **2i** (scale bar 100 nm). Spectra and TEM pictures are shown in Figures 33 and 34.

Incubations of IAPP with equimolar **2i** revealed the occurrence of an interaction until 6 h, confirming that the interaction is concentration-dependent and can slow down IAPP misfolding but not suppress it. Finally, only a transient interaction between monomeric IAPP and **2g linear** was observed, confirming a) that minimal IAPP-derived residues are sufficient for the interaction between IAPP and MIMs sequences and b) that the head-to-tail cyclisation stabilises structural elements of the peptide sequences promoting high-affinity interaction.

Eisenberg and coworkers suggested that in the first steps of the amyloid assembly, IAPP monomers can fold into helical structures that dimerise via π–π stacking interaction on the hydrophobic surfaces of two Phe[15][101]. This dimer is on-pathway to IAPP fibrillogenesis. The Phe[15] residue is critical for IAPP self-assembly, as confirmed by the single and double Ala mutation studies performed by Bakou et al.[100]. Remarkably, this residue is included in the binding core region of **2i**. However, imagining that a small peptide-like **2i** could interfere with the helical intermediate is difficult, due to the large surfaces involved in this process.

A previous study by Kayed et al.[57] suggested a different view of the mIAPP structure. In this study, the authors followed the thermal denaturing pathway of IAPP with CD. They proposed

that IAPP monomers adopt two distinct conformers: one non-amyloidogenic and another amyloidogenic, with the latter having higher contributions of both β-sheet and α-helix. The study suggested that at room temperature, mIAPP would populate both conformers at equilibrium.

Dupuis et al.[40] investigated the structural elements of mIAPP via ion mobility mass spectrometry (IMS/MS) and replica exchange molecular dynamics (REMD) simulations. Their results revealed the presence of two highly populated species of mIAPP, which could be identified as β-hairpin and helix-coil. Finally, Gazit and colleagues' work supported the hypothesis that π-π stacking interactions may provide energetic contribution, order, and directionality in the self-assembly of amyloid structures [193,194].

Taken together, the CD and the cross-linking studies suggest that **2i** and **2g** could stabilise the β-hairpin structure of monomeric IAPP, thus competing with IAPP amyloid assembly. π–π stacking between the aromatic side chains of Phe^{15} of IAPP with either Phe^{2} or Phe^{5} contained in MIMs sequences might mediate such interaction (Figure 79). Furthermore, hydrophobic interactions between the hydrophobic residues of MIMs' sequence and IAPP(11-16) might occur, as reported for other inhibitors[99,187,192]. This observation is supported by the fact that a similar mechanism was suggested for explaining the inhibitory activity of the templates MCIPs and ISMs. Altogether, the results suggested that MIMs contains the minimal IAPP derived elements necessary to display an inhibitory activity through the stabilization of a structure mimicking the β-hairpin conformation of IAPP, according to their design.

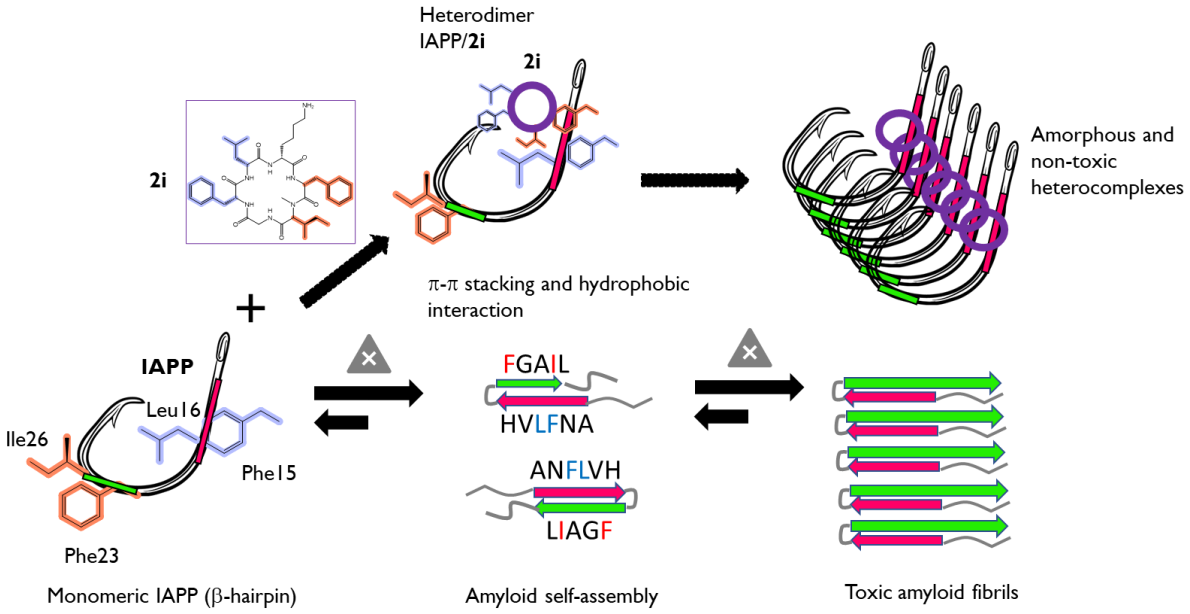

Figure 79. IAPP/2i interactions yield an off-pathway hetero-dimer. IAPP monomers adopt an amyloidogenic β-hairpin conformation. MIMs might compete with the self-association of IAPP β-hairpin monomers through a π–π stacking interaction between Phe^{15} and Phe^{5} (or Phe^{2}) and hydrophobic interactions with IAPP(11-16), indicated in magenta. This interaction might be responsible for redirecting the amyloid self-assembly to forming unstructured and non-cytotoxic hetero-assemblies. Scheme based on references [10, 100].

5.4.2 Interaction between MIMs and mAβ42

2f, 2g, **2 h** and **2i** strongly suppress Aβ42 amyloidogenesis and mediated cell damage (Figure 44). ThT studies revealed that all MIMs could inhibit Aβ42 fibril formation in 5-fold excess, and titrations of cytotoxic Aβ42 after six days of aging yielded IC_{50}s (Aβ42500 nM) in the submicromolar range (Figure 45a and b). TEM analysis confirmed the presence of unstructured species, suggesting that MIMs redirect Aβ42 amyloid assembly to off-pathway co-assemblies (Figure 45e).

The app K_D values for cross-interaction between MIMs and Aβ42 were obtained by fluorescence titration assays and supported the strong inhibitory potential of MIMs. (Figure 46, Table 26) . **2f**, **2g**, **2h** and **2i** bound monomeric FITC-Aβ42 with an app. K_D value that is close to these of Aβ42 self-assembly and cross-assembly with IAPP[28]. This evidence supports the hypothesis that MIMs may act as an alternative binding partner in the interaction between Aβ42 and other species.

The Aβ42 binding sites of **2i** include the cores Aβ(12-19) segment, or VHHQKLVF, and Aβ(28-34) or KGAIIGL. The results of three peptide arrays revealed that **2i** binds with higher affinity the first segment, suggesting that the interaction might occur between Phe^{19} and Phe^{5} or Phe^{2}, as for IAPP. Of note, Cukalevski et al.[172] reported that Phe^{19} has a pivotal role in Aβ assembly, as Leu substituting this residue readily reduced the aggregation rate.

The second and weaker binding core contains a sequence of apolar amino acids, which might interact with MIMs through hydrophobic interaction.

However, previously reported mechanistic studies on the interaction between the parent peptide **R3-GI** and Aβ42 [97] revealed that the ISMs are active at very low concentrations and use multivalent interactions, which may dramatically increase their ability to sequestrate Aβ42 monomers. **R3-GI** self-assembly is likely required but not sufficient for its amyloid inhibitor function. Due to their self-assembly propensity, MIMs and the ISMs might share similar mechanistic features for inhibiting Aβ40(42) amyloidogenesis.

Altogether, the fact that the inhibitory effect of MIMs towards IAPP and Aβ42 fibrillation is alike, suggests that the amyloid targets of MIMs interaction must share some structural similarities.

Hoyer et al.[38] reported that stabilising β-hairpin in monomeric Aβ40 can inhibit its amyloid self-assembly. In their studies, NMR spectroscopy was used to determine the complex structure formed by Aβ40 β-hairpin and the inhibitor $Z_{Aβ3,}$ a small affibody. The selected conformation of Aβ40 complex consisted of four-stranded antiparallel β-sheets and four α-helices. The characterization revealed that the chosen conformation of Aβ40 is β-a hairpin structure and that the segments Aβ(17-A23) and Aβ(30-36) make intramolecular backbone hydrogen bonds to form the two central strands of the β-sheet. Numerous studies[37,41,99,183,195] have identified Aβ β-hairpin conformation as the target to block its amylogenesis. The current results indicate that also MIMs might adopt this mechanism.

5.5 Identification of amyloid oligomeric species

Due to their transient nature, developing a robust methodology to identify cytotoxic amyloid oligomers in both *in vivo* and *in vitro* systems remained challenging for decades[53,177,180,196]. Several reports have pointed out that simple methods such as SDS-PAGE, Western blotting or SEC can be misleading when used to reveal the distribution of the size of the oligomers before electrophoresis or elution [176,179].

In 2003, Kayed and coworkers reported an antibody, A11, [52] that specifically recognises micellar and not soluble, low MW amyloid fibrils and soluble oligomers. To produce it, Kayed and coworkers synthesised a molecular mimic of soluble oligomers based on a structural oligomeric model of Aβ42. TEM analysis determined the morphology of the immunoreactive species and revealed that the antibody recognised the same structure shared by both spherical oligomers, formed at early time points, and by elongated "protofibrils" that predominate in later time points[53]. Notably, the antibody recognises structural elements shared by amyloid oligomers of different peptides and proteins.

After characterising the interaction between MIMs and amyloid monomers, and their potent anti-amyloidogenic effect, one of the questions of this work was whether MIMs could interact, and possibly interfere, with the cell damage caused by aged amyloidogenic species. Such property is desirable to develop molecules effective in the late stages of amyloid diseases when preformed oligomers and fibrils display their toxicity[33,42,43,45,52,127].

To answer this question, a method based on three known characteristics of amyloid oligomers was established: lack of amyloid-like structures[177], cytotoxicity[56], and immunoreactivity towards (anti-)oligomer A11 polyclonal antibody [52].

Four techniques were applied in this thesis to study the presence and maturation of the oligomers:

i) ThT binding to follow the kinetics of amyloidogenesis.
ii) Quantification of the cell damage via MTT assay.
iii) Oligomer-specific immunoreactivity via (anti-)oligomer A11 polyclonal antibody.
iv) Morphological characterization via TEM.

Regarding the ThT reactivity, the unordered and prefibrillar oligomeric species were non-ThT reactive, as expected by the limited amount of β-sheet in their structure. Cytotoxicity studies performed at different incubation times and previous fibril formation revealed a steady increase in cytotoxicity. This effect has been previously explained by the cell membrane disruption mediated by the oligomers, displayed by forming ion-leaking pores and by upregulating oxidative stress [45–48].

Regarding DB analysis with (anti-)oligomer A11 polyclonal antibody, IAPP species showed the highest immunoreactivity between 1 and 3 h of incubation, suggesting that low-MW oligomers and protofibrils are formed within this time point.

Aβ42 species were reactive within 2 and 6 h of incubation. In agreement with the previous observation, morphological analysis performed by TEM revealed the presence of unordered and dispersed structures for all the time points. In contrast, typical amyloid fibrils were observed for IAPP and Aβ42 aged for 24 h. Oligomeric Aβ42 was also found to affect the LTP in an ex vivo model, as previously reported[55,99,127]. Additionally, the oligomerisation of N-terminally labelled TAMRA-Aβ42 was characterised by studying the effect of the ACMs inhibitors on the microglia uptake of oAβ42[127]. The results showed that the label does not affect the amyloid assembly of Aβ42, and the oligomerisation of TAMRA-Aβ42 was comparable to that of immunoreactivity, cytotoxicity, and morphology (Figure 50).

5.6 Effect of MIMs on the amyloid assembly of oIAPP

Developing amyloid inhibitors that interact with preformed cytotoxic and on-pathway aggregates is crucial for drug development and treatment of misfolding diseases after their onset.

In this work, after establishing a system for detecting the presence of already formed IAPP oligomers (oIAPP), three questions were assessed: a) does the inhibitor **2i** block the formation of oIAPP? b) does **2i** interfere with the amyloid assembly of oIAPP formed early point? And c) does **2i** block the amyloidogenesis of oIAPP formed later (protofibrils)?

Effect of **2i** on oIAPP formation

The inhibitory effect of **2i** on the formation of oIAPP was followed via ThT assay, MTT reduction assay, DB studies and TEM characterization.

As expected from the studies performed on the self-assembly of monomeric IAPP in the presence of MIMs, no ThT binding was detected. DB studies confirmed that in the presence of **2i**, the immunoreactivity towards A11 was suppressed entirely. In contrast, MTT assays revealed that **2i** blocks the cell damage mediated by the formation of cytotoxic oIAPP within the first 6 h of incubations. Evidence of the effect of **2i** against the formation of cytotoxic species after this time point was given by the cytotoxicity assays performed in the context of the amyloidogenesis of IAPP monomers. Thus, the results confirm that **2i** interacts with the very early steps of the amyloid formation and readily redirects IAPP self-assembly to form off-pathway aggregates.

Interestingly, while several classes of peptide inhibitors were developed against the formation of Aβ40(42) oligomers[90,93,127], mainly small molecules have been tested against oligomeric IAPP.

An example is epigallocatechin gallate (EGCG)[197], a naturally occurring flavonoid extracted from green tea that has entered early clinical trials for treating Alzheimer's, Parkinson`s, and Huntington's diseases. When tested as an anti-IAPP inhibitor, EGCG showed a partial effect at substoichiometric molar ratios and full inhibition of the ThT binding in equimolar to excess amounts[197]. NMR studies revealed that the decrease in ThT signal might be due to a competing mechanism between EGCG and ThT for the binding sites on the fibril surface. However, it was also found that EGCG redirects the aggregation through a fast consumption of IAPP monomer to a larger nonfibrillar aggregate, which EGCG may interact with[197]. Ion mobility mass spectrometry studies were performed to elucidate the possible inhibition mechanisms. The results revealed that EGCG binds to the monomer (up to 3 molecules of EGCG), inducing a conformational change inhibiting the fibril formation through hydrophobic interactions, as confirmed via ThT and TEM studies[198]. Interestingly, this small molecule was found to interact also with preformed IAPP oligomers and fibrils through a complex mechanism involving π–π stacking interaction, as proposed for MIMs activity[197]. Of note, EGCG and MIMs share some similar structural features. ECGG is just 1/3 smaller than MIMs (MW= 458,372 g/mol); it includes three aromatic rings (MIMs bear two) and eight H-donor groups, whereas **2g** and **2i** contain nine and seven, respectively.

5.7 Effect of 2i on oIAPP formed in the early steps of the amyloidogenic process

ThT binding assay, MTT reduction assay, Dot Blotting and TEM imaging were used to characterise the effect of **2i** on the maturation of oligomers formed at early time points of the IAPP amyloidogenesis (Figure 20). The studies revealed reduced A11-reactivity, which suggests that oIAPP, in complex with **2i**, undergoes a conformational transition that interferes with the antibody recognition. This hetero-complex is non-cytotoxic, non-ThT reactive and

morphologically amorphous, indicating that **2i** redirects the amyloid assembly to forming off-pathway hetero-complexes.

In detail, ThT studies revealed no increase of the binding within 24 h of incubation and complete suppression of the cytotoxic effect of the oligomers on RIN-5mf cells. The DB analysis performed with (anti-)oligomer A11 polyclonal antibody revealed decreased immunoreactivity upon incubation with the inhibitor. TEM imaging showed a structural transition from IAPP amorphous structures to non-amyloid-like assemblies.

In its activity towards already formed oIAPP and fIAPP, **2i** shares further similarities with the small molecule EGCG[197]. The addition of EGCG at various points of the IAPP fibrillation pathway modifies the morphology of the aggregates, depending on the time point of EGCG addition[199]. Interestingly, when EGCG is added to early nuclei, the preformed oligomers were remodelled to smaller, thinner aggregates with minimal β-sheet structure and were classified as off-pathway species[197]. In contrast, when EGCG was added to late-stage oligomers and fibrils, the morphology of the resulting aggregates maintained an overall fibrillar shape[197].

These observations suggest that the small cyclic peptides **2i** share some interesting properties of small molecules and the small β-breakers described by Gazit and coworkers. The results suggest that the shortening conferred inhibitory properties towards different targets, which might be driven by π–π stacking interactions between the hydrophobic surfaces of the Phe and the amyloidogenic substrate[191,193,194].

5.8 Effect of 2i on oIAPP formed in the late steps of the amyloidogenic process

The anti-amyloidogenic effect of **2i** on mature oIAPP was investigated via ThT binding assay, MTT reduction assay and TEM characterization. Of note, DB was not used as a method, as the immunoreactivity of A11 towards IAPP decreases after 3 h. This result suggests that non-soluble fibrillar species form after this time, as previously reported[52]. The studies revealed that the amyloidogenesis and cytotoxicity of aged oIAPP, and possibly protofibrils, was suppressed upon incubation with **2i** (Figure 41). TEM analysis of incubations at late time points revealed a highly structured network of needle-like species, which does not resemble the canonical amyloid morphology.

The morphological difference between these “needles” and the amorphous co-assemblies formed with monomeric IAPP or early-stage oligomers could be explained by different populations of A11 reactive species. However, TEM analysis did not show a clear difference between 1 h aged and 3 h aged oIAPP.

The results suggest that the interaction of **2i** with unordered oligomers redirects the amyloid misfolding towards forming amorphous but structured co-assemblies. In contrast, higher amounts of soluble and structured protofibrils might be a template for developing needle-like

structures. Despite their different morphologies, all the species are not binding ThT and are non-cytotoxic.

Interestingly, other peptides, such as the ACM[127], were found to redirect the amyloid self-assembly of IAPP and Aβ42 to the formation of hetero-fibrillar structures. The hetero-fibrils formed between the ACM and IAPP present beneficial differences from amyloid assemblies, such as lack of cytotoxicity, lack of ThT binding, effective cellular clearance and reduced thermostability. Even though the structure of IAPP/ACM hetero-fibrils has not been elucidated yet, their proposed formation mechanism may involve lateral co-assembly of two or more "protofilament"-like stacks of IAPP and ACM molecules[127].

Abedini et al.[45] reported that, in contrast to β-sheet rich oAβ40(42), toxic, IAPP lag phase oligomers revealed an apparent partial helical structure, which is consistent with studies of truncated h-IAPP analogues fused to maltose binding protein; studies of h-IAPP aromatic residue mutants, and NMR studies of soluble IAPP variants [101,200]. The authors reported that Phe^{15}, Phe^{23} and Tyr^{37} are largely solvents exposed in the lag phase of IAPP aggregation[45], allowing them to interact with the reactive groups of the inhibitor. On the other hand, Kayed et al.[57] and Dupuis et al. [40] showed that IAPP monomers could adopt an β-hairpin-rich structure on-pathway to amylogenesis[183]. Mirecka et al. reported the structural characterization via NMR of IAPP-β-hairpin in a complex with an inhibitor, HI18. The study revealed that the β-hairpin is formed by the segments IAPP(12-29) and stabilised through hydrophobic and aromatic interactions between Phe^{15} and Phe^{23}, involved in the complex with H18.

Taken together, this evidence supports the hypothesis that the potent inhibitory effect of MIMs towards IAPP monomers and oligomers might occur by the same mechanism. The inhibition might occur through stabilising IAPP β-hairpin by aromatic interactions between Phe^{5} and Phe^{2} of **2i** and Phe^{15} of IAPP and hydrophobic interactions between **2i** and IAPP(11-16). It has also been reported that structural features of the parent peptides ISMs might redirect the formation of -amyloid co-assemblies through the generation of alternative reactive surfaces[97]. The addition of **2i** at different steps of the IAPP self-assembly might generate morphologically distinct intermediates depending on the structure of the substrates and the transient nature of the species involved in the process.

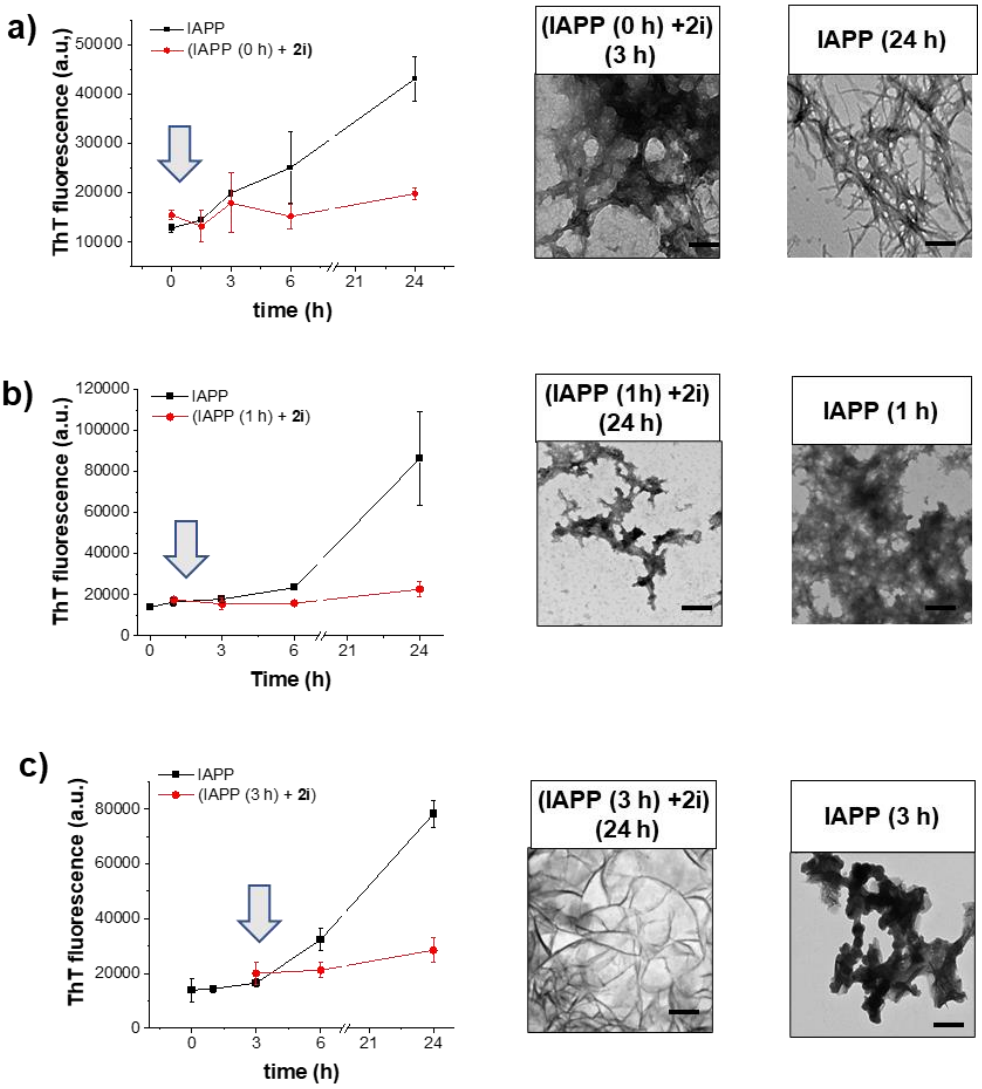

Figure 80. Comparison of the morphologies observed via TEM after incubating different IAPP species and 2i. (a-c, left panel) ThT assays from Figures 40, 41 and 42 respectively, showing when the time of inhibitor addition. Large amorphous structures were observed after incubating mIAPP with **2i** for 24 h (a). Structured but non-fibrillar morphologies were observed after incubating oIAPP (1 h) and **2i** for 24 h (b). A complex network of needles was imaged after incubating mature oIAPP (3 h) and **2i** for 24 (c) (scale bar, 100 nm).

5.9 Effect of MIMs on oAβ42

The inhibitory potential of MIMs towards the highly neurotoxic Aβ42 oligomers was also investigated. In this context, the characterization was limited to the study of oligomers formed in the early stage of the amyloid assembly. The studies used ThT binding assay, MTT binding assay and TEM imaging as methods.

As observed for oIAPP in chapters 4.9.3 and 4.9.4, the incubation of preformed Aβ42 oligomers (oAβ42) with **2i** redirected the amyloid self-assembly to form non-toxic and non-amyloidogenic species. The decrease of the ThT binding when **2i** was incubated in higher fold excess could be explained in two ways: the interaction could reverse oAβ42 by shifting the transient oligomeric species to their monomeric state, or **2i** could interact with oAβ42 by

forming off-pathway hetero-oligomers. These hetero-oligomers are non-cytotoxic and non-amyloidogenic. However, the morphology of the species observed after six days of incubation revealed the presence of highly organised structures that do not resemble either amyloid fibrils or amorphous monomers (Figure 53).

Of note, the property of inhibiting the cytotoxicity mediated by preformed oAβ42 was previously reported for the Amyloid Core Mimics (ACM). My work on their effect on the oAβ42 cytotoxicity, the inhibition of the LTP mediated by oAβ42, and the phagocytosis of Aβ42 oligomeric species were published in "Taş et al." [127]. The ACMs did not reverse the formation of amyloidogenic species after addition to preformed oligomers but instead blocked it until 5 h of incubation[127]. Conversely, MIMs were found to reverse or dissolve oAβ42 in a concentration-dependent fashion. A similar result was reported by Richman et al.[93] when characterising cyclic hexamers self-assembling in nanotubular structures. In fact, in the presence of CP-2, the amount of A11 reactive Aβ42 oligomers significantly diminished, supporting the evidence that the interaction between CP-2 and Aβ40(42) may alter the aggregation of Aβ from an "on-pathway" to an "off-pathway" mechanism.

Other classes of small cyclic peptides displayed desirable inhibitory properties towards Aβ42 oligomer formation and amyloidogenesis. The work of Tadamasa et al. can give an example.[90], in which head-to-tail cyclised pentapeptides were designed by using the amyloidogenic region Aβ(16-20) as a template. The peptide sequences, stable in the human plasma until 6 h, were further modified by incorporating an additional phenyl group at the βPhe4 side chain (β-Ph) position. The lead compound 3 was found to induce the production of an inhibitor-embedded off-pathway oligomeric species that exhibited a lower β-sheet content, lower seeding ability, and less toxicity than the native oligomers.

5.10 Effects of 2i on preformed fIAPP and fAβ42

The effect of **2i** on preformed fibrillar IAPP (fIAPP) and Aβ42 fibrils (fAβ42) supports the hypothesis of an interaction that can interfere with different phases of the amyloid formation.

The ThT results presented in Figure 43, chapter 4.9.5, still need clarification. Although a decrease of ThT binding in a mixture of fIAPP/**2i** could be explained with the disaggregation or remodeling of the fibrils, the increase of ThT fluorescence of fIAPP incubations cannot be explained. However, the cytotoxic effect of preformed fIAPP coated with an excess of the inhibitor was significantly suppressed. These results suggest that **2i** could either a) disassemble the preformed IAPP seeds and redirect them to off-pathway species or b) interfere with the "dock-lock" mechanism of the fibril elongation, which sees monomers docking the fibril tips and then undergoing structural organisation to fold into the fibrillar morphology [35].

The results observed by incubating late-stage oligomeric IAPP or protofibrils with **2i** suggested that the inhibitor might compete with monomeric IAPP in the fibril elongation process, as the species observed via TEM were mainly fibrillar but non-amyloid. However, TEM characterization of the complex formed by (fIAPP/ **2i)** after 6 days of incubation

revealed the presence of amorphous species. Of note, TEM analysis of the hetero complexes formed by oIAPP and **2i** was performed after 24 h of incubation, therefore, a complete transition of the needle-like structures into into an amorphous species cannot be excluded.

Our group has previously reported that a selectively N-methylated IAPP analogue (**IAPP-GI**) could suppress completely IAPP fibrillation, regardless of the stage of its amyloidogenesis[95]. Most importantly, **IAPP-GI** (1/1) redissolved IAPP fibrils and reversed already-started fibrillogenesis, as revealed by ThT and MTT studies[95].

Recently, Abyoie et al.[201] reported that the tetrapeptide TNGQ and analogues could inhibit IAPP fibril formation by stabilising its helical intermediate. TEM imaging revealed that TNGQ could effectively disaggregate 72 h aged fIAPP within a few hours of co-incubation. Maity and coworkers reported a naphthalimide-appended oligopyridyl amide based α-helical mimetic, DM 1, added at different points along the IAPP fibrillation curve, completely perturbed IAPP amyloidogenesis, including the disaggregation of mature IAPP fibrils[202]. Interestingly, both classes of compounds were found to interact with and stabilise the helical structure of IAPP. Finally, the small molecule EGCG was found to disaggregate preformed fIAPP through a complex mechanism, including also π–π stacking interaction on the hydrophobic surfaces of the fibrils[197].

As shown in chapter 4.13.4, incubation of preformed fAβ42 with a high excess of **2i** resulted in decreased ThT signal and reduction of fAβ42 cytotoxicity within 24 h. Interestingly, TEM analysis revealed the presence of a complex network of hollow spherical species (Figure 53), which were observed only when the cytotoxicity of fAβ42 was reduced. The results suggest this morphology is linked to a non-toxic heterocomplex formed by Aβ42 and **2i**. Of note, based on the current results, it cannot be excluded that the fibril dissolution mediated by **2i** might generate cytotoxic intermediates[93].

It is essential to notice that evidence of this mechanism was also given by the ThT studies performed on oAβ42 in the presence of **2i** in 20-fold excess. The ThT signal increase observed previous **2i** addition is proportional to the formation of fAβ42 in the system. The fluorescence decrease upon **2i** addition suggests that the peptide might disassemble (or coat) the preformed fibrils.

Richman et al.[93] reported that cyclic peptide hexamers forming nanotubes could effectively disassemble preformed Aβ42 fibrils, as the ThT signal of 4-days aged Aβ42 was reduced by the addition of the cyclic peptide CP-2[93]. The disaggregation of fibrillar Aβ42 by CP-2 was also confirmed by TEM analysis which showed the transformation of the fibrillar network to amorphous structures.

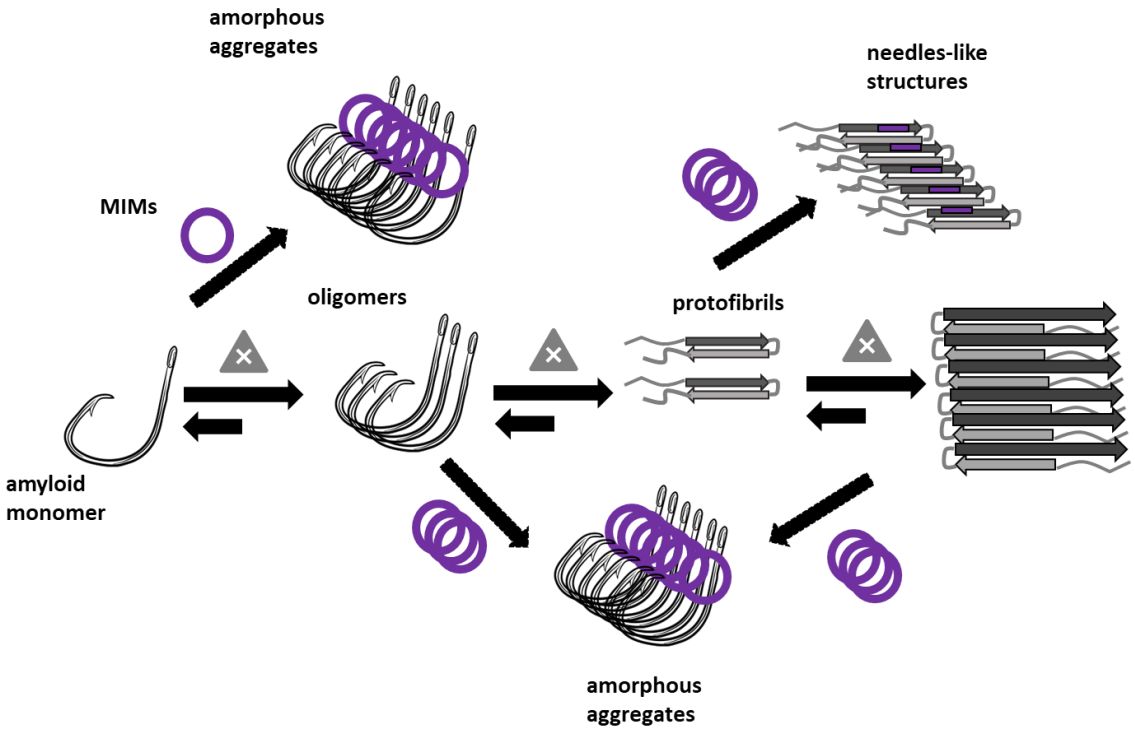

Figure 81. 2i redirects different amyloid species to off-pathway non-toxic co-assemblies. The addition of **2i** at different stages of the amyloid assembly suppresses amyloidogenesis and cytotoxicity. The mechanism of MIMs is not elucidated yet, but it could involve aromatic interactions and the capacity to sequestrate different amyloid species through their strong self-assembly propensity; the interaction between **2i** and different amyloid species has other effects, including redirecting, remodelling, and possibly disaggregating the preformed amyloidogenic species.

Altogether, the results suggest that **2i** effectively remodels preformed fibrillar structures into hetero-assemblies of diverse morphology, with decreased cytotoxic effect. According to the current results, this inhibitory potential is stronger in the case of fIAPP, whereas it is only transient when it comes to fAβ42 remodelling.

5.11 Effects of 2i and 2g on self- and cross-seeding events

The interaction between amyloid monomers and a preorganised fibrillar surface is a process known as nucleation. This process is dependent a) on the amount of fibrils, which provide a catalytic surface enhancing the rate of nucleation, and b) on the concentration of monomers in the system, forming the nuclei on the surface of an already existing aggregate [33,168–170,177].

The self-seeding experiments revealed that **2i** effectively suppresses the monomeric nucleation of IAPP and Aβ42 fibrillogenesis mediated by adding their preformed seeds.

It has been previously suggested that cross-seeding of mAβ42 by fIAPP accelerates Aβ42 amyloid self-assembly and vice versa. This could be the molecular link between the pathogenesis of T2D with AD[29–32]. In this work, I described how **2i** was found to suppress various cross-seeding events mediated by fAβ42 or fIAPP.

This effect can be explained by a mechanism of action involving the interaction with both monomers and fibrils. I have previously discussed how **Fluos-2i** is a potent ligand of three

of the five regions involved in the Aβ42/IAPP self- and cross-interactions. This is important in explaining its inhibitory function towards the amyloid assembly of monomeric species.

The results obtained when coating preformed fIAPP or fAβ42 with **2i** (Chapters 4.9.5 and 4.13.4) revealed that the inhibitor could effectively remodel the fibrils to non-toxic and non-amyloidogenic assemblies. These results suggest a synergic effect of MIMs towards the different species involved in the cross-seeding events.

Inhibition of self- and cross-seeding events is a property that was previously observed for the parent generations of peptides, designed by using IAPP and Aβ40 interaction surfaces as templates. In particular, some of the ISMs showed a strong suppression of IAPP cross-seeding mediated by adding preformed Aβ42 seeds [97]. The presence of N-methylation plays an essential role in the seeding events, as revealed by the potent inhibitory activity of IAPP-GI towards IAPP self-seeding[95]. Furthermore, peptides mimicking Aβ core regions[127] were found to display a strong inhibitory effect towards the self- and cross-seeding of Aβ42 and to redirect the fibrillogenesis to the formation of non-toxic or seeding competent heterofibrils. Remarkably, in the context of inhibiting the cross-seeding events, peptides able to inhibit IAPP were high-affinity ligands of Aβ and vice versa, according to their design[95,97,127,137].

5.12 Proteolytic stability, BBB crossing potential and effect of 2g and 2i on oAβ42 mediated hippocampal LTP impairment

Proteolytic stability (*in vitro*) and drug-like properties

Proteolytic stability is a vital requirement in drug development and represents one of the significant drawbacks of peptide drug candidates. The head-to-tail cyclisation is a powerful tool to confer proteolytic stability towards both exopeptidases due to the lack of free N- and C- termini, and endopeptidases, thanks to the increased rigidity of the molecule compared to the linear precursors[87]. Overall, structural rigidity, receptor selectivity and biochemical stability allow cyclic peptides to be promising therapeutic agents or biochemical tools[86,87,119].

Small cyclic peptides may be broadly applicable for bactericidal, immunosuppressive, and anti-angiogenic uses. Furthermore, they can be used as biochemical tools due to their properties as receptor ligands, RNA binders and enzyme inhibitors[87].

Examples of bactericidal agents are cyclodecapeptide tyrocidine and analogues from a culture extract of a soil bacillus[203]. This class of cyclic peptides is characterised by high structural rigidity and amphipathic nature, conferred by the presence of two β-chains linked by proline residues and four intramolecular hydrogen bonds. This model was proposed in the 1950s [204] and later confirmed by X-ray crystallography[205]. The mode of action of the molecule is driven by the interaction between hydrophobic portions of cyclic peptide and membrane lipid, resulting in the lysis of the bacterial cell membrane. However, tyrocidine A is limited to topical use, as membrane lysis can happen even in mammalian cells[87].

Cyclosporin A is a cyclic peptide isolated from a natural source, and it is an immunosuppressant clinically used to prevent graft rejection. Cyclosporin A can freely pass the cell membrane, probably due to its cyclic structure[87].

Another therapeutic application of small cyclic peptides involves anti-angiogenic application. Integrins modulate the signalling regulating the interaction between the cell and extracellular matrix. A functional integrin unit comprises two subunits, a and b, in various combinations of isotypes. Many integrins recognise the tripeptide sequence -Arg-Gly-Asp- (RGD) for interacting with the extracellular ligands. Interestingly, it was found that peptides containing RGD could inhibit tumour cell growth[87]. Cyclic peptides with RGD sequence were more potent than the linear counterparts Cyclo-RGDfV (EMD 66203, f stands for D-Phe) itself can promote tumour regression by inducing apoptosis of angiogenic blood vessels. In addition, the cyclo-RGD compound can deliver nanoparticles filled with an anticancer drug to the area where the tumour is growing[87].

The first question assessed in this work regarding the drug-like properties of MIMs concerned their proteolytic stability in human plasma.

The analysis of the resistance of **2g** and **2i** towards human plasma proteases in vitro was performed by HPLC and MALDI-TOF MS. Both **2g** and **2i** were found to be highly stable in human plasma ($t_{1/2}$ > 48 h). In contrast, their linear precursors were readily degraded within 1 h. The results also indicate that MIMs showed enhanced stability towards plasma proteases compared to template **2e**, as they are circa 4-fold more resistant ($t_{1/2}$ > 11 h).

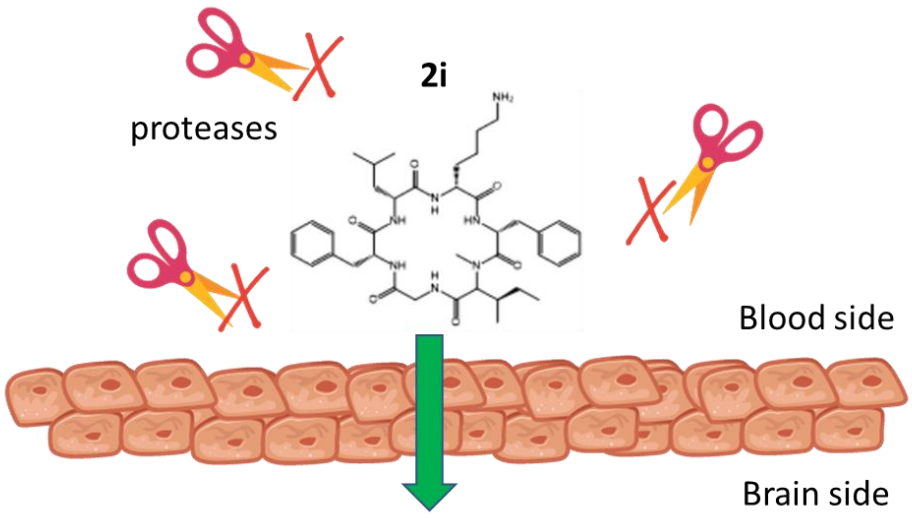

Figure 82. 2i is proteolytically resistant towards plasma proteases (in vitro) and crosses a BBB cell model. Proteolytic stability and membrane permeability are critical requirements in drug development. **2i** displayed optimal drug-like properties in *vitro* system, as it was proteolytically stable for 48 h and crossed a BBB cell model with a good Papp.

The results suggest two key features conferring enhanced pharmacokinetics properties: a) the head-to-tail cyclisation, compared to the linear sequences and b) a dramatic shortening of the parental sequence, compared to **2e**.

Such results are in good agreement with the literature, as cyclisation and N-methylation of peptides of ring size 3-7 were found to enhance pharmacokinetic properties, such as passive membrane permeability and metabolic stability[206] when compared to the linear precursors.

BBB crossing properties (*in vitro*)

Penetration of the blood-brain barrier (BBB) is a challenging but critical property of drug candidates targeting central nervous system disorders (CNS). Several approaches have been developed to confer BBB permeability to peptides, including coupling to molecular vectors[146], known as shuttles. The BBB shuttle concept includes Trojan horse antibodies and any other molecule capable of transporting cargo into the brain parenchyma without affecting the BBB integrity[145–147].

However, MIMs present similar characteristics to other cell-penetrating peptides (CPPs), such as a molecular weight below one kilodalton, a minimum number of hydrogen bond donor groups, and a small polar surface, which make them potential candidates for cytosolic delivery through blood–brain barrier or the gastrointestinal barrier[88,145–147], without structural modifications. In fact, small cyclic peptides are thought to cross physiological membranes through passive diffusion as small molecules[86–88,164]

Thus, the permeability of N-terminally fluorescein-labelled **2i** (**Fluos-2i**) through the BBB was assessed by using a well-established of human cerebral microvascular endothelial cells (hCMECs) grown as confluent monolayers on Transwell membranes[143,148]. **Fluos-2i** crossed the monolayer with an apparent permeability (Papp) at 2 h of 11.99 x 10^{-6} (± 1.41) cms^{-6} (mean (± SEM), which is comparable to the Papp value of **2e**.

Effects of 2g and 2i on oAβ42-mediated impairment of hippocampal LTP.

Evidences for the theory of oAβ42 oligomer involvement in the pathology of AD comes from studies showing that Aβ42 oligomers negatively affect long-term potentiation (LTP) in the hippocampus [55,175], a phenomenon thought to underlie the synaptic plasticity necessary for memory formation and learning [204]. Intriguingly, it has also been demonstrated that picomolar concentrations of Aβ42 (as in physiological conditions) positively affect synaptic plasticity [7,175]. It has been previously reported that the detrimental effects of nM concentrations of Aβ42 oligomers on LTP can be reversed by therapeutically-relevant concentrations of memantine (1 μM)[207]. Thus, soluble and neurotoxic Aβ oligomers are suggested to mediate the impairment in glutamatergic signalling associated with AD pathology[55]. Aβ42 is thought to affect N-methyl-d-aspartate (NMDA) receptor function and abolish the induction of long-term potentiation (LTP), which is a crucial phenomenon in memory formation (136).

2i and **2g**, like previously reported classes of inhibitors derived from IAPP or Aβ40(42) sequences, displayed a potent effect against oAβ42 mediated impairment of hippocampal LTP[98,99,127]. These findings support the physiological relevance of the *in vitro* results and suggest that MIMs are potential anti-amyloid leads for AD and T2D.

6 Conclusion and outlook

Elucidating the molecular mechanism of amyloid formation and conferring drug-like properties to peptides are ambitious but crucial challenges.

In my PhD thesis work, I characterized the properties of peptide inhibitors abbreviated MIMs, derived from the minimal IAPP elements involved in the amyloid self- and cross- assembly of IAPP with Aβ40(42). In fact, my thesis is the final step -for now- of several rounds of optimization of peptides designed by using the putative IAPP interacting surface with itself and Aβ42 as template.

The sequence of MIMs is 2/3 shorter than the template peptide **2e**, nevertheless, MIMs are potent inhibitors of both IAPP and Aβ42 amyloidogenesis and cytotoxicity. This evidence is supported by their IC_{50}s, which are in the nanomolar to sub micromolar range. Despite the minimal IAPP-derived elements, MIMs bind with high affinity different intermediates of the amyloidogenic pathway, and they seem to interfere with the structural organization of amyloid core-regions of IAPP and Aβ42. This suggestion is in accordance with previous studies from our group[81,137] and several structural models of fIAPP and fAβ42 [28,61–63]. Importantly, MIMs were found to interact and suppress amyloid self-assembly of monomers and oligomers, and to remodel preformed fibrillar aggregates.

Furthermore, in this work, I combined different techniques to follow the formation of IAPP and Aβ42 oligomers, considered the most toxic species involved in the amyloidogenesis. Finally, but not less importantly, MIMs showed high proteolytic stability in human plasma *in vitro*, BBB crossing in a cell model and a clear effect on Aβ42-mediated hippocampal LTP impairments in an ex-vivo system, which supports the in vitro findings.

Taken together, these results indicate that MIMs are valuable molecular tools to gain a better understanding of the amyloidogenesis and potential leads for anti-amyloid drugs in AD and T2D.

The foreseeable steps to continue the studies on MIMs include:

- Understanding the molecular determinants of MIMs activity via selective Ala mutations and scrambled sequences.
- Elucidating the mechanism of action and the role of the self-assembly propensity via NMR and DLS characterization.
- Studying the selectivity of MIMs by testing their interaction and activity towards other amyloidogenic and non-amyloidogenic proteins and polypeptides.
- Characterizing the needles-like structures observed when incubating aged oIAPP and **2i**, and their putative beneficial properties.
- Obtaining a deeper insight into the property of disaggregating preformed amyloid fibrils.
- Expanding their pharmacokinetics characterization by studying the permeability of other physiological membranes (i.e., gastric membrane).
- Studying the effect of MIMs in mouse models of AD and T2D *in vivo*.

7 Appendix

7.1 Appendix Figures

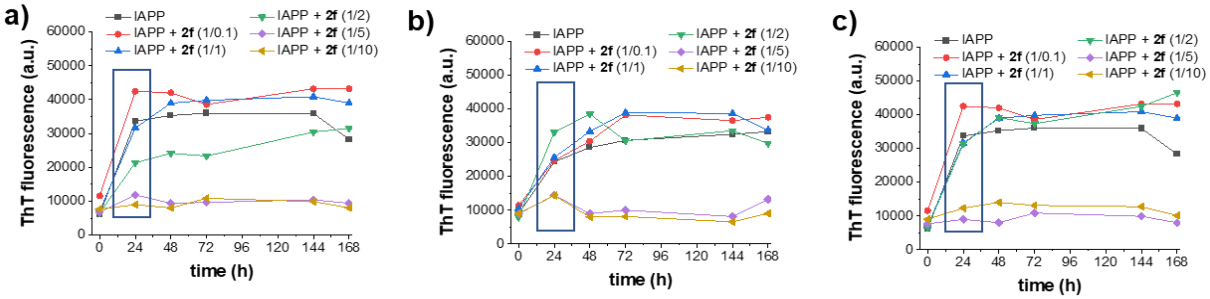

Figure A1. Effects of 2f on IAPP fibrillation. (a-c) The effects of **2f** on IAPP fibril formation was monitored via ThT binding assay (IAPP/**2f**, 1/0.1-1/10) in three independent assays. The time point at which aliquots of these solutions were administered to RIN-5mf cells is marked with a blue frame (24 h); the results of the corresponding MTT assays are shown in Figure A2. Incubations were prepared in IAPP ThT buffer containing 0.5% HFIP (IAPP, 6 μM) and incubated at 20ºC for 7 days. These three independent assays were used to generate Figure 27a, left panel.

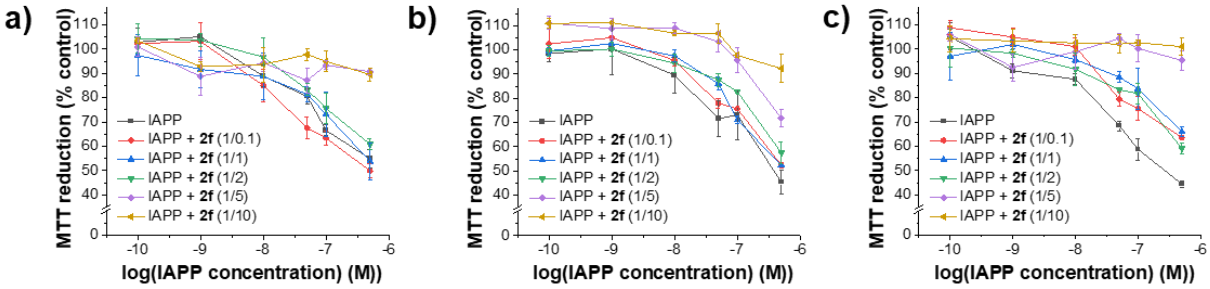

Figure A2. Effect of 2f on IAPP cytotoxicity after 24 h of incubations. (a-c) Effects of IAPP and IAPP/**2f** mixtures on IAPP cytotoxicity after 24 h of incubation (IAPP/**2f**, 1/0.1-1/10) followed via MTT assay (means (±SD) 3 wells). These three independent experiments were performed by administering aliquots of the peptide incubations used for the ThT assays shown in Figure A1 to RIN-5mf cells. Incubations were prepared as described in Figure A1. The mean of the IC_{50}s obtained from these assays (Figure A3) are reported in Table 23.

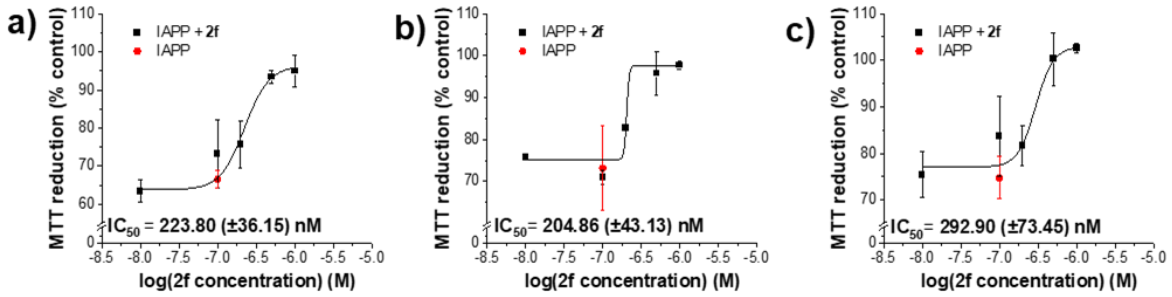

Figure A3. IC_{50}s curves of inhibitory effects of 2f on the formation of cell damaging IAPP fibrils after 24 h of aging. (a-c) Sigmoidal curves were obtained with the same values of the three independent MTT reduction assays shown in Figures 2a-c (IAPP 100 nM) (means (±SD) 3 wells). Cell damage was determined by the MTT reduction assay as described in 3.2.9. The cytotoxicity of IAPP alone is included in each graph for comparison (red symbol). The mean of the IC50s obtained at this time point is reported in Table 23.

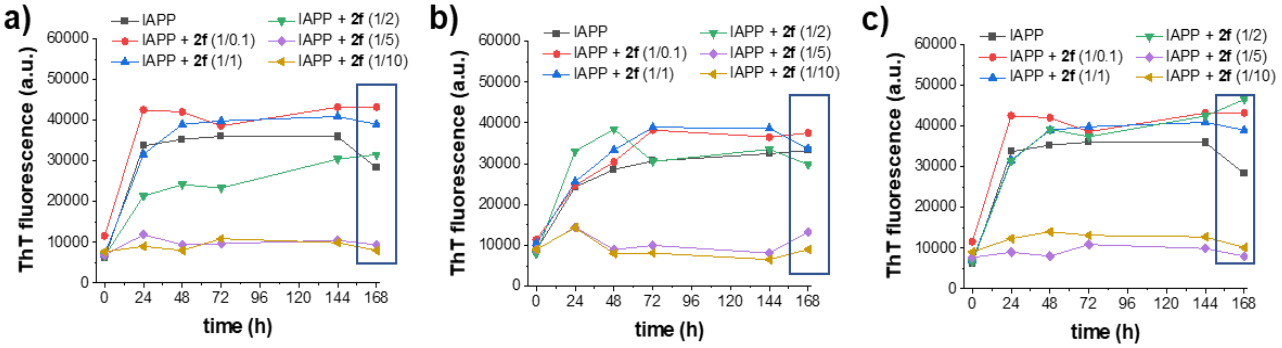

Figure A4. Effects of 2f on IAPP fibrillation after 7 days of incubation. (a-c) Effects of **2f** on IAPP fibril formation after 7 days of incubation (IAPP/**2f**, 1/0.1-1/10) as revealed by three independent ThT assays. Incubations were prepared in IAPP ThT buffer containing 0.5% HFIP (IAPP, 6 μM) and incubated at 20ºC. After 7 days of incubation, aliquots of these solution were used to perform the three independent MTT assays shown in Figure A5. The ThT binding at the time point of cell-administration is marked with blue frame. These three independent assays were used to generate Figure 27a, left panel.

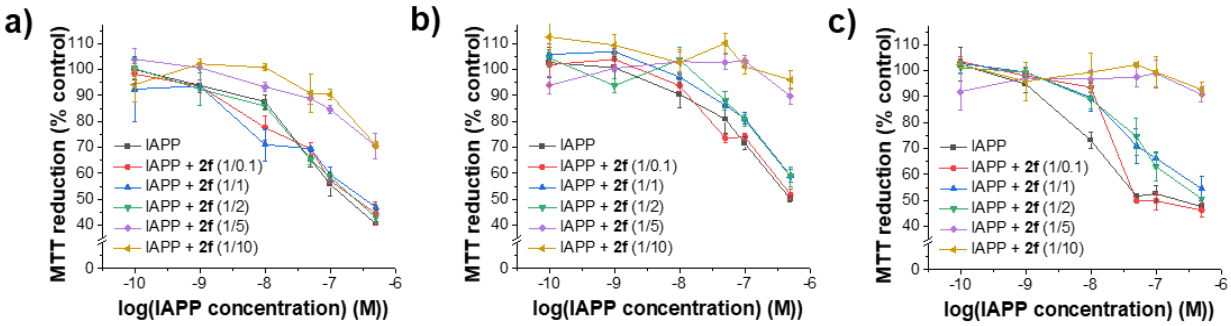

Figure A5. Effect of 2f on IAPP cell-damage after 7 days of incubation. (a-c) The effects of **2f** on IAPP cytotoxicity on RIN-5mf cell after 7 days of incubation was followed via MTT assay (IAPP/**2f** 1/0.1-1/10) (means (±SD) 3 wells). These three independent assays were performed with aliquots of peptide incubations used for the ThT assays shown in Figure A4. Incubations were prepared in IAPP ThT buffer containing 0.5% HFIP (IAPP, 6 μM) and incubated at 20ºC. These assays were used to generate Figure 27a, right panel.

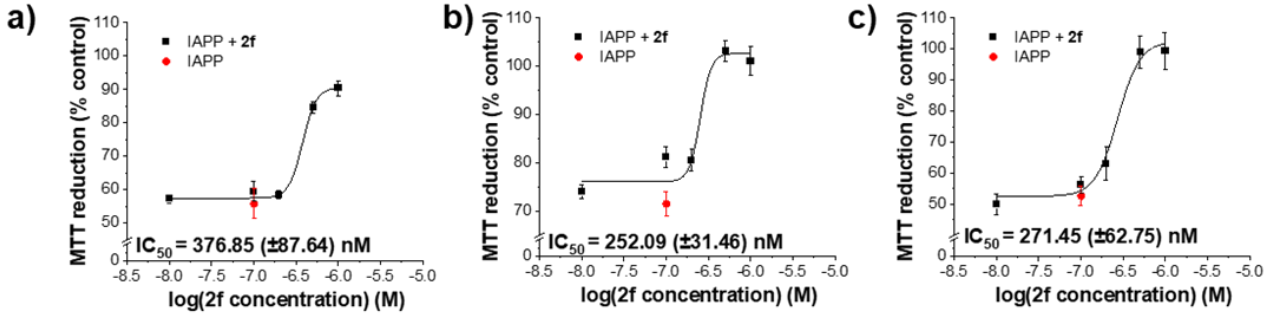

Figure A6. IC_{50} curves of inhibitory effects of 2f on the formation of cell damaging IAPP fibrils after 7 days of incubation. (a-c) Sigmoidal curves were obtained with the values of the three independent MTT reduction assays shown in Figures 2a-c (IAPP 100 nM) (means (±SD) 3 wells) and used to obtain the IC_{50}s reported in Table 23. Cell damage was determined by the MTT reduction assay as described in 3.2.9. The cytotoxicity of IAPP alone is included in each graph for comparison (red symbol). These assays were used to generate Figure 28d.

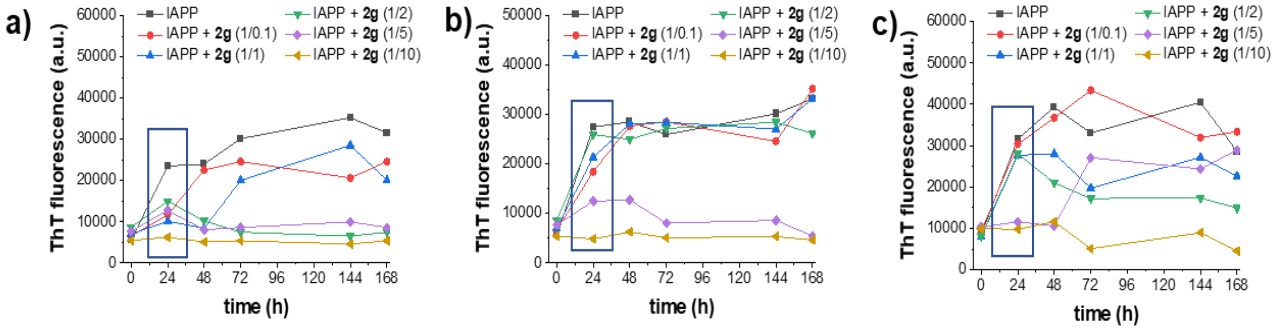

Figure A7. Effects of 2g on IAPP amyloid self-assembly after 24 h of incubation. (a-c) Effects of **2g** on IAPP amyloid self-assembly (IAPP/**2g**, 1/0.1-1/10) as revealed by three independent ThT assays. Incubations were prepared in IAPP ThT buffer containing 0.5% HFIP (IAPP, 6 μM) and incubated at 20ºC. After 24 h of aging, aliquots of these solutions were administered to RIN-5mf cells to evaluate the effect of **2g** on IAPP cell damage. Results are shown in Figure A8. These three independent assays were used to generate Figure 27b, left panel.

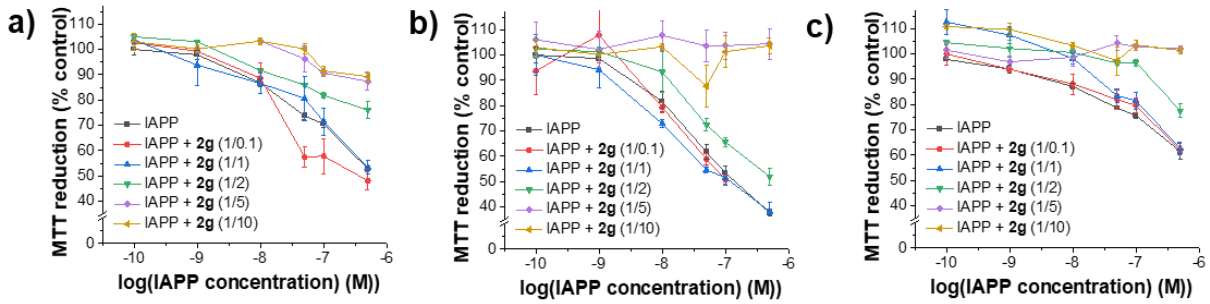

Figure A8. Effects of 2g on IAPP cell-damage after 24 h of incubation. (a-c) The effects of **2g** on IAPP cytotoxicity after 24 h of incubation was studied via MTT reduction assay (IAPP/**2f**, 1/0.1-1/10). These three independent assays were performed by administering aliquots of the peptide solutions used for the ThT assays shown in Figure A7 to RIN-5mf cells (means (±SD) 3 wells) as described in 3.2.9. The mean of the IC_{50}s obtained from these assays (Figure A9) are reported in Table 23.

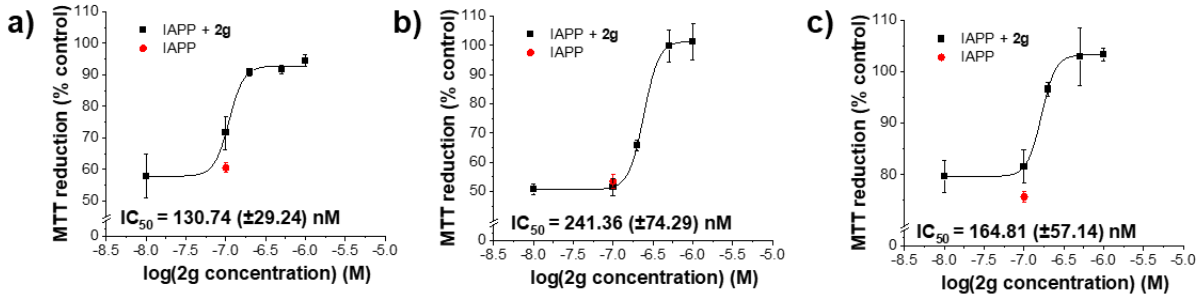

Figure A9. IC_{50}s of inhibitory effects of 2g on the formation of cell damaging IAPP fibrils after 24 h of incubation. (a-c) Sigmoidal curves were obtained with the values of the three independent MTT assays shown in Figure A8 (IAPP, 100 nM) (means (±SD) 3 wells). The cytotoxicity of IAPP alone is included in each graph for comparison (red symbol). The mean of the three IC_{50}s is reported in Table 23.

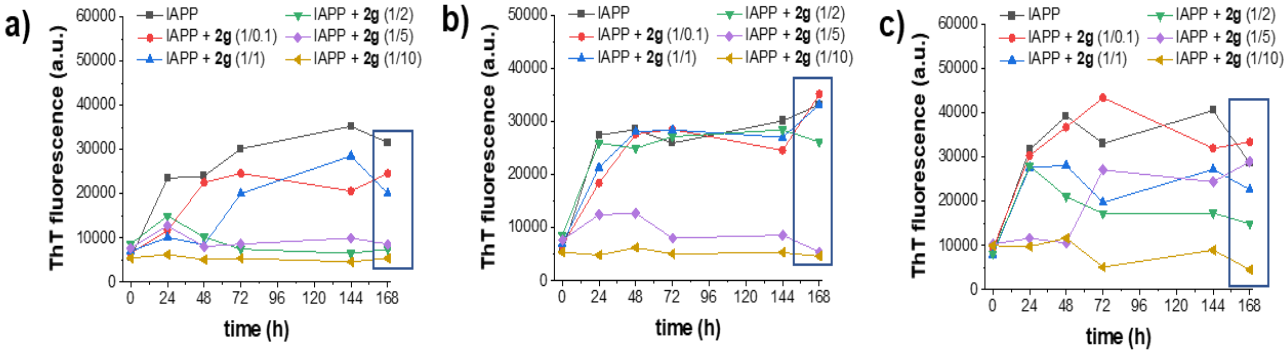

Figure A10. Effects of 2g on IAPP fibril formation after 7 days of incubation. (a-c) The effects of **2g** on IAPP fibrillation as determined by three independent ThT binding assays (IAPP/**2g**, 1/0.1-1/10). Incubations were prepared in IAPP ThT buffer containing 0.5% HFIP (IAPP, 6 μM) and incubated at 20ºC. The time point at which aliquots of the same incubations were administered to RIN-5mf cells for the cytotoxicity studies is indicated with a blue frame. These three independent assays were used to generate Figure 27b, left panel.

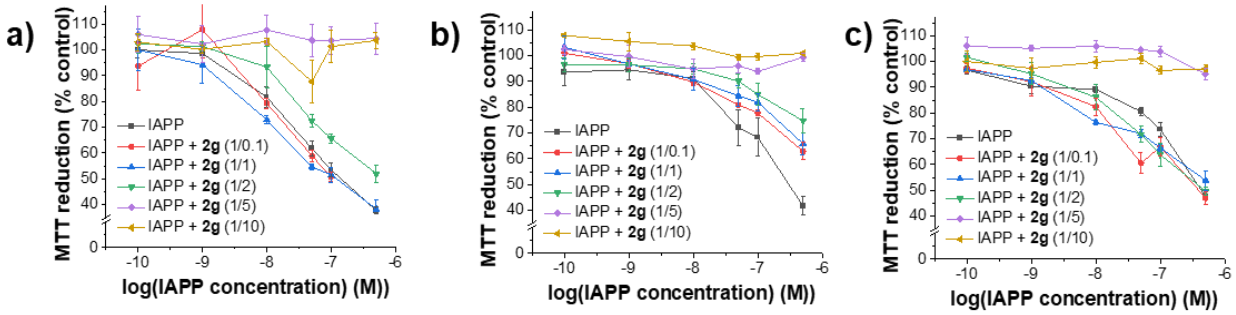

Figure A11.Effects of 2g on IAPP cell-damage after 7 days of incubation. (a-c) The effects of **2g** on IAPP cell-damage on RIN-5mf cells after 7 days of incubation was determined via MTT assay (IAPP/**2g**, 1/0.1-1/10). These three independent assays were performed by administering aliquots of the peptide solutions used for the ThT assays shown in Figure A10 to RIN-5mf cells (means (±SD) 3 wells). Incubations were prepared as described in Figure A10. Thes results of three independent assays were used to generate Figure 27b, right panel.

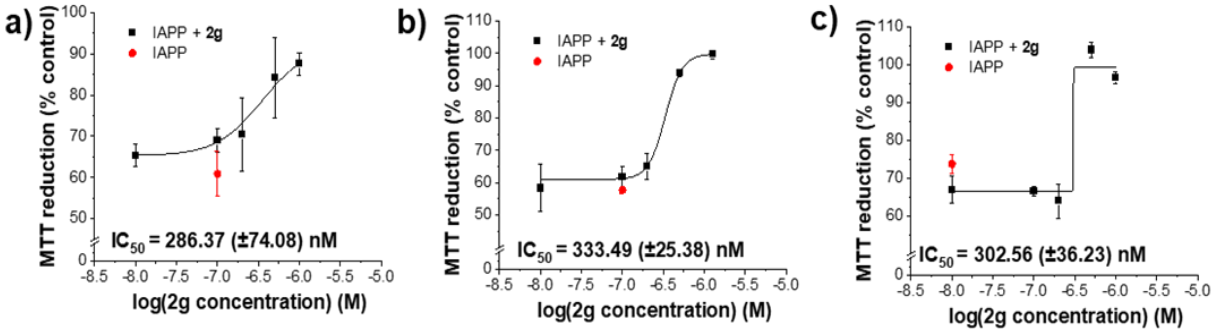

Figure A12. IC_{50}s values of inhibitory effects of 2g on the formation of cell damaging IAPP fibrils after 7 days of incubation. (a-c) Sigmoidal curves were obtained with the values of the three independent MTT assays shown in Figure A11 (IAPP, 100 nM) (means (±SD) 3 wells). The cytotoxicity of IAPP alone is included in each graph for comparison (red symbol). These three independent assays were used to generate Figure 28e and the mean of their values is reported in Table 23.

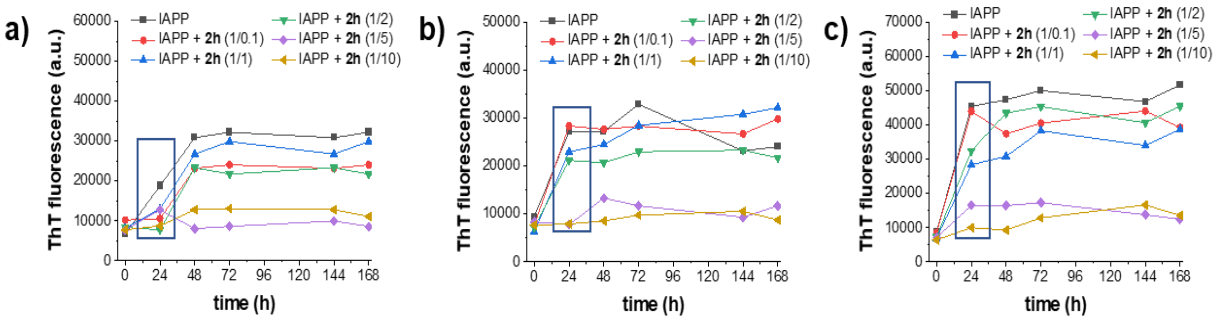

Figure A13. Effects of 2h on IAPP fibril formation after 24 h of incubation. (a-c) The effects of **2h** on IAPP fibrillation as determined by three independent ThT binding assays (IAPP/**2h**, 1/0.1-1/10).is shown. Incubations were prepared in IAPP ThT buffer containing 0.5% HFIP (IAPP, 6 μM) and incubated at 20ºC. Aliquots of the peptide solutions aged for 24 h were administered to RIN-5mf cells to perform the cytotoxicity studies shown in Figure A14. The ThT fluorescence of the time point of cell-administration is marked with a blue frame. These three independent assays were used to generate Figure 27c, left panel.

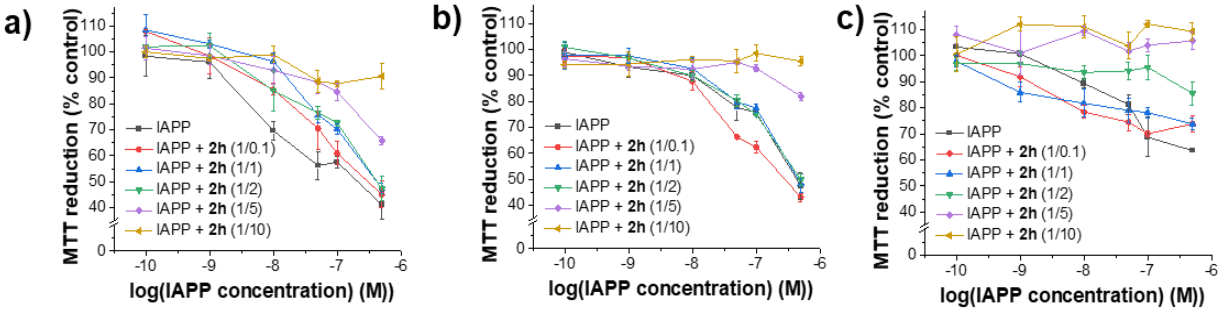

Figure A14. Effects of 2h on IAPP cell damage after 24 h of incubation. (a-c) The effects of **2h** on IAPP cytotoxicity on RIN-5mf cell after 24 h of incubation was followed via MTT assay (IAPP/**2h**, 1/0.1-1/10). These three independent assays were performed by administering aliquots of the incubations used for the ThT assays shown in Figure A13 to RIN-5mf cells (means (±SD) 3 wells). The mean of the IC_{50}s obtained from these assays (Figure A15) are reported in Table 23.

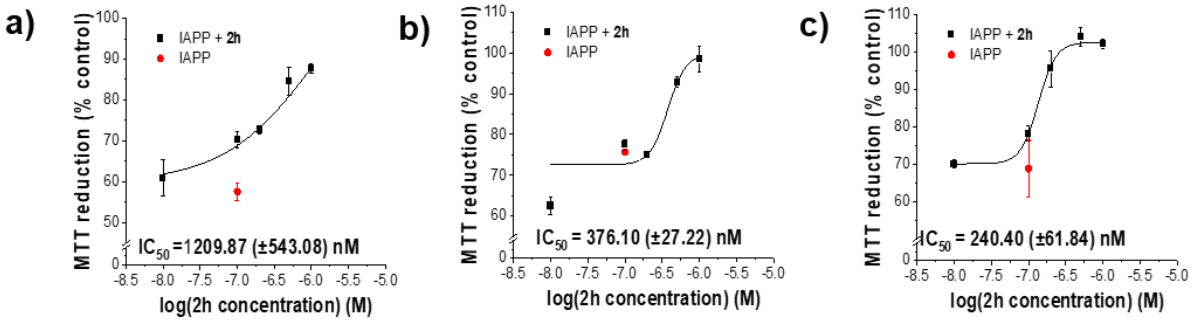

Figure A15. IC_{50}s of inhibitory effects of 2h on the formation of cell damaging IAPP fibrils after 24 h of aging. (a-c) Sigmoidal curves were obtained with the values of the three independent MTT assays shown in Figure A14 (IAPP, 100 nM) (means (±SD) 3 wells). The cytotoxicity of IAPP alone is included in each graph for comparison (red symbol). The mean of the three IC_{50} values obtained from these curves is reported in Table 23.

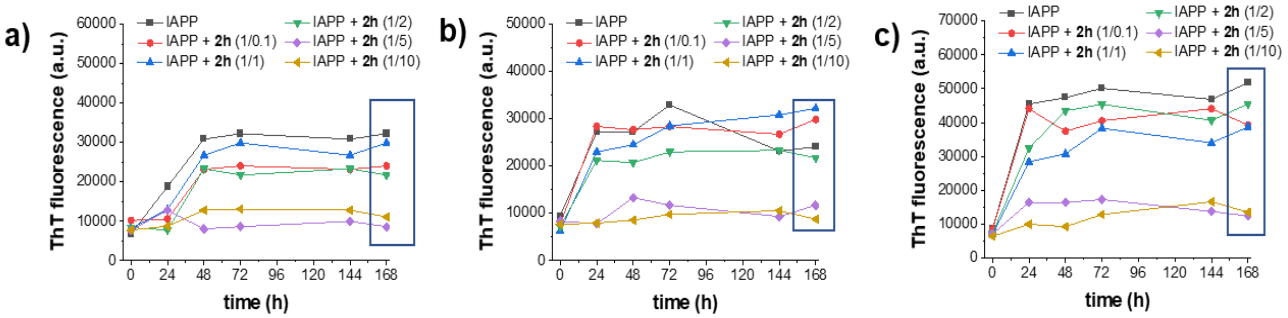

Figure A16. Effects of 2h on IAPP fibril formation after 7 days of aging. (a-c) The effects of **2h** on the amyloid self-assembly of IAPP were determined by three independent ThT binding assays (IAPP/**2h**, 1/0.1-1/10). Incubations were prepared in IAPP ThT buffer containing 0.5% HFIP (IAPP, 6 μM) and incubated at 20ºC. After 7 days of aging, aliquots of the same peptide solutions were incubated with RIN-5mf cells for performing the MTT assays shown in Figure 17. These three independent assays were used to generate Figure 27c, left panel.

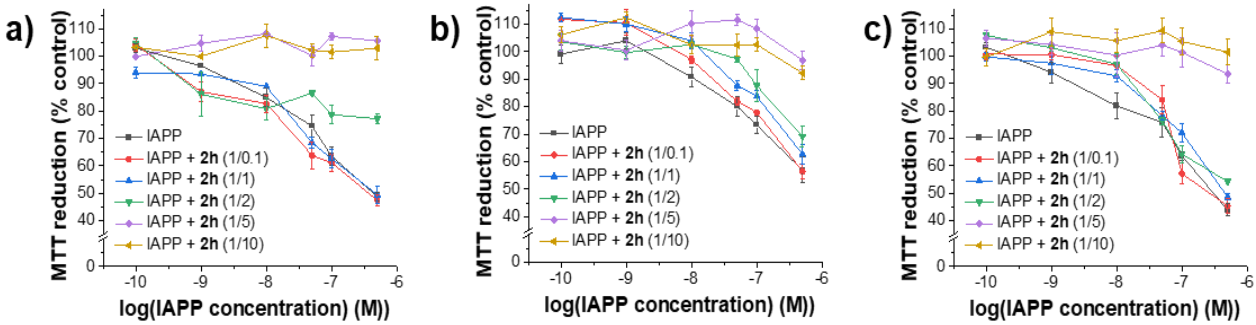

Figure A17. Effect of 2h on IAPP cell damage after 7 days of incubation. (a-c) Effects of **2h** on IAPP cytotoxicity on RIN-5mf cell after 7 days of incubation followed via MTT assay (IAPP/**2h** 1/0.1-1/10). Aliquots of the solutions described in Figure A16 were used to perform these three independent assays (means (±SD) 3 wells); their mean was used to generate Figure 27c, right panel.

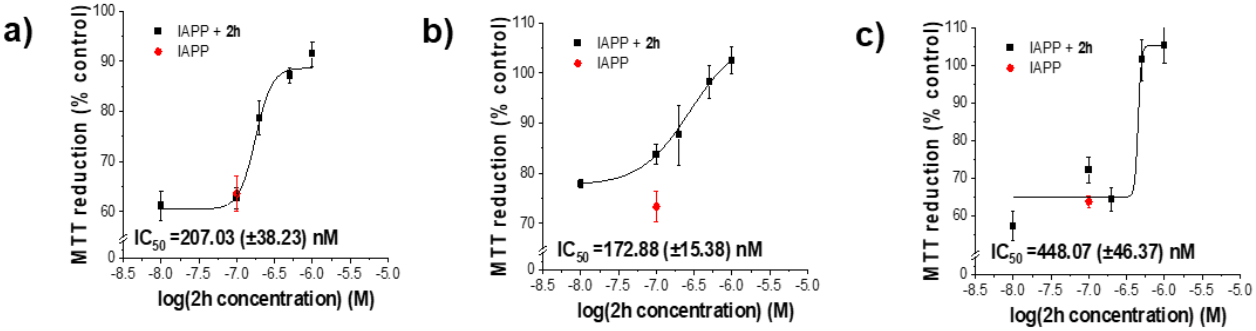

Figure A18. IC_{50}s of inhibitory effects of 2h on the formation of cell damaging IAPP fibrils after 7 days of aging (a-c) Sigmoidal curves were obtained from the data of the three independent MTT assays shown in Figure A17 (IAPP, 100 nM) (means (±SD) 3 wells). The cytotoxicity of IAPP alone is included in each graph for comparison (red symbol). These assays were used to generate Figure 28c, whereas the mean of the three IC_{50}s obtained from these curves is reported in Table 23.

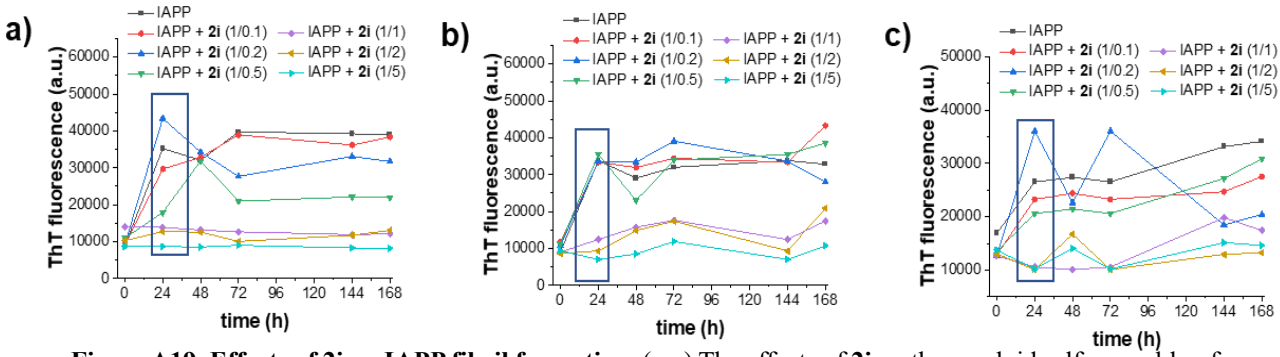

Figure A19. Effects of 2i on IAPP fibril formation. (a-c) The effects of **2i** on the amyloid self-assembly of IAPP was determined by three independent ThT binding assays (IAPP/**2i**, 1/0.1-1/10). Incubations were prepared in IAPP ThT buffer containing 0.5% HFIP (IAPP, 6 μM) and incubated at 20ºC. After 24 h days of aging, aliquots of these solutions were incubated with RIN-5mf cells for performing the three MTT assays shown in Figure A20. These three independent experiments were used to generate Figure 27d, left panel.

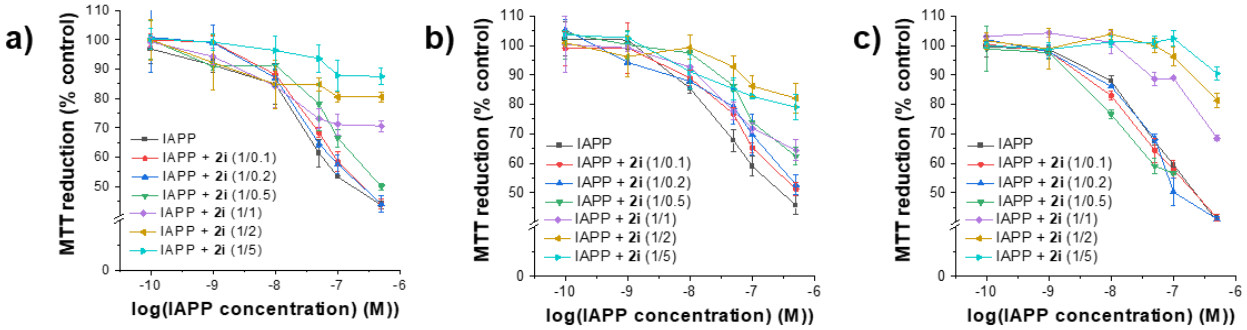

Figure A20. Effects of 2i on IAPP cell-damage after 24 h of incubation. (a-c) The effects of **2i** on IAPP cytotoxicity on RIN-5mf cell after 24 hours of incubation was assessed via MTT assay (IAPP/**2i**, 1/0.1-1/10). Aliquots of the solutions used for the ThT assays shown in Figure A19 were used to perform these three independent assays (means (±SD) 3 wells). The mean of the IC_{50}s obtained from these assays (Figure A21) are reported in Table 23.

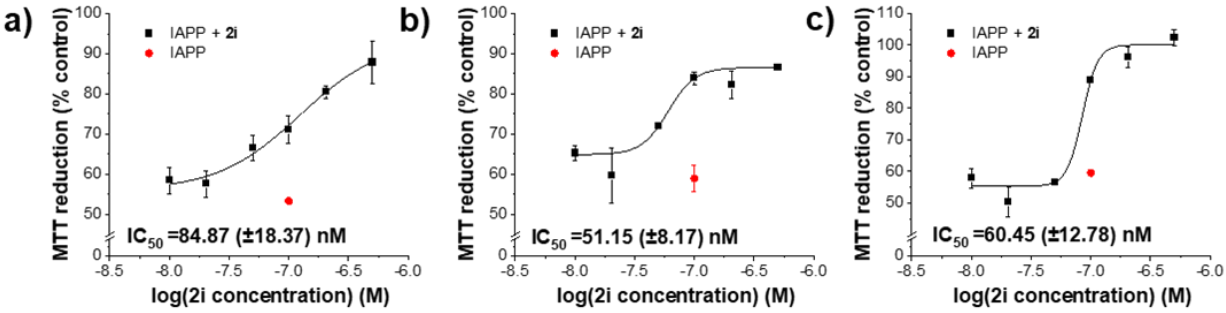

Figure A21. IC_{50} curves of inhibitory effects of 2i on the formation of cell damaging IAPP fibrils after 24 h of incubation. (a-c) Sigmoidal curves were obtained with the data of the three independent MTT assays shown in Figure A20 (IAPP, 100 nM) (means (±SD) 3 wells). The cell damage of IAPP alone is included in each graph for comparison (red symbol). The mean of the three IC_{50} values obtained from these curves is reported in Table 23.

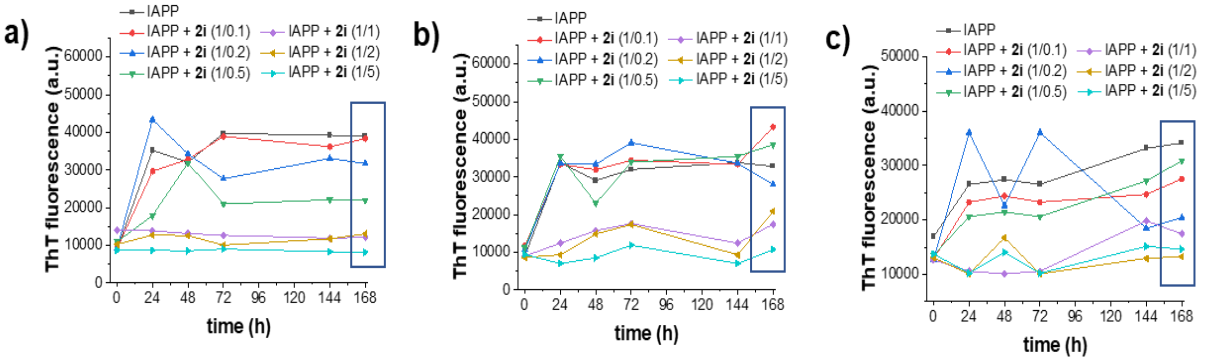

Figure A22. Effects of 2i on IAPP fibril formation. (a-c) The effects of **2i** on IAPP amyloid self-assembly as determined by three ThT binding assays (IAPP/**2i**, 1/0.1-1/10). Incubations were prepared in IAPP ThT buffer containing 0.5% HFIP (IAPP, 6 μM) and incubated at 20ºC. The ThT binding at the time point of administration to RIN-5mf cells for the cytotoxicity studies is shown with a blue frame. These three independent assays were used to generate Figure 27d, left panel.

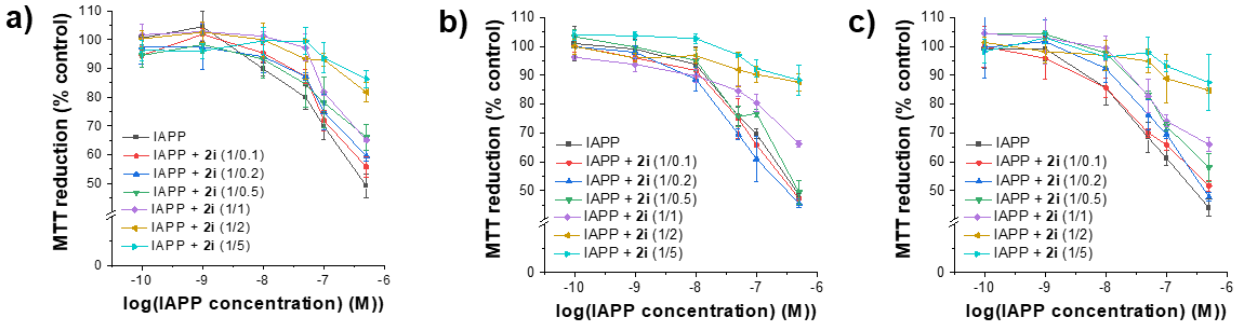

Figure A23. Effects of 2i on IAPP cell-damage after 7 days of incubation. (a-c) The effects of **2i** on IAPP cytotoxicity on RIN-5mf cell after 7 days of incubation was determined by MTT assay (IAPP/**2i**, 1/0.1-1/10). Incubations were prepared in IAPP ThT buffer containing 0.5% HFIP (IAPP, 6 μM) and incubated at 20ºC. These three independent assays were used to generate. Figure 27d, right panel.

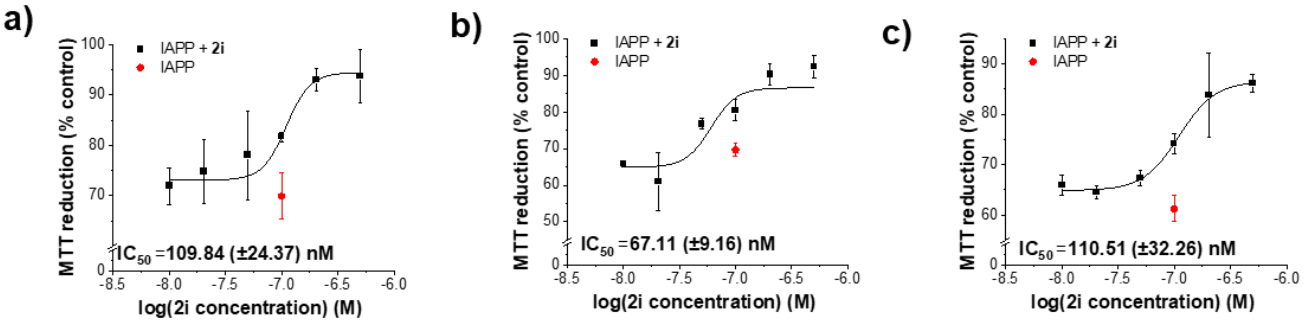

Figure A24. IC_{50} determination of inhibitory effects of 2i on the formation of cell damaging IAPP fibrils after 7 days of aging. (a-c) Sigmoidal curves were obtained from the three independent MTT assays shown in Figure A23 (IAPP, 100 nM) (means (±SD) 3 wells). The cell damage of IAPP alone is included in each graph for comparison (red symbol). The mean of the three IC_{50} values obtained from these curves is reported in Table 23.

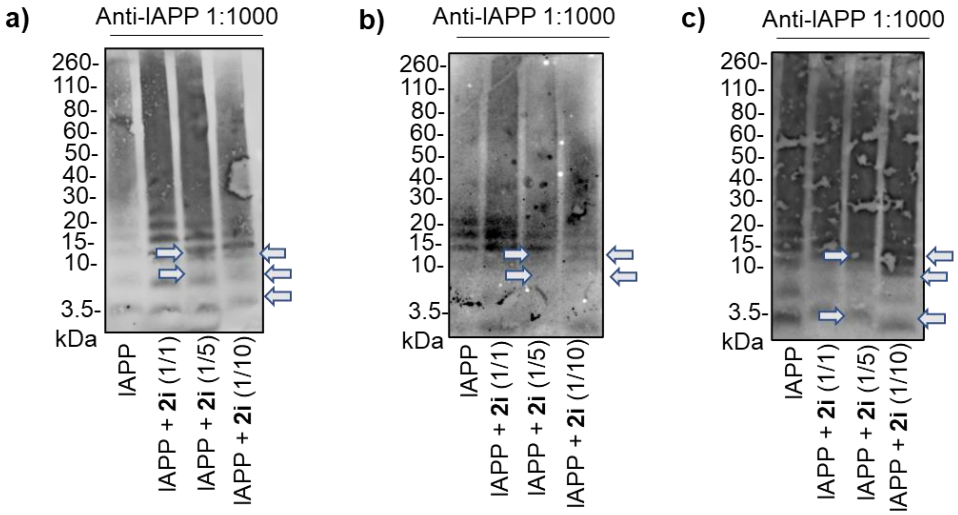

Figure A25. Characterization of hetero-assemblies of IAPP with 2i via cross-linking with glutaraldehyde, NuPAGE, and Western blot (WB) with anti-IAPP antibody. (a-c) Characterization of 30 minutes aged IAPP with various molar ratios of **2i** was characterized via cross-linking, NuPAGE and Western blot with anti-IAPP antibody. Incubations of IAPP (30 μM), and IAPP/**2i** (1/1; 1/5, 1/10) were prepared in 1xb (pH 7.4) containing 1% HFIP (pH 7.4). (a) is shown in Figure 36.


a)
1 8 15 23 28 37
KCNTATCATQRLANFLVHSSNNFGAILSSTNVGSNTY
KCNTATCATQRLANFLVHSSNNFGAILSSTNVGSNTY
KCNTATCATQRLANFLVHSSNNFGAILSSTNVGSNTY
KCNTATCATQRLANFLVHSSNNFGAILSSTNVGSNTY
KCNTATCATQRLANFLVHSSNNFGAILSSTNVGSNTY
KCNTATCATQRLANFLVHSSNNFGAILSSTNVGSNTY
KCNTATCATQRLANFLVHSSNNFGAILSSTNVGSNTY
KCNTATCATQRLANFLVHSSNNFGAILSSTNVGSNTY
KCNTATCATQRLANFLVHSSNNFGAILSSTNVGSNTY
KCNTATCATQRLANFLVHSSNNFGAILSSTNVGSNTY
KCNTATCATQRLANFLVHSSNNFGAILSSTNVGSNTY
KCNTATCATQRLANFLVHSSNNFGAILSSTNVGSNTY
KCNTATCATQRLANFLVHSSNNFGAILSSTNVGSNTY
KCNTATCATQRLANFLVHSSNNFGAILSSTNVGSNTY
KCNTATCATQRLANFLVHSSNNFGAILSSTNVGSNTY
KCNTATCATQRLANFLVHSSNNFGAILSSTNVGSNTY
KCNTATCATQRLANFLVHSSNNFGAILSSTNVGSNTY
KCNTATCATQRLANFLVHSSNNFGAILSSTNVGSNTY
KCNTATCATQRLANFLVHSSNNFGAILSSTNVGSNTY
KCNTATCATQRLANFLVHSSNNFGAILSSTNVGSNTY
KCNTATCATQRLANFLVHSSNNFGAILSSTNVGSNTY
KCNTATCATQRLANFLVHSSNNFGAILSSTNVGSNTY
KCNTATCATQRLANFLVHSSNNFGAILSSTNVGSNTY
KCNTATCATQRLANFLVHSSNNFGAILSSTNVGSNTY
Control


b)
1 8 15 23 28 37
KCNTATCATQRLANFLVHSSNNFGAILSSTNVGSNTY
KCNTATCATQRLANFLVHSSNNFGAILSSTNVGSNTY
KCNTATCATQRLANFLVHSSNNFGAILSSTNVGSNTY
KCNTATCATQRLANFLVHSSNNFGAILSSTNVGSNTY
KCNTATCATQRLANFLVHSSNNFGAILSSTNVGSNTY
KCNTATCATQRLANFLVHSSNNFGAILSSTNVGSNTY
KCNTATCATQRLANFLVHSSNNFGAILSSTNVGSNTY
KCNTATCATQRLANFLVHSSNNFGAILSSTNVGSNTY
KCNTATCATQRLANFLVHSSNNFGAILSSTNVGSNTY
KCNTATCATQRLANFLVHSSNNFGAILSSTNVGSNTY
KCNTATCATQRLANFLVHSSNNFGAILSSTNVGSNTY
KCNTATCATQRLANFLVHSSNNFGAILSSTNVGSNTY
KCNTATCATQRLANFLVHSSNNFGAILSSTNVGSNTY
KCNTATCATQRLANFLVHSSNNFGAILSSTNVGSNTY
KCNTATCATQRLANFLVHSSNNFGAILSSTNVGSNTY
KCNTATCATQRLANFLVHSSNNFGAILSSTNVGSNTY
KCNTATCATQRLANFLVHSSNNFGAILSSTNVGSNTY
KCNTATCATQRLANFLVHSSNNFGAILSSTNVGSNTY
KCNTATCATQRLANFLVHSSNNFGAILSSTNVGSNTY
KCNTATCATQRLANFLVHSSNNFGAILSSTNVGSNTY
KCNTATCATQRLANFLVHSSNNFGAILSSTNVGSNTY
KCNTATCATQRLANFLVHSSNNFGAILSSTNVGSNTY
KCNTATCATQRLANFLVHSSNNFGAILSSTNVGSNTY
Control

Figure A26. Identification of IAPP segments that bind Fluos-2i using peptide microarrays. (a-c) Glass slides with synthetic IAPP decamers (bold) consisting of overlapping IAPP sequences incubated for 12 h at 8° C with **Fluos-2i** (1 µM) (a-b) or **Fluos-2i** (0.5 µM) (c) prepared in 1% BSA in TBS-T (w/v). The visualization was performed by fluorescence. Dashed blue line frames underline identified **Fluos-2i** binding clusters; IAPP "binding cores", or common residues between consecutive binding regions, are indicated as red letters. (b) is shown in Figure 37.

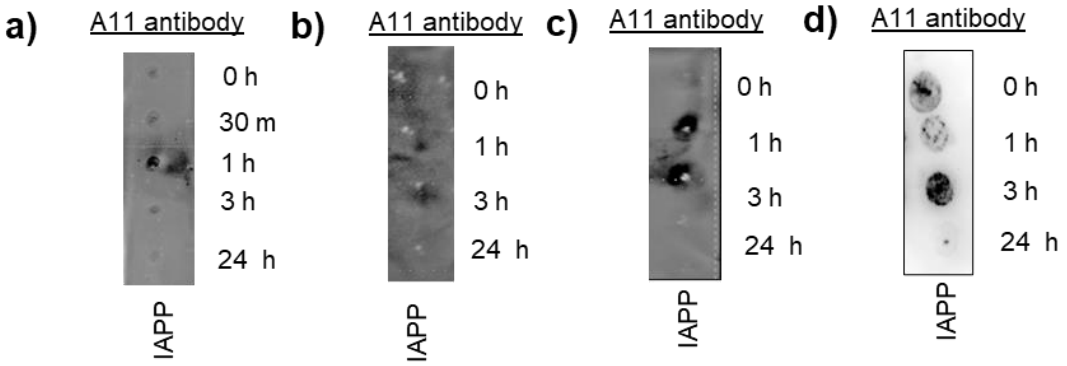

Figure A27. DB analysis with (anti-)oligomer A11 polyclonal antibody of IAPP solutions aged for different time points. (a-d) IAPP (12 μM) was prepared in IAPP ThT buffer containing 0.5% HFIP and aged at 20ºC for the indicated time points. Aliquots of the incubation (0.5 μg) were spotted on DB membrane and developed with (anti-)oligomer A11 polyclonal antibody. Immunoreactive species were detected between 1 and 3 h of aging. (c) is shown in Figure 38c, (d) in Figure 40c.

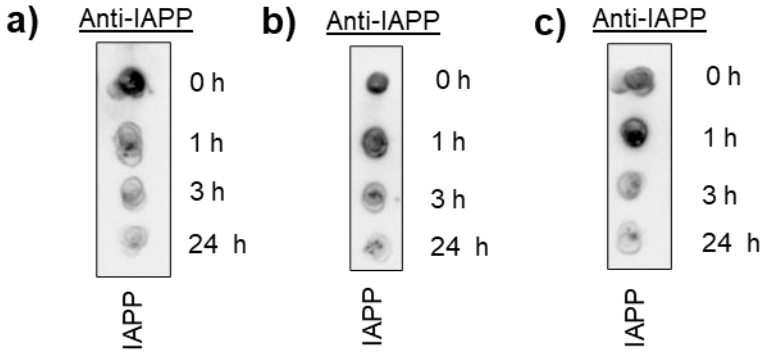

Figure A28. DB analysis with anti-IAPP of IAPP solutions aged for different time points. (a-c) IAPP (12 μM) was prepared in IAPP ThT buffer containing 0.5% HFIP and aged at 20ºC for the indicated time points. Aliquots of the incubation (0.5 μg) were spotted on DB membrane and developed with anti-IAPP, in parallel to those developed with (anti-)oligomer A11 polyclonal antibody. These experiments were performed to confirm the data shown in Figure 40c, left panel.

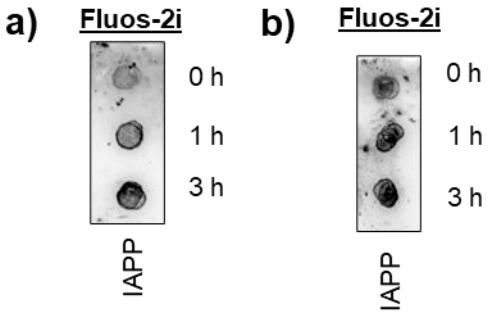

Figure A29. DB analysis shows that Fluos-2i binds to IAPP monomers and oligomers. (a) IAPP incubations (12 μM) were prepared in IAPP ThT buffer containing 0.5% HFIP and aged at 20ºC. At the indicated time points, peptide aliquots were spotted on a DB membrane (1 μg). A solution of **Fluos-2i** (2 μM) was prepared in IAPP ThT buffer containing 0.5% HFIP. Membranes were incubated in **Fluos-2i** solutions for 12 h at 8ºC. (a) is shown in Figure 39a.

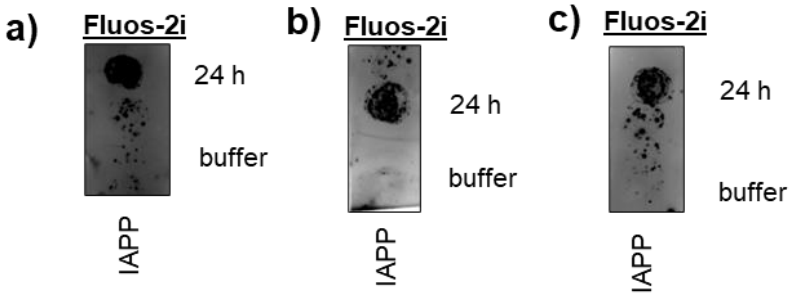

Figure A30. DB analysis of Fluos-2i binding to IAPP fibrils. (a-c) IAPP incubations (12 μM) were prepared in IAPP ThT buffer containing 0.5% HFIP and aged at 20ºC. At the indicated time points, peptide aliquots were spotted on a DB membrane (1 μg). A solution of **Fluos-2i** was prepared in IAPP ThT buffer containing 0.5% HFIP (1 μM). Membranes were incubated in **Fluos-2i** solutions for 12 h at 8ºC. (a) is shown in Figure 40b.

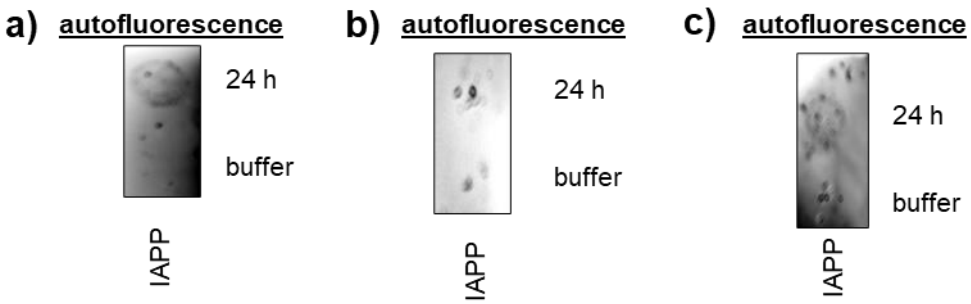

Figure A31. fIAPP autofluorescence analysed via DB. (a-c) IAPP incubations (12 μM) were prepared in IAPP ThT buffer containing 0.5% HFIP and aged at 20ºC. At the indicated time points, peptide aliquots were spotted on a DB membrane (1 μg). The autofluorescence of fIAPP was measured prior incubation with **Fluos-2i** . These experiments were performed to confirm the data shown in Figure 40b.

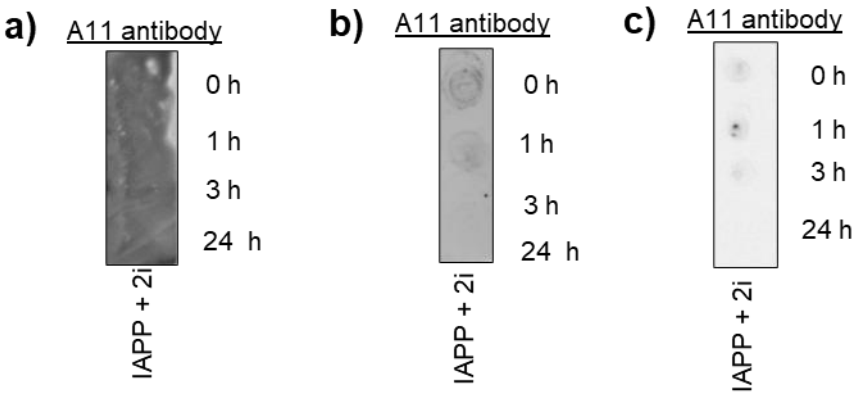

Figure A32. Dot blot analysis of mixture of IAPP/2i with (anti-)oligomer A11 polyclonal antibody. (a-c) Peptide incubations (IAPP 12 μM, IAPP/**2i**, 1/10) were prepared in IAPP ThT buffer containing 0.5% HFIP and aged at 20ºC for the indicated time points. Peptide aliquots were spotted on a DB membrane (1 μg) and incubated with A11 for 12 h at 8ºC. (b) is shown in Figure 40c right panel.

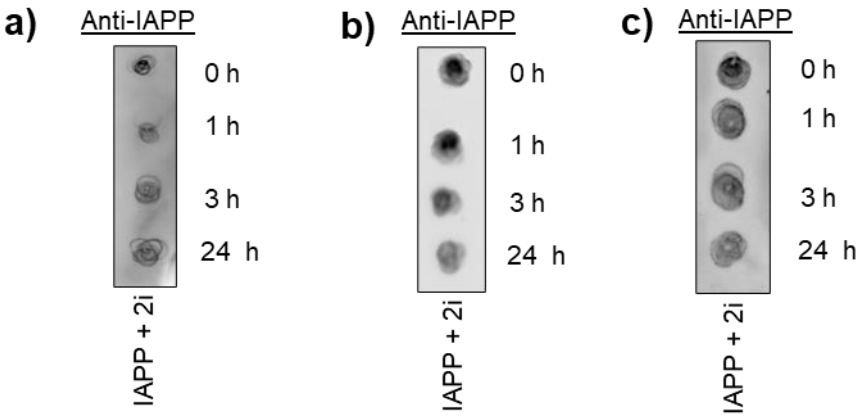

Figure A33. Dot blot analysis of mixture of IAPP/2i with anti-IAPP. (a-c) Peptide mixtures (IAPP 12 μM, IAPP/**2i**, 1/10) were prepared in IAPP ThT buffer containing 0.5% HFIP and aged at 20ºC for the indicated time points. Peptide aliquots were spotted on a DB membrane (1 μg) and incubated with anti-IAPP for 12 h at 8ºC. These experiments were performed to confirm the data shown in Figure 38c an Figure 40c right panel.

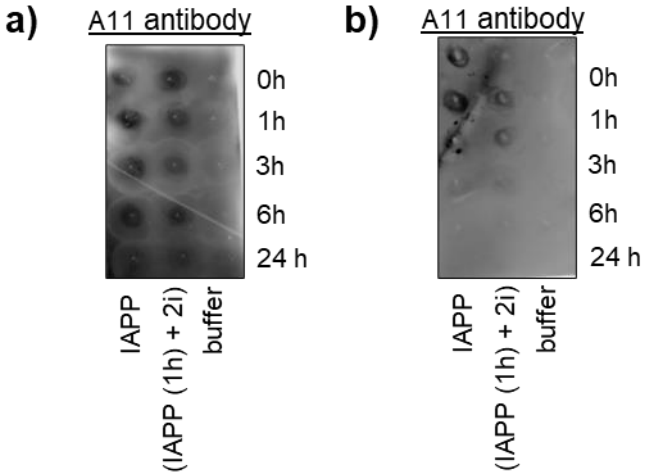

Figure A34. DB analysis of mixture of oIAPP(1 h)/2i with (anti-)oligomer A11 polyclonal antibody. IAPP (12 μM) was prepared in IAPP ThT buffer containing 0.5% HFIP and aged at 20ºC. After 1 h of aging, oIAPP was mixed with **2i** (10-fold) and spotted on a DB membrane (0.5 μg) at the indicated time points. The membrane was incubated with (anti-)oligomer A11 polyclonal antibody for 12 h at 8ºC. (a) is shown in Figure 41c.

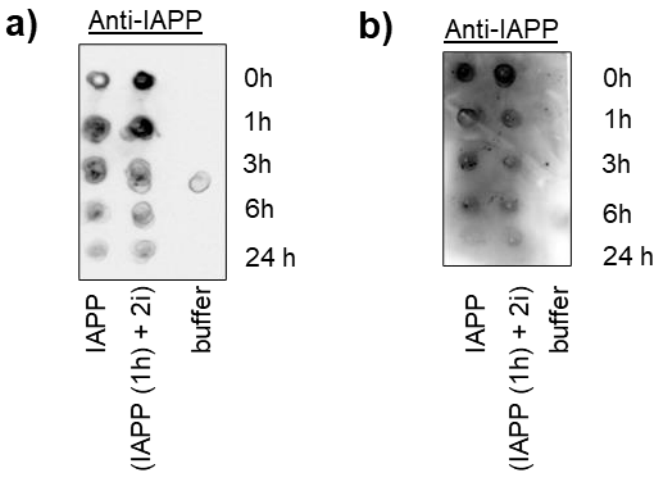

Figure A35. DB analysis of mixture of oIAPP(1 h)/2i with anti-IAPP. IAPP (12 μM) was prepared in IAPP ThT buffer containing 0.5% HFIP and aged at 20ºC. After 1 h of aging, oIAPP was mixed with **2i** (10-fold) and spotted on a DB membrane (0.5 μg) at the indicated time points. The membrane was incubated with (anti-)oligomer A11 polyclonal antibody for 12 h at 8ºC. These experiments were performed to confirm the data shown in Figure 41c.

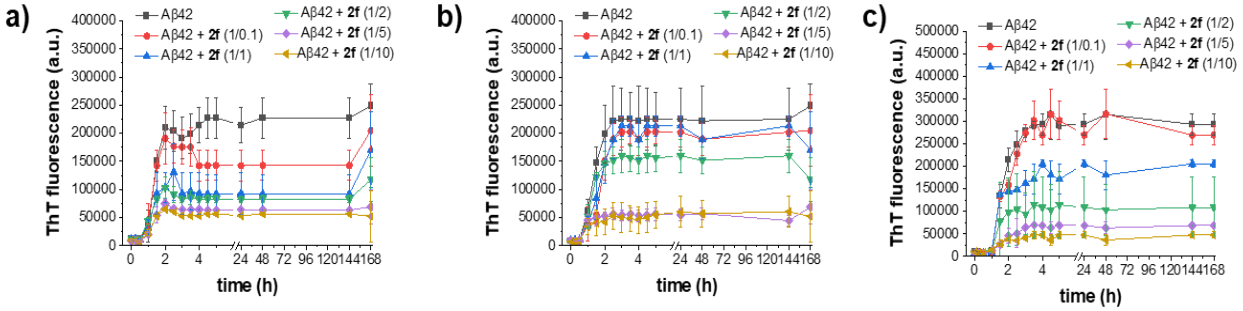

Figure A36. Effects of 2f on the amyloid self-assembly of Aβ42. (a-c) Effects of **2f** on Aβ42 self-assembly as determined by ThT binding assay (Aβ42/**2f**, 1/0.1-1/10) (means (±SD) 3 wells). Incubations were prepared using SEC-disaggregated Aβ42 (5 μM) in Aβ42 ThT buffer and aged at 37ºC under shaking conditions for the first 5 h. Incubations were kept at the same temperature, without shaking for the rest of the experiments. These three independent assays were used to generate Figure 44a, left panel.

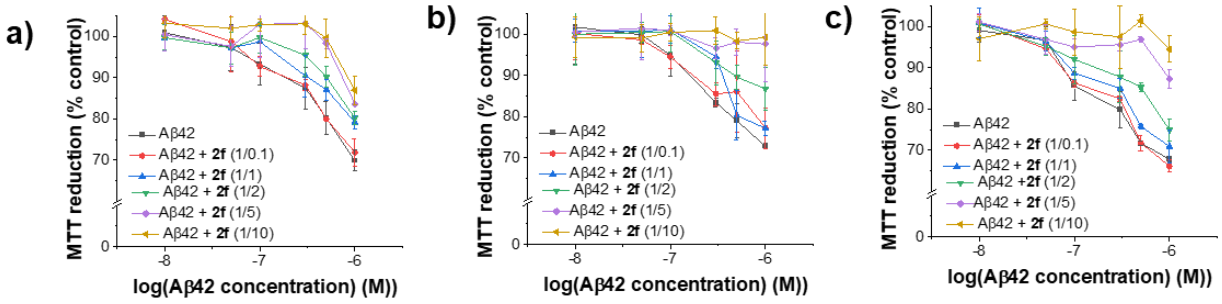

Figure A37. Effects of 2f on Aβ42 cytotoxicity. After 6 days of incubation, the peptide solutions described in Figure A36 were administered to PC-12 cells. Cell-viability was determined via MTT reduction assay (Aβ42/**2f**, 1/.01-1/10) (means (±SD) 3 wells). These three independent assays were used to generate Figure 44a, right panel.

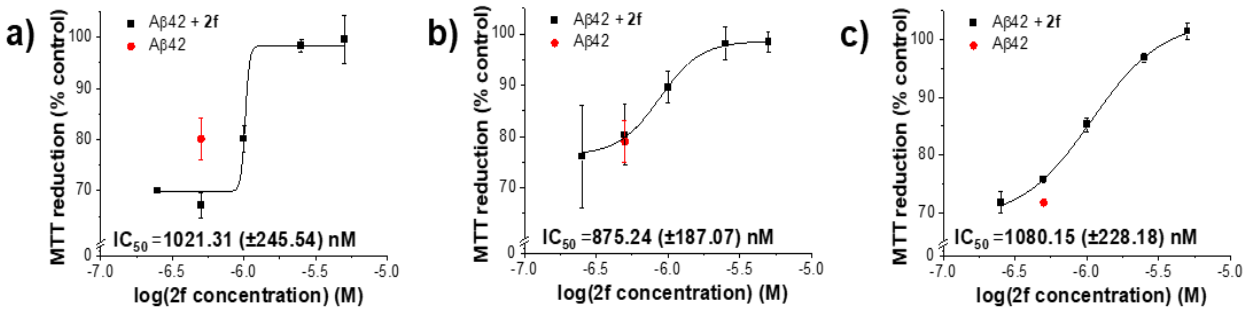

Figure A38. IC_{50} curves of inhibitory effects of 2f on the formation of cell damaging Aβ42. IC_{50} curves were obtained with the cell viability assays data shown in Figure A37 (Aβ42, 500 nM). Cell damage was determined by the MTT reduction assay for mixtures of Aβ42 with **2f** as indicated; cytotoxicity of Aβ42 alone is included in each graph for comparison (red symbol). (Data are means (±SD) from 3 wells). These three independent assays were used to generate Figure 45d, the mean of these IC_{50} values is reported in Table 25.

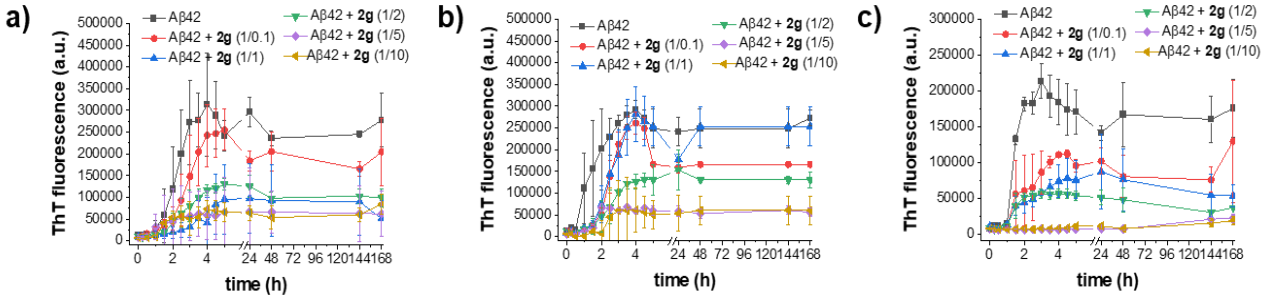

Figure A39. Concentration-dependent effect of 2g on Aβ42 fibrillation. (a-c) The effects of **2g** on Aβ42 self-assembly was determined by ThT binding assay (Aβ42/**2g**, 1/0.1-1/10) (means (±SD) 3 wells). Incubations were prepared using SEC-disaggregated Aβ42 (5 μM) in Aβ42 ThT buffer and aged at 37ºC under shaking conditions for the first 5 h. Thereafter they were kept at the same temperature without shaking conditions. These three independent assays were used to generate Figure 44b, left panel.

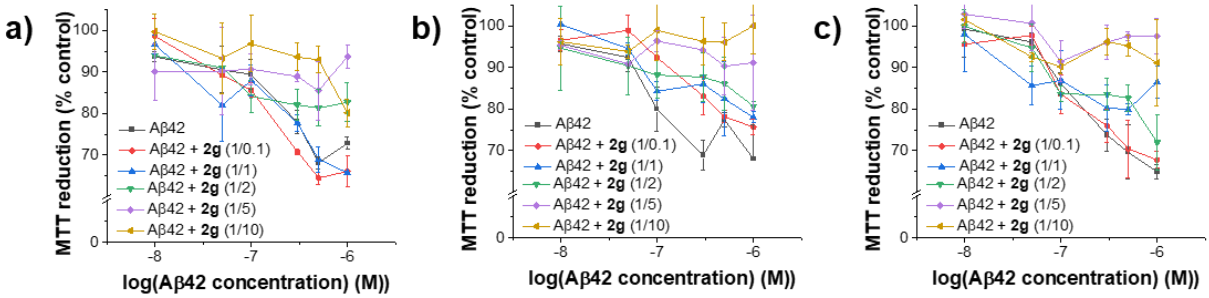

Figure A40. Effect of 2g on Aβ42 cytotoxicity. Aβ42/**2g** mixtures from the incubations described in Figure A39 were administered to PC-12 cells after 6-days of aging. The cell-viability was determined via MTT reduction assay (Aβ42/**2g**, 1/.01-1/10) (means (±SD), 3 wells). These three independent assays were used to generate Figure 44b, right panel.

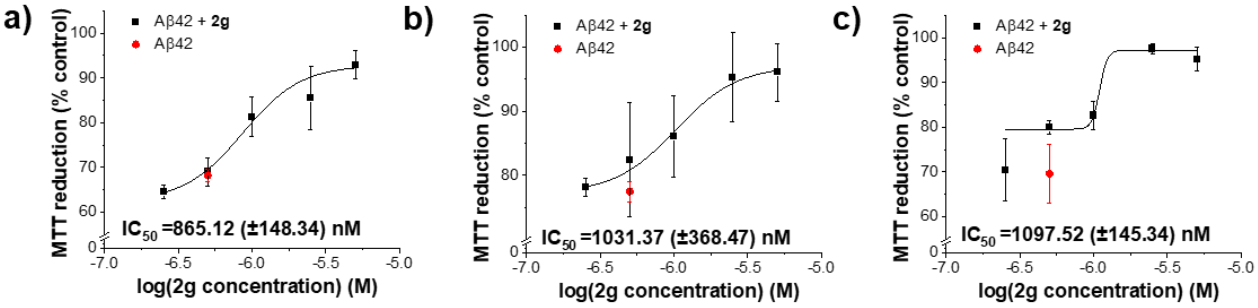

Figure A41. IC_{50} curves of inhibitory effects of 2g on formation of cell damaging Aβ42 amyloid assemblies. Sigmoidal curves were obtained from the cell viability assays shown in Figure A40 (Aβ42, 500 nM). Cell damage was determined by the MTT reduction assay for mixtures of Aβ42 with **2g** as indicated; cytotoxicity of Aβ42 alone is included in each graph for comparison (red symbol). (Data are means (±SD) from 3 wells). These three independent assays were used to generate Figure 45e, the mean of these IC_{50} values is reported in Table 25.

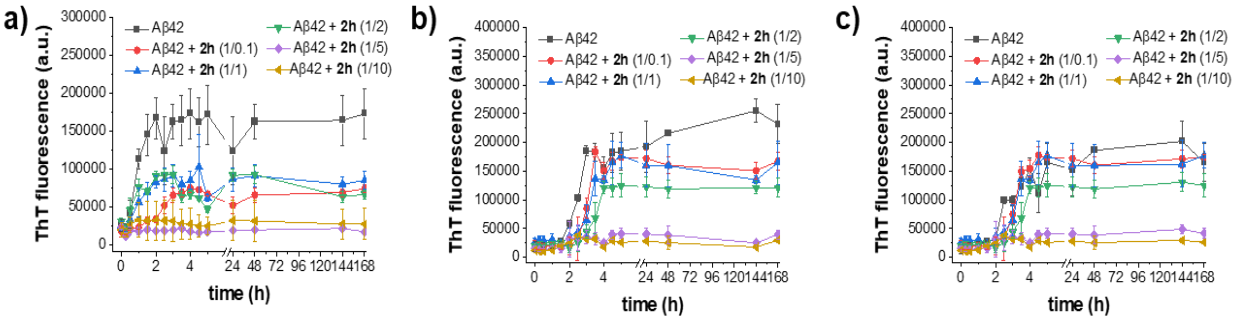

Figure A42. Concentration-dependent effect of 2h on Aβ42 fibril formation. (a-c) Effects of **2h** on Aβ42 self-assembly as determined by ThT binding assay (Aβ42/**2h**, 1/0.1-1/10) (means (±SD) 3 wells). Incubations were prepared using SEC-disaggregated Aβ42 (5 μM) in Aβ42 ThT buffer and aged at 37ºC under shaking conditions for the first 5 h. Thereafter, the incubations were kept at the same temperature without shaking conditions. These three independent assays were used to generate Figure 44c, left panel.

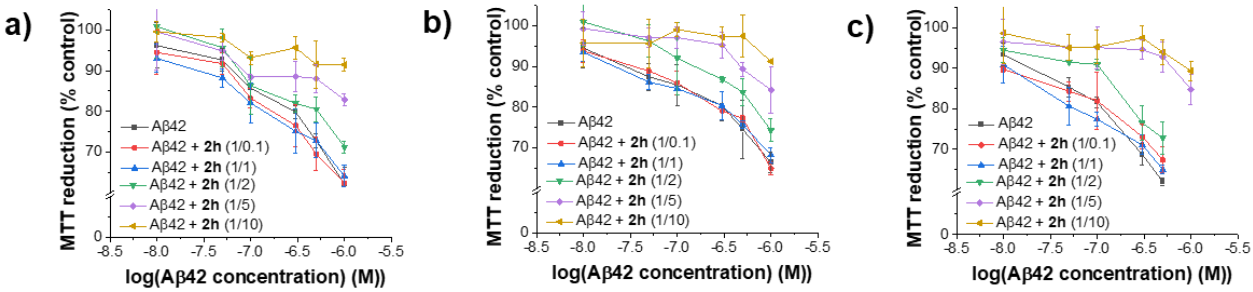

Figure A43. Effect of 2h on Aβ42 cytotoxicity. Aβ42/**2h** mixtures from the peptide solutions described in Figure A42 were administered to PC-12 cells after 6-days of incubation. The cell-viability was determined via MTT reduction assay (Aβ42/**2h**, 1/.01-1/10) (means (±SD), 3 wells). These three independent assays were used to generate Figure 44c, right panel.

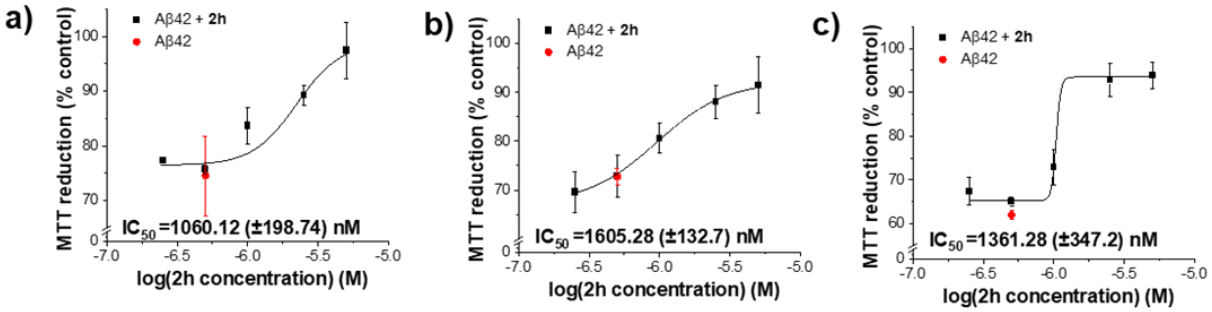

Figure A44. IC_{50}s of inhibitory effects of 2h on formation of cell damaging Aβ42 amyloid assemblies. Sigmoidal curves were obtained from the three independent MTT assays shown in Figure A43 (Aβ42, 500 nM). Each graph includes the cytotoxicity of Aβ42 alone for comparison (red symbol). (Data are means (±SD) from 3 wells). These three independent assays were used to generate Figure 45f, the mean of these IC_{50} values is reported in Table 25.

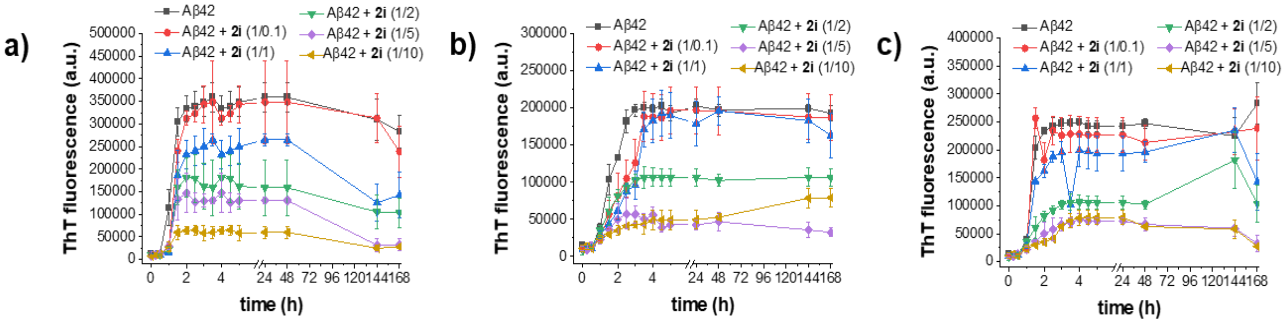

Figure A45. Concentration-dependent effect of 2i on Aβ42 amyloid self-assembly. (a-c) Effects of **2i** on Aβ42 amyloid formation as followed by ThT binding assay (Aβ42/**2i** 1/0.1-1/10) (means (±SD) 3 wells). Incubations were prepared using SEC-disaggregated Aβ42 (5 μM) in Aβ42 ThT buffer and aged at 37ºC under shaking conditions for the first 5 h. Thereafter the incubations were kept at the same temperature without shaking conditions. These three independent assays were used to generate Figure 44d, left panel.

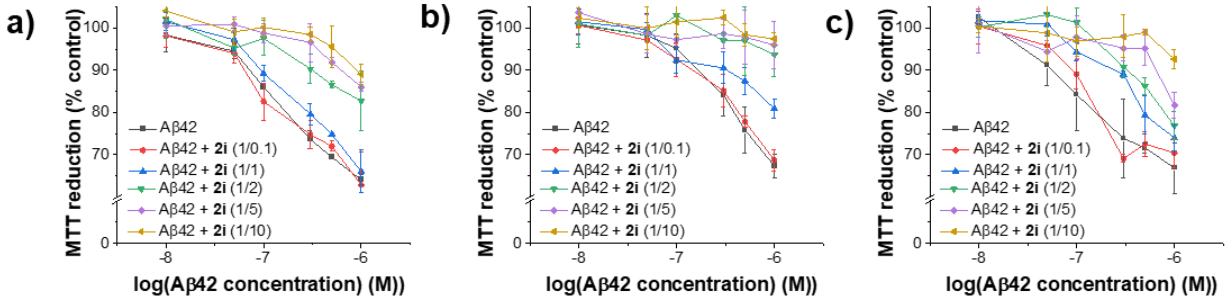

Figure A46. Effect of 2i on Aβ42 cytotoxicity. Aβ42/**2i** mixtures from the peptide incubations described in Figure A45 were administered to PC-12 cells after 6-days of incubation. The cell-viability was determined via MTT reduction assay (Aβ42/**2i**, 1/.01-1/10) (means (±SD), 3 wells). Incubations were prepared as described under Figure A45. These three independent assays were used to generate Figure 44d, right panel.

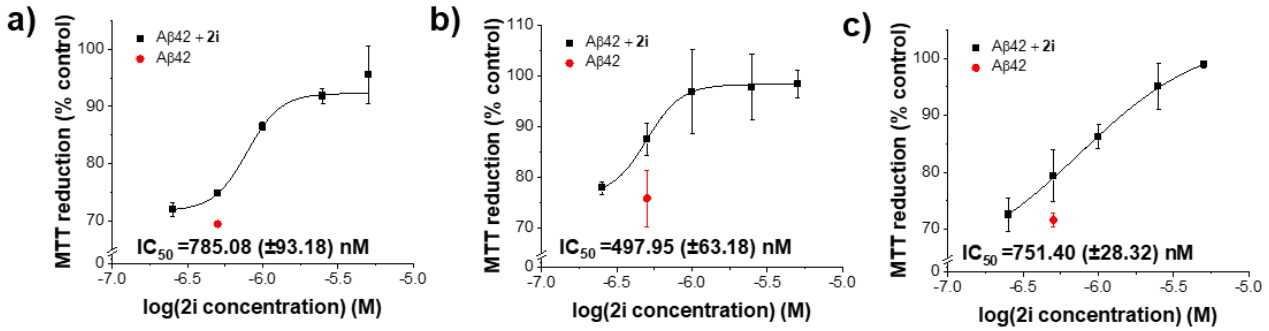

Figure A47. IC_{50}s of inhibitory effects of 2i on formation of cell damaging Aβ42 amyloid assemblies. Sigmoidal curves were obtained from the three independent MTT assays shown in Figure A43 (Aβ42, 500 nM). Each graph includes the cytotoxicity of Aβ42 alone for comparison (red symbol). (Data are means (±SD) from 3 wells). These three independent assays were used to generate Figure 45g, the mean of these IC_{50} values is reported in Table 25.

a)

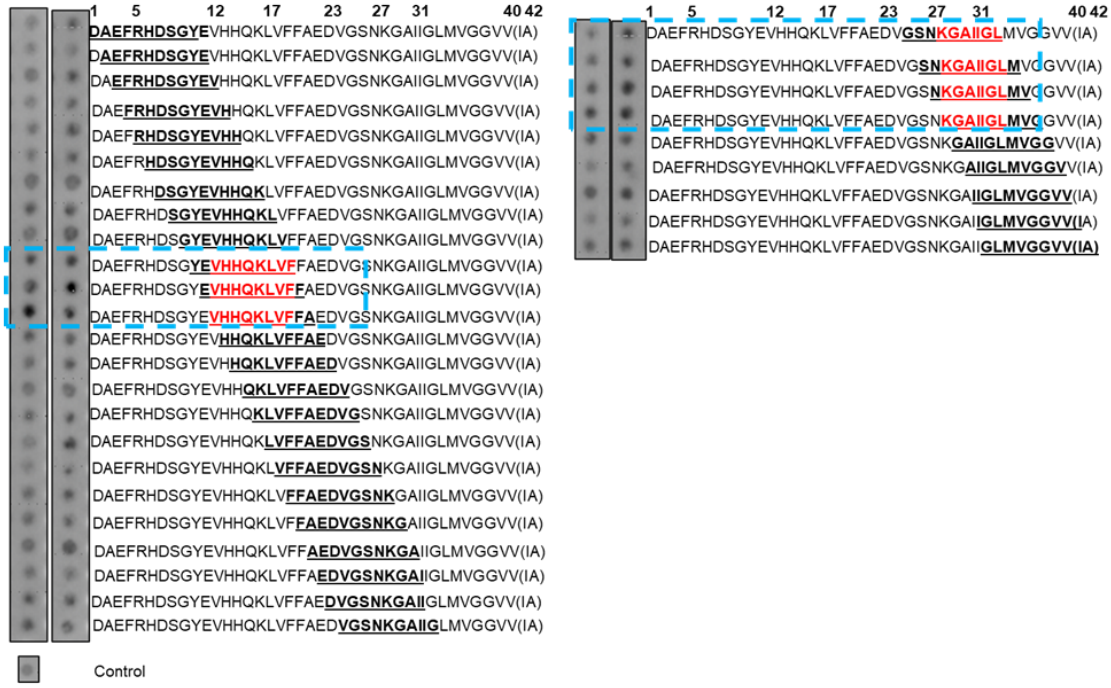
1 5 12 17 23 27 31 40 42
DAEFRHDSGYEVHHQKLVFFAEDVGSNKGAIIGLMVGGVV(IA)
DAEFRHDSGYEVHHQKLVFFAEDVGSNKGAIIGLMVGGVV(IA)
DAEFRHDSGYEVHHQKLVFFAEDVGSNKGAIIGLMVGGVV(IA)
DAEFRHDSGYEVHHQKLVFFAEDVGSNKGAIIGLMVGGVV(IA)
DAEFRHDSGYEVHHQKLVFFAEDVGSNKGAIIGLMVGGVV(IA)
DAEFRHDSGYEVHHQKLVFFAEDVGSNKGAIIGLMVGGVV(IA)
DAEFRHDSGYEVHHQKLVFFAEDVGSNKGAIIGLMVGGVV(IA)
DAEFRHDSGYEVHHQKLVFFAEDVGSNKGAIIGLMVGGVV(IA)
DAEFRHDSGYEVHHQKLVFFAEDVGSNKGAIIGLMVGGVV(IA)
DAEFRHDSGYEVHHQKLVFFAEDVGSNKGAIIGLMVGGVV(IA)
DAEFRHDSGYEVHHQKLVFFAEDVGSNKGAIIGLMVGGVV(IA)
DAEFRHDSGYEVHHQKLVFFAEDVGSNKGAIIGLMVGGVV(IA)
DAEFRHDSGYEVHHQKLVFFAEDVGSNKGAIIGLMVGGVV(IA)
DAEFRHDSGYEVHHQKLVFFAEDVGSNKGAIIGLMVGGVV(IA)
DAEFRHDSGYEVHHQKLVFFAEDVGSNKGAIIGLMVGGVV(IA)
DAEFRHDSGYEVHHQKLVFFAEDVGSNKGAIIGLMVGGVV(IA)
DAEFRHDSGYEVHHQKLVFFAEDVGSNKGAIIGLMVGGVV(IA)
DAEFRHDSGYEVHHQKLVFFAEDVGSNKGAIIGLMVGGVV(IA)
DAEFRHDSGYEVHHQKLVFFAEDVGSNKGAIIGLMVGGVV(IA)
DAEFRHDSGYEVHHQKLVFFAEDVGSNKGAIIGLMVGGVV(IA)
DAEFRHDSGYEVHHQKLVFFAEDVGSNKGAIIGLMVGGVV(IA)
DAEFRHDSGYEVHHQKLVFFAEDVGSNKGAIIGLMVGGVV(IA)
DAEFRHDSGYEVHHQKLVFFAEDVGSNKGAIIGLMVGGVV(IA)
DAEFRHDSGYEVHHQKLVFFAEDVGSNKGAIIGLMVGGVV(IA)
Control
1 5 12 17 23 27 31 40 42
DAEFRHDSGYEVHHQKLVFFAEDVGSNKGAIIGLMVGGVV(IA)
DAEFRHDSGYEVHHQKLVFFAEDVGSNKGAIIGLMVGGVV(IA)
DAEFRHDSGYEVHHQKLVFFAEDVGSNKGAIIGLMVGGVV(IA)
DAEFRHDSGYEVHHQKLVFFAEDVGSNKGAIIGLMVGGVV(IA)
DAEFRHDSGYEVHHQKLVFFAEDVGSNKGAIIGLMVGGVV(IA)
DAEFRHDSGYEVHHQKLVFFAEDVGSNKGAIIGLMVGGVV(IA)
DAEFRHDSGYEVHHQKLVFFAEDVGSNKGAIIGLMVGGVV(IA)
DAEFRHDSGYEVHHQKLVFFAEDVGSNKGAIIGLMVGGVV(IA)
DAEFRHDSGYEVHHQKLVFFAEDVGSNKGAIIGLMVGGVV(IA)

b)

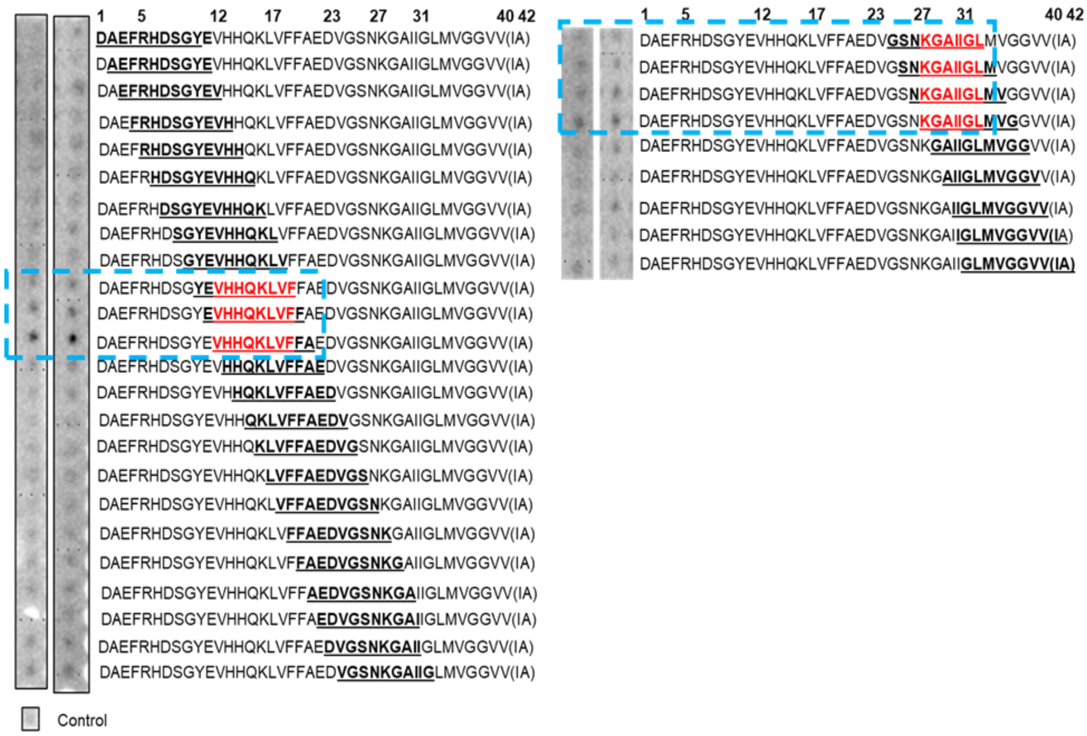
1 5 12 17 23 27 31 40 42
DAEFRHDSGYEVHHQKLVFFAEDVGSNKGAIIGLMVGGVV(IA)
DAEFRHDSGYEVHHQKLVFFAEDVGSNKGAIIGLMVGGVV(IA)
DAEFRHDSGYEVHHQKLVFFAEDVGSNKGAIIGLMVGGVV(IA)
DAEFRHDSGYEVHHQKLVFFAEDVGSNKGAIIGLMVGGVV(IA)
DAEFRHDSGYEVHHQKLVFFAEDVGSNKGAIIGLMVGGVV(IA)
DAEFRHDSGYEVHHQKLVFFAEDVGSNKGAIIGLMVGGVV(IA)
DAEFRHDSGYEVHHQKLVFFAEDVGSNKGAIIGLMVGGVV(IA)
DAEFRHDSGYEVHHQKLVFFAEDVGSNKGAIIGLMVGGVV(IA)
DAEFRHDSGYEVHHQKLVFFAEDVGSNKGAIIGLMVGGVV(IA)
DAEFRHDSGYEVHHQKLVFFAEDVGSNKGAIIGLMVGGVV(IA)
DAEFRHDSGYEVHHQKLVFFAEDVGSNKGAIIGLMVGGVV(IA)
DAEFRHDSGYEVHHQKLVFFAEDVGSNKGAIIGLMVGGVV(IA)
DAEFRHDSGYEVHHQKLVFFAEDVGSNKGAIIGLMVGGVV(IA)
DAEFRHDSGYEVHHQKLVFFAEDVGSNKGAIIGLMVGGVV(IA)
DAEFRHDSGYEVHHQKLVFFAEDVGSNKGAIIGLMVGGVV(IA)
DAEFRHDSGYEVHHQKLVFFAEDVGSNKGAIIGLMVGGVV(IA)
DAEFRHDSGYEVHHQKLVFFAEDVGSNKGAIIGLMVGGVV(IA)
DAEFRHDSGYEVHHQKLVFFAEDVGSNKGAIIGLMVGGVV(IA)
DAEFRHDSGYEVHHQKLVFFAEDVGSNKGAIIGLMVGGVV(IA)
DAEFRHDSGYEVHHQKLVFFAEDVGSNKGAIIGLMVGGVV(IA)
DAEFRHDSGYEVHHQKLVFFAEDVGSNKGAIIGLMVGGVV(IA)
DAEFRHDSGYEVHHQKLVFFAEDVGSNKGAIIGLMVGGVV(IA)
DAEFRHDSGYEVHHQKLVFFAEDVGSNKGAIIGLMVGGVV(IA)
DAEFRHDSGYEVHHQKLVFFAEDVGSNKGAIIGLMVGGVV(IA)
Control
1 5 12 17 23 27 31 40 42
DAEFRHDSGYEVHHQKLVFFAEDVGSNKGAIIGLMVGGVV(IA)
DAEFRHDSGYEVHHQKLVFFAEDVGSNKGAIIGLMVGGVV(IA)
DAEFRHDSGYEVHHQKLVFFAEDVGSNKGAIIGLMVGGVV(IA)
DAEFRHDSGYEVHHQKLVFFAEDVGSNKGAIIGLMVGGVV(IA)
DAEFRHDSGYEVHHQKLVFFAEDVGSNKGAIIGLMVGGVV(IA)
DAEFRHDSGYEVHHQKLVFFAEDVGSNKGAIIGLMVGGVV(IA)
DAEFRHDSGYEVHHQKLVFFAEDVGSNKGAIIGLMVGGVV(IA)
DAEFRHDSGYEVHHQKLVFFAEDVGSNKGAIIGLMVGGVV(IA)
DAEFRHDSGYEVHHQKLVFFAEDVGSNKGAIIGLMVGGVV(IA)

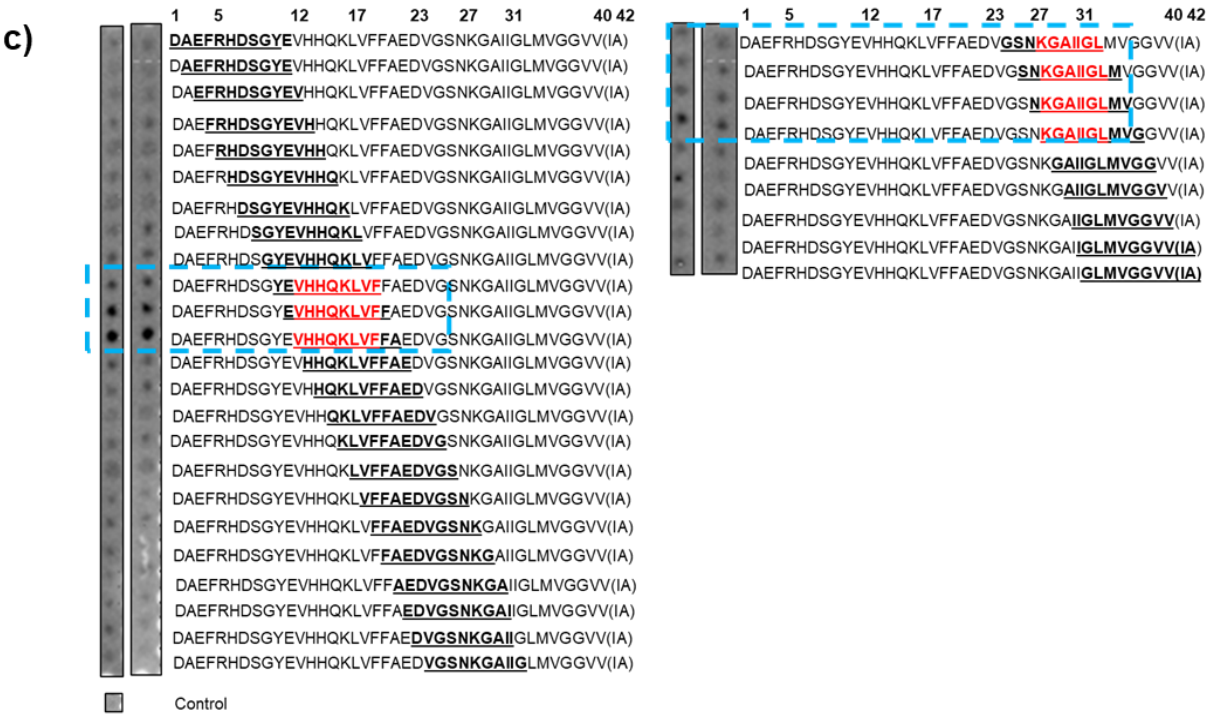

Figure A48. Identification of the regions of Aβ42 interacting with Fluos-2i using peptide microarrays.(a-c) Glass slides with decamers consisting of overlapping Aβ42 sequences (bold) were incubated for 12 h at 8ºC with **Fluos-2i** (1 µM) (a and c) or **Fluos-2i** (0.5 µM) (b), prepared in 1% BSA in TBS-T (w/v). Dashed blue line frames underline the identified **Fluos-2i** binding cluster, whereas the Aβ42 "binding cores" of **Fluos-2i** are indicated as red letters and correspond to the shared residues between binding segments. (c) is shown in Figure 49.

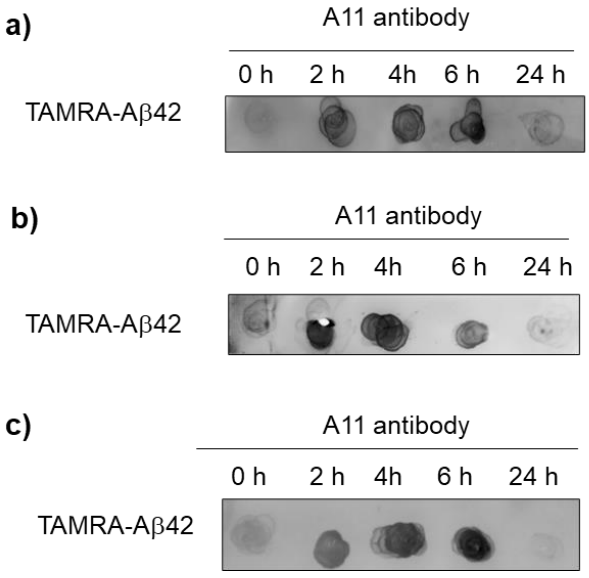

Figure A49. Identification of TAMRA-Aβ42 oligomers via DB analysis with (anti-)oligomer A11 polyclonal antibody. (a-c) DB analysis with (anti-)oligomer A11 polyclonal antibody of TAMRA-Aβ42 solutions (4.9 µg) aged for the indicated time point, confirmed the presence of A11 immunoreactive species between 2 and 6 h of aging. TAMRA-Aβ42 incubations were prepared in IAPP ThT buffer containing 1% HFIP and aged at 37°C under shaking conditions for the first 5 h. Thereafter the peptide solutions were kept at the same temperature without shaking conditions. (c) is shown Figure 50a.

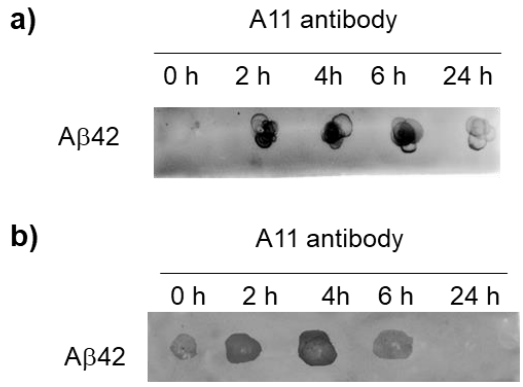

Figure A50. Identification of Aβ42 oligomers via DB analysis with (anti-)oligomer A11 polyclonal antibody. (a-b) DB analysis with (anti-)oligomer A11 polyclonal antibody of Aβ42 solutions (4.5 µg) aged for the indicated time point, confirmed the presence of A11 immunoreactive species between 2 and 6 h of aging. SEC-disaggregated Aβ42 (5 µM) was prepared in Aβ42 ThT buffer and incubated at 37°C under shaking conditions for the first 5 h of incubation. Thereafter the incubations were kept at the same temperature without agitation. (b) is shown in Figure 50b.

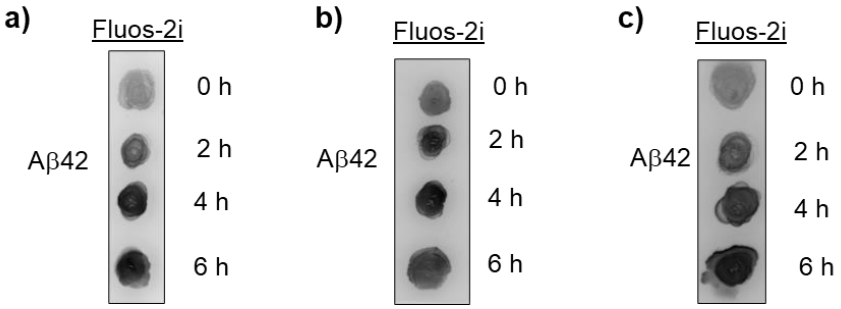

Figure A51. DB analysis shows that Fluos-2i binds to Aβ42 monomers, oligomers, and fibrils. SEC-disaggregated Aβ42 (11 µM), was prepared in Aβ42 ThT buffer and aged at 37°C under shaking conditions for the first 5 h. Thereafter the incubations were kept at the same temperature without agitation. At the indicated time points, aliquots of the peptide solutions were spotted on a DB membrane (1 µg) and probed with **Fluos-2i** (5 µM), prepared in IAPP ThT buffer containing 1% HFIP (incubation for 12 h, 8°C). The visualization was performed by fluorescence. (a) is shown in Figure 51.

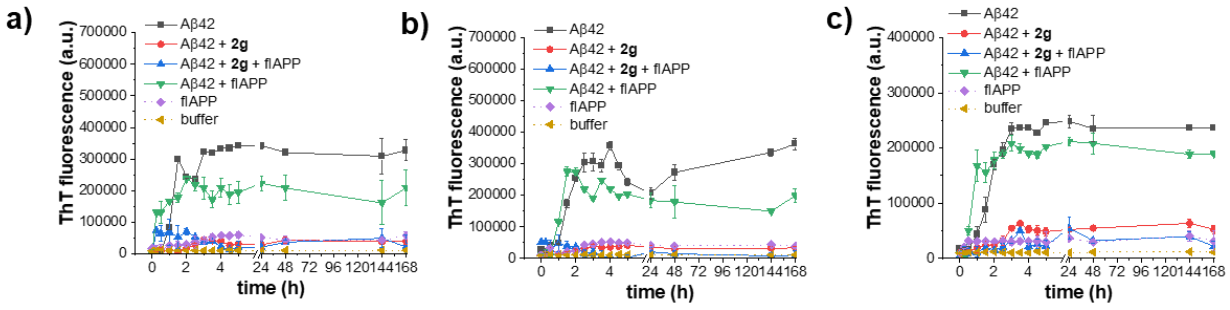

Figure A52. Effect of 2g on the amyloid assembly of Aβ42 seeded by fIAPP. (a) The amyloid self-assembly of Aβ42 (5 µM) alone or seeded by 30% fIAPP and of the complex of Aβ42/**2g** (1/10) seeded by fIAPP was followed via the ThT binding assay (means (±SD), 3 wells). SEC-disaggregated Aβ42 (5 µM) was prepared in Aβ42 ThT buffer and aged at 37°C under shaking conditions for the first 5 h. Thereafter the incubations were kept at the same temperature without agitation. (a) is shown in Figure 57a.

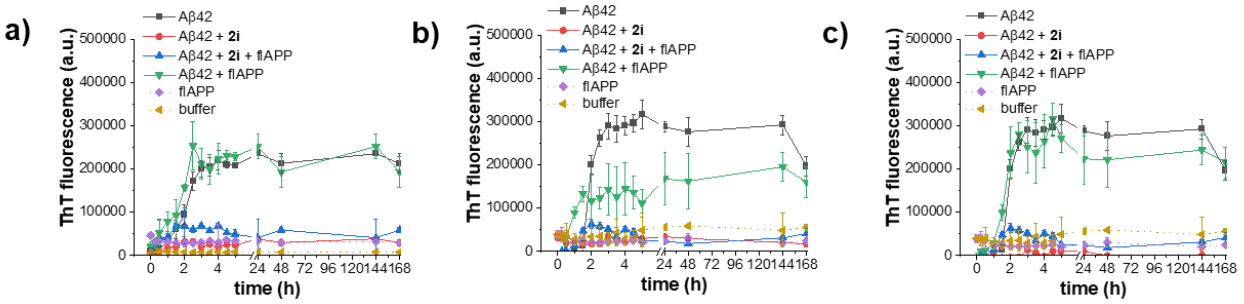

Figure A53. Effect of 2i on the amyloid assembly of Aβ42 seeded by fIAPP. (a) The fibrillation of Aβ42 (5 μM) alone or seeded by 30% fIAPP and of the complex of Aβ42/**2g** (1/10) seeded by fIAPP was characterized via the ThT binding assay (means (±SD), 3 wells). SEC-disaggregated Aβ42 (5 μM) was prepared in Aβ42 ThT buffer and aged at 37°C under shaking conditions for the first 5 h. Thereafter the incubations were kept at the same temperature but without agitation. (b) is shown in Figure 57a.

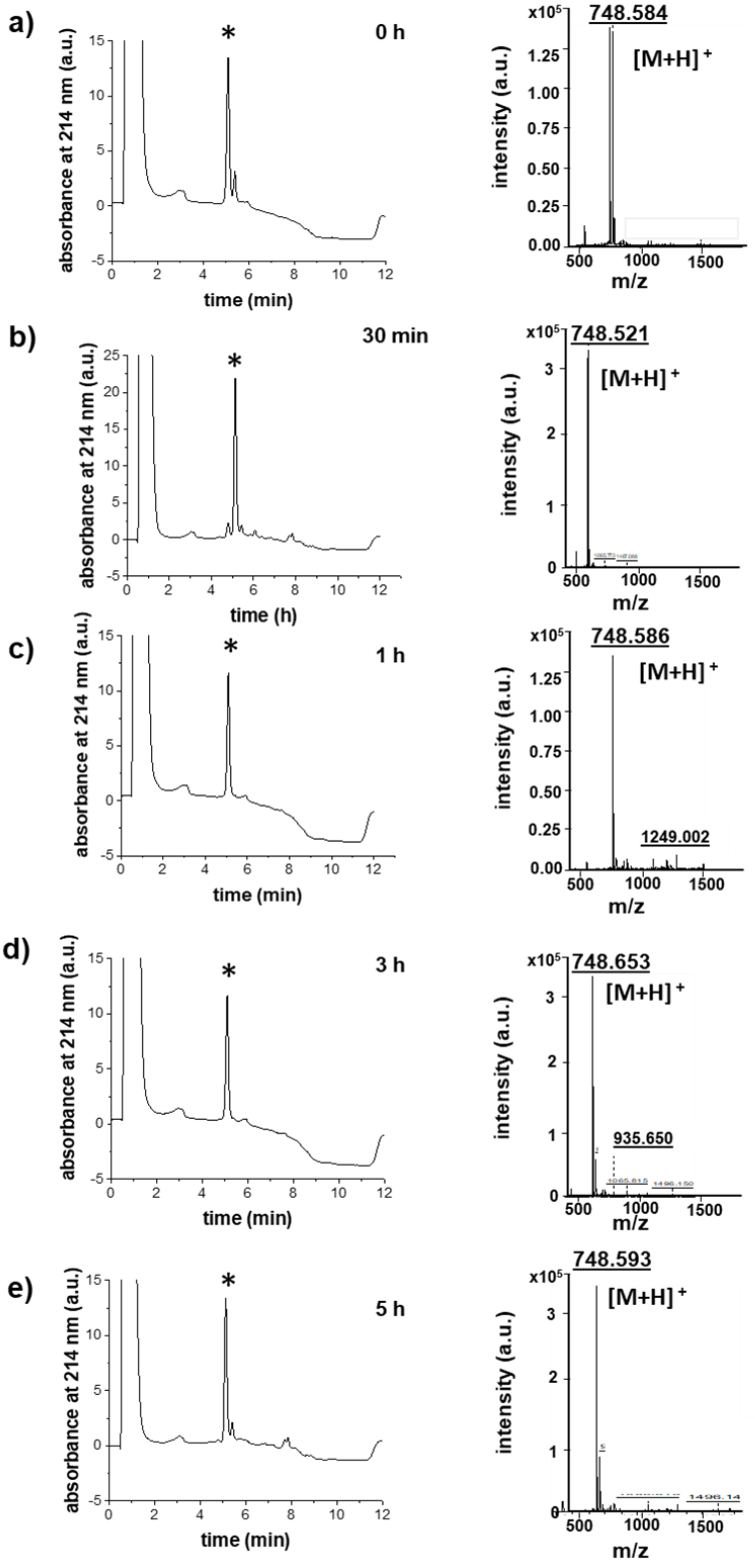
a)
0 h
absorbance at 214 nm (a.u.)
time (min)
748.584
[M+H]+
intensity (a.u.)
m/z
b)
30 min
absorbance at 214 nm (a.u.)
time (h)
748.521
[M+H]+
intensity (a.u.)
m/z
c)
1 h
absorbance at 214 nm (a.u.)
time (min)
748.586
[M+H]+
1249.002
intensity (a.u.)
m/z
d)
3 h
absorbance at 214 nm (a.u.)
time (min)
748.653
[M+H]+
935.650
intensity (a.u.)
m/z
e)
5 h
absorbance at 214 nm (a.u.)
time (min)
748.593
[M+H]+
intensity (a.u.)
m/z

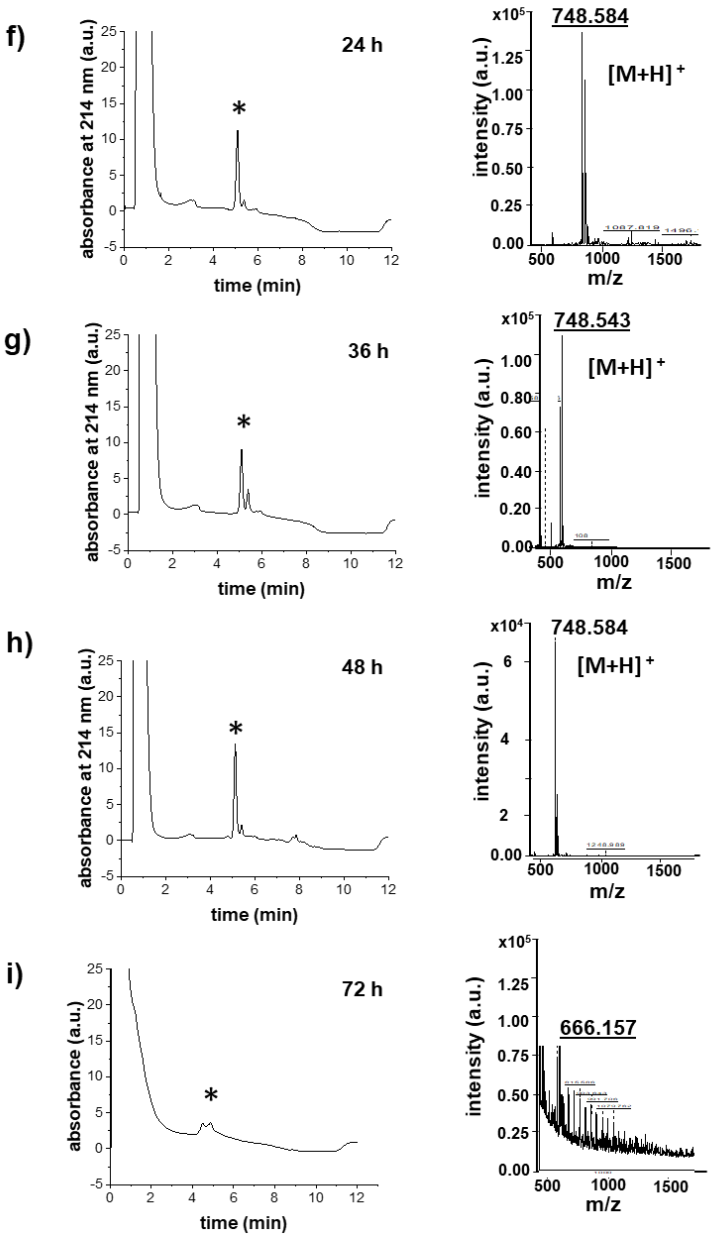

Figure A54. HPLC and MALDI-MS characterization of 2g after incubation in human plasma in vitro (37oC) for the indicated time points. Left panels show HPLC chromatograms of supernatant of **2g** after 0 h (a), 30 min (b), 1 h (c), 3 h (d), 5 h I, 24 h (f), 36 h (g), 48 h (h) and 72 h (i) as detected by RP-HPLC (214 nm). Right panels show MALDI spectra of the collected peak (*) with t_R≈5.8 min with the found $[M+H]^+$ or $[M+Na]^+$ until 48 h. Chromatograms and MALDI spectra are representatives of at least three sets of independent experiments (one shown in Figure 59, the other in Figure A55).

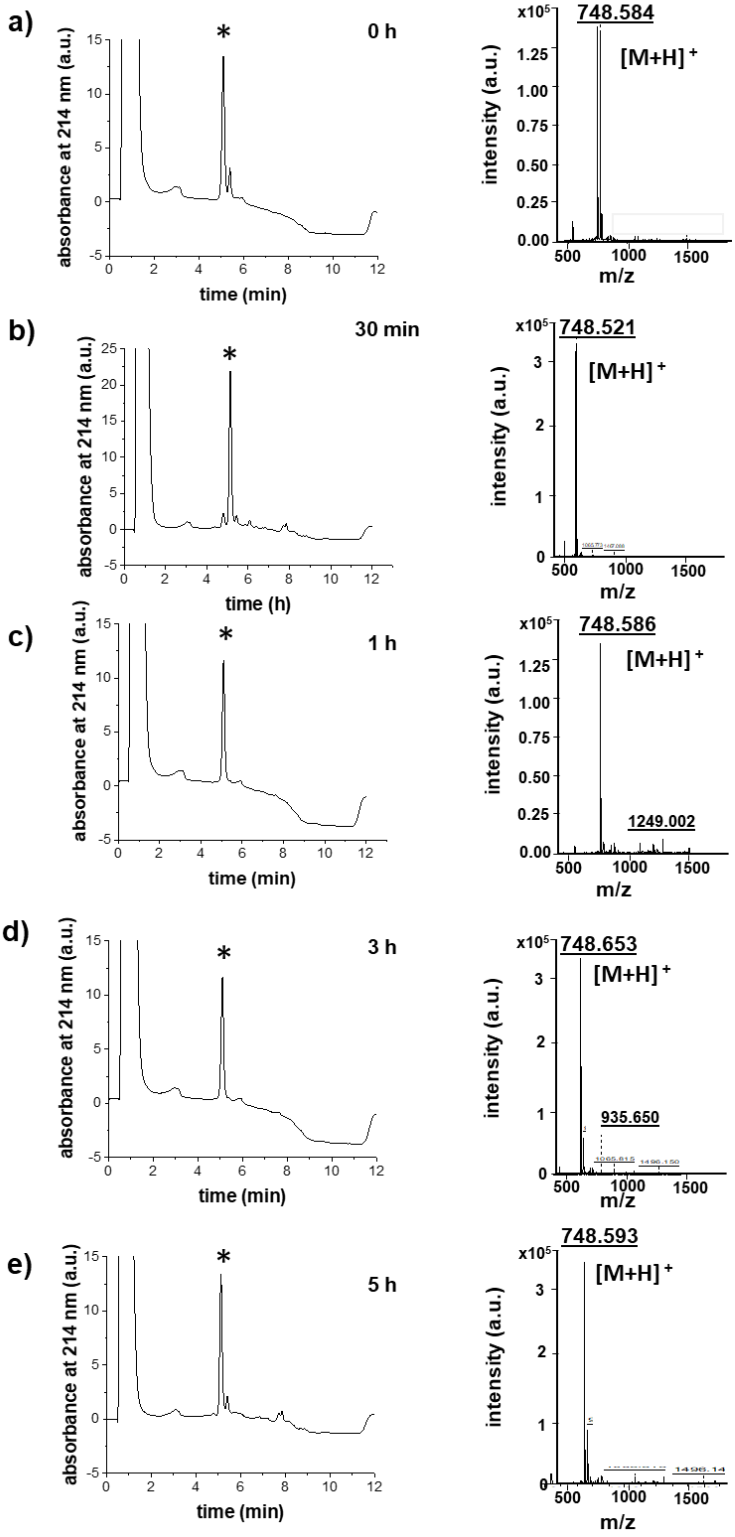
a)
0 h
absorbance at 214 nm (a.u.)
time (min)
748.584
[M+H]+
intensity (a.u.)
m/z
b)
30 min
absorbance at 214 nm (a.u.)
time (h)
748.521
[M+H]+
intensity (a.u.)
m/z
c)
1 h
absorbance at 214 nm (a.u.)
time (min)
748.586
[M+H]+
1249.002
intensity (a.u.)
m/z
d)
3 h
absorbance at 214 nm (a.u.)
time (min)
748.653
[M+H]+
935.650
intensity (a.u.)
m/z
e)
5 h
absorbance at 214 nm (a.u.)
time (min)
748.593
[M+H]+
intensity (a.u.)
m/z

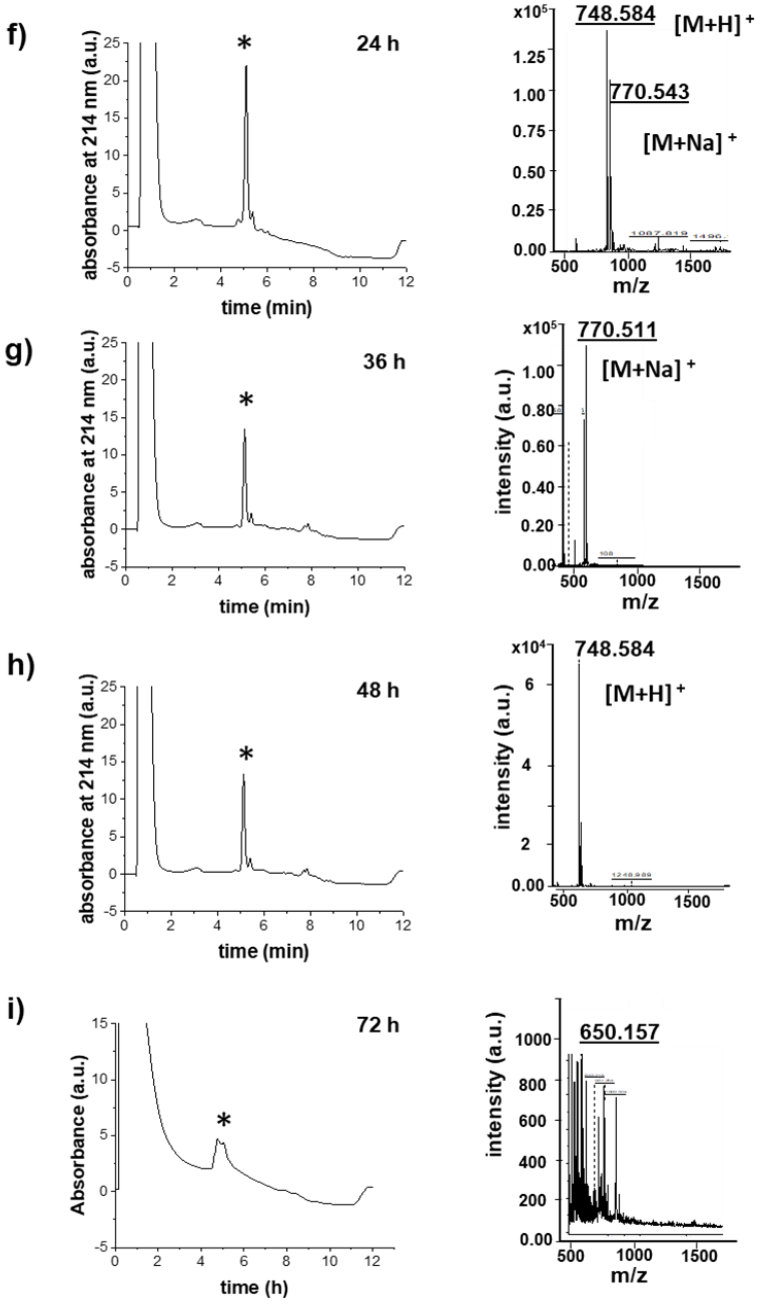

Figure A55. HPLC and MALDI-MS characterization of 2g after incubation in human plasma in vitro (37oC) for the indicated time points. Left panel show HPLC chromatograms of supernatant of **2g** after 0 h (a), 30 min (b), 1 h (c), 3 h (d), 5 h I, 24 h (f), 36 h (g), 48 h (h) and 72 h (i) as detected by RP-HPLC (214 nm). Right panels show MALDI spectra of the collected peak (*) with t_R≈5.8 min with the found $[M+H]^+$ or$[M+Na]^+$ until 48 h. Chromatograms and MALDI spectra are representatives of at least three sets of independent experiments, one set of experiments is shown in Figure 59, the other in Figure A54 .

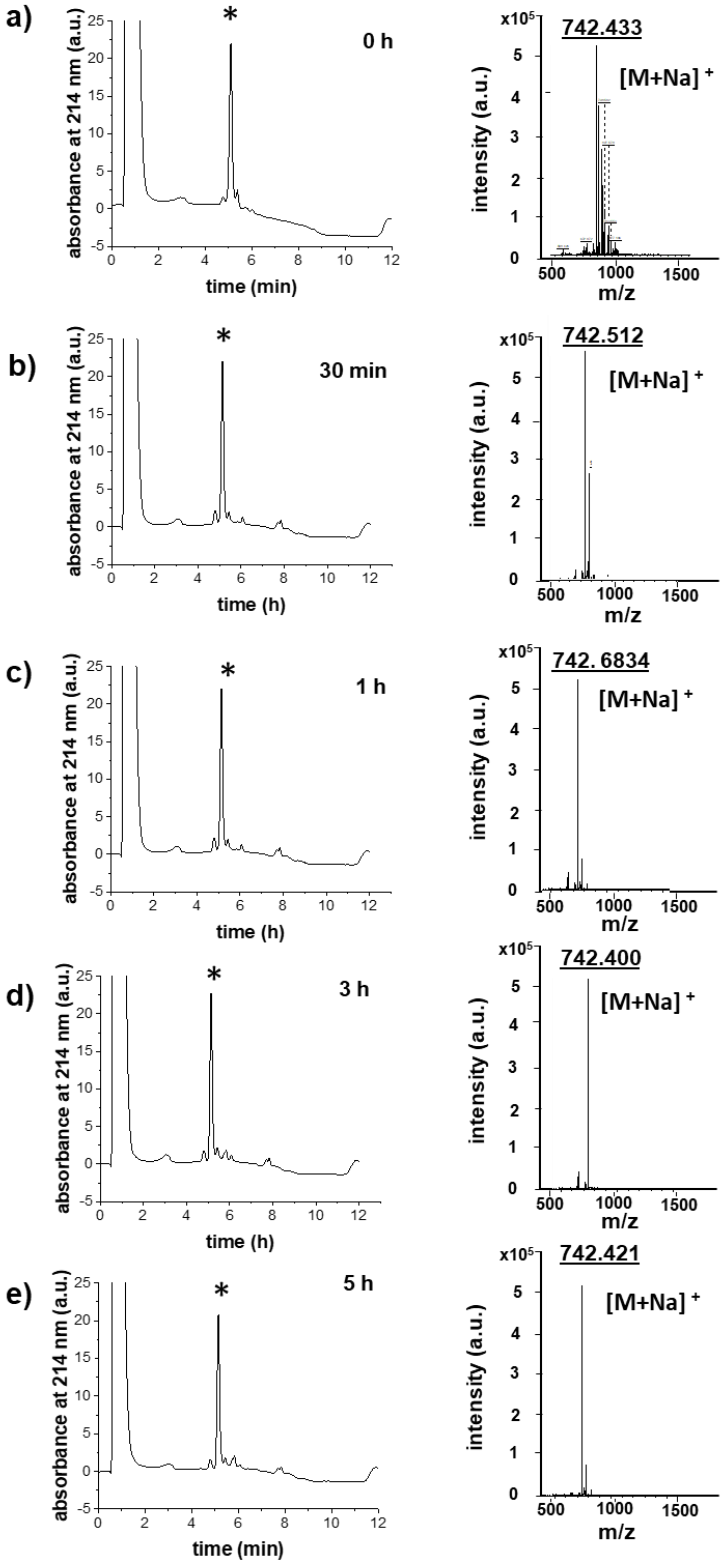
a)
0 h
absorbance at 214 nm (a.u.)
time (min)
742.433
[M+Na] +
intensity (a.u.)
m/z
b)
30 min
absorbance at 214 nm (a.u.)
time (h)
742.512
[M+Na] +
intensity (a.u.)
m/z
c)
1 h
absorbance at 214 nm (a.u.)
time (h)
742. 6834
[M+Na] +
intensity (a.u.)
m/z
d)
3 h
absorbance at 214 nm (a.u.)
time (h)
742.400
[M+Na] +
intensity (a.u.)
m/z
e)
5 h
absorbance at 214 nm (a.u.)
time (min)
742.421
[M+Na] +
intensity (a.u.)
m/z

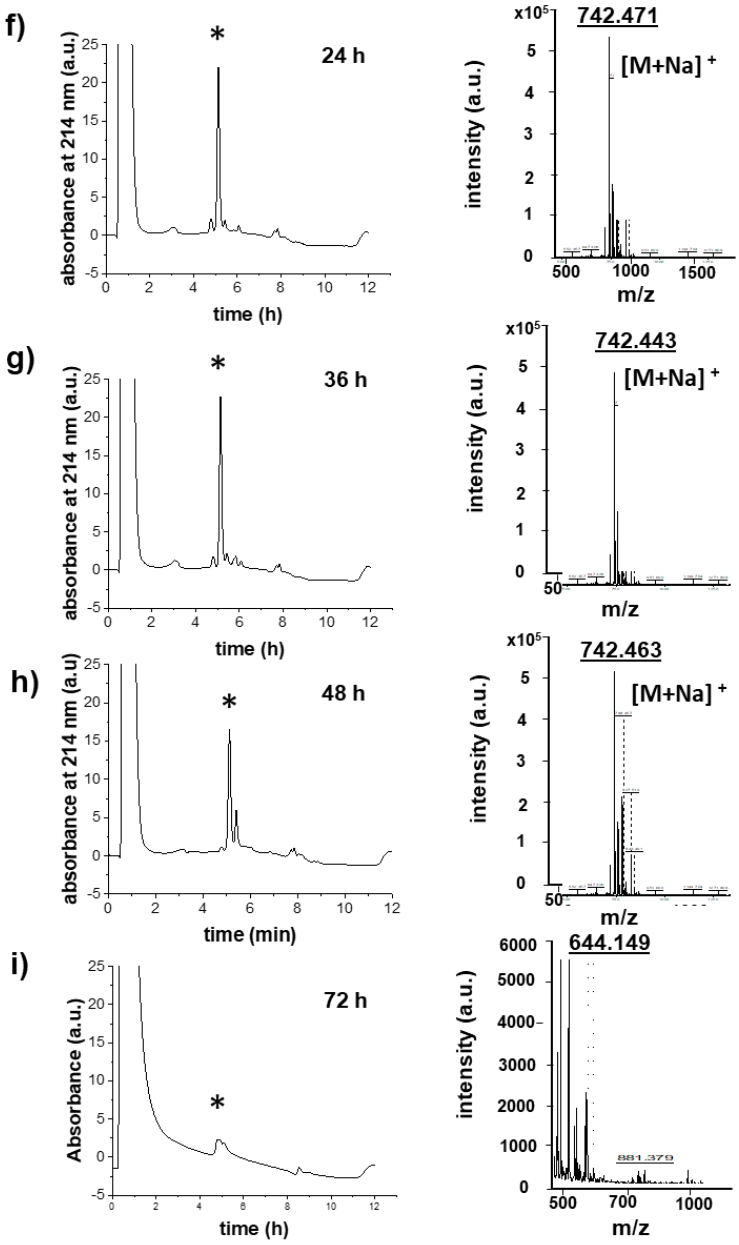

Figure A56. HPLC and MALDI-MS characterization of 2i after incubation in human plasma in vitro (37oC) for the indicated time points. Left panels show HPLC chromatograms of the supernatants of plasma incubations of **2i** after 0 h (a), 30 min (b), 1 h (c), 3 h (d), 5 h I, 24 h (f), 36 h (g), 48 h (h) and 72 h (i) as detected by RP-HPLC (214 nm). Right panels show MALDI spectra of the collected peak (*) with t_R≈5.8 min with the found $[M+H]^+$ or $[M+Na]^+$ until 48 h. One set of experiments is shown in Figure 60, the other in Figure A57.

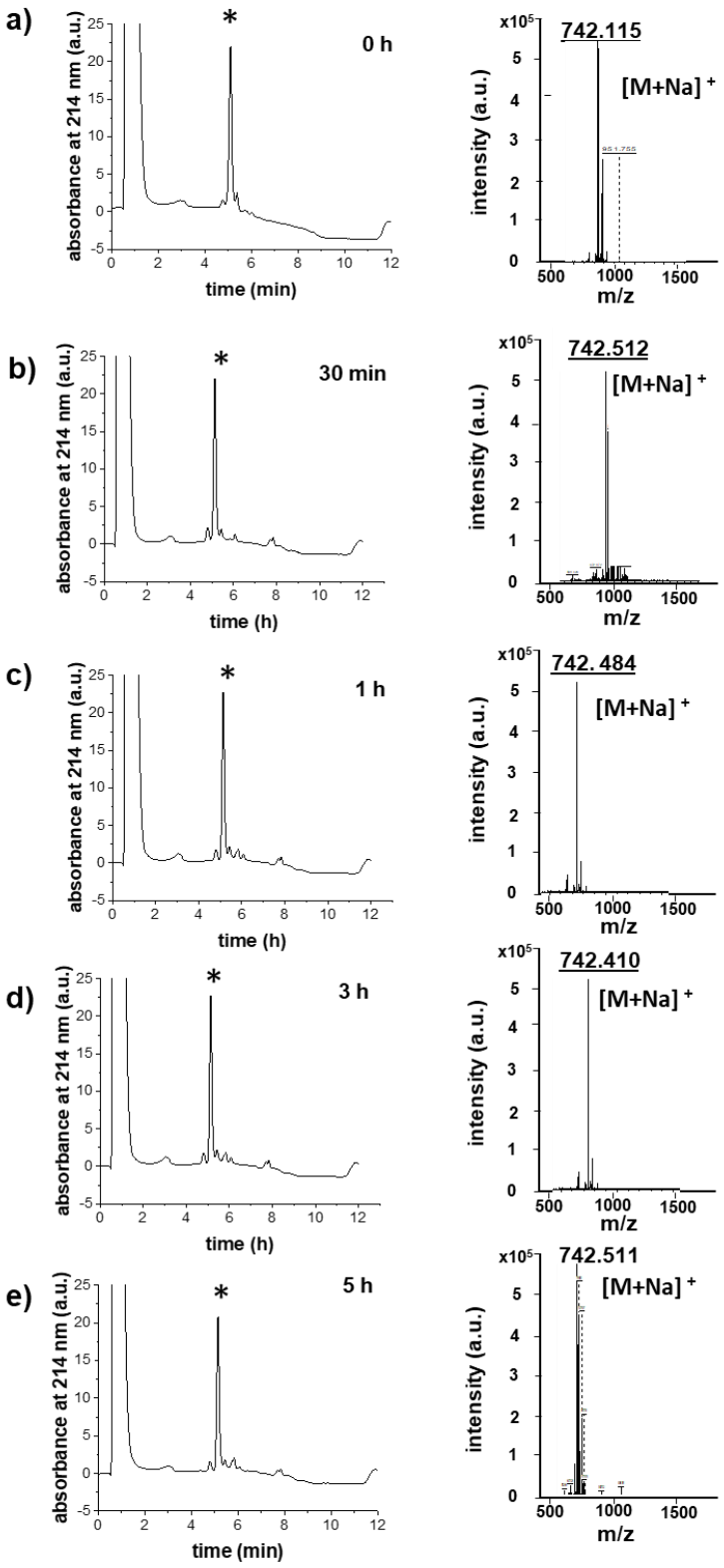
a)
0 h
absorbance at 214 nm (a.u.)
time (min)
742.115
[M+Na]+
intensity (a.u.)
m/z
b)
30 min
absorbance at 214 nm (a.u.)
time (h)
742.512
[M+Na]+
intensity (a.u.)
m/z
c)
1 h
absorbance at 214 nm (a.u.)
time (h)
742. 484
[M+Na]+
intensity (a.u.)
m/z
d)
3 h
absorbance at 214 nm (a.u.)
time (h)
742.410
[M+Na]+
intensity (a.u.)
m/z
e)
5 h
absorbance at 214 nm (a.u.)
time (min)
742.511
[M+Na]+
intensity (a.u.)
m/z

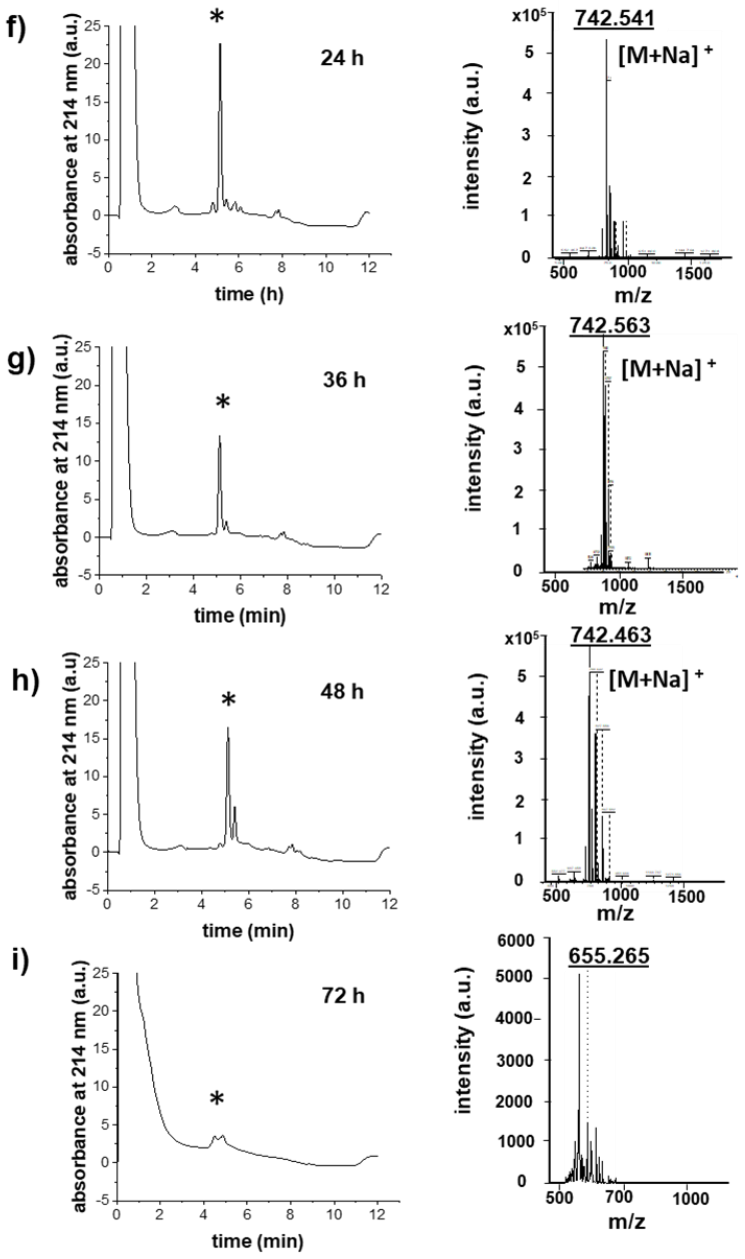

Figure A57. HPLC and MALDI-MS characterization of 2i after incubation in human plasma in vitro (37oC) for the indicated time points. Left panels show HPLC chromatograms of the supernatants of plasma incubations of **2i** after 0 h (a), 30 min (b), 1 h (c), 3 h (d), 5 h, 24 h (f), 36 h (g), 48 h (h) and 72 h (i) as detected by RP-HPLC (214 nm). Right panels show MALDI spectra of the collected peak (*) with t_R≈5.8 min with the found $[M+H]^+$ or $[M+Na]^+$ until 48 h. One set of experiments is shown in Figure 60, the other in Figure A56.

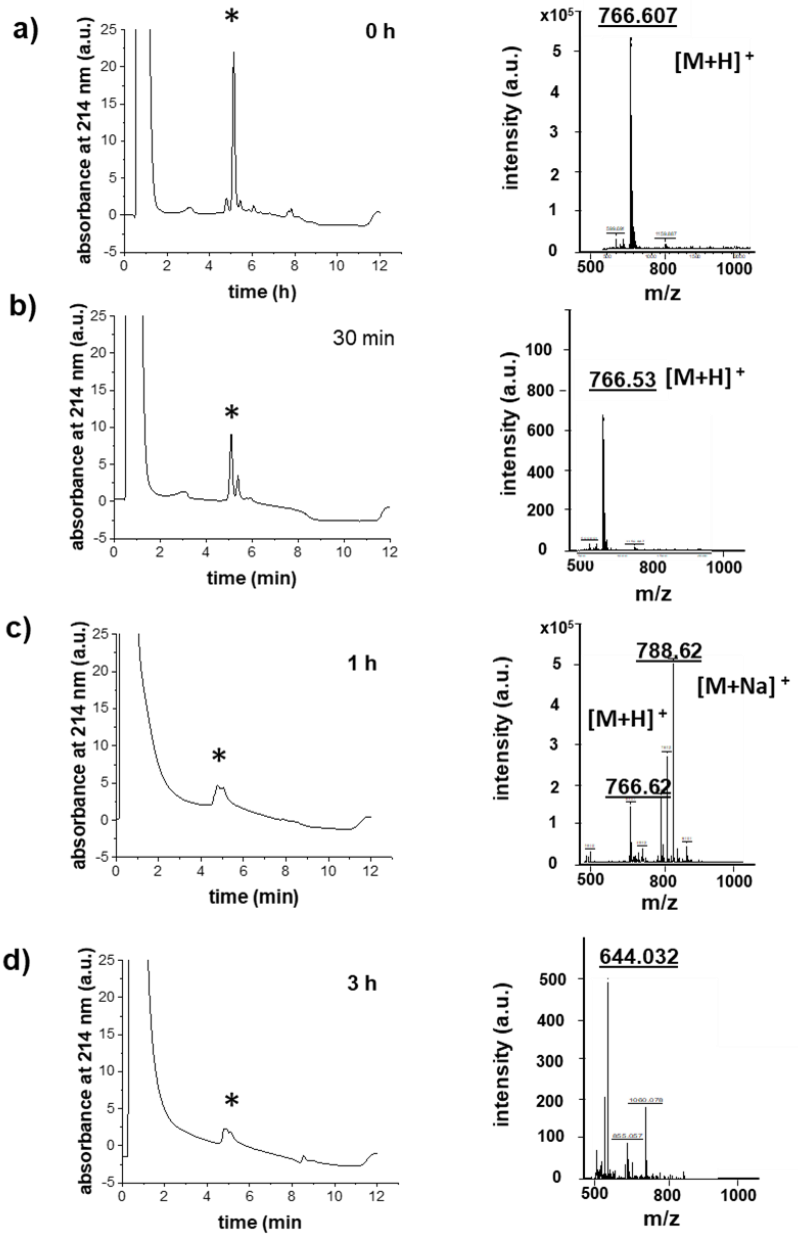

Figure A58. Proteolytic stability of 2g linear determined via HPLC and MALDI-MS. (a-d)Left panels show RP-HPLC-(214 nm) of **2g linear** after incubation in human plasma in vitro (37°C) at the indicated time points. Right panels show HPLC MALDI spectra of the collected peak (*) with $t_R \approx 5$ min with the found $[M+H]^+$ or $[M+Na]^+$ until 1 h. MALDI spectra are representatives of at least three sets of independent experiments. One set of experiments is shown in Figure 61, the other in Figure A59.

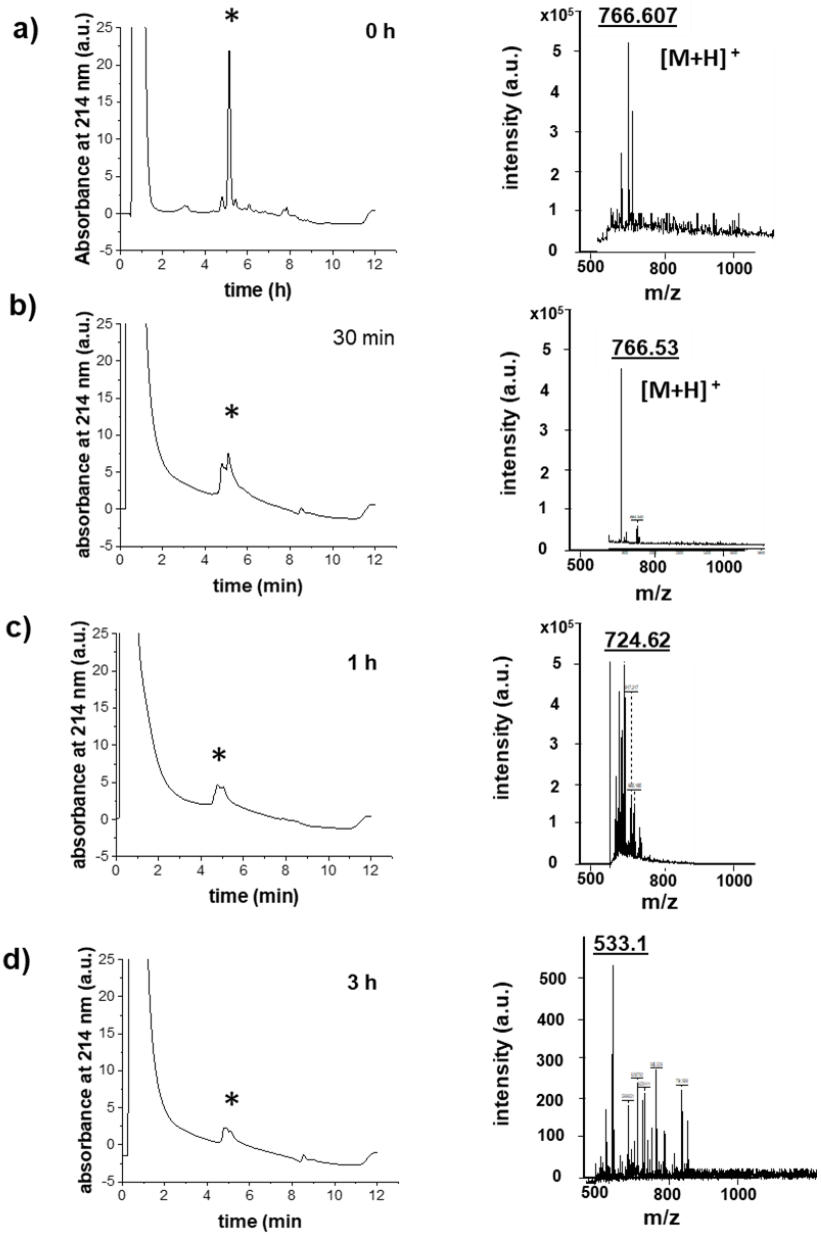

Figure A59. Proteolytic stability of 2g linear determined via HPLC and MALDI-MS. Left panels show RP-HPLC-(214 nm) of **2g linear** after incubation in human plasma in vitro (37°C) at the indicated time points (a-d). Right panels show HPLC MALDI spectra of the collected peak (*) with $t_R \approx 5$ min with the found $[M+H]^+$ or $[M+Na]^+$ until 1 h. One set of experiments is shown in Figure 61, the other in Figure A58.

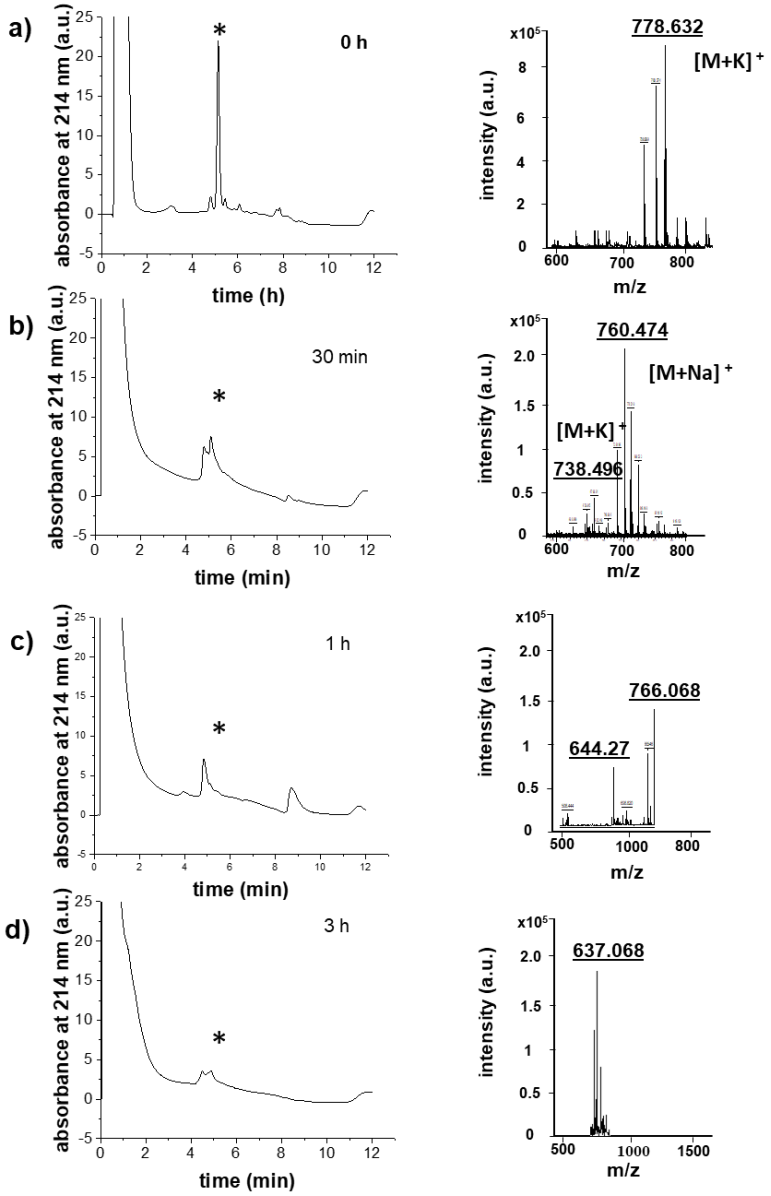

Figure A60. Proteolytic digestion of 2i linear characterized via HPLC and MALDI. Left panels show incubation of **2i linear** in human plasma in vitro (37°C) for 0 h (a), 30 min (b), 1 h (c), 3 h, and 3 h (d) that were analysed via HPLC. Right panels show MALDI analysis of the collected peak (*) revealing the presence of the intact compound with the found $[M+H]^+$ or$[M+Na]^+$ until 30 minutes. One set of experiments is shown in Figure 62, the other in Figure A61.

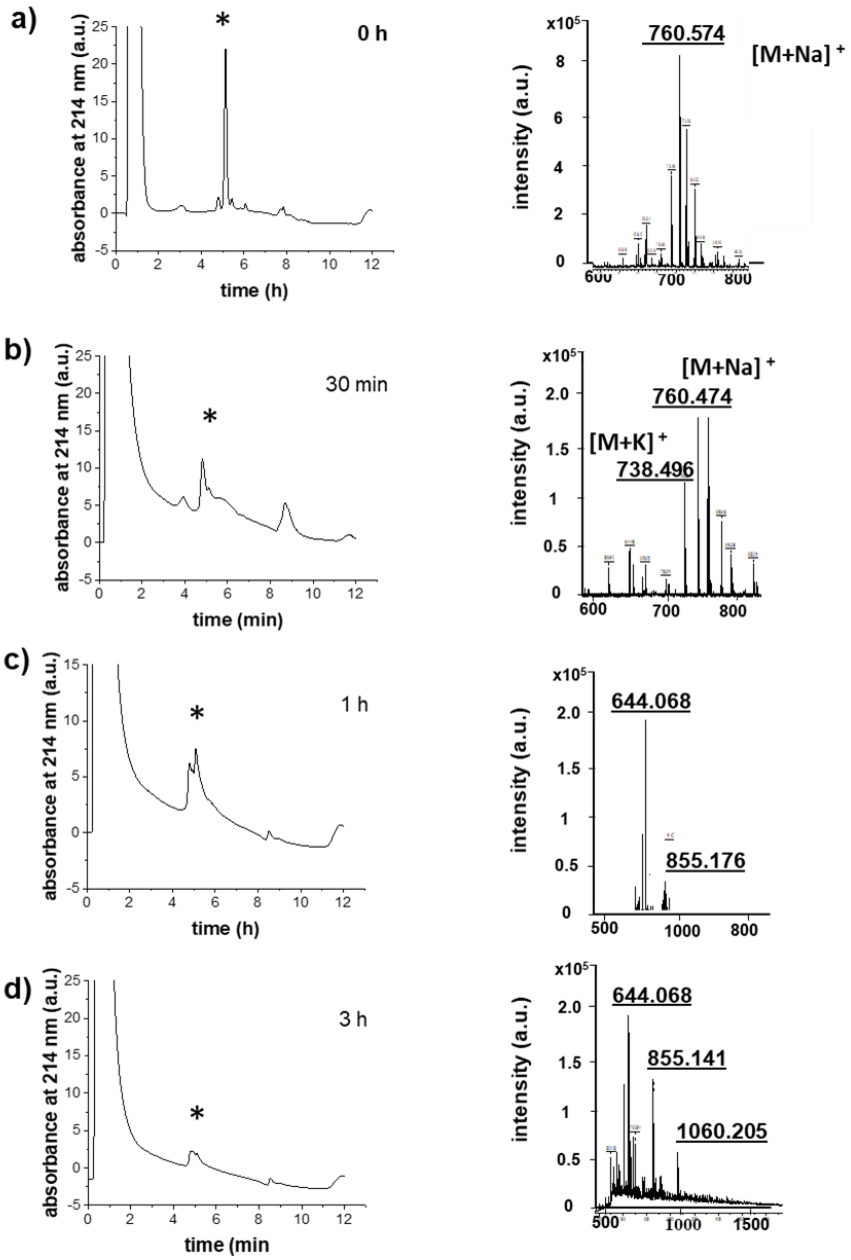

Figure A61. Proteolytic stability of 2i linear determined via HPLC and MALDI-MS. Left panels show RP-HPLC-(214 nm) of **2i linear** after incubation in human plasma in vitro (37°C) at the indicated time points (a-d). Right panels show HPLC MALDI spectra of the collected peak (*) with t_R≈5 min with the found $[M+H]^+$ or $[M+Na]^+$ until 3 h. One set of experiments is shown in Figure 62, the other in Figure A60.

7.2 List of Figures

7.4 List of Tables

7.5 List of Appendix Figures

8 Contributions

The people reported in this section contributed to the peptide synthesis, HPLC purification and /or the generation of part of the data in the corresponding manuscript parts.

Peptide	Synthesis	Purification
2f	Melanie Roth	Melanie Roth
2g	Rafaela Kendel	Kathleen Hille*
2h	Bettina Bernard	Bettina Bernard
2i	Sarah Herterich	Sarah Herterich, Kathleen Hille*, Jana Jekel *
2f linear	Bettina Bernard/Rafaela Kendel	Bettina Bernard
2g linear	Bettina Bernard/Rafaela Kendel	Bettina Bernard/ Rafaela Kendel
2h linear	Bettina Bernard	Bettina Bernard
2i linear	Rafaela Kendel	Rafaela Kendel
Fluos-2i	Pierre Gommeringer/ Kathleen Hille*/Victoria Maier***	Pierre Gommeringer/ Kathleen Hille*/Victoria Maier***
Fluos-2e	Kathleen Hille*	Kathleen Hille*
Fluos-Tfrb	Rafaela Kendel	Rafaela Kendel
Fluos-IAPP	Kathleen Hille*/Denise Naltsas**	Denise Naltsas**
Aβ42	Kathleen Hille*	
IAPP	Kathleen Hille*/ Victoria Maier	Denise Naltsas**/Simon Hornung**/ Alessia Calzi**
2e	Kathleen Hille*/ Rafaela Kendel	Kathleen Hille*/ Rafaela Kendel

*= technical assistant at the Division of Peptide Biochemistry (TUM) ** = PhD candidate at the Division of Peptide Biochemistry*** = HIWI student. Synthesis and peptide purifications were done by internship students co-supervised by me in the same Division, if not stated otherwise.

The data showed in this study was generated by me, if not stated otherwise. Some of the research internship students that I co-supervised performed preliminary studies and characterization of some of MIMs. The data is included in their internship reports and not in my thesis. The IAPP and Aβ40 decamers contained in the peptide array n.5 used for this study, were synthesized by Dr. Valentina Armiento, Dr. Karin Taş, Dr. Christos Kontos and Kathleen Hille at the Division of Peptide Biochemistry (TUM). The peptides were dissociated from cellulose membrane and spotted on coated slides by Dr. Christine Krammer, member of the group of Prof. Dr. Jürgen Bernhagen at the chair of Vascular Biology, ISD (LMU). The BBB permeability studies shown in this thesis were carried out by Dr. Yuan Tian, member of the group of Prof. Dr. Jürgen Bernhagen, ISD (LMU). The characterization of the effect of **2i** and **2g** on the inhibition of hippocampal synaptic long term potentiation (LTP) mediated by Aβ42 was carried out by Markus Ballmann, group of Prof. Dr. Gerhard Rammes, Department of Anaesthesiology and Intensive Care at TUM Klinikum Rechts der Isar.

9 References

1. Soto C. Unfolding the role of protein misfolding in neurodegenerative diseases. Nature Review Neuroscience 2003;4(1):49–60.
2. Chiti F, Dobson CM. Protein Misfolding, Functional Amyloid, and Human Disease. Annual Review of Biochemistry 2006;75(1):333–66.
3. Chiti F, Dobson CM. Protein Misfolding, Amyloid Formation, and Human Disease: A Summary of Progress Over the Last Decade. Annual Review of Biochemistry 2017;86(1):27–68.
4. Hampel H, Hardy J, Blennow K, Chen C, Perry G, Kim SH, et al. The Amyloid-β Pathway in Alzheimer's Disease. Molecular Psychiatry 2021;26(10):5481–503.
5. Thal DR, Rüb U, Orantes M, Braak H. Phases of Aβ-deposition in the human brain and its relevance for the development of AD. Neurology 2002;58(12):1791–800.
6. Akter R, Cao P, Noor H, Ridgway Z, Tu LH, Wang H, et al. Islet Amyloid Polypeptide: Structure, Function, and Pathophysiology. Journal of Diabetes Research 2016(1):1–18.
7. Kent SA, Spires-Jones TL, Durrant CS. The physiological roles of tau and Aβ: implications for Alzheimer's disease pathology and therapeutics. Acta Neuropathologica 2020;140(4):417–47.
8. Müller UC, Deller T, Korte M. Not just amyloid: physiological functions of the amyloid precursor protein family. Nature Reviews Neuroscience 2017;18(5):281–98.
9. Malenka RC, Bear MF. LTP and LTD. Neuron 2004;44(1):5–21.
10. Armiento V, Spanopoulou A, Kapurniotu A. Peptide-Based Molecular Strategies To Interfere with Protein Misfolding, Aggregation, and Cell Degeneration. Angewandte Chemie International Edition 2020;59(9):3372–84.
11. Whitson JS, Selkoe DJ, Cotman CW. Amyloid β Protein Enhances the Survival of Hippocampal Neurons in Vitro. Science 1989;243(4897):1488–90.
12. Durrant CS, Ruscher K, Sheppard O, Coleman MP, Özen I. Beta secretase 1-dependent amyloid precursor protein processing promotes excessive vascular sprouting through NOTCH3 signaling. Cell Death and Diseases 2020,11(2):98–113.
13. De Strooper B, Vassar R, Golde T. The secretases: enzymes with therapeutic potential in Alzheimer disease. Nature Reviews Neurology 2010;6(2):99–107.
14. Hampel H, Vassar R, De Strooper B, Hardy J, Willem M, Singh N, et al. The β-Secretase BACE1 in Alzheimer's Disease. Biological Psychiatry 2021;89(8):745–56.
15. Steiner H, Fukumori A, Tagami S, Okochi M. Making the final cut: pathogenic amyloid-β peptide generation by γ-secretase. Cell Stress 2018;2(11):292–310.
16. Bateman RJ, Munsell LY, Morris JC, Swarm R, Yarasheski KE, Holtzman DM. Human amyloid-β synthesis and clearance rates as measured in cerebrospinal fluid in vivo. Nature Medicine 2006;12(7):856–61.
17. Weller RO, Massey A, Kuo YM, Roher AE. Cerebral Amyloid Angiopathy: Accumulation of Abeta in Interstitial Fluid Drainage Pathways in Alzheimer's Disease. Annals of the New York Academy of Sciences 2000;903(1):110–7.
18. Westermark P, Eizirik DL, Pipeleers DG, HellerstroemM C, Andersson A. Rapid deposition of amyloid in human islets transplanted into nude mice. Diabetologia 1995;38(5):543–9.
19. Frances, Rorsman P. Diabetes Mellitus and the β Cell: The Last Ten Years. Cell 2012;148(6):1160–71.
20. Westermark GT, Westermark P. Transthyretin and Amyloid in the Islets of Langerhans in Type-2 Diabetes. Experimental Diabetes Research 2008;2008:1–7.
21. Westermark P, Andersson A, Westermark GT. Islet Amyloid Polypeptide, Islet Amyloid, and Diabetes Mellitus. Physiological Reviews 2011;91(3):795–826.
22. Lutz TA. The role of amylin in the control of energy homeostasis. American Journal of Physiology-Regulatory, Integrative and Comparative Physiology 2010;298(6):1475–84.
23. Press M, Jung T, König J, Grune T, Höhn A. Protein aggregates and proteostasis in aging: Amylin and β-cell function. Mechanisms of Aging and Development 2019;177:46–54.
24. Hamzé R, Delangre E, Tolu S, Moreau M, Janel N, Bailbé D, et al. Type 2 Diabetes Mellitus and Alzheimer's Disease: Shared Molecular Mechanisms and Potential Common Therapeutic Targets. International Journal of Molecular Sciences 2022;23(23):15287.

25. Raimundo AF, Ferreira S, Martins IC, Menezes R. Islet Amyloid Polypeptide: A Partner in Crime With Aβ in the Pathology of Alzheimer's Disease. Front Mol Neurosci 2020;13:35.
26. Miklossy J, Qing H, Radenovic A, Kis A, Vileno B, Làszló F, et al. Beta amyloid and hyperphosphorylated tau deposits in the pancreas in type 2 diabetes. Neurobiology of Aging 2010;31(9):1503–15.
27. O'Nuallain B, Williams AD, Westermark P, Wetzel R. Seeding Specificity in Amyloid Growth Induced by Heterologous Fibrils. Journal of Biological Chemistry 2004;279(17):17490–9.
28. Andreetto E, Yan LM, Tatarek-Nossol M, Velkova A, Frank R, Kapurniotu A. Identification of Hot Regions of the Aβ-IAPP Interaction Interface as High-Affinity Binding Sites in both Cross- and Self-Association. Angewandte Chemie International Edition 2010;49(17):3081–5.
29. Oskarsson ME, Paulsson JF, Schultz SW, Ingelsson M, Westermark P, Westermark GT. In Vivo Seeding and Cross-Seeding of Localized Amyloidosis. The American Journal of Pathology 2015;185(3):834–46.
30. Yang Y, Song W. Molecular links between Alzheimer's disease and diabetes mellitus. Neuroscience 2013;250:140–50.
31. Moreno-Gonzalez I, Edwards Iii G, Salvadores N, Shahnawaz M, Diaz-Espinoza R, Soto C. Molecular interaction between type 2 diabetes and Alzheimer's disease through cross-seeding of protein misfolding. Molecular Psychiatry 2017;22(9):1327–34.
32. Janson J, Laedtke T, Parisi JE, O'Brien P, Petersen RC, Butler PC. Increased Risk of Type 2 Diabetes in Alzheimer Disease. Diabetes 2004;53(2):474–81.
33. Arosio P, Michaels TCT, Linse S, Månsson C, Emanuelsson C, Presto J, et al. Kinetic analysis reveals the diversity of microscopic mechanisms through which molecular chaperones suppress amyloid formation. Nature Communications 2016;7(1):10948.
34. Törnquist M, Michaels TCT, Sanagavarapu K, Yang X, Meisl G, Cohen SIA, et al. Secondary nucleation in amyloid formation. Chemical Communications 2018;54(63):8667–84.
35. Han W, Schulten K. Fibril Elongation by $A\beta_{17-42}$: Kinetic Network Analysis of Hybrid-Resolution Molecular Dynamics Simulations. J Am Chem Soc 2014;136(35):12450–60.
36. Xue WF, Hellewell AL, Hewitt EW, Radford SE. Fibril fragmentation in amyloid assembly and cytotoxicity. Prion 2010;4(1):20–5.
37. Kreutzer AG, Nowick JS. Elucidating the Structures of Amyloid Oligomers with Macrocyclic β-Hairpin Peptides: Insights into Alzheimer's Disease and Other Amyloid Diseases. Accounts of Chemical Research 2018;51(3):706–18.
38. Hoyer W, Grönwall C, Jonsson A, Ståhl S, Härd T. Stabilization of a β-hairpin in monomeric Alzheimer's amyloid-β peptide inhibits amyloid formation. Proceedings of the National Academy of Sciences of the Unisted States of America 2008;105(13):5099–104.
39. Kayed R, Bernhagen J, Greenfield N, Sweimeh K, Brunner H, Voelter W, et al. Conformational transitions of islet amyloid polypeptide (IAPP) in amyloid formation in Vitro. Journal of Molecular Biology 1999;287(4):781–96.
40. Dupuis NF, Wu C, Shea JE, Bowers MT. Human Islet Amyloid Polypeptide Monomers Form Ordered β-hairpins: A Possible Direct Amyloidogenic Precursor. Journal of the American Chemical Society 2009;131(51):18283–92.
41. Liu C, Sawaya MR, Cheng PN, Zheng J, Nowick JS, Eisenberg D. Characteristics of Amyloid-Related Oligomers Revealed by Crystal Structures of Macrocyclic β-Sheet Mimics. Journal of the American Chemical Society 2011;133(17):6736–44.
42. Bucciantini M, Giannoni E, Chiti F, Baroni F, Formigli L, Zurdo J, et al. Inherent toxicity of aggregates implies a common mechanism for protein misfolding diseases. Nature 2002;416(6880):507–11.
43. Baglioni S, Casamenti F, Bucciantini M, Luheshi LM, Taddei N, Chiti F, et al. Prefibrillar Amyloid Aggregates Could Be Generic Toxins in Higher Organisms. The Journal of Neuroscience 2006;26(31):8160–7.
44. Shankar GM, Li S, Mehta TH, Garcia-Munoz A, Shepardson NE, Smith I, et al. Amyloid-β protein dimers isolated directly from Alzheimer's brains impair synaptic plasticity and memory. Nature Medicine 2008;14(8):837–42.
45. Abedini A, Plesner A, Cao P, Ridgway Z, Zhang J, Tu LH, et al. Time-resolved studies define the nature of toxic IAPP intermediates, providing insight for anti-amyloidosis therapeutics. eLife 2016;5, e12977

46. Sepehri A, Nepal B, Lazaridis T. Distinct Modes of Action of IAPP Oligomers on Membranes. Journal of Chemical Information and Modeling 2021;61(9):4645–55.
47. Gurlo T, Ryazantsev S, Huang CJ, Yeh MW, Reber HA, Hines OJ, et al. Evidence for Proteotoxicity in β Cells in Type 2 Diabetes. The American Journal of Pathology 2010;176(2):861–9.
48. Li X, Wan M, Gao L, Fang W. Mechanism of Inhibition of Human Islet Amyloid Polypeptide-Induced Membrane Damage by a Small Organic Fluorogen. Scientific Reports 2016;6(1):21614.
49. Huang CJ, Gurlo T, Haataja L, Costes S, Daval M, Ryazantsev S, et al. Calcium-activated Calpain-2 Is a Mediator of Beta Cell Dysfunction and Apoptosis in Type 2 Diabetes. Journal of Biological Chemistry 2010;285(1):339–48.
50. Williams AD, Sega M, Chen M, Kheterpal I, Geva M, Berthelier V, et al. Structural properties of Aβ protofibrils stabilized by a small molecule. Proceedings of the National Academy of Sciences 2005;102(20):7115–20.
51. Harper' JD, Wong S, Lieber M, Lansbury PT. Observation of metastable Aβ amyloid protofibrils by atomic force microscopy. Chemistry & Biology. 1997;4:119–25.
52. Kayed R, Head E, Thompson JL, McIntire TM, Milton SC, Cotman CW, et al. Common Structure of Soluble Amyloid Oligomers Implies Common Mechanism of Pathogenesis. Science 2003;300(5618):486–9.
53. Lasagna-Reeves CA, Castillo-Carranza DL, Sengupta U, Sarmiento J, Troncoso J, Jackson GR, et al. Identification of oligomers at early stages of tau aggregation in Alzheimer's disease. The FASEB Journal 2012;26(5):1946–59.
54. Ono K, Tsuji M. Protofibrils of Amyloid-β are Important Targets of a Disease-Modifying Approach for Alzheimer's Disease. International Journal of Molecular Sciences 2020;21(3):952.
55. Rammes G, Hasenjäger A, Sroka-Saidi K, Deussing JM, Parsons CG. Therapeutic significance of NR2B-containing NMDA receptors and mGluR5 metabotropic glutamate receptors in mediating the synaptotoxic effects of β-amyloid oligomers on long-term potentiation (LTP) in murine hippocampal slices. Neuropharmacology 2011;60(6):982–90.
56. Sengupta U, Nilson AN, Kayed R. The Role of Amyloid-β Oligomers in Toxicity, Propagation, and Immunotherapy. EBioMedicine 2016;6:42–9.
57. Kayed R, Bernhagen J, Greenfield N, Sweimeh K, Brunner H, Voelter W, et al. Conformational transitions of islet amyloid polypeptide (IAPP) in amyloid formation in Vitro. Journal of Molecular Biology 1999;287(4):781–96.
58. Biancalana M, Koide S. Molecular mechanism of Thioflavin-T binding to amyloid fibrils. Biochimica et Biophysica Acta (BBA) - Proteins and Proteomics 2010;1804(7):1405–12.
59. Dzwolak W, Pecul M. Chiral bias of amyloid fibrils revealed by the twisted conformation of Thioflavin T: An induced circular dichroism/DFT study. FEBS Letters 2005;579(29):6601–3.
60. Kollmer M, Close W, Funk L, Rasmussen J, Bsoul A, Schierhorn A, et al. Cryo-EM structure and polymorphism of Aβ amyloid fibrils purified from Alzheimer's brain tissue. Nature Communications 2019;10(1):4760
61. Yang Y, Arseni D, Zhang W, Huang M, Lövestam S, Schweighauser M, et al. Cryo-EM structures of amyloid-β 42 filaments from human brains. Science 2022;375(6577):167–72.
62. Röder C, Kupreichyk T, Gremer L, Schäfer LU, Pothula KR, Ravelli RBG, et al. Cryo-EM structure of islet amyloid polypeptide fibrils reveals similarities with amyloid-β fibrils. Nature Structural & Molecular Biology 2020;27(7):660–7.
63. Cao Q, Boyer DR, Sawaya MR, Ge P, Eisenberg DS. Cryo-EM structure and inhibitor design of human IAPP (amylin) fibrils. Nature Structural & Molecular Biology 2020;27(7):653–9.
64. Gremer L, Schölzel D, Schenk C, Reinartz E, Labahn J, Ravelli RBG, et al. Fibril structure of amyloid-β(1–42) by cryo–electron microscopy. Science 2017;358(6359):116–9.
65. Paravastu AK, Leapman RD, Yau WM, Tycko R. Molecular structural basis for polymorphism in Alzheimer's β-amyloid fibrils. Proceedings of the National Academy of Sciences 2008;105(47):18349–54.
66. Petkova AT, Yau WM, Tycko R. Experimental Constraints on Quaternary Structure in Alzheimer's β-Amyloid Fibrils. Biochemistry 2006;45(2):498–512.
67. Lu JX, Qiang W, Yau WM, Charles, Stephen, Tycko R. Molecular Structure of β-Amyloid Fibrils in Alzheimer's Disease Brain Tissue. Cell 2013;154(6):1257–68.

68. Petkova AT, Ishii Y, Balbach JJ, Antzutkin ON, Leapman RD, Delaglio F, et al. A structural model for Alzheimer's β-amyloid fibrils based on experimental constraints from solid state NMR. Proceedings of the National Academy of Sciences 2002;99(26):16742–7.
69. Charidimou A, Boulouis G, Gurol ME, Ayata C, Bacskai BJ, Frosch MP, et al. Emerging concepts in sporadic cerebral amyloid angiopathy. Brain 2017;140(7):1829–50.
70. Pettersen EF, Goddard TD, Huang CC, Couch GS, Greenblatt DM, Meng EC, et al. UCSF Chimera?A visualization system for exploratory research and analysis. Journal of Computational Chemistry 2004;25(13):1605–12.
71. Wälti MA, Ravotti F, Arai H, Glabe CG, Wall JS, Böckmann A, et al. Atomic-resolution structure of a disease-relevant Aβ(1–42) amyloid fibril. Proceedings of the National Academy of Sciences 2016;113(34):4976–84.
72. Xiao Y, Ma B, Mcelheny D, Parthasarathy S, Long F, Hoshi M, et al. Aβ(1–42) fibril structure illuminates self-recognition and replication of amyloid in Alzheimer's disease. Nature Structural & Molecular Biology 2015;22(6):499–505.
73. Colvin MT, Silvers R, Ni QZ, Can TV, Sergeyev I, Rosay M, et al. Atomic Resolution Structure of Monomorphic Aβ42 Amyloid Fibrils. Journal of the American Chemical Society 2016;138(30):9663–74.
74. Westermark P, Engström U, Johnson KH, Westermark GT, Betsholtz C. Islet amyloid polypeptide: pinpointing amino acid residues linked to amyloid fibril formation. Proceedings of the National Academy of Sciences 1990;87(13):5036–40.
75. Nishi M, Chan SJ, Nagamatsu S, Bell GI, Steiner DF. Conservation of the sequence of islet amyloid polypeptide in five mammals is consistent with its putative role as an islet hormone. The Proceedings of the National Academy of Science 1989;86(15):5738–42.
76. Goldsbury C, Goldie K, Pellaud J, Seelig J, Frey P, Müller SA, et al. Amyloid Fibril Formation from Full-Length and Fragments of Amylin. Journal of Structural Biology 2000;130(2–3):352–62.
77. Sawaya MR, Sambashivan S, Nelson R, Ivanova MI, Sievers SA, Apostol MI, et al. Atomic structures of amyloid cross-β spines reveal varied steric zippers. Nature 2007;447(7143):453–7.
78. Luca S, Yau WM, Leapman R, Tycko R. Peptide Conformation and Supramolecular Organization in Amylin Fibrils: Constraints from Solid-State NMR. Biochemistry 2007;46(47):13505–22.
79. Weirich F, Gremer L, Mirecka EA, Schiefer S, Hoyer W, Heise H. Structural Characterization of Fibrils from Recombinant Human Islet Amyloid Polypeptide by Solid-State NMR: The Central FGAILS Segment Is Part of the β-Sheet Core. PLOS ONE 2016;11(9):1–20.
80. Gallardo R, Iadanza MG, Xu Y, Heath GR, Foster R, Radford SE, et al. Fibril structures of diabetes-related amylin variants reveal a basis for surface-templated assembly. Nature Structural & Molecular Biology 2020;27(11):1048–56.
81. Kapurniotu A. Enlightening amyloid fibrils linked to type 2 diabetes and cross-interactions with Aβ. Nature Structural & Molecular Biology 2020;27(11):1006–8.
82. Sperling RA, Jack CR, Black SE, Frosch MP, Greenberg SM, Hyman BT, et al. Amyloid-related imaging abnormalities in amyloid-modifying therapeutic trials: Recommendations from the Alzheimer's Association Research Roundtable Workgroup. Alzheimer's & Dementia 2011;7(4):367–85.
83. Hruby VJ. Designing peptide receptor agonists and antagonists. Nature Reviews Drug Discovery 2002;1(11):847–58.
84. Young LM, Ashcroft AE, Radford SE. Small molecule probes of protein aggregation. Current Opinion in Chemical Biology 2017;39:90–9.
85. Eisele YS, Monteiro C, Fearns C, Encalada SE, Wiseman RL, Powers ET, et al. Targeting protein aggregation for the treatment of degenerative diseases. Nature Reviews Drug Discovery 2015;14(11):759–80.
86. Chatterjee J, Mierke D, Kessler H. N-Methylated Cyclic Pentaalanine Peptides as Template Structures. Journal of the American Chemical Society 2006;128(47):15164–72.
87. Joo SH. Cyclic Peptides as Therapeutic Agents and Biochemical Tools. Biomolecules and Therapeutics 2012;20(1):19–26.
88. Kong XD, Heinis C. Towards the Development of Orally Available Peptide Therapeutics. CHIMIA 2021;75(6):514.

89. Dougherty PG, Qian Z, Pei D. Macrocycles as protein–protein interaction inhibitors. Biochemical Journal 2017;474(7):1109–25.
90. Arai T, Sasaki D, Araya T, Sato T, Sohma Y, Kanai M. A Cyclic KLVFF-Derived Peptide Aggregation Inhibitor Induces the Formation of Less-Toxic Off-Pathway Amyloid-β Oligomers. ChemBioChem 2014;15(17):2577–83.
91. Ghadiri MR, Granja JR, Milligan RA, Mcree DE, Khazanovich N. Self-assembling organic nanotubes based on a cyclic peptide architecture. Nature 1993;366(6453):324–7.
92. Lührs T, Ritter C, Adrian M, Riek-Loher D, Bohrmann B, Döbeli H, et al. 3D structure of Alzheimer's amyloid-β(1–42) fibrils. Proceedings of the National Academy of Sciences 2005;102(48):17342–7.
93. Richman M, Wilk S, Chemerovski M, Wärmländer SKTS, Wahlström A, Gräslund A, et al. In Vitro and Mechanistic Studies of an Antiamyloidogenic Self-Assembled Cyclic d,l-α-Peptide Architecture. Journal of the American Chemical Society 2013;135(9):3474–84.
94. Chemerovski-Glikman M, Rozentur-Shkop E, Richman M, Grupi A, Getler A, Cohen HY, et al. Self-Assembled Cyclicd,l-α-Peptides as Generic Conformational Inhibitors of the α-Synuclein Aggregation and Toxicity: In Vitro and Mechanistic Studies. Chemistry - A European Journal 2016;22(40):14236–46.
95. Yan LM, Tatarek-Nossol M, Velkova A, Kazantzis A, Kapurniotu A. Design of a mimic of nonamyloidogenic and bioactive human islet amyloid polypeptide (IAPP) as nanomolar affinity inhibitor of IAPP cytotoxic fibrillogenesis. Proceedings of the National Academy of Sciences 2006;103(7):2046–51.
96. Yan LM, Velkova A, Tatarek-Nossol M, Rammes G, Sibaev A, Andreetto E, et al. Selectively N-Methylated Soluble IAPP Mimics as Potent IAPP Receptor Agonists and Nanomolar Inhibitors of Cytotoxic Self-Assembly of Both IAPP and Aβ40. Angewandte Chemie International Edition 2013;52(39):10378–83.
97. Niu Z, Prade E, Malideli E, Hille K, Jussupow A, Mideksa YG, et al. Structural Insight into IAPP-Derived Amyloid Inhibitors and Their Mechanism of Action. Angewandte Chemie International Edition 2020;59(14):5771–81.
98. Andreetto E, Malideli E, Yan L, Kracklauer M, Farbiarz K, Tatarek-Nossol M, et al. A Hot-Segment-Based Approach for the Design of Cross-Amyloid Interaction Surface Mimics as Inhibitors of Amyloid Self-Assembly. Angewandte Chemie International Edition 2015;54(44):13095–100.
99. Spanopoulou A, Heidrich L, Chen HR, Frost C, Hrle D, Malideli E, et al. Designed Macrocyclic Peptides as Nanomolar Amyloid Inhibitors Based on Minimal Recognition Elements. Angewandte Chemie International Edition 2018;57(44):14503–8.
100. Bakou M, Hille K, Kracklauer M, Spanopoulou A, Frost CV, Malideli E, et al. Key aromatic/hydrophobic amino acids controlling a cross-amyloid peptide interaction versus amyloid self-assembly. Journal of Biological Chemistry 2017;292(35):14587–602.
101. Wiltzius JJW, Sievers SA, Sawaya MR, Eisenberg D. Atomic structures of IAPP (amylin) fusions suggest a mechanism for fibrillation and the role of insulin in the process. Protein Science 2009;18(7):1521–30.
102. Merrifield RB. Solid Phase Peptide Synthesis. I. The Synthesis of a Tetrapeptide. Journal of the American Chemical Society 1963;85(14):2149–54.
103. Palomo JM. Solid-phase peptide synthesis: an overview focused on the preparation of biologically relevant peptides. RSC Advances 2014;4(62):32658–72.
104. Shelton PT, Jensen KJ. Linkers, Resins, and General Procedures for Solid-Phase Peptide Synthesis. Methods in Molecular Biology. Humana Press; 2013;1047: 23–41.
105. Guillier F, Orain D, Bradley M. Linkers and Cleavage Strategies in Solid-Phase Organic Synthesis and Combinatorial Chemistry. Chemical Reviews 2000;100(6):2091–158.
106. Sarin VK, Kent SBH, Tam JP, Merrifield RB. Quantitative monitoring of solid-phase peptide synthesis by the ninhydrin reaction. Analytical Biochemistry 1981;117(1):147–57.
107. Barlos K, Chatzi O, Gatos D, Stavropoulos G. 2-Chlorotrityl chloride resin. Studies on anchoring of Fmoc-amino acids and peptide cleavage. International Journal of Peptide and Protein Research 1991;37(6):513–20.
108. Athanassopoulos P, Barlos K, Gatos D, Hatzi O, Tzavara C. Application of 2-Chlorotrityl Chloride in Convergent Peptide Synthesis. Tetrahedron Letters 1995;36(31):5645-5648.

109. García-Martín F, Bayó-Puxan N, Cruz LJ, Bohling JC, Albericio F. Chlorotrityl Chloride (CTC) Resin as a Reusable Carboxyl Protecting Group. QSAR & Combinational Science 2007;26(10):1027–35.
110. Orosz G, Kiss LászlóP. Simple and efficient synthesis of 2-chlorotritylchloride resin. Tetrahedron Letters 1998;39(20):3241–2.
111. Gairí M, Lloyd-Williams P, Albericio F, Giralt E. Use of BOP reagent for the suppression of diketopiperazine formation in boc/bzl solid-phase peptide synthesis. Tetrahedron Letters 1990;31(50):7363–6.
112. Brunfeldt K, Christensen T, Roepstorff P. Acetylation an artefact in solid phase peptide synthesis. A mass spectrometrical investigation. FEBS Letters 1972;25(1):184–8.
113. Wang J, Berglund MR, Braden T, Embry MC, Johnson MD, Groskreutz SR, et al. Mechanistic Study of Diketopiperazine Formation during Solid-Phase Peptide Synthesis of Tirzepatide. ACS Omega 2022;7(50):46809–24.
114. Nieuwland M, Van Gijzel N, Van Hest JCM, Löwik DWPM. The influence of amino acid sequence on structure and morphology of polydiacetylene containing peptide fibres. Soft Matter 2015;11(7):1335–44.
115. Khosla MC, Smeby RR, Bumpus FM. Failure sequence in solid-phase peptide synthesis due to the presence of an N-alkylamino acid. Journal of the American Chemical Society 1972;94(13):4721–4.
116. Lü JM, Rosokha SV, Neretin IS, Kochi JK. Quinones as Electron Acceptors. X-Ray Structures, Spectral (EPR, UV−vis) Characteristics and Electron-Transfer Reactivities of Their Reduced Anion Radicals as Separated vs Contact Ion Pairs. Journal of the American Chemical Society 2006;128(51):16708–19.
117. Aletras A, Barlos K, Gatos D, Koutsogianni S, Mamos P. Preparation of the very acid-sensitive Fmoc-Lys(Mtt)-OH Application in the synthesis of side-chain to side-chain cyclic peptides and oligolysine cores suitable for the solid-phase assembly of MAPs and TASPs. International Journal of Peptide and Protein Research 2009;45(5):488–96.
118. Chatzi KBarlosO, Gatos D, Stavropoulos G. 2-Chlorotrityl chloride resin: Studies on anchoring of Fmoc-amino acids and peptide cleavage. International Journal of Peptide and Protein Research 2009;37(6):513–20.
119. Chatterjee J, Laufer B, Kessler H. Synthesis of N-methylated cyclic peptides. Nature Protocols 2012;7(3):432–44.
120. Kolesnichenko IV, Goloverda GZ, Kolesnichenko VL. A Versatile Method of Ambient-Temperature Solvent Removal. Organic Process Research & Development 2020;24(1):25–31.
121. Sabir AM, Moloy M, Bhasin PS. HPLC-Methods and validation review. International Research Journal of Pharmacy 2016;4(4):39–46.
122. Koehbach J, Gruber CW, Becker C, Kreil DP, Jilek A. MALDI TOF/TOF-Based Approach for the Identification of d- Amino Acids in Biologically Active Peptides and Proteins. Journal of Proteome Research 2016;15(5):1487–96.
123. Ryan DJ, Spraggins JM, Caprioli RM. Protein identification strategies in MALDI imaging mass spectrometry: a brief review. Current Opinion in Chemical Biology 2019;48:64–72.
124. Darie-Ion L, Whitham D, Jayathirtha M, Rai Y, Neagu AN, Darie CC, et al. Applications of MALDI-MS/MS-Based Proteomics in Biomedical Research. Molecules 2022;27(19):6196.
125. Kassem T, Sabatino D, Jia X, Zhu XX, Lubell WD. To Rink or Not to Rink Amide Link, that is the Question to Address for More Economical and Environmentally Sound Solid-Phase Peptide Synthesis. International Journal of Peptide Research and Therapeutics 2009;15(3):211–8.
126. Yan LM, Velkova A, Tatarek-Nossol M, Andreetto E, Kapurniotu A. IAPP Mimic Blocks Aβ Cytotoxic Self-Assembly: Cross-Suppression of Amyloid Toxicity of Aβ and IAPP Suggests a Molecular Link between Alzheimer's Disease and Type II Diabetes. Angewandte Chemie International Edition 2007;46(8):1246–52.
127. Taş K, Volta BD, Lindner C, El Bounkari O, Hille K, Tian Y, et al. Designed peptides as nanomolar cross-amyloid inhibitors acting via supramolecular nanofiber co-assembly. Nature Communications 2022;13(1):5004.
128. Mayerhöfer TG, Pahlow S, Popp J. The Bouguer-Beer-Lambert Law: Shining Light on the Obscure. ChemPhysChem 2020;21(18):2029–46.

129. Armiento V, Hille K, Naltsas D, Lin JS, Barron AE, Kapurniotu A. The Human Host-Defense Peptide Cathelicidin LL-37 is a Nanomolar Inhibitor of Amyloid Self-Assembly of Islet Amyloid Polypeptide (IAPP). Angewandte Chemie International Edition 2020;59(31):12837–41.
130. Smith PK, Krohn RI, Hermanson GT, Mallia AK, Gartner FH, Provenzano MD, et al. Measurement of protein using bicinchoninic acid. Analytical Biochemistry 1985;150(1):76–85.
131. Krebs MRH, Bromley EHC, Donald AM. The binding of thioflavin-T to amyloid fibrils: localisation and implications. Journal of Structural Biology 2005;149(1):30–7.
132. Xue C, Lin TY, Chang D, Guo Z. Thioflavin T as an amyloid dye: fibril quantification, optimal concentration and effect on aggregation. Royal Society Open Science 2017;4(1):160696.
133. Walsh DM, Thulin E, Minogue AM, Gustavsson N, Pang E, Teplow DB, et al. A facile method for expression and purification of the Alzheimer's disease-associated amyloid β-peptide. FEBS Journal 2009;276(5):1266–81.
134. Ghasemi M, Turnbull T, Sebastian S, Kempson I. The MTT Assay: Utility, Limitations, Pitfalls, and Interpretation in Bulk and Single-Cell Analysis. International Journal of Molecular Sciences 2021;22(23):12827.
135. Tenidis K, Waldner M, Bernhagen J, Fischle W, Bergmann M, Weber M, et al. Identification of a penta- and hexapeptide of islet amyloid polypeptide (IAPP) with amyloidogenic and cytotoxic properties. Journal of Molecular Biology 2000;295(4):1055–71.
136. Yan LM, Tatarek-Nossol M, Velkova A, Kazantzis A, Kapurniotu A. Design of a mimic of nonamyloidogenic and bioactive human islet amyloid polypeptide (IAPP) as nanomolar affinity inhibitor of IAPP cytotoxic fibrillogenesis. Proceedings of the National Academy of Sciences 2006;103(7):2046–51.
137. Andreetto E, Yan LM, Caporale A, Kapurniotu A. Dissecting the Role of Single Regions of an IAPP Mimic and IAPP in Inhibition of Aβ40 Amyloid Formation and Cytotoxicity. ChemBioChem 2011;12(9):1313–22.
138. Holzwarth G, Doty P. The Ultraviolet Circular Dichroism of Polypeptides1. Journal of the American Chemical Society 1965;87(2):218–28.
139. Johnson WC. Protein secondary structure and circular dichroism: A practical guide. Proteins: Structure, Function, and Genetics 1990;7(3):205–14.
140. Greenfield NJ. Using circular dichroism spectra to estimate protein secondary structure. Nature Protocols 2006;1(6):2876–90.
141. Sreerama N, Venyaminov SYU, Woody RW. Estimation of the number of α-helical and β-strand segments in proteins using circular dichroism spectroscopy. Protein Science 2008;8(2):370–80.
142. Greenfield NJ. Analysis of the kinetics of folding of proteins and peptides using circular dichroism. Nature Protocols 2006;1(6):2891–9.
143. Weksler B, Romero IA, Couraud PO. The hCMEC/D3 cell line as a model of the human Blood-Brain Barrier. Fluids and Barriers of the CNS 2013;10(1):16.
144. Poller B, Gutmann H, Krähenbühl S, Weksler B, Romero I, Couraud PO, et al. The human brain endothelial cell line hCMEC/D3 as a human blood-brain barrier model for drug transport studies. Journal of Neurochemistry 2008;107(5):1358–68.
145. Malakoutikhah M, Teixidó M, Giralt E. Toward an Optimal Blood−Brain Barrier Shuttle by Synthesis and Evaluation of Peptide Libraries. Journl of Medicinal Chemistry 2008;51(16):4881–9.
146. Díaz-Perlas C, Oller-Salvia B, Sánchez-Navarro M, Teixidó M, Giralt E. Branched BBB-shuttle peptides: chemoselective modification of proteins to enhance blood–brain barrier transport. Chemical Science 2018;9(44):8409–15.
147. Sánchez-Navarro M, Teixidó M, Giralt E. Just passing through. Nature Chemistry 2017;9(8):727–8.
148. Oller-Salvia B, Sánchez-Navarro M, Giralt E, Teixidó M. Blood–brain barrier shuttle peptides: an emerging paradigm for brain delivery. Chemical Society Reviews 2016;45(17):4690–707.
149. Wang Y, Westermark GT. The Amyloid Forming Peptides Islet Amyloid Polypeptide and Amyloid β Interact at the Molecular Level. International Journal of Molecular Science 2021;22(20):11153.
150. Isidro-Llobet A, Guasch-Camell J, Álvarez M, Albericio F. p-Nitrobenzyloxycarbonyl (pNZ) as a TemporaryNα-Protecting Group in Orthogonal Solid-Phase Peptide Synthesis - Avoiding

Diketopiperazine and Aspartimide Formation. European Journal of Organic Chemistry 2005(14):3031–9.
151. Yang Y, Hansen L. Optimized Fmoc-Removal Strategy to Suppress the Traceless and Conventional Diketopiperazine Formation in Solid-Phase Peptide Synthesis. ACS Omega 2022;7(14):12015–20.
152. Bourel L, Carion O, Gras-Masse H, Melnyk O. The deprotection of Lys(Mtt) Journal of Peptide Science 2000;6(6):264–70.
153. Kocsis L, Ruff F, Orosz G. The effect of peptide length on the cleavage kinetics of 2-chlorotrityl resin-bound ethers. Journal of Peptide Science 2006;12(6):428–36.
154. Kontos C, El Bounkari O, Krammer C, Sinitski D, Hille K, Zan C, et al. Designed CXCR4 mimic acts as a soluble chemokine receptor that blocks atherogenic inflammation by agonist-specific targeting. Nature Communications 2020;11(1):5981.
155. Li D, Elbert DL. The kinetics of the removal of the N -methyltrityl (Mtt) group during the synthesis of branched peptides. The Journal of Peptide Research 2002;60(5):300–3.
156. Sherrington DC. Preparation, structure and morphology of polymer supports. Chemical Communications 1998;(21):2275–86.
157. Akintayo DC, Manne SR, De La Torre BG, Li Y, Albericio F. A Practical Peptide Synthesis Workflow Using Amino-Li-Resin. Methods and Protocols 2022;5(5):72.
158. Wei G, Shea JE. Effects of Solvent on the Structure of the Alzheimer Amyloid-β(25–35) Peptide. Biophysical Journal 2006;91(5):1638–47.
159. Berkessel A, Adrio JA, Hüttenhain D, Neudörfl JM. Unveiling the "Booster Effect" of Fluorinated Alcohol Solvents: Aggregation-Induced Conformational Changes and Cooperatively Enhanced H-Bonding. Journal of the American Chemical Society 2006;128(26):8421–6.
160. Roccatano D, Fioroni M, Zacharias M, Colombo G. Effect of hexafluoroisopropanol alcohol on the structure of melittin: A molecular dynamics simulation study. Protein Science 2005;14(10):2582–9.
161. Jasanoff A, Fersht AR. Quantitative Determination of Helical Propensities from Trifluoroethanol Titration Curves. Biochemistry 1994;33(8):2129–35.
162. Hirota N, Goto Y, Mizuno K. Cooperative α-helix formation of β-lactoglobulin and melittin induced by hexafluoroisopropanol: Hexafluoroisopropanol-induced α-helix formation. Protein Science 1997;6(2):416–21.
163. Kaiser ET, Kézdy FJ. Secondary structures of proteins and peptides in amphiphilic environments. (A review). Proceedings of the National Academy of Sciences 1983;80(4):1137–43.
164. Kessler H, Gratias R, Hessler G, Gurrath M, Mueller G. Conformation of cyclic peptides. Principle concepts and the design of selectivity and superactivity in bioactive sequences by 'spatial screening'. Pure & Applied Chemistry 1996;68(6):1201–5.
165. MacPhee CE, Perugini MA, H. Sawyer W, Howlett GJ. Trifluoroethanol induces the self-association of specific amphipathic peptides. FEBS Letters 1997;416(3):265–8.
166. Zheng J, Fayer MD. Hydrogen Bond Lifetimes and Energetics for Solute/Solvent Complexes Studied with 2D-IR Vibrational Echo Spectroscopy. Journal of the American Chemical Society 2007;129(14):4328–35.
167. Mabesoone MFJ, Palmans ARA, Meijer EW. Solute–Solvent Interactions in Modern Physical Organic Chemistry: Supramolecular Polymers as a Muse. Journal of American Chemistry Society. 2020;142(47):19781–98.
168. Novelli F, Vilela M, Pazó A, Amorín M, Granja JR. Molecular Plumbing to Bend Self-Assembling Peptide Nanotubes. Angewandte Chemie International Edition 2021;60(34):18838–44.
169. André I, Linse S, Mulder FAA. Residue-Specific p K_a Determination of Lysine and Arginine Side Chains by Indirect ^{15}N and ^{13}C NMR Spectroscopy: Application to *apo* Calmodulin. Journal of American Chemistry Society 2007;129(51):15805–13.
170. Srivastava A, Singh PK, Kumbhakar M, Mukherjee T, Chattopadyay S, Pal H, et al. Identifying the Bond Responsible for the Fluorescence Modulation in an Amyloid Fibril Sensor. Chemistry - A European Journal 2010;16(30):9257–63.

171. Cohen SIA, Linse S, Luheshi LM, Hellstrand E, White DA, Rajah L, et al. Proliferation of amyloid-β42 aggregates occurs through a secondary nucleation mechanism. Proceedings of the National Academy of Sciences 2013;110(24):9758–63.
172. Cukalevski R, Boland B, Frohm B, Thulin E, Walsh D, Linse S. Role of Aromatic Side Chains in Amyloid β-Protein Aggregation. ACS Chemical Neuroscience 2012;3(12):1008–16.
173. Thacker D, Sanagavarapu K, Frohm B, Meisl G, Knowles TPJ, Linse S. The role of fibril structure and surface hydrophobicity in secondary nucleation of amyloid fibrils. Proceedings of the National Academy of Sciences 2020;117(41):25272–83.
174. He Y, Wei M, Wu Y, Qin H, Li W, Ma X, et al. Amyloid β oligomers suppress excitatory transmitter release via presynaptic depletion of phosphatidylinositol-4,5-bisphosphate. Nature Communications 2019;10(1):1193.
175. Gulisano W, Melone M, Ripoli C, Tropea MR, Li Puma DD, Giunta S, et al. Neuromodulatory Action of Picomolar Extracellular Aβ42 Oligomers on Presynaptic and Postsynaptic Mechanisms Underlying Synaptic Function and Memory. The Journal of Neuroscience 2019;39(30):5986–6000.
176. Bitan G, Fradinger EA, Spring SM, Teplow DB. Neurotoxic protein oligomers—what you see is not always what you get. Amyloid 2005;12(2):88–95.
177. Morel B, Carrasco MP, Jurado S, Marco C, Conejero-Lara F. Dynamic micellar oligomers of amyloid beta peptides play a crucial role in their aggregation mechanisms. Physical Chemistry Chemical Physics 2018;20(31):20597–614.
178. Sang JC, Lee JE, Dear AJ, De S, Meisl G, Thackray AM, et al. Direct observation of prion protein oligomer formation reveals an aggregation mechanism with multiple conformationally distinct species. Chemical Science 2019;10(17):4588–97.
179. Hayden EY, Teplow DB. Amyloid β-protein oligomers and Alzheimer's disease. Alzheimer's Research & Therapy 2013;5(6):60.
180. Scarff CA, Ashcroft AE, Radford SE. Characterization of Amyloid Oligomers by Electrospray Ionization-Ion Mobility Spectrometry-Mass Spectrometry (ESI-IMS-MS) Methods in Molecular Biology. Springer New York; 2016:115–32.
181. Törnquist M, Michaels TCT, Sanagavarapu K, Yang X, Meisl G, Cohen SIA, et al. Secondary nucleation in amyloid formation. Chemical Communications 2018;54(63):8667–84.
182. Mathur D, Prakash S, Anand P, Kaur H, Agrawal P, Mehta A, et al. PEPlife: A Repository of the Half-life of Peptides. Scientific Reports 2016;6(1):36617.
183. Robinson JA. β-Hairpin Peptidomimetics: Design, Structures and Biological Activities. Accounts of Chemical Research 2008;41(10):1278–88.
184. Bozovičar K, Bratkovič T. Small and Simple, yet Sturdy: Conformationally Constrained Peptides with Remarkable Properties. International Journal of Molecular Sciences 2021;22(4):1611.
185. Fang Z, Song Y, Zhan P, Zhang Q, Liu X. Conformational restriction: an effective tactic in 'follow-on'-based drug discovery. Future Medicinal Chemistry 2014;6(8):885–901.
186. Krotee P, Griner SL, Sawaya MR, Cascio D, Rodriguez JA, Shi D, et al. Common fibrillar spines of amyloid-β and human islet amyloid polypeptide revealed by microelectron diffraction and structure-based inhibitors. Journal of Biological Chemistry 2018;293(8):2888–902.
187. Mirecka EA, Feuerstein S, Gremer L, Schröder GF, Stoldt M, Willbold D, et al. β-Hairpin of Islet Amyloid Polypeptide Bound to an Aggregation Inhibitor. Scientific Reports 2016;6(1):33474.
188. Reddy AS, Wang L, Singh S, Ling YL, Buchanan L, Zanni MT, et al. Stable and metastable states of human amylin in solution. Biophysical Journal 2010;99(7):2208–16.
189. Padrick SB, Miranker AD. Islet amyloid polypeptide: identification of long-range contacts and local order on the fibrillogenesis pathway. Journal of Molecular Biology 2001;308(4):783–94.
190. Marek P, Abedini A, Song B, Kanungo M, Johnson ME, Gupta R, et al. Aromatic interactions are not required for amyloid fibril formation by islet amyloid polypeptide but do influence the rate of fibril formation and fibril morphology. Biochemistry 2007;46(11):3255–61.
191. Porat Y, Mazor Y, Efrat S, Gazit E. Inhibition of Islet Amyloid Polypeptide Fibril Formation: A Potential Role for Heteroaromatic Interactions. Biochemistry 2004;43(45):14454–62.
192. Lesma J, Bizet F, Berardet C, Tonali N, Pellegrino S, Taverna M, et al. β-Hairpin Peptide Mimics Decrease Human Islet Amyloid Polypeptide (hIAPP) Aggregation. Front Cell Dev Biol 2021;9:729001.

193. Azriel R, Gazit E. Analysis of the Minimal Amyloid-forming Fragment of the Islet Amyloid Polypeptide. Journal of Biological Chemistry 2001;276(36):34156–61.
194. Zaguri D, Zimmermann MR, Meisl G, Levin A, Rencus-Lazar S, Knowles TPJ, et al. Kinetic and Thermodynamic Driving Factors in the Assembly of Phenylalanine-Based Modules. ACS Nano 2021;15(11):18305–11.
195. Larini L, Shea JE. Role of β-Hairpin Formation in Aggregation: The Self-Assembly of the Amyloid-β(25–35) Peptide. Biophysical Journal 2012;103(3):576–86.
196. Dear AJ, Meisl G, Šarić A, Michaels TCT, Kjaergaard M, Linse S, et al. Identification of on- and off-pathway oligomers in amyloid fibril formation. Chemical Science 2020;11(24):6236–47.
197. Pithadia A, Brender JR, Fierke CA, Ramamoorthy A. Inhibition of IAPP Aggregation and Toxicity by Natural Products and Derivatives. Journal of Diabetes Research 2016;2016:1–12.
198. Meng F, Abedini A, Plesner A, Verchere CB, Raleigh DP. The Flavanol (−)-Epigallocatechin 3-Gallate Inhibits Amyloid Formation by Islet Amyloid Polypeptide, Disaggregates Amyloid Fibrils, and Protects Cultured Cells against IAPP-Induced Toxicity. Biochemistry 2010;49(37):8127–33.
199. Suzuki Y, Brender JR, Hartman K, Ramamoorthy A, Marsh ENG. Alternative Pathways of Human Islet Amyloid Polypeptide Aggregation Distinguished by 19F Nuclear Magnetic Resonance-Detected Kinetics of Monomer Consumption. Biochemistry 2012;51(41):8154–62.
200. Tu LH, Raleigh DP. Role of Aromatic Interactions in Amyloid Formation by Islet Amyloid Polypeptide. Biochemistry 2013;52(2):333–42.
201. Abioye RO, Okagu OD, Udenigwe CC. Disaggregation of Islet Amyloid Polypeptide Fibrils as a Potential Anti-Fibrillation Mechanism of Tetrapeptide TNGQ. International Journal of Molecular Sciences 2022;23(4):1972.
202. Maity D, Kumar S, Alhussein R, Gremer L, Howarth M, Karpauskaite L, et al. Sub-stoichiometric inhibition of IAPP aggregation: a peptidomimetic approach to anti-amyloid agents. RSC Chemical Biology 2020;1(4):225–32.
203. Dubos RJ, Cattaneo C. Studies on a bactericidal agent extracted from a soil bacillus.. Journal of Experimental Medicine 1939;70(3):249–56.
204. Hodgkin DC, Oughton BM. Appendix 2—Possible molecular models for gramicidin S and their relationship to present ideas of protein structure. Biochemical Journal 1957;65(4):752–6.
205. Hull SE, Karlsson R, Main P, Woolfson MM, Dodson EJ. The crystal structure of a hydrated gramicidin S–urea complex. Nature 1978;275(5677):206–7.
206. Linker SM, SchellhAAs C, Kamenik AS, Veldhuizen MM, Waibl F, Roth HJ, et al. Lessons for Oral Bioavailability: How Conformationally Flexible Cyclic Peptides Enter and Cross Lipid Membranes. Journal of Medicinal Chemistry 2023;66(4):2773–88.
207. Hu NW, Klyubin I, Anwyl R, Rowan MJ. GluN2B subunit-containing NMDA receptor antagonists prevent Aβ-mediated synaptic plasticity disruption in vivo. Proceedings of the National Academy of Sciences 2009;106(48):20504–9.

10 Acknowledgements

This work would not have been possible without the constant guidance of Prof. Dr. Aphrodite Kapurniotu, who played an important role in my professional and personal development. I thank her for assigning me projects that allowed me to learn and apply several techniques, and for teaching me a rigorous scientific method throughout the years. I am very thankful for her trust, support, and investment in my growth as a young researcher. Furthermore, I want to thank her for her patience and all the time she took to give me meaningful advice. Her supervision had a powerful impact on my preparation, but more importantly, my curiosity towards the amyloid research field. Finally, I want to thank her personally, as she always believed in me. She has been a very inspiring role model and a special person for my maturation.

I am thankful for having been associated with the Collaborative Research Center SFB1035 (Control of protein function by conformational switching), which represented a vital network opportunity and an excellent occasion for improving my scientific education.

I thank the late Prof. Dr. Iris Antes and Prof. Dr. Dimitri Frischmann for being my mentors.

I thank Prof. Dr. Jürgen Bernhagen for the fruitful collaboration and scientific discussions. I am also very thankful to his team at the Institute for Stroke and Dementia Research (ISD) at LMU, especially Dr. Yuan Tian, who performed the BBB permeability *in vitro* electrophysical studies.

I would like to also thank Markus Ballmann, who performed the hippocampal LTP studies reported in this thesis, and his supervisor Prof. Dr. Gerhard Rammes, at the Department of Anaesthesiology and Intensive Care at TUM Klinikum Rechts der Isar.

I also want to thank Dr. Carsten Peters and the late Prof. Dr. Sevil Weinkauf, and the Bavarian Center for Biomolecular Mass Spectrometry at TUM for the support with TEM and MALDI-MS, respectively.

I thank Dr. Adam Sorbie, Dr. Valentina Armiento and Victoria Maier for proofreading this Thesis, and Jana Jekel for her valuable suggestions.

The members of the Peptide Biochemistry group made an important direct and indirect contribution to this work. I must thank Dr. Karin Taş, who shared her knowledge with me, allowing me to learn numerous techniques, and Kathleen Hille, for her help with the synthesis and purification of the peptides. I also want to thank Dr. Eleni Malideli who supported me in my first steps in the lab, and my undergraduate students Bettina Bernard, Sarah Herterich and Rafaela Kendel who run preliminary biophysical characterization of peptides reported in my work.

Through pursuing my PhD, Dr. Christos Kontos, Dr. Valentina Armiento, Denise Naltsas, Simon Hornung and Hendrik Wunderlich have been more than colleagues. I thank them for

all the scientific discussions, for sharing their knowledge, and for the deep connection that made our daily challenges more pleasant.

Finally, I thank my family for giving me opinionated support and loving guidance, even if I was far away. This work would not have been possible without the interest and encouragement of all my beloved ones.

11 Curriculum Vitae

PERSONAL INFORMATION

- Name: Dalla Volta, Beatrice
- Degree: M.Sc. Pharmaceutical Chemist (Diploma)

EDUCATION

- Ph.D student (2019 - present): Division of Peptide Biochemistry, TUM School of Life Sciences, Technical University of Munich (TUM), supervisor: Prof. Dr. A. Kapurniotu.
- Master Thesis (Erasmus + Traineeship at Division of Peptide Biochemistry TUM School of Life Sciences, Technical University of Munich (TUM)) (2016-2017), supervisors: Professor Paolo Rovero and Prof. Dr. Aphrodite. Kapurniotu)
- M.Sc. (Diploma) (2010- 2017): Pharmaceutical Chemistry and Technology-School of Life Science,-University of Florence: "Excellent" 108/110,

WORK EXPERIENCE

- 07/2018 – present: Research associate, Division of Peptide Biochemistry, School of Life Sciences, Technical University of Munich
- 06/2017-06/2018: Research associate, Division of Protein Engineering, University of Leipzig

PUBLICATIONS

1 Karin Taş, Beatrice Dalla Volta, Christina Lindner, Omar El Bounkari, Kathleen Hille, Yuan Tian, Xènia Puig-Bosch, Markus Ballmann, Simon Hornung, Martin Ortner, Sophia Prem, Laura Meier, Gerhard Rammes, Martin Haslbeck, Christian Weber, Remco T. A. Megens, Jürgen Bernhagen, and Aphrodite Kapurniotu. Designed peptides as nanomolar cross-amyloid inhibitors acting via supramolecular nanofiber co-assembly Nat. Commun 13, 5004 (2022)

2 Christine Krammer, Christos Kontos, Manfred Dewor, Kathleen Hille, Beatrice Dalla Volta, Omar El Bounkari, Karin Taş, Dzmitry Sinitski, Markus Brandhofer, Remco T. A. Megens, Christian Weber, Joshua R. Schultz, Jürgen Bernhagen and Aphrodite Kapurniotu. A MIF-Derived Cyclopeptide that Inhibits MIF Binding and Atherogenic Signaling via the Chemokine Receptor CXCR2. ChemBioChem 22, 1012 (2021)

PRESENTATIONS

1. Poster at the 36th European Peptide Symposium and 12th International Peptide Symposium; Barcelona, Spain (2022). "Designed cyclic peptides as potent inhibitors of amyloid self-assembly of both IAPP and Aβ42". Beatrice Dalla Volta, Melanie Roth, Yuan Tian, Jürgen Bernhagen, and Aphrodite Kapurniotu.

2. Poster at the 17th Naples Workshop on Bioactive Peptides; Naples, Italy.(2022). "Molecular mechanism of inhibitory effects of designed conformationally constrained peptides on amyloid self- and cross-assembly of IAPP and Aβ42". Authors: Karin Taş, Beatrice Dalla Volta, Christina Lindner, Omar El Bounkari, Kathleen Hille, Yuan Tian,

Xènia Puig-Bosch, Gerhard Rammes, Remco T.A. Megens, Christian Weber, Jürgen Bernhagen, and Aphrodite Kapurniotu.

3. Oral Presentation at the SFB1035 Retreat; Hohenkammer, Germany (2022). Designed cyclic peptides as potent inhibitors of amyloid self-assembly of both IAPP and Aβ42.

Eidesstattliche Erklärung

Ich, Beatrice Dalla Volta erkläre an Eides statt, dass ich die bei der promotionsführenden Einrichtung
TUM School of Life Sciences, Professur Peptidbiochemie

der TUM zur Promotionsprüfung vorgelegte Arbeit mit dem Titel:
Synthesen und Untersuchungen von Wechselwirkungen und Amyloid-inhibitorischer Funktion von Peptiden mit zyklischen Konformationseinschränkungen.

unter der Anleitung und Betreuung durch:

Professor Dr. Aphrodite Kapurniotu

ohne sonstige Hilfe erstellt und bei der Abfassung nur die gemäß § 7 Abs. 6 und 7 angegebenen Hilfsmittel benutzt habe.

☒ Ich habe keine Organisation eingeschaltet, die gegen Entgelt Betreuer*innen für die Anfertigung von Dissertationen sucht, oder die mir obliegenden Pflichten hinsichtlich der Prüfungsleistungen für mich ganz oder teilweise erledigt.

☒ Ich habe die Dissertation in dieser oder ähnlicher Form in keinem anderen Prüfungsverfahren als Prüfungsleistung vorgelegt.

☒ Teile der Dissertation wurden in Karin Taş, Beatrice Dalla Volta, Christina Lindner, Omar El Bounkari, Kathleen Hille, Yuan Tian, Xènia Puig-Bosch, Markus Ballmann, Simon Hornung, Martin Ortner, Sophia Prem, Laura Meier, Gerhard Rammes, Martin Haslbeck, Christian Weber, Remco T. A. Megens, Jürgen Bernhagen and Aphrodite Kapurniotu. Designed peptides as nanomolar cross-amyloid inhibitors acting via supramolecular nanofiber co-assembly. Nat. Commun 2022;13(1):5004. veröffentlicht.

☒ Ich habe den angestrebten Doktorgrad noch nicht erworben und bin nicht in einem früheren Promotionsverfahren für den angestrebten Doktorgrad endgültig gescheitert.

☐ Ich habe bereits am _____ bei der promotionsführenden Einrichtung _____ der Hochschule _____ unter Vorlage einer Dissertation mit dem Thema _____
die Zulassung zur Promotion beantragt mit dem Ergebnis:

_____

☒ Ich habe keine Kenntnis über ein strafrechtliches Ermittlungsverfahren in Bezug auf wissenschaftsbezogene Straftaten gegen mich oder eine rechtskräftige strafrechtliche Verurteilung mit Wissenschaftsbezug.

Die öffentlich zugängliche Promotionsordnung sowie die Richtlinien zur Sicherung guter wissenschaftlicher Praxis und für den Umgang mit wissenschaftlichem Fehlverhalten der TUM sind mir bekannt, insbesondere habe ich die Bedeutung von § 27 PromO (Nichtigkeit der Promotion) und § 28 PromO (Entzug des Doktorgrades) zur Kenntnis genommen. Ich bin mir der Konsequenzen einer falschen Eidesstattlichen Erklärung bewusst.

Mit der Aufnahme meiner personenbezogenen Daten in die Alumni-Datei bei der TUM bin ich

☒ einverstanden, ☐ nicht einverstanden.

Ort, Datum, Unterschrift